



The
University
Of
Sheffield.

Synthesis and Photophysics
of Nitrogen and Sulfur Containing Heteroacenes:
Towards Emissive High Mobility Materials

Oleksandra Korychenska

University of Sheffield
Faculty of Science
Department of Chemistry

A dissertation submitted for the degree of
Doctor of Philosophy

September 2019

Declaration

The research described in this thesis is original work carried out by me at the University of Sheffield from October 2015 and September 2019. This thesis includes nothing which is the outcome of work done in collaboration except where specifically indicated in the text. The use of the first-person plural is strictly a matter of style in keeping with standard scientific convention. This dissertation has not been submitted in whole or in part for the award of a degree at this, or any other university.

- Oleksandra Korychenska

*You can't always get what you want
But if you try sometimes, well, you might find
You get what you need*

- Keith Richards and Mick Jagger

Abstract

Heteroacenes form a family of organic conjugated molecules that are well known for their extraordinary charge carrier mobility. One of the most prominent examples is 2,7-dioctylbenzothieno[3,2-*b*]benzothiophene (C8-BTBT); the reported charge mobility of this compound ranges from 0.4-31 cm²/Vs. Despite the fact that it has been well studied in transistors, the optical properties of this molecule and its derivatives remain largely unexplored. Understanding the photophysics of high mobility semiconductors could lead to improvements in solar cells, light emitting transistors and organic lasing.

We studied photophysical properties of benzothieno[3,2-*b*]benzothiophenes (BTBTs) and their nitrogen analogues - indolo[3,2-*b*]indole (ININ) derivatives in solutions and in thin films. We use steady-state and transient absorption and emission spectroscopy at a range of temperatures. We find that the photoluminescence quantum yield of BTBT derivatives in solution is extremely low (about 2%) as a result of fast (120 ps) intersystem crossing to form triplets. Such fast intersystem crossing in planar molecules is unexpected. We show that we can explain our results by considering the *ensemble* of molecular geometries in the excited state, which demonstrates the need to take molecular dynamics into account when considering spin-orbit coupling and intersystem crossing.

On the other hand, the ININ derivatives exhibit unity photoluminescence quantum efficiency in solution due to much slower intersystem crossing (~ 10 ns). Unexpectedly, the singlet state emission of these molecules persists for up to 5 μs. This delayed fluorescence does not follow the kinetics of triplet states, instead showing a power-law dependence. We discuss the origin of the long-lived emission and the several order of magnitude difference in the intersystem crossing rate between nitrogen- and sulphur-containing heteroacenes. Further, we demonstrate the change in photophysics of ININ derivatives when transitioning from a solution to solid state. We find that due to structural differences within the ININ derivatives, they exhibit very different packing and solid-state electronic behaviour.

Finally, we explore the possibility of achieving thermally activated delayed fluorescence in planar nitrogen-containing donor-acceptor heterocycles. We show our work on the attempted synthesis of these derivatives

Acknowledgments

I would like to take this opportunity to thank all of the people who supported me, taught me and helped me with science over these four years. First of all, I would like to thank my Physics supervisor Dr. Jenny Clark for her support, positive attitude, photophysics theory explanations and for believing in me. Likewise, I would like to thank my Chemistry supervisor Dr. Ahmed Iraqi, for his continuous support and optimism towards organic synthesis that kept me calm and motivated.

I also would like to thank Prof. (!) Andrew Musser for teaching me to deal with lasers and answering thousands of my questions. I really appreciated all of your great house parties, puppy pubs and board game nights.

I'd like to acknowledge my collaborators. Dr. Theo Keane, who was very excited about my projects. Dr. Dan Toolan, Dr. Sai Rajendran, Dr. Naoum Vaenas, Zahrah J Alqahtani, Guy Mayneord who provided very valuable advice and data for my projects. I also would like to thank Prof. Sophia Hayes for inviting me to work in her lab for a brief period of time. Prof. Anna Kohler and her student Stefan Wedler provided an invaluable help with understanding of multimode Frank-Condon analysis. I also like to thank the great facility managers, Dr. Sandra van Meurs for valuable NMR experiments and discussions, and Dr. Craig Robertson for his help with XRD. I would like to acknowledge the Lord Porter Laser facility users and, particularly, Dr. Dimitrii Chekulaev for technical support and advice during my PhD.

I also would like to thank fellow PhD students in both my chemistry and physics research groups. Harry Robson for keeping me safe and sane in the chemistry lab. Daniel Polak for his useful advices and fun times at the conferences. A special acknowledgement to Jozra Garrido Velasco for being my lab partner and all of the laughs we had while working together. Thanks for teaching me to say “thank you” and “please” in appropriate situations. I think I get it now. David Bossanyi for his support, optimism, superior coding skills and willingness to share them! I also would like to thank members of EPMM group: Dr. Kyriacos Georgiou and Dr. Rahul Jayaprakash for taking me in and being so generous and helpful; Harriet Coulthard for making the evaporator less terrifying for me.

I thank my parents for their constant encouragement and support. I also thank my friends Prea, Alex, Ben, Reza, Christian and Denisa for their support, life advice, great movie nights and

pub Fridays. Most of all, I would like to thank my partner Guy for his love, support, sense of humor and understanding over these years.

Table of Contents

<i>Abstract</i>	<i>i</i>
<i>Acknowledgments</i>	<i>ii</i>
<i>List of Abbreviations</i>	<i>vii</i>
<i>List of Figures</i>	<i>ix</i>
<i>List of Schemes</i>	<i>xvi</i>
<i>List of Tables</i>	<i>xviii</i>
1 Introduction	1
2 Background theory	4
2.1 Light-matter interaction	5
2.1.1 Describing molecular states	6
2.1.2 Singlet and triplet states	7
2.2 Transitions between states	9
2.2.1 Fermi's Golden Rule.....	9
2.2.2 Electronic radiative transitions	10
2.2.3 Taking vibrations into account: Frank-Condon Principle.....	11
2.2.4 Non-radiative transitions: Internal conversion and Intersystem crossing.....	15
2.2.5 Transitions between states of different multiplicity.....	17
2.3 Properties of organic semiconductors in solid state	21
2.3.1 Basic molecular packing motifs of organic molecules	21
2.3.2 Optical properties of π -conjugated molecules in solid state	23
2.3.3 Energy transfer process.....	24
2.3.4 Influence of molecular packing on optical properties of conjugated molecules	27
2.3.5 High mobility in organic solids.....	29
2.3.6 Organic field effect transistors.....	33
3 Materials and Methods	36
3.1 Materials	37
3.2 Characterization of organic compounds	37
3.2.1 Thin Layer Chromatography (TLC)	37
3.2.2 Melting points (Mp).....	37

3.2.3	Mass Spectrometry (MS)	37
3.2.4	Fourier Transform Infrared spectroscopy (FT-IR)	37
3.2.5	Nuclear magnetic resonance (NMR)	38
3.2.6	Elemental analysis	38
3.3	Materials characterization	38
3.3.1	Cyclic voltammetry (CV)	38
3.3.2	Thermogravimetric analysis (TGA).....	39
3.3.3	Differential Scanning Calorimetry (DSC)	39
3.3.4	X-Ray crystallography and diffraction	39
3.3.5	Grazing incidence X-ray scattering (GIWAXS).....	40
3.3.6	Atomic force microscopy (AFM)	41
3.4	Photophysics.....	41
3.4.1	Sample preparation for photophysics measurements.....	41
3.4.2	UV-Visible absorption.....	42
3.4.3	Steady state photoluminescence	43
3.4.4	Photoluminescence quantum yield (PLQY)	44
3.4.5	Triplet yields	45
3.4.6	Rate constants calculation.....	46
3.4.7	Laser setup	46
3.4.8	Time resolved photoluminescence spectroscopy using Time Gated Intensified Charge-Couples Device (ICCD)	47
3.4.9	Streak camera.....	49
3.4.10	Transient absorption (TA).....	49
3.4.11	Resonance Raman spectroscopy	51
3.5	Computational Methods.....	53
3.5.1	Molecular dynamics (MD) and spin-orbit coupling matrix element (SOCME).....	53
3.5.2	Frank-Condon analysis	54
3.6	Devices preparation and performance evaluation.....	55
3.6.1	OLEDs	55
3.6.2	Organic Thin Film Transistors (OFETs).....	56
3.7	Synthetic procedures	58
3.7.1	Benzothieno[3,2- <i>b</i>]benzothiophene (BTBT) derivatives.....	58
3.7.2	Indolo[3,2- <i>b</i>]indole (ININ) derivatives	65
3.7.3	Dicarbazolophenanthrene (DCP) derivatives	74
4	<i>Intersystem crossing in benzo[<i>b</i>]thiophene derivatives</i>	92
4.1	Intersystem crossing in planar organic molecules.....	93
4.2	Results and Discussion	97

4.2.1	Synthesis of benzothieno[3,2- <i>b</i>]benzothiophene	97
4.2.2	Photophysics of benzo[<i>b</i>]thiophene derivatives	101
4.3	Conclusions.....	129
5	<i>Synthesis and spectroscopy of indolo[3,2-<i>b</i>]indoles</i>	130
5.1	From indole to indolo[3,2-<i>b</i>]indoles and derivatives	131
5.2	Results and discussion	133
5.2.1	Synthesis of ININ derivatives	133
5.2.2	Photophysics of ININ derivatives in solutions	136
5.3	Conclusions.....	178
6	<i>Solid state properties of indolo[3,2-<i>b</i>]indole</i>	180
6.1	Introduction	181
6.2	Results and Discussion	182
6.2.1	Thermal properties	182
6.2.2	Single crystal X-ray diffraction (XRD) analysis	185
6.2.3	Crystallinity and morphology analysis of the films.....	190
6.2.4	Thin films characterization using grazing incidence x-ray scattering (GIWAXS).....	195
6.2.5	Thin film field effect transistors	196
6.2.6	Steady state spectroscopy of ININ derivatives in films.....	198
6.2.7	Time-resolved temperature dependent photoluminescence.....	202
6.2.8	OLEDs and electroluminescence.....	213
6.3	Conclusions.....	215
7	<i>Attempted synthesis of dicarbazolo[<i>a,c</i>]phenazines.....</i>	216
7.1	Introduction	217
7.2	Theoretical calculations	218
7.3	Synthesis of dicarbazolo[<i>a,c</i>]phenazines.....	219
7.4	Conclusions.....	240
8	<i>Summary and Outlook.....</i>	241
	<i>References</i>	244

List of Abbreviations

ININ	Indolo[3,2- <i>b</i>]indole
AFM	Atomic force microscopy
BHT	Butylhydroxytoluene
BO approximation	Born-Oppenheimer approximation
CRIP	Contact radical pair
CV	Cyclic voltammetry
DFT	Density functional theory
DMF	Dimethyl formamide
DMSO	Dimethyl sulfoxide
DSC	Differential scanning calorimetry
Eq	Equivalents
FCWD	Frank-Condon weighted density of states
FET	Field effect transistor
FT-IR	Fourier transform infrared spectroscopy
HOMO	Highest occupied molecular orbital
IC	Internal conversion
ICCD	Intensified charge coupled device
ISC	Intersystem crossing
LUMO	Lowest unoccupied molecular orbital
Mp	Melting point
MS	Mass spectroscopy
NMR	Nuclear magnetic resonance
OLED	Organic light emitting diode
PIA	Photoinduced absorption
PLQY	Photoluminescence quantum yield
PMMA	Polymethylmethacrylate
PS	Polystyrene
SOC	Spin-orbit coupling
SOCME	Spin-orbit coupling matrix element
TA	Transient absorption

TADF	Thermally activated delayed fluorescence
TGA	Thermal gravimetric analysis
THF	Tetrahydrofuran
TLC	Thin layer chromatography
TRPL	Time-resolved photoluminescence
XRD	X-Ray diffraction

List of Figures

Figure 2.1. Scheme of energy levels of molecular orbitals.....	6
Figure 2.2. Vectorial representation of spin in two-particle system.....	8
Figure 2.3. Illustration of Frank-Condon principle for absorption and emission of organic compounds.....	12
Figure 2.4. The potential energy curves (a) for the case of weak coupling and (b) for strong coupling between two states.	15
Figure 2.5. Heavy atom effect in heteroarenes.	19
Figure 2.6. Molecular packing motifs in crystals.	22
Figure 2.7. A – rubrene structure, B – orthorhombic, crystallographic structure of a single crystal of rubrene shows the enhanced π - π overlap along the ‘b’ direction and reduced overlap along the ‘a’ direction (herringbone structure).	22
Figure 2.8. Schematic illustration of stabilizing effect of intermolecular interactions on ground state and excited states energies.	23
Figure 2.9. Illustration of Förster and Dexter resonance energy transfer.	25
Figure 2.10. Schematic illustration of ground and excited state energies of two interacting molecules and their dipole arrangement, which leads to formation of J- and H-aggregate.....	27
Figure 2.11. Schematic illustration of dimer and excimer potential energy surfaces: potential energy of ground and excited states of interacting molecules as a function of the intermolecular distance.	29
Figure 2.12. The bonding–antibonding interactions between the HOMO/LUMO levels of two ethylene molecules in a cofacial configuration and the valence and conduction bands formed as a result of interaction of many molecules.	31
Figure 2.13. a) Dependence of transfer integral on the intramolecular distance between a tetracene cofacial dimer; b) Dependence of transfer integral for pentacene dimer on the tilt angle.....	32
Figure 2.14. Effect of cofacial displacement on tetracene dimer.	32
Figure 2.15. Basic scheme of field effect transistor.....	34
Figure 2.16. A - Intrachain transport, along the π -conjugation direction and interchain transport, along the π -stacking direction or alkyl stacking direction. B - edge-on orientation of the polymer molecules on the substrates.....	34
Figure 2.17. Structures and mobility values in of the organic molecules used in OFETs.....	35

Figure 3.1. Basic working principle of time-gated ICCD and the resulting data output.	49
Figure 3.2. Basic principle of transient absorption.	50
Figure 3.3. Schematic illustration of signals types in transient absorption.	51
Figure 3.4. Resonance Raman theoretical principle	52
Figure 3.5. Schematic representation of the OLED architecture (left) and picture of fabricated device and pixel emission (right).	56
Figure 3.6. Chemical structure of substances used for monolayers.	57
Figure 3.7. Schematic layout of thin film transistor (left) and a photo of fabricated device (5 transistors per substrate) (right).	57
Figure 4.1. Mechanisms of excited state relaxation in thiophene derivatives: bithiophene [72] and 2-methyl-5-phenylthiophene.	94
Figure 4.2. Structures of studied compounds.	97
Figure 4.3. Steady state photophysical properties and DFT calculations of benzo[<i>b</i>]thiophene derivatives.	102
Figure 4.4. Absorption spectra of C8-BTBT in toluene solutions of different concentration (left) and in solvents of different polarity (10 μ M).	103
Figure 4.5. Fluorescence of different concentration C8-BTBT in toluene (left) and all of the molecules in 10 μ M in toluene (right), $\lambda=320$ nm.	105
Figure 4.6. Resonance Raman spectra of benzo[<i>b</i>]thiophene derivatives in cyclohexane solutions ($\lambda=282$ nm).	107
Figure 4.7. Transient absorption spectra of benzo[<i>b</i>]thiophene derivatives in toluene solutions at $\lambda=330$ nm.	112
Figure 4.8. Triplet emission spectrum of C8-BTBT in toluene:ethanol:diethyl ether (1:1:2) mixture at 4ns time delay at 77K.	113
Figure 4.9. Spin-orbit couplings of BTBT derivatives at different temperatures, the number on each graph corresponds an overall SOC.	118
Figure 4.10. Photoluminescence decay kinetics of n-BTBT in Me-THF recorded at different temperatures using streak camera $\lambda=330$ nm.	118
Figure 4.11. Transient absorption spectra of BTBT derivatives in toluene at room temperature (solid line) and 60 $^{\circ}$ C (dotted line) at $\lambda=330$ nm.	119
Figure 4.12. Frank-Condon fitting results for solutions of benzo[<i>b</i>]thiophene derivatives in 10 μ M toluene.	121

Figure 4.13. Frank-Condon fitting results for solutions of C8-BTBT in 10 μ M toluene:ethanol:diethyl ether (1:1:2) at 77K.	122
Figure 4.14. Possible potential energy surfaces arrangements that involve one ground state, one singlet and one triplet state and the corresponding $\Delta Q_{S1 - T12}$	124
Figure 4.15. Calculated spin-orbit coupling matrix elements between S_1-T_n vs the energy gap between the involved states vs calculated Frank-Condon weighted density of states	126
Figure 4.16. Comparing calculated and experimental ISC in benzo[<i>b</i>]thiophene derivatives.	126
Figure 4.17. Steady state absorption and PL of C8-DNTT (a), transient absorption (330nm) (b), kinetics of PAI signals of singlet (600-610nm) and triplet (435-335) states (c).	128
Figure 4.18. Frank-Condon fitting results for solution of C8-DNTT in THF.	128
Figure 5.1. Structures of nitrogen containing heterocycles.	131
Figure 5.2. Absorption (left) and steady state photoluminescence spectra ($\lambda_{ex} = 330$ nm) (right) of ININ derivatives in toluene (10 μ M).	137
Figure 5.3. Absorption (left) and room temperature steady state fluorescence (right) of C8-C-inin in different solvents, $\lambda_{ex} = 330$ nm.	138
Figure 5.4. Concentration effects on absorption and steady state PL of C8-C-inin in toluene.	138
Figure 5.5. Steady state emission of C8-C-inin (10 μ M) in toluene excited at different wavelengths.....	141
Figure 5.6. Frank-Condon fitting results for ININ derivatives in 10 μ M toluene solutions.....	141
Figure 5.7. Cyclic voltammogram of ININ derivatives taken with scan rate 50 mV/s.	143
Figure 5.8. Absorption (left), fluorescence (middle) and phosphorescence (right) at 77 K of 100 μ M solutions in ethanol : diethyl ether (1:1), $\lambda_{ex} = 330$ nm.	144
Figure 5.9. Kinetic profile of the emission detected at 420-430nm in ethanol:diethyl ether (1:1) , $\lambda_{ex} = 355$ nm.....	146
Figure 5.10. Transient absorption spectra of Ph-N-inin in toluene, $\lambda_{ex} = 355$ nm.	146
Figure 5.11. Part 1. Computational excited state analysis.	147
Figure 5.12. Part 2. Computational excited state analysis.	148
Figure 5.13. Spectra of ININ series in ethanol:diethyl ether (1:1) at 77K taken at time period of 1.3-1.5 μ s, $\lambda_{ex} = 355$ nm.	149
Figure 5.14. Prompt and delayed luminescence spectra of C8-N-inin (100 μ M) at 77 K (left) and at room temperature (right).	150
Figure 5.15. Power dependence of integrated delayed emission.....	151
Figure 5.16. C8-C-inin in ethyl acetate (100 μ M) taken at 420 – 430 nm, $\lambda_{ex} = 355$ nm.	153

Figure 5.17. Chemical structure of Br-C-inin.....	153
Figure 5.18. Transient absorption spectral evolution of Br-C-inin in toluene, $\lambda=355\text{nm}$	154
Figure 5.19. Kinetics of Br-C-inin and Me-N-inin in toluene taken at 420-430 nm.	155
Figure 5.20. Transient absorption of Me-N-inin in toluene (top) and iodobenzene (bottom)..	157
Figure 5.21. Normalized steady state photoluminescence of Me-N-inin (10 μM) in toluene and iodobenzene solutions.....	157
Figure 5.22. Kinetics of Me-N-inin in toluene and iodobenzene degassed solutions taken at 420-430nm (right) and spectral evolution of emission in iodobenzene (left).....	158
Figure 5.23. Normalized absorption of Me-N-inin (600 μM) in iodobenzene before and after TA experiment.....	158
Figure 5.24. Schematic representation of electron transfer process.	159
Figure 5.25. "Trivial" mechanism of electron transfer and its application to explain photophysics of acridine.	160
Figure 5.26. Electron transfer as a result of exciplex (path A) or ground state charge transfer state formation (path B).....	161
Figure 5.27. Kinetics (left) and delayed emission spectra (right) in solutions of C8-N-inin (10 μM), $\lambda_{\text{ex}} = 355\text{nm}$	162
Figure 5.28. Kinetics of photoluminescence decay of C8-N-inin (10 μM) in THF and PMMA THF solutions	163
Figure 5.29. Absorption of C8-N-inin in polymer films, thickness of the films varied.	164
Figure 5.30. Kinetics of C8-N-inin in polymer films taken at 420-430nm (left) and spectral evolution of C8-N-inin in polystyrene film, $\lambda_{\text{ex}} = 355\text{ nm}$	164
Figure 5.31. Comparison of kinetics of C8-N-inin in polystyrene film and THF solution.	165
Figure 5.32. Radical quenchers structures.	166
Figure 5.33. Kinetics of C8-N-inin with different emission quenchers.....	166
Figure 5.34. ININ derivatives in chloroform (10 μM), $\lambda = 330\text{ nm}$ (left) and excitation scans of Ph-N-inin in THF (400 nm) and CHCl_3 (510 nm).....	169
Figure 5.35. Difference in spectral evolution of Me-N-inin solution in chloroform when prepared in oxygen and nitrogen atmosphere	169
Figure 5.36. Chloroform to other solvents transitions of Me-N-inin (10 μM) solutions.....	170
Figure 5.37. Me-N-inin in CHCl_3 (10 μM) with and without radical scavenger (BHT) at $\lambda = 330\text{nm}$ (left) and $\lambda = 355\text{nm}$ (right), inert atmosphere.	171

Figure 5.38. Absorption of Me-N-inin (left) and steady state emission of Me-N-inin in chloroform (10 μ M, degassed) with and without radical scavenger (BHT), $\lambda = 355$ nm. The solutions were irradiated with 254 nm light prior this measurement.....	171
Figure 5.39. Kinetics of Me-N-inin luminescence decay in chloroform, $\lambda=355$ nm.....	172
Figure 5.40. Me-N-inin solution in CHCl ₃ irradiated with 254 nm lamp for 20 mins without air, then 20mins with air and 50 mins with air (left) and Me-N-inin solution in CHCl ₃ made in air and after irradiation with no air.	172
Figure 5.41. NMR spectra of Me-N-inin in chloroform-d (top) and DMSO-d ₆ (bottom).	174
Figure 5.42. NMR spectra of C8-C-inin in CDCl ₃ at -10°C and -60°C.	174
Figure 5.43. NMR spectra of ININ derivatives in CDCl ₃	175
Figure 6.1. Structures of pyrrolo[3,2-b]pyrrole derivatives and corresponding hole mobility values found in literature	182
Figure 6.2. Thermogravimetric analysis results of ININ derivatives.	183
Figure 6.3. Calorimetric curves of the C8-C-inin (crystallized from toluene - left; crystallized from hexane - right) recorded at 10 °C/min.....	184
Figure 6.4. Calorimetric curves of the C8-N-inin (white needles) recorded at 10°C/min.....	185
Figure 6.5. Calorimetric curves of C8-N-inin polycrystalline sample recorded at 10°C/min. .	185
Figure 6.6. Unit cell structure of C8-N-inin single crystal.	188
Figure 6.7. Unit cell structure of C8-C-inin single crystal polymorph (1).	188
Figure 6.8. Unit cell of C8-C-inin single crystal polymorph (2).	189
Figure 6.9. Unit cell structure of Me-N-inin single crystal.....	189
Figure 6.10. Unit cell structure of Ph-N-inin single crystal.....	190
Figure 5.6.11. AFM of evaporated films: A - C8-C-inin (20 nm); B- C8-N-inin (80 nm); C- Me-N-inin (80 nm).	191
Figure 6.12. AFM of evaporated films: a - C8-C-inin (20 nm) 1 day after evaporation; b and c - C8-C-inin (80 nm) 4 months after evaporation; d - C8-N-inin (80 nm) 1 day after evaporation; e and f - C8-N-inin (80 nm) 6 months after evaporation.	192
Figure 6.13. AFM images of C8-C-inin (20 nm) obtained by continuous measurement of the film over 8 hours. The size of the image is 2×2 μ m.	192
Figure 6.14. Out-of-plane XRD pattern of C8-C-inin 80 nm film on Si/SiO ₂ substrate.	194
Figure 6.15. <i>b</i> -axis projection representing a lamella structure of C _n -BTBT derivatives.....	194
Figure 6.16. Out-of-plane XRD patterns of C8-N-inin, Me-N-inin and Ph-N-inin 80 nm film on Si/SiO ₂ substrate.....	195

Figure 6.17. GIWAXS image of the evaporated films C8-C-inin on Si/SiO ₂ substrate: left – one day old sample, right – one month old sample.	196
Figure 6.18. Steady state absorption, emission ($\lambda_{ex} = 355\text{nm}$) and PLQY of ININ evaporated (80nm) films (solid lines) compared to spectra in 10uM toluene solutions (thin solid lines). .	199
Figure 6.19. Steady state absorption and emission spectra of evaporated (60 nm) C8-BTBT film compared to 10 μM solution of C8-BTBT in toluene, ($\lambda_{ex} = 330 \text{ nm}$).....	200
Figure 6.20. Aging of C8-N-inin vacuum deposited film (80nm), $\lambda_{ex} = 355\text{nm}$	201
Figure 6.21. Aging of C8-C-inin films made by vacuum deposition, $\lambda_{ex} = 355\text{nm}$	201
Figure 6.22. Aging of Me-N-inin and Ph-N-inin films made by vacuum deposition.....	202
Figure 6.23. Kinetics of C8-N-inin evaporated (80nm) film excited state decay at different temperatures (A) and a spectral evolution at 77K (B)	204
Figure 6.24. Dependence of C8-N-inin photoluminescence intensity on temperature.....	204
Figure 6.25. Kinetics of excited state decay of C8-C-inin evaporated (80nm) film at different temperatures (A) and spectral evolution at 77K (B).....	206
Figure 6.26. Dependence of C8-C-inin photoluminescence intensity on temperature.....	207
Figure 6.27. Schematic illustration of the photophysical process in C8-C-inin film.	207
Figure 6.28. Steady state emission of Ph-N-inin evaporated film at different temperatures....	209
Figure 6.29. Dependence of Me-N-inin photoluminescence intensity on temperature.	209
Figure 6.30. Kinetics of excited state decay of Ph-N-inin evaporated film at different temperatures (A) and spectral evolution at 77K (B) and 320K (C).....	210
Figure 6.31. Schematic illustration of the mechanism of blueshift of excimer emission in a π - π stack given by Y. Shen <i>et al.</i>	211
Figure 6.32. Steady state emission of Me-N-inin evaporated film at different temperatures...	212
Figure 6.33. Dependence of Me-N-inin photoluminescence intensity on temperature.. ..	212
Figure 6.34. Kinetics of excited state decay of Me-N-inin evaporated film at different temperatures (A) and spectral evolution at 77K (B) and 320K (C).....	213
Figure 6.35. Steady state absorption and emission of C8-C-inin made by vacuum deposition (80nm) and spin-coating (57 nm)	214
Figure 6.36. Comparison of electroluminescence and photoluminescence spectra of C8-C-inin.	214
Figure 7.1. Structures of target compounds.	219
Figure 7.2. Structures and molecular weights of the possible products of the sigmatropic reorganization.	224

Figure 7.3. ^1H NMR in CDCl_3 of one of the fractions obtained from silicagel column chromatography.	225
Figure 7.4. Using cross-coupling reactions for dicarbazolo[a,c]phenazines synthesis.....	226
Figure 7.5. NMR in CDCl_3 of a monosubstituted product of the Suzuki cross-coupling reaction.	229
Figure 7.6. Structures of phosphine ligands.....	229
Figure 7.7. NMR in CDCl_3 of a disubstituted product of the Suzuki cross-coupling reaction.	231
Figure 7.8. ^1H NMR of the condensation reaction product in DMSO-d_6	238
Figure 7.9. ^1H NMR spectrum of the compound (25'), peaks assigned using COSY NMR. ...	239

List of Schemes

Scheme 4.1. Synthetic route to obtain BTBT framework.....	97
Scheme 4.2. Catalytic cycle of Sonogashira coupling reaction.....	98
Scheme 4.3. Mechanism of electrophilic thiophene ring closer.....	98
Scheme 4.4. Catalytic cycle of direct arylation ring closure.....	99
Scheme 4.5. Functionalization of BTBT core.....	99
Scheme 4.6. Friedel-Crafts acylation of benzothieno[3,2-b]benzothiophene core.....	100
Scheme 4.7. Mechanism of Wolff-Kishner reduction.....	100
Scheme 4.8. Synthesis of diBT.....	101
Scheme 5.1. Synthetic route to ININ heterocyclic core.....	133
Scheme 5.2. Functionalization of ININ core.....	135
Scheme 5.3. Synthesis of C8-C-inin.....	135
Scheme 5.4. Kumada cross-coupling reaction mechanism.....	136
Scheme 5.5. Mechanism of photoinitiated reaction of indole with chloroform.....	167
Scheme 5.6. Scheme of ININ core conjugation.....	173
Scheme 5.7. Scheme of cation-radical conjugation and its reaction with chloroform.....	176
Scheme 5.8. Proposed mechanism of delayed emission and charge-transfer complex formation between ININ and iodine and chlorine ions.....	178
Scheme 7.1. General strategy for synthesis of dicarbazolo[a,c]phenazines.....	219
Scheme 7.2. 1 st synthetic route for synthesis of dicarbazolo[a,c]phenazines (molecule M1). The numbers in brackets correspond to the numbers in Chapter 3.....	220
Scheme 7.3. Mechanism of acid catalysed reaction of carbonyl group with alcohols.....	221
Scheme 7.4. Catalytic cycle of the modified Goldberg reaction.....	221
Scheme 7.5. Proposed catalytic cycle of Buchwald-Hartwig coupling reaction.....	222
Scheme 7.6. Mechanism of Boc-protecting group cleavage.....	223
Scheme 7.7. Mechanism of formation of dicarbazolo[a,c]phenazines as a result of acid catalysed sigmatropic rearrangement of corresponding hydrazide (4).....	223
Scheme 7.8. 2 nd synthetic route to obtain dicarbazolo[a,c]phenazines.....	227
Scheme 7.9. Steps of synthesis of 2-nitrophenylboronic acid.....	227
Scheme 7.10. General catalytic cycle of Suzuki-Miyaura cross-coupling reaction.....	228

Scheme 7.11. 1st Suzuki coupling reaction method.	228
Scheme 7.12. 2nd Suzuki coupling reaction method.	231
Scheme 7.13. 3rd Suzuki coupling reaction method.	232
Scheme 7.14. Catalytic cycle of the Miyaura coupling reaction.	232
Scheme 7.15. Suzuki coupling reaction with MIDA-boronic ester.	233
Scheme 7.16. 3rd synthetic route to obtain dicarbazolo[<i>a,c</i>]phenazines.	233
Scheme 7.17. Mechanism of benzosulfonyl protection of the aminogroup.	235
Scheme 7.18. Mechanism of copper-catalysed C-N bond formation.	235
Scheme 7.19. Cyclization substrates options.	236
Scheme 7.20. Condensation and alkylation synthetic options.	237
Scheme 7.21. Mechanism of acid catalysed condensation reaction with an aromatic diamine.	237
Scheme 7.22. Synthetic strategy to obtain benzo[<i>a,c</i>]dicarbazole.	238
Scheme 7.23. Synthetic route to preparation of 2,7-dibromophenontrene.	239

List of Tables

Table 2.1. Values of spin-orbit constant for selected elements. [5].....	18
Table 2.2. Heavy atom effect on ISC rate in naphthalene derivatives. [14].....	19
Table 2.3. λ_{reorg} values (eV) for Pentacene and DT-TTF (taken from [29]).	33
Table 3.1. Photoluminescence quantum yields of the reference materials. [40]	44
Table 4.1. Intersystem crossing rates and structures of different organic molecules [ps].	96
Table 4.2. Steady state absorption and fluorescence of C8-BTBT in different solvents.....	103
Table 4.3. Steady state characteristics of benzo[<i>b</i>]thiophene derivatives in 10 μM toluene solutions.	103
Table 4.4. Quantitative results of DFT calculations.	104
Table 4.5. Raman shifts and cross sections of benzo[<i>b</i>]thiophene derivatives.....	108
Table 4.6. Calculated and measured Raman shifts, visualisation and description of corresponding vibrations.....	109
Table 4.7. Time constants of the excited states decay and generation determined by transient absorption and streak camera measurements in toluene and Me-THF.	112
Table 4.8. Energies of singlet and triplet states of BTBT derivatives at 77 K in Ethanol:Toluene:Diethyl Ether (1:2:1).	113
Table 4.9. Rate constants of excited state relaxation processes in BTBT derivatives.....	114
Table 4.10. SOCME and states coupling elements (λ) based on relaxed singlet state (S_1) geometries obtained by MD simulations on n-BTBT and diBT.....	116
Table 4.11. SOCME and states coupling elements (λ) based on geometries obtained by MD simulations on n-BTBT and diBT at different temperatures.	119
Table 4.12. Results of FC analysis of luminescence at 77 K.....	123
Table 4.13. Huang-Rhys parameters of S_1 - T_1 transition for vibrational modes coupled to fluorescence and phosphorescence in C8-BTBT and diBT at 77K.	124
Table 5.1. Results of DFT calculations on ININ molecules in toluene.	139
Table 5.2. Photophysical characterization of C8-C-inin in different solvents (onsets values).	140
Table 5.3. Photophysical characterization of ININ derivatives in toluene (10 μM).	140
Table 5.4. Frank-Condon analysis results (using equation (2.13)).	140
Table 5.5. Cyclic voltammetry results and estimation of HOMO/LUMO energy levels of ININ derivatives.	142

Table 5.6. Photophysical characterization of ININ derivatives in ethanol : diethyl ether (onset values).....	144
Table 5.7. Transient absorption and photoluminescence results.	155
Table 6.1. Results of thermal analysis of ININ derivatives.....	183
Table 6.2. XRD parameters of ININs single crystals.	187
Table 6.3. FET characteristics of C8-BTBT and C8-C-inin devices fabricated on Si/SiO ₂ substrates with different monolayers.	197
Table 6.4. Aging of TFT devices based on C8-C-inin: transistor characteristics after one month of storage.....	198
Table 7.1. Calculated vertical singlet and triplet excitation energies and oscillator strength...	219
Table 7.2. Reaction conditions for Suzuki coupling reaction (Scheme 7.11).....	230

1 Introduction

The efficient use of energy resources is essential to address the biggest challenge that humanity currently faces – climate change. It is estimated that 83% of energy used during the life cycle of a computer is spent on manufacturing. In comparison, manufacturing takes only 11% of the life cycle energy of a refrigerator. [1] The most energy demanding part of electronics production is semiconductor manufacture. To produce a commonly used semiconductor – crystalline silicon, temperatures as high as 1900°C are required. [2] Alternatively, organic molecules can be used as semiconductors, which could allow for a significant reduction in production energy intake. A crystalline organic film can usually be made at less than 100°C, thus usage of organic materials can improve sustainability of electronics devices. Other advantages of organic molecules include the possibility of an easy alteration of properties through chemical structure. This allows for absorption and emission colour tuning, tuning of crystal packing and electrical properties.

Organic molecules have already found applications in a wide range of electronic devices, such as organic light emitting diodes, thin film transistors, sensors, solar cells and photodiodes. Therefore, a large variety of materials have been developed for different applications over the years of research in organic electronics. However, the exact structure-property relationship remains to be the biggest challenge for the progress of the field. A number of the fundamental issues are still unsolved, *e.g.* controlling the rate of intersystem crossing, luminescence yields, charge carrier mobility etc. The development of a meaningful structure property relationship is challenging since it requires an interdisciplinary collaboration in order to introduce little changes in molecular structure and to study their effect on the certain physical properties of the materials.

In this thesis, we were specifically interested in structure-property relationship in planar organic molecules that exhibit high charge carrier mobility and their potential for application as light emitting materials. A combination of these properties is required for application of organic molecules in organic light emitting transistors and electrically pumped organic lasers. We started by studying an organic molecule that is reported to have one of the highest charge carrier mobilities to date, however, its photophysics has not been yet reported. We synthesised derivatives based on these molecules to achieve understanding of the radiative and non-radiative photophysical processes in these molecules.

This thesis is arranged as follows. Chapter 2 gives a background on the relevant fundamental theory. It starts with discussion of the basic principles of light absorption and emission, followed by the discussion of the spin nature of excited states. Then we focus on the rules, mechanisms and factors that have strong influence on the transitions between electronic states of the same and different multiplicity. Further we summarise the expected changes in molecular photophysics when transitioning from a solution to solid state. Finally, we discuss strategies for achieving high charge carrier mobility and application of organic molecules in field effect transistors.

Chapter 3 contains information on synthesis and structural characterization of the organic molecules used in this thesis. It also describes general sample preparation methods and outlines the techniques that were used for photophysical characterization of the molecules, along with their basic operation principles.

Chapter 4 describes the synthesis and photophysics of planar derivatives of benzo[*b*]thiophene, including a state of art hole transporting material – C8-BTBT. These molecules demonstrate a sub-nanosecond intersystem crossing (ISC), which cannot be explained by any available theoretical model when the molecule is considered to be in its equilibrium excited-state geometry. Our results can only be explained by considering the *ensemble* of molecular geometries in the excited state. These results demonstrate the need to take molecular dynamics into account when considering spin-orbit coupling and ISC. We also discuss the issue of correct approximation of the Frank-Condon weighted density of states for ISC rate calculation.

In Chapter 5 we present the synthesis and photophysics of indolo[3,2-*b*]indole derivatives. These molecules are sulfur-free analogues of the molecules discussed in the previous chapter. They exhibit high photoluminescence quantum efficiency in solution due to much slower intersystem crossing (~ 10 ns). Unexpectedly, the singlet state emission of these molecules

persists for up to 5 μs . This delayed fluorescence does not follow the kinetics of triplets, instead showing a power-law dependence. We study the origin of the long-lived emission and come to the conclusion that delayed emission is a result of electron ejection from the molecules, similar to what has been reported for indole derivatives.

In Chapter 6 we study solid state properties of indolo[3,2-*b*]indole derivatives, showing their solid state molecular arrangement and its influence on the photophysical and electronic properties. We find intermolecular interactions in these molecules result in excimer formation, which is the main radiative relaxation pathway in these molecules. We also demonstrate the state of art charge carrier mobility for one of the synthesised molecules, which is on the level of what has been reported for C8-BTBT.

In Chapter 7 we explore the possibility of achieving thermally activated delayed fluorescence in thin films with high charge carrier mobilities ($>1\text{cm}^2/\text{V}\times\text{s}$). This approach has a potential to drive new applications, such electrical-injection lasing in organic semiconductors. Aided by quantum chemical calculations, we have designed a series of planar stiff molecules with singlet-triplet gaps on the order of 0.4eV. This value is expected to be significantly reduced in the solid-state due to stabilization of the singlet, leading to singlet-triplet gaps suitable for thermally activated delayed fluorescence. We present our work on the attempted synthesis of these molecules.

Chapter 8 summarises the key findings of this thesis and suggests possible directions for the future work in this field.

2 Background theory

This chapter gives a background on the relevant fundamental theory. It starts with discussion of the basic principles of light absorption and emission, followed by the discussion of the spin nature of excited states. Then we focus on the rules, mechanisms and factors that have strong influence on the transitions between electronic states of the same and different multiplicity. Further we summarise the expected changes in molecular photophysics when transitioning from a solution to solid state. Finally, we discuss strategies for achieving high charge carrier mobility and application of organic molecules in field effect transistors.

2.1 Light-matter interaction

Absorption of light (a photon) by a molecule causes transfer of an electron from a higher occupied molecular orbital (HOMO) to a lower unoccupied molecular orbital (LUMO) (**Figure 2.1**). An electron does not stay in the excited state for a long time and returns to its original energy level. This transition is accompanied by photon emission (photoluminescence). The energy of this transition is proportional to the energy gap between the HOMO and LUMO levels. [3]

In aromatic hydrocarbons HOMO and LUMO are often formed by bonding and antibonding π -orbitals, which is the reason why organic conjugated molecules can be used as semiconductors. The main advantage of π -orbitals is that their overlap electron density is further away from internuclear axis, which results in smaller contribution of π -orbitals (compared to σ orbitals) to attractive force between nuclei. This is reflected in smaller splitting between bonding and antibonding π -orbitals compared to σ -orbitals.

The π - π^* electronic transition tends to have an energy of 2.5 ± 0.5 eV, that is suitable for absorption and emission of visible light (unlike σ - σ^* transition). In addition, it has high molecular absorption coefficients and radiative decay rate. The energetic position of the HOMO and LUMO π -orbitals is around -5 eV and -2 eV compared to vacuum (respectively) and is suitable for electron and hole injection from a readily available electrode materials (*e.g.* indium-tin-oxide, calcium, aluminium etc). π -orbitals allow efficient electron delocalization, which can result in efficient charge transfer. The combination of these properties is desirable for optoelectronic applications. Therefore, organic aromatic compounds with π -electron systems are of particular interest for applications in organic electronics. [4]

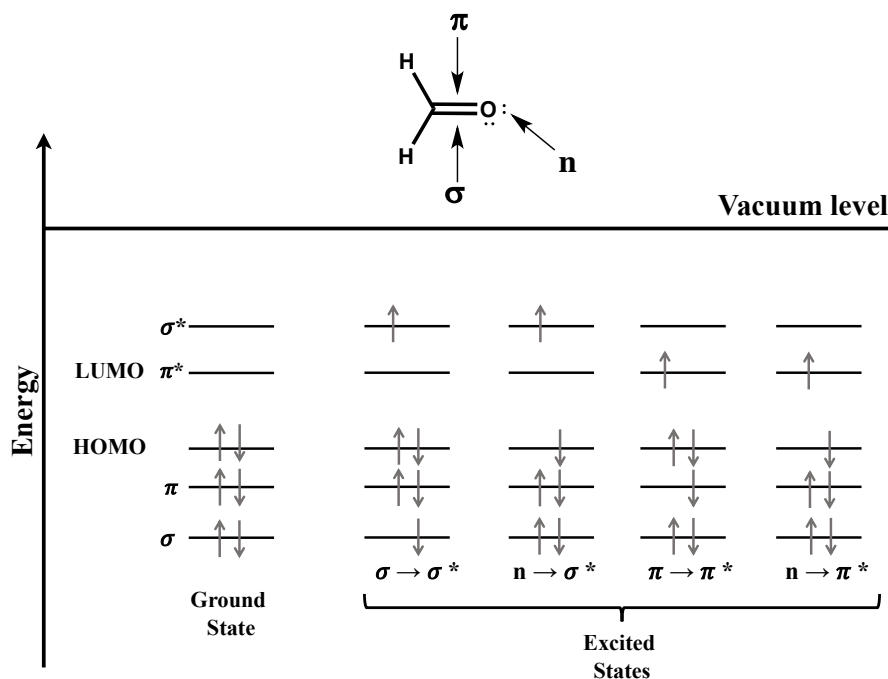


Figure 2.1. Scheme of energy levels of molecular orbitals. Horizontal lines represent orbitals; arrows represent electron spin configuration. [3]

2.1.1 Describing molecular states

Figure 2.1 is a simplistic representation of molecular orbitals and electronic transitions between them. It does not take into account electron-electron interactions, *e.g.* Coulomb and exchange interactions and spin of the electrons. To take these into account requires a different representation. The process of light absorption can be discussed in terms of transition between ground and excited states. The ground state is the lowest possible state of the molecule. Its energy is arbitrarily set to zero. Note that this is unlike the HOMO and LUMO energies, since HOMO and LUMO are orbitals and electrons in orbitals are bound to nuclei, thus, their energy has to be below vacuum energy (0 eV). [4]

In quantum mechanics electronic states can be described by total molecular wavefunctions (Ψ_{total}), which contain information about electrons' spatial coordinates and the position of the nuclei. Accurate description of molecular states is one of the current challenges of quantum mechanics and is beyond the scope of this thesis. Here we use a set of widely accepted approximations to describe our experimental observations.

Electronic excitation happens within 10^{-15} s, but the characteristic time of molecular vibrations is longer than that (10^{-10} - 10^{-12} s). On this basis, the *Born-Oppenheimer (BO)*

approximation states that electrons move much faster than nuclei following the interaction with the electromagnetic field. This approximation allows us to talk about electronic and vibrational processes separately. However, when there is a significant interaction between electrons and vibrations (nuclear movement), the BO approximation can break down, which will be discussed further in this chapter.

The accurate description of an excited state of a molecule is impossible without taking into account spin of the involved electrons. Spin (S) is a fundamental property of electrons. It represents the inherent angular momentum of an electron. The value of the spin of an electron is $\pm 1/2$. The spin of a state is determined by the total spin of all of the electrons on all of the orbitals that compose the state. Paired electrons give a zero contribution to the total spin and, thus, ground states of the majority of organic molecules have a zero spin. [5] The spin of a system is described by the spin wavefunction (spin wavefunction of one-electron states are further labeled α or β). As a result, the total molecular wavefunction can be described as a product of electron, vibrational and spin wavefunctions:

$$\Psi_{total} = \Psi_{el} \Psi_{vib} \Psi_{spin} \quad (2.1)$$

where Ψ_{el} can be approximated as a sum of one-electron wavefunctions of molecular orbitals, each molecular orbital can, in turn, be described as a sum of one-electron atomic electron wavefunctions. [4]

2.1.2 Singlet and triplet states

In this section, we will further consider the spin of the electrons involved in transitions between electronic states. In an electronic excited state, the unpaired electrons of π and π^* (HOMO and LUMO) orbitals form a two-particle system that has four eigenstates. Only certain orientations of spin in a magnetic field are quantum mechanically allowed, these orientations are given by the spin multiplicity. Multiplicity equals $2S+1$, where S stands for the total spin value. Therefore, for $S=0$, there is only one possible orientation (one eigenstate). $S=1$ gives three possible orientations and, thus, three eigenstates. The vectorial representation of these eigenstates is given in **Figure 2.2**.

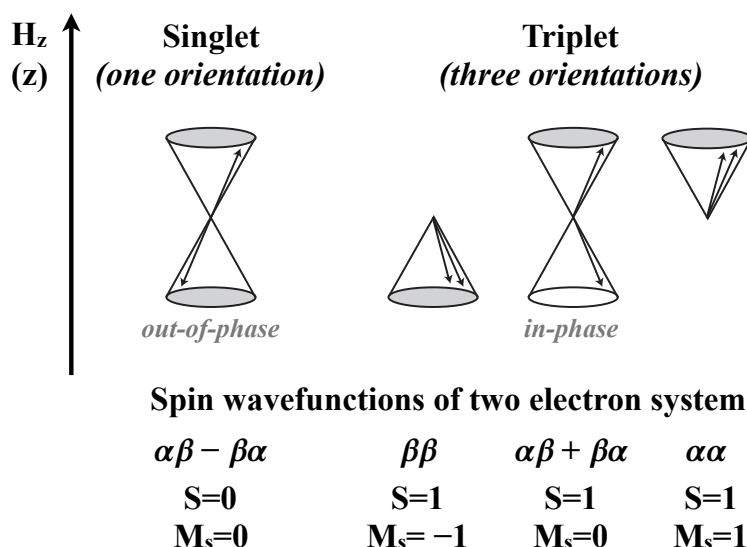


Figure 2.2. Vectorial representation of spin in two-particle system, showing cones of possible orientations of two electrons in singlet and triplet states according to uncertainty principle. Reprinted from [6]. Copyright 2009, with permission from Elsevier.

Spin has a significant influence on the energies of electronic states. The difference in energies between the first triplet and the singlet states is determined by twice the value of the exchange integral, which depends on the overlap of electrons' wavefunctions in the HOMO and LUMO. Small overlap of electron wavefunctions yields small singlet-triplet splitting, this phenomenon is readily demonstrated in materials that possess thermally activated delayed fluorescence. [7]

In the case of light absorption (optical excitation), the spin of the transferred electron remains unchanged, therefore only singlet excited states are initially created. Excited states are also created during electrical excitation in diode configuration, where a film of semiconducting material is sandwiched between two electrodes. In this case, an electron is injected into the LUMO and another electron is withdrawn from the HOMO (a hole is created). In the case of electrical excitation, the spin of the system is not preserved, so both singlet and triplet excited states are generated. The proportion of singlet to triplet states formed during electrical excitation is 1:3. Hence triplets are the majority excited state in organic light emitting diodes. [4]

The spin nature of the excited state is extremely important because the properties of these two types of excited states are very different and this has to be considered when using organic molecules as semiconductors, light emitters etc.

2.2 Transitions between states.

2.2.1 Fermi's Golden Rule.

Absorption and emission cause a change in overall energy of the system. This can be represented through a change in the energy operator of the system (Hamiltonian):

$$\hat{H} = \hat{H}_0 + \hat{H}' \quad (2.2)$$

\hat{H}_0 is the initial Hamiltonian that corresponds to the energy of the system in its initial state. \hat{H}' represents a perturbation that produces a small change in overall energy of the system. On the basis of above, the rate of the transition (k_{if}) between initial and final states can be expressed by Fermi's Golden Rule:

$$k_{if} = \frac{2\pi}{\hbar} |\langle \Psi_f | \hat{H}' | \Psi_i \rangle|^2 \rho \quad (2.3)$$

ρ is the density of final states. This is the number of states of Ψ_f that are of a similar energy to Ψ_i and those that are capable of being in resonance with Ψ_i through the perturbation (\hat{H}'). The higher the density of states, the more probable the transition. The density of states is a very important parameter, which ensures energy conservation.

Fermi's golden rule is applicable to all types of transitions caused by weak perturbations (weak in comparison to the energy separation between Ψ_f and Ψ_i) such as electronic, vibrational and spin transitions.

Within the BO approximation, the total molecular wavefunction components (equation (2.1)) can also be incorporated into the Fermi's Golden rule expression:

$$\begin{aligned} k_{if} &= \frac{2\pi}{\hbar} \rho |\langle \Psi_{el,f} \Psi_{vib,f} \Psi_{spin,f} | \hat{\mu} | \Psi_{el,i} \Psi_{vib,i} \Psi_{spin,i} \rangle|^2 = \\ &= \frac{2\pi}{\hbar} \rho |\langle \Psi_{el,f} | \hat{\mu} | \Psi_{el,i} \rangle|^2 |\langle \Psi_{vib,f} | \Psi_{vib,i} \rangle|^2 |\langle \Psi_{spin,f} | \Psi_{spin,i} \rangle|^2 \end{aligned} \quad (2.4)$$

$\hat{\mu}$ is dipole operator which represents interaction with the electromagnetic field. The spin and vibrational wavefunctions are insensitive to dipole operator. [4][5]

2.2.2 Electronic radiative transitions

2.2.2.1 Selection rules of electronic transitions

- *Momentum conservation.* Photons possess one unit of angular momentum. Due to momentum conservation requirement, in the event of light absorption or emission, the angular momentum of a molecule has to change by exactly one unit. Which in other words means that the transition between orbitals must create or destroy a node. [5]
- *Spin.* The dipole operator acts only on electronic part of the wavefunction. States of different multiplicity are orthogonal, thus, transitions between states of different multiplicity are spin forbidden. Singlet-singlet transitions, such as fluorescence are allowed and carry significant oscillator strength. Singlet-triplet transitions are spin forbidden. However, this rule can be relaxed through multiple mechanisms, which is further discussed in section 2.2.5.
- *Symmetry selection rules.* Transitions between electronic states result from interaction of molecular dipole moment with electromagnetic radiation. The dipole moment operator can be split in to three components along the Cartesian axes:

$$\langle \Psi_{el,f} | \hat{\mu} | \Psi_{el,i} \rangle = \langle \Psi_{el,f} | \hat{\mu}_x | \Psi_{el,i} \rangle + \langle \Psi_{el,f} | \hat{\mu}_y | \Psi_{el,i} \rangle + \langle \Psi_{el,f} | \hat{\mu}_z | \Psi_{el,i} \rangle \quad (2.5)$$

where Ψ_f and Ψ_i are the molecular electronic wavefunctions of the final and initial states (respectively).

The probability of an electronic transition is non-zero when one of the integrals is non-zero, which could happen only if the direct product of $\Psi_{el,f} \hat{\mu} \Psi_{el,i}$ contains a totally symmetrical irreducible representation (the character of all symmetry operations of all the relevant point groups is +1). The symmetry properties of the dipole moment along a specific Cartesian axis are the same as those of translation vectors along the corresponding axis (T_x , T_y , T_z). [8] This rule allows to explain low intensities of absorption and emission in a $n \rightarrow \pi^*$ transition in formaldehyde, which is orbital symmetry forbidden. To make any predictions about more complicated molecules one would have to carry out calculations to figure out the symmetry of the HOMO and LUMO.

Electronic transitions in molecules that possess a centre of symmetry with their wavefunctions being symmetric (gerade - *g*) or antisymmetric (ungerade - *u*) must occur with a change of symmetry. This is due to the symmetry of dipole moment vector being

ungerade. Therefore, transitions between states of u and g symmetry are allowed, whereas transitions between u and u or g and g are symmetry forbidden. [9]

2.2.2.2 Oscillator strength

Experimentally the selection rules and the probability of electronic transition are reflected in oscillator strength. Absorption of light by a molecule causes an oscillation of the electrons involved in transition, the size of a created dipole (the strength of the oscillator) is related to the strength of light absorption (or emission). Oscillator strength (f) can be calculated using the following equation:

$$f = \frac{4.39 \cdot 10^{-9}}{n} \int \varepsilon(\nu) d\nu \quad (2.6)$$

where $\varepsilon(\nu)$ is the molar extinction coefficient at a wavenumber ν (cm^{-1}), which can be determined experimentally by evaluation of absorption spectra. n is the refractive index of the environment. The oscillator strength is a very important value, it is directly related to excited state radiative lifetime through the Strickler-Berg equation:

$$\frac{1}{\tau} = 2.88 \times 10^{-9} n^2 \nu^2 \int \varepsilon(\nu) d\nu \quad (2.7)$$

Oscillator strength is also related to matrix element of dipole transition:

$$f = 4.7 \times 10^{29} \langle \nu \rangle |\langle \Psi_{el,f} | \hat{\mu} | \Psi_{el,i} \rangle|^2 \quad (2.8)$$

$\langle \nu \rangle$ is average frequency in cm^{-1} .

High oscillator strength (approaching unity) is a basic characteristic of strong absorption and emission. This value for π - π^* transitions is usually in the range of 10^{-2} to 1. When HOMO and LUMO are spatially separated, the oscillator strength tends to decrease which results in a weak absorption and fluorescence, *e.g.* an n - π^* transition has an oscillator strength in the range of 10^{-5} to 10^{-3} . [4]

2.2.3 Taking vibrations into account: Frank-Condon Principle

The Frank-Condon principle is based on the BO approximation: electronic transitions occur without changes in the position of nuclei, resulting in a so-called Frank-Condon state (vertical transition). [3] This principle is illustrated in **Figure 2.3**.

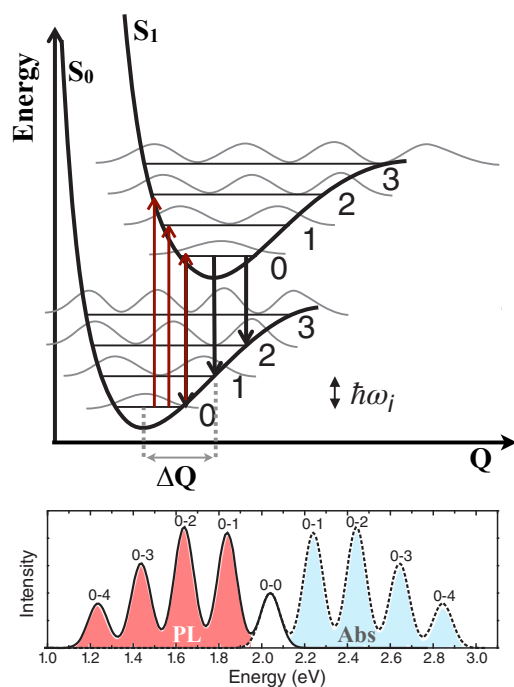


Figure 2.3. Illustration of Frank-Condon principle for absorption and emission of organic compounds. [4]

According to Fermi's golden rule, one of the rate-determining factors for a transition is an overlap of vibrational wavefunction. The square of the overlap is called the Frank-Condon factor:

$$F = |\langle \psi_{vib,f} | \psi_{vib,i} \rangle|^2 \quad (2.9)$$

where $\Psi_{vib,i}$ and $\Psi_{vib,f}$ are the vibrational wavefunctions of the initial and final states. The factor itself represents the probability of transition from the 0th vibration level of the initial state to the mth vibrational level of the final state.

The Frank-Condon factor is related to the nuclear displacement (ΔQ) through a series of important equations:

$$I_{0 \rightarrow m} = |\langle \psi_{vib,m} | \psi_{vib,0} \rangle|^2 = \frac{S^m}{m!} e^{-S} \quad (2.10)$$

where $I_{0 \rightarrow m}$ is the probability of a transition between 0 and m vibrational states, S is Huang-Rhys parameter. The Huang-Rhys parameter represents nuclear displacement and is essentially the number of quanta involved in vibrational excitation:

$$S = \frac{1}{2} k \frac{\Delta Q^2}{\hbar \omega} \quad (2.11)$$

where ΔQ is displacement of the minima of the potential energy surface along the configurational coordinate upon excitation and k is the force constant associated with the vibration. Typical vibrational quanta have energies in range of 10-300 meV, therefore, only lowest vibrational levels are occupied at room temperature.

The FC factor is small between states with energy separation larger than 2.17 eV (50 kcal/mol), however, it becomes more significant for radiationless transitions between excited states (both internal conversion and intersystem crossing). Here we will consider the Frank-Condon factor's role in radiative transitions. In this case, the Frank-Condon factor determines the relative intensities of vibrational bands in electronic absorption and emission spectra, and it is directly related to resonance Raman cross-sections of an electronic transition. [10]

The Huang-Rhys parameter can be determined as a relation of the intensity of 0-0 and 0-1 vibronic peaks in absorption or emission spectra:

$$S = \frac{I_{0-1}}{I_{0-0}} \quad (2.12)$$

Normalized intensities of absorption and emission spectra can be modelled using the following equations:

$$I_{PL}(\hbar\omega) = [n(\hbar\omega) \cdot \hbar\omega]^3 \cdot \sum_m \frac{S^m}{m!} e^{-S} \cdot \Gamma(\hbar\omega - (\hbar\omega_0 - mE^{vib})) \quad (2.13)$$

$$I_{Abs}(\hbar\omega) = [n(\hbar\omega) \cdot \hbar\omega] \cdot \sum_m \frac{S^m}{m!} e^{-S} \cdot \Gamma(\hbar\omega - (\hbar\omega_0 + mE^{vib})) \quad (2.14)$$

E^{vib} is the vibrational quanta energy, $n(\hbar\omega)$ is the refractive index at transition energy $\hbar\omega$, $\hbar\omega_0$ is the 0-0 transition energy. The width of a band in the absorption spectra is affected by the existence of many vibrational sublevels – homogeneous broadening. However, broadening of the spectra can also result from chromophore – solvent interaction (or fluctuation in solvation shell) – inhomogeneous broadening. For the case of inhomogeneous line broadening, a lineshape function Γ should be Gaussian function:

$$\Gamma = \exp\left(-\frac{(\hbar\omega)^2}{2\sigma^2}\right) \quad (2.15)$$

where σ is width of Gaussian. [4]

This model allows accurate determination of Huang-Rhys parameter from experimental data. Equations (2.13) and (2.14) use a single dominating (effective) vibrational mode, which is

correct for spectra collected at room temperature since low frequency vibrations cannot be resolved due to inhomogeneous broadening. When several vibrational modes (or several effective vibrational modes, due to limits of experimental resolution) couple to an electronic transition, and they can be visibly distinguished, a more complex equation must be used for modelling:

$$I_{PL}(\hbar\omega) = [n(\hbar\omega) \cdot \hbar\omega]^3 \cdot \sum_{m_i} \left[\left(\prod_i \frac{S_i^{m_i} \exp(-S_i)}{m_i!} \right) \Gamma \left[\hbar\omega - \left(\hbar\omega_0 - \sum_i m_i E_i^{vib} \right) \right] \right] \quad (2.16)$$

In the first sum, the value of m corresponds to the number of vibrations that are involved, *e.g.* for four vibrations there would need to be four sums. The intensities of the peaks are given by the product in brackets, which is essentially the product of single mode FC factors. The sum inside the lineshape function relates to a shift of the vibrational peak from 0-0 peak, for multimode function, this shift would correspond to each combination of a number of vibrational excitation and corresponding vibrations.

The Huang-Rhys parameter is very valuable because it allows to calculate the reorganization energy of a transition on the basis of experimental data. The geometric reorganization energy (λ_{reorg}) is related to Huang-Rhys parameter [4]:

$$\lambda_{reorg} = S \cdot E_{vib} - \text{for single vibrational mode} \quad (2.17)$$

$$\lambda_{reorg} = \sum_i S_i \cdot E_i^{vib} - \text{for multiple vibrational modes} \quad (2.18)$$

In the case of light absorption or emission, this energy is released as a result nuclei relaxation into an equilibrium geometry of an electronic state. The reorganization energy is an important parameter for radiative and non-radiative optical transitions, as well as being crucial for charge transport in organic semiconductors or charge transfer in charge transfer complexes and solar cells. [11][12]

2.2.4 Non-radiative transitions: Internal conversion and Intersystem crossing

2.2.4.1 Energy Gap Law

The energy gap law considers nonradiative transitions between two electronic states. This generally occurs from the 0th vibrational level of the initial into nth vibrational level of the final electronic state. The rate of the nonradiative transitions depends on the Frank-Condon factor. The value of FC factor changes with the energy gap (the energy difference between an initial and final states) value. Two cases need to be considered: weak and strong electron-vibrational coupling limits (**Figure 2.4**).

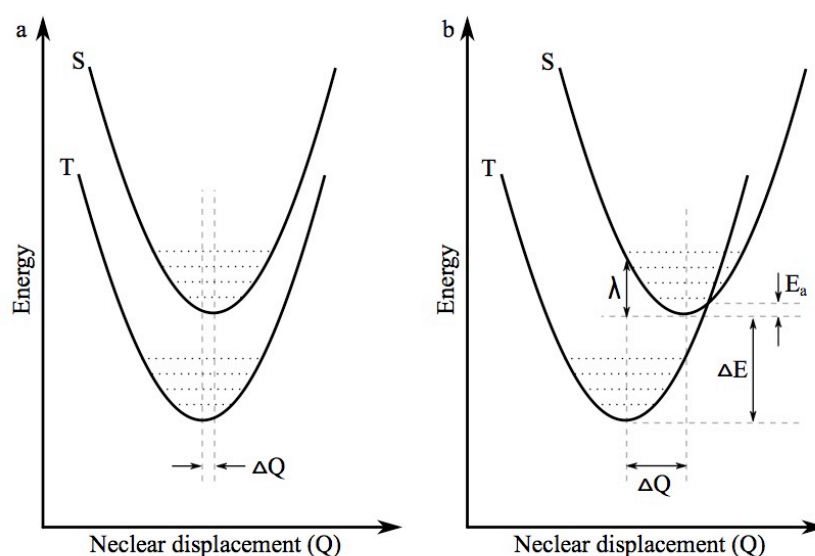


Figure 2.4. The potential energy curves (a) for the case of weak coupling and (b) for strong coupling between two states. Adopted from ref. [13]. Copyright 1970 Taylor&Francis.

The weak coupling limit is used for potential energy surfaces that are displaced only slightly and intersect far away from the minimum of the upper energy surface (**Figure 2.4a**). In this limit, only one, the highest frequency (ω_m), vibrational mode of the final state is considered. The nonradiative transition rate has an exponential dependence on the energy gap:

$$k_{if} \propto \exp\left(-\frac{\Delta E}{\hbar\omega_m}\right) \quad (2.19)$$

where ΔE is the energy gap between the equilibrium geometries of states. Most of the organic aromatic molecules will exhibit nonradiative relaxation that follows the exponential decay and, hence, weak coupling limit.

The weak coupling limit explains the isotope effect on nonradiative decay rate in aromatic compounds. The vibrational frequency ω_m depends on mass of the atoms involved:

$$\omega_m = \sqrt{\frac{k}{m_{eff}}} \quad (2.20) \quad m_{eff} = \frac{m_1 m_2}{m_1 + m_2} \quad (2.21)$$

k is the force constant and m_{eff} is the effective mass.

Therefore, introduction of the heavier atom into the molecule can potentially change the highest vibrational mode. This is true for substituting C-H (3000 cm^{-1}) to C-D (2200 cm^{-1}), that results in reduction of the nonradiative decay rate.

The strong coupling limit (**Figure 2.4b**) applies when the potential surface minimum of the initial state and final states are strongly displaced, and the potential energy surfaces intersect near the potential energy minimum of the excited state. This case can be considered for compounds where the bond length can change significantly during a nonradiative transition from one state to the other. For the “low” temperature case, when $\hbar\omega \gg kT$, the nonradiative rate constant has a Gaussian dependence on the energy gap:

$$k_{if} \propto \frac{1}{\sqrt{\lambda_{reorg}}} \exp\left(-\frac{2E_a}{\hbar\omega}\right) \quad (2.22)$$

where:

$$E_a = \frac{(\Delta E - \lambda_{reorg})^2}{4\lambda_{reorg}} \quad (2.23)$$

In this equation λ_{reorg} is reorganization energy. As a rule of thumb: $\sum_j S_j \gg 2$ corresponds to strong coupling regime and $\sum_j S_j \leq 1$ corresponds to weak coupling. [4], [13] In the strong coupling limit the rate is controlled not by the highest energy vibration but by an effective mode of mean energy and it can be any (or all) of the vibrations. This is why nonradiative transitions governed by the strong coupling limit do not exhibit an isotope effect.

For ISC, the reorganization energy is the energy variation in the initial singlet excited state when switching from singlet equilibrium geometry to triplet equilibrium geometry. [14]

2.2.5 Transitions between states of different multiplicity

2.2.5.1 Spin-orbit coupling

Spin-orbit coupling (SOC) plays a crucial role in the transitions between states of different multiplicities and allows spin-forbidden processes (such as phosphorescence and ISC) to happen. SOC is a relativistic effect that can be described by the interaction of two magnetic fields: the one due to relative nuclear motion and the other due to electron spin motion. If SOC between states is large they no longer can be classified as states of “pure” multiplicity. [15]

SOC was introduced in fully relativistic one-particle theory for spin – 1/2 systems. In this theory, spin and angular momentum are not separately conserved, instead only the resulting total electronic angular momentum is meaningful. Of course, this theory is not very useful for many electrons complex chemical systems and requires a lot of approximations. For the case of multi-particle systems, the Breit-Pauli SOC operator is commonly used, and it can be written for one or two electrons [16]:

$$\hat{H}_{SO}^{BP} = \underbrace{\frac{1}{2m_e^2 c^2} \sum_I \sum_i \frac{Z_I}{r_{iI}^3} (\hat{r}_{iI} \times \hat{p}_i) \cdot \hat{s}_i}_{\text{one-electron term}} - \underbrace{\frac{1}{2m_e^2 c^2} \sum_i \sum_{j \neq i} \frac{1}{r_{ij}^3} (\hat{r}_{ij} \times \hat{p}_i) \cdot (\hat{s}_i + 2\hat{s}_j)}_{\text{two-electron term}} \quad (2.24)$$

$\hat{r}_{iI} \times \hat{p}_i$ is the angular momentum of electron i with respect to nuclei I , $\hat{r}_{ij} \times \hat{p}_i$ is the angular momentum of electron i with respect to electron j and s_i – spin-operator of electron i .

The first (one-electron term) describes interaction between the magnetic spin moment of an electron with the magnetic moment induced by it orbiting in the nuclei electrostatic field. The second term takes into account the presence of a second electron that orbits a different nucleus; thus, the electrostatic field is generated by another electron rather than the nucleus (as in the one-electron term). This term is important for molecules composed only of “light” elements. [16]

2.2.5.2 Heavy atom effect

If the two-electron term of Breit-Pauli operator is ignored, SOC can be expressed in a simplistic way as:

$$H_{SO} \sim \zeta_{SO} \mu_S \mu_L \quad (2.25)$$

where μ_S is the magnetic moment due to the electron's spin angular momentum, μ_L is the magnetic moment due to the electron's orbital angular momentum and ζ_{SO} is the spin-orbit coupling constant which is representative of the nuclear charge that the electron "sees". [5]

The spin-orbit coupling constant is the key element to a 'heavy atom effect' (**Table 2.1**).

Table 2.1. Values of spin-orbit constant for selected elements. [5]

Atom	Atomic number	$\zeta_{SO}(\text{kcal}\cdot\text{mol}^{-1})$	$\zeta_{SO}(\text{cm}^{-1})$
C	6	0.1	35
N	7	0.2	70
O	8	0.4	140
S	16	1	350
Cl	17	1.7	595
Br	35	7.0	2400
I	53	14.0	4900

For atoms, a spin-orbit coupling constant is due to the Coulomb nature of the field and is proportional to Z^4 (Z -atomic number). The larger the nucleus charge, the larger the magnetic field that it produces, and thus the larger the spin-orbit coupling. However, for more complex potentials (many-electron systems), the atomic number dependence will not necessarily be Z^4 . [15] This also means that for the "heavy atom effect" to happen the electron that is involved in the nonradiative transition must be in the proximity of a heavy atom to allow close approach to the nucleus (*i.e.* orbital with some s character). The spin-orbit coupling constant for organic molecules that have only atoms from first two rows of the periodic table ("light" atoms, *e.g.* H, N, O, F) is usually smaller ($3.5 - 35 \text{ cm}^{-1}$) than vibrational energies ($175 - 1700 \text{ cm}^{-1}$). However, for "heavy" atoms the value of the constant can exceed the vibrational energy. [5]

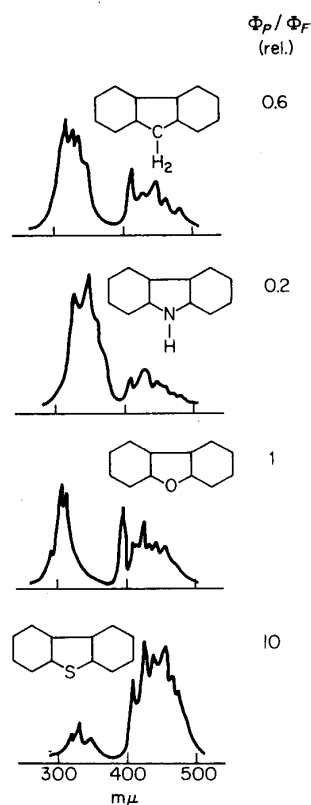
The spin-orbit coupling has an effect on the rate of spin-forbidden transitions, such as ISC.

Table 2.2 features the influence of the heavy atoms on the ISC rate in naphthalene derivatives.

Table 2.2. Heavy atom effect on ISC rate in naphthalene derivatives. [14]

Molecule	k_{ISC} (sec ⁻¹)
Naphthalene	$\sim 10^5$
1-Chloronaphthalene	$\sim 1.5 \times 10^7$
1-Bromonaphthalene	$\sim 5 \times 10^8$
1-Iodonaphthalene	$>3 \times 10^9$

This effect is also observed in heteroacene compounds with no heavy atoms. **Figure 2.5** shows the effect of heavier atom compared to carbon on the ratio of the quantum yield of phosphorescence and fluorescence and it is clear that even small increase in SOC has a pronounced effect on ISC and phosphorescence rates. [15] However, the “heavy atom effect” cannot by itself explain the trend.

**Figure 2.5. Heavy atom effect in heteroarenes. Reprinted from ref. [15].**

The heavy atom effect has a different influence on the scaling of transition rate constants and SOC constant itself. This follows from Fermi’s golden rule (equation (2.3)) expression of the ISC rate constant on the integral value between the two states involved:

$$k_{ISC} = \frac{2\pi}{\hbar} \langle \Psi_{T_m} | \widehat{\mathcal{H}}_{SOC} | \Psi_{S_n} \rangle \rho \quad (2.26)$$

Ψ_{T_m} – wavefunction of the triplet state, Ψ_{S_n} - wavefunction of the singlet state. This integral is usually referred to as the spin-orbit coupling matrix element (SOCME). Thus, the rate of a transition depends on the nature of involved electronic states. This is fundamental basis of the El-Sayed's rule. [5][14]

2.2.5.3 El-Sayed's rule

The rule is based on publication by *El-Sayed* [17] in which he concluded that the size of SOCME is determined by symmetry and the electronic configuration of the interacting molecular orbitals. The general concept of this rule is based on the requirement of momentum conservation during intersystem crossing. To conserve the total angular momentum of a system, the change in spin angular momentum must be compensated by a change in orbital angular momentum.

The main conclusion is that the transition will be fast if the states that are involved have a different symmetry with respect to molecular plane reflection and the transition involves a different orbital type. The rule explains why transitions between $(n, \pi^*)^1$ and $(\pi, \pi^*)^3$ are faster than transitions between $(\pi, \pi^*)^1$ and $(\pi, \pi^*)^3$. [18] Therefore, it basically can be applied to explain the rate of ISC and phosphorescence in a huge number of organic molecules. The rule is based on the one-electron term of the SOC operator and, of course, the rotation symmetry of the orbital angular momentum. It only takes into account electronic states of pure multiplicity with a fixed nuclear geometry (so-called “direct mechanism”).

2.2.5.4 Vibronic (nonadiabatic) coupling and Spin-Vibronic Coupling

The Born-Oppenheimer approximation allows to treat the electronic wavefunction separately from the vibrational wavefunction based on assumption that electrons move much faster than nuclei. However, it is often the case that vibrations play significant role in transitions between excited states. The nuclear geometry changes upon excitation and, in some cases, its evolution leads to breaking of BO approximation. [14] As a rule of thumb, vibronic interactions do not significantly affect states with energy separation greater than 2.17 eV. [5] Therefore, vibronic coupling needs to be taken into account when considering ISC and IC in organic molecules. [5]

Spin-vibronic coupling can be described using the second order perturbation theory and theoretical modelling of this process is very complicated. In basic terms, spin-vibronic coupling makes spin-forbidden transitions partially allowed *via* coupling to specific vibrations that are responsible for spin-allowed transitions. A classic example of the consequence of spin-vibronic coupling is phosphorescence of benzene. In benzene, the transition between the first triplet state ($^3B_{1u}$) and the ground state ($^1A_{1g}$) is orbital and spin-forbidden. Nonetheless, phosphorescence is still observed because of intensity borrowing (or mixing) from the $^1B_{2u} \leftrightarrow ^1A_{1g}$ transition (the transition that results in fluorescence of benzene). The latter transition is also orbital forbidden, but this condition is relaxed *via* vibronic coupling to $^1E_{1u} \leftrightarrow ^1A_{1g}$ and $^1A_{2u} \leftrightarrow ^1A_{1g}$ allowed transitions. [15]

2.3 Properties of organic semiconductors in solid state

2.3.1 Basic molecular packing motifs of organic molecules

Molecular packing is a crucial property that determines photophysical and charge transport behaviour of organic solids. There are four packing motifs in organic crystals (**Figure 2.6**):

- herringbone packing without π - π overlap between adjacent molecules and face to edge interaction between aromatic moieties (A);
- herringbone packing with π - π overlap between adjacent molecules and face to face interaction (B);
- lamellar packing (slipped stacking) with one-dimensional π - π overlap (stacking) (C);
- lamellar packing with two-dimensional π -stacking (D). [19]

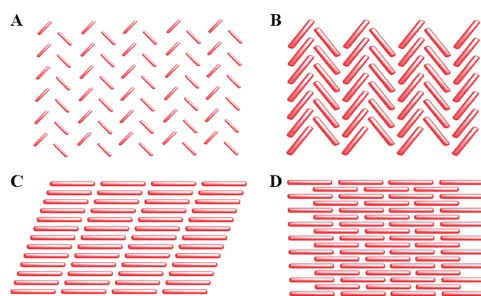


Figure 2.6. Molecular packing motifs in crystals. Reprinted with permission from [19].

Copyright 2012, American Chemical Society.

Packing type B and D usually allow two-dimensional charge transport, where charge carrier mobility is significantly lower between layers than within the layer. This effect is called mobility anisotropy and was reported for rubrene single crystal transistor (**Figure 2.7**). Mobilities measured along the ‘a’ and ‘b’ axes are $4.4 \text{ cm}^2\text{V}^{-1}\text{s}^{-1}$ and $15.4 \text{ cm}^2\text{V}^{-1}\text{s}^{-1}$ respectively. [20]

A lot of organic molecules adopt herringbone molecular packing which allows to avoid energetically unfavourable repulsive electronic interactions and to increase the packing efficiency. This type of packing could produce a significant π - π overlap. Generally, packing that allows for a significant π - π overlap results in organic solids with high charge carrier mobility but the emission from such solids is often quenched completely. A lot of research has been done on the strategies of crystal engineering to promote the desirable optical or transporting. [19][21][22][23] The approaches to enhance one or the other are quite different and, thus, creating a material that is both emissive and shows efficient charge transport remains challenging.

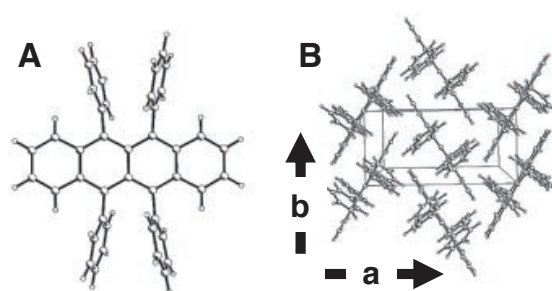


Figure 2.7. A – rubrene structure, B – orthorhombic, crystallographic structure of a single crystal of rubrene shows the enhanced π - π overlap along the ‘b’ direction and reduced overlap along the ‘a’ direction (herringbone structure). From [20]. Reprinted with permission from AAAS.

2.3.2 Optical properties of π -conjugated molecules in solid state

Van-der-Waals interactions of a chromophore with the environment such as solvent or other chromophore molecule results in lowering of the electronic states energies. This is observed in absorption and emission spectra of the chromophore as a redshift. The phenomenon is called polarization effect (**Figure 2.8**) and it occurs because the chromophore induces electric dipoles in adjacent molecules. The electrostatic interaction between these new dipoles and the chromophore's dipole results in a reduction of the potential energy of the chromophore, in both the ground and excited state. For non-polar molecules this reduction is larger when the excited state is involved (D') compared to the interaction of the two molecules in ground state (D). This is because excited states generally possess higher dipole moments.

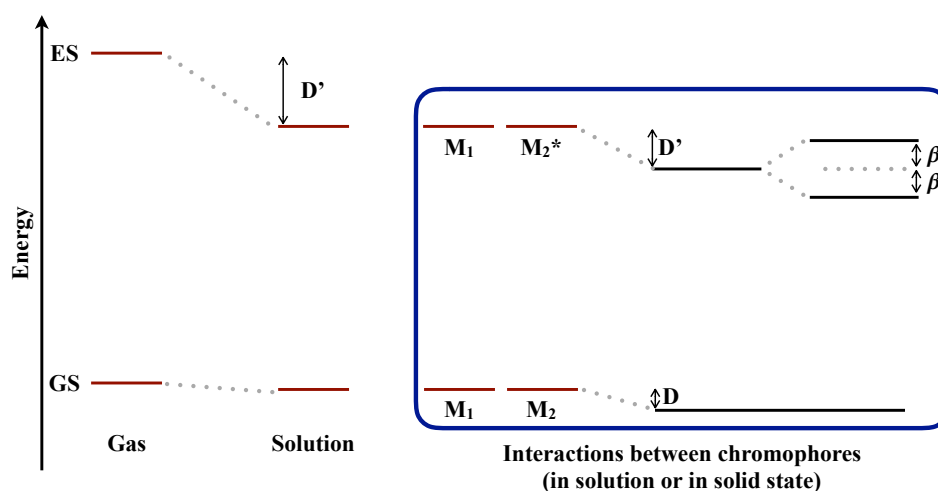


Figure 2.8. Schematic illustration of stabilizing effect of intermolecular interactions on ground state and excited states energies. GS is ground state, ES is excited state, M_1 and M_2 stand for two interacting molecules of the same kind. D and D' is polarization energy in ground and excited state, respectively. β is resonance interaction energy. [4]

The scale of the polarization effect depends on the mutual orientation and distance between molecules. In solution, solvent molecules will reorient to optimize the interaction and achieve the largest stabilization energy. This effect contributes to a shift between 0-0 peaks of absorption and emission (*Stokes shift*). In general, this interaction increases with polarizability of the adjacent molecule and the dipole moment of the chromophore.

Figure 2.8 illustrates another important outcome of the interaction between two molecules. The excited state energy level of the two interacting molecules of the same kind splits into two levels. The magnitude of splitting depends on resonance interaction energy (β) which is

determined by the distance and orientation between the molecules. The resonance interaction can be described as an energy transfer between molecules M_1 and M_2 .

2.3.3 Energy transfer process

Energy transfer between molecules can be split into three cases:

- “Strong”: the reorganization energy of the molecules is much smaller than the resonance interaction energy ($\beta \gg E_{\text{reorg}}$).
- “Intermediate”: the reorganization energy of the molecules is in range of the resonance interaction energy ($\beta \sim E_{\text{reorg}}$).
- “Weak”: the reorganization energy of the molecules is much bigger than the resonance interaction energy ($\beta \ll E_{\text{reorg}}$).

When the reorganization energy of the molecules is much smaller than the resonance interaction energy ($\beta \gg E_{\text{reorg}}$), the energy can be transferred from one molecule to the other in a coherent (wave-like energy propagation) manner. In this case, the relaxation of the excited molecule from the Frank-Condon state does not have time to occur and, thus, energy transfer occurs from the vibronically unrelaxed electronic state. This can occur in a well-ordered array of the molecules (*e.g.* as organic crystals) and results in excited state delocalization over multiple molecules. This collective excited state is called *Frenkel exciton*. The characteristic property of a Frenkel exciton is a coherent energy transfer. However, the term exciton is now also used for non-crystalline systems where the energy transfer occurs in an incoherent manner due to high energy variations between different molecules.

The reorganization energy of the molecules is much bigger than the resonance interaction energy ($\beta \ll E_{\text{reorg}}$), this results in localized states and the excitation can only hop from one molecular site to another (an incoherent energy transfer). The “intermediate” resonance interaction is considered when β is on the order of the reorganization energy, in this case electron-vibronic coupling need to be taken into account when accessing the energy transfer process.

Energy transfer between the molecules could occur through Dexter or Förster energy transfer mechanisms (**Figure 2.9**).

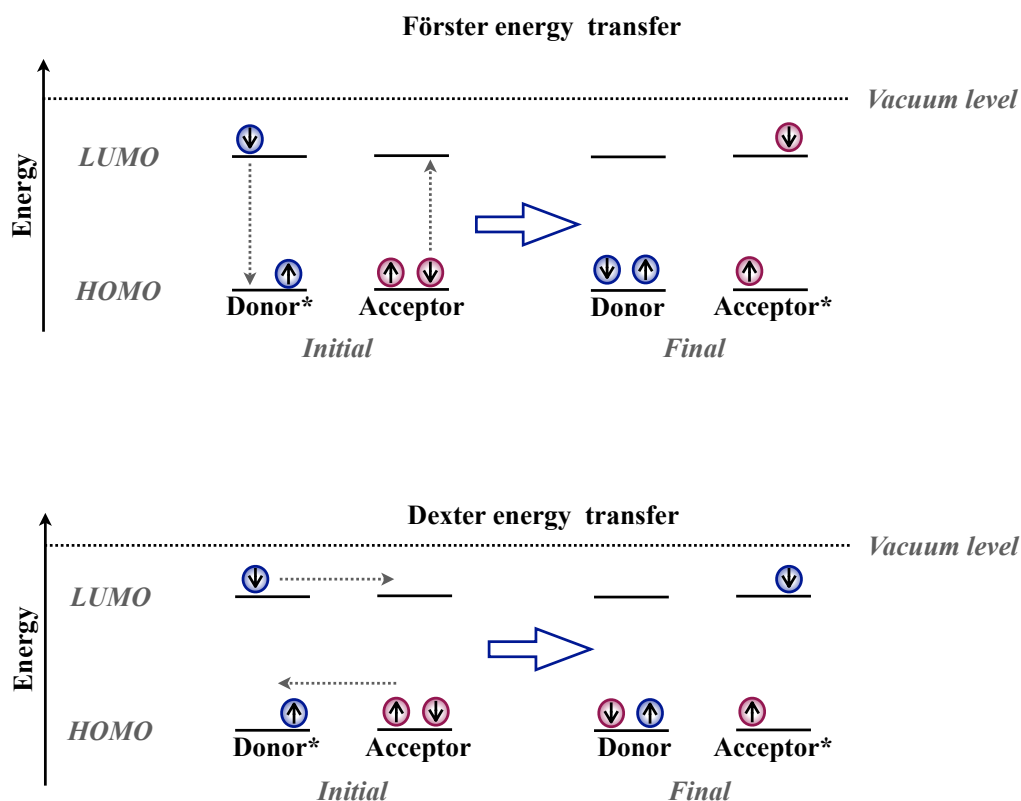


Figure 2.9. Illustration of Förster and Dexter resonance energy transfer. [4]

Förster resonance energy transfer occurs *via* through space Coulomb interaction. In the *point-dipole approximation*, which is valid when intermolecular distances are larger than the size of the chromophore, the coupling energy can be approximated by:

$$\beta^C \propto \frac{|\mu_D||\mu_A|}{R^3} \kappa \quad (2.27)$$

where β^C is Coulomb electronic interaction energy, R is intermolecular distance, κ is an orientation factor, which can be calculated from the mutual orientation of the molecules. If $\beta \ll E_{reorg}$, we can use Fermi's Golden rule to describe the rate constant of this process, thus, the rate constant is proportional to square of the electronic coupling energy:

$$k_{ET} \propto \frac{|\mu_D|^2 |\mu_A|^2}{R^6} \kappa^2 J(\epsilon_a) \quad (2.28)$$

κ^2 is 0 for perpendicular, 2/3 for random, 1 for parallel and 4 for collinear molecular arrangements. $J(\epsilon_a)$ is the spectral density integral which is essentially the overlap between the donor emission and acceptor absorption spectra. The value of extinction coefficient of the acceptor is particularly important since it implies large oscillator strength of the acceptor which means that it can easily be set into resonance to form an excited state. [5]

The rate constant can be related to the lifetime of donor emission:

$$k_{ET} = \frac{1}{\tau_D^0} \left(\frac{R_0}{R} \right)^6 \quad (2.29)$$

In this expression τ_D^0 is the lifetime of the donor in the absence of an acceptor, R_0 is the Förster radius, which includes the spectral density integral value. The Förster radius is usually 1-4 nm. It represents the distance at which both an energy transfer and simple decay of an excited state through donor emission are equally possible.

The exchange-based energy transfer (*Dexter* energy transfer) is more sensitive to a distance between molecules, because it requires an overlap between the molecular orbitals of donor and acceptor. The molecular overlap can be substantial in π -stacks due to close contacts between the neighbouring molecules, which could result in dissociation of a localized exciton into charge transfer state with hole and electron being on two different molecules. [24] The interaction energy value in the case of Dexter energy transfer can be evaluated as:

$$\beta^E \propto e^{-\frac{R}{L}} \quad (2.30)$$

where R is distance between the molecules, L is a constant that takes into account effective average orbital radius of the participating molecules.

The rate constant of the transfer in this case could be expressed as:

$$k_{ET} \propto J e^{-\frac{2R}{L}} \quad (2.31)$$

J is the normalized spectral overlap which means that the magnitude of overlap does not actually depend on the value of extinction coefficient of energy acceptor (unlike in the Förster case).

Both Förster and Dexter transfer can potentially occur in the same film of organic molecules ($\beta = \beta^C + \beta^E$), however, due to a stronger distance dependence and orbital overlap requirement of Dexter energy transfer, Förster energy transfer is observed more frequently. Dexter energy transfer is observed for intermolecular distances that are smaller than 1 nm. Förster energy transfer can occur only between states of the same multiplicity (since it depends directly on the value of the extinction coefficient of the acceptor), whereas Dexter allows for the transfer between states of different multiplicity (*e.g.* singlet-triplet transfer).

2.3.4 Influence of molecular packing on optical properties of conjugated molecules

As discussed in section 2.2.2.2, the strength of the electronic transition between the ground and excited singlet states of a molecule depends on the transition dipole moment. For two interacting (coupled) molecules, the strength of the transition depends on the combined transition dipole moment. However, the mutual alignment of dipoles also needs to be taken into account. **Figure 2.10** shows two limiting cases of molecular arrangements that lead to two different dipole moment alignments.

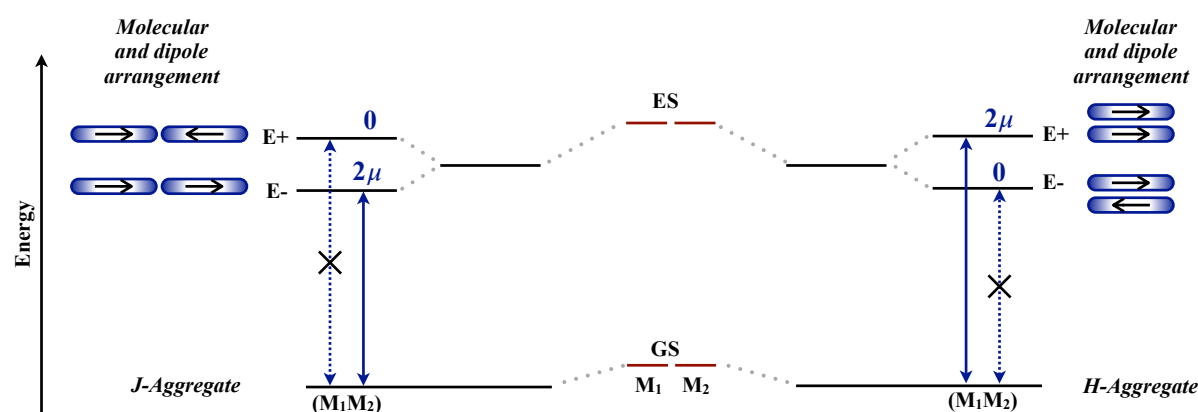


Figure 2.10. Schematic illustration of ground and excited state energies of two interacting molecules and their dipole arrangement, which leads to formation of J-aggregate (head-to-tail molecular orientation) and H-aggregate (side-by-side molecular orientation). [4]

A side-by-side molecular orientation (**Figure 2.10, right**) leads to H-aggregate formation ($\kappa^2 = 1$). Dipole arrangement in a perfect H-aggregate leads to a complete cancellation of transition dipole moment at the lowest excited state (E^-) of an aggregate, whereas the transition dipole moment of the E^+ state is 2μ (μ is transition dipole moment of a single molecule). This has significant consequences for absorption and emission, as the lowest excited state of the aggregate has no oscillator strength. This means that absorption of H-aggregate is blue-shifted compared to monomer absorption and the radiative rate is zero due to *Kasha's rule*, which states that emission in a majority of organic molecules occurs from the lowest lying electronic excited state, due to internal conversion from higher lying excited states to the lowest excited state being much faster than radiative decay from those states to the ground state.

In real systems the emission from H-aggregates is, nonetheless, observed. This occurs due to vibronic coupling and (or) slight misalignment between the molecules (disorder). As a result, the transition has a weak oscillator strength which results in a long-lived emission.

A head-to-tail arrangement ($\kappa^2 = 4$) leads to cancelation of the transition dipole moment of the higher excited state of an aggregate (E+) and the lowest lying excited state carries all the oscillator strength (2μ). Therefore, J-aggregates have a redshifted absorption and higher radiative decay rate compared to monomer.

H- and J-aggregates are two limiting cases of the dipole moment alignment. However, molecules in films are often not arranged in these two ways. In this case the absorption of the monomer still splits into two, but the dipole moment of the aggregate transitions will correspond to the vectorial sum of the monomer dipole moments. Therefore, all of the transitions will gain certain oscillator strength. The lifetime of emission is often reported to be longer than that of the monomer. [4]

The mechanism for the interaction can be either Coulombic or exchange and, depending on molecular orientation can be either negative (*i.e.* J-like) or positive (*i.e.* H-like). The situation when both of the described interactions are present can lead to a formation of a so-called ‘null’ or HJ-aggregate in which the spectral signatures of electronic interaction between the chromophores is essentially diminished. [24] In terms of interaction energy this can be represented as:

$$\beta^C = -\beta^E \quad (2.32)$$

where β^C is Förster (Coulomb) resonance interaction energy and β^E is exchange interaction energy.

Taking both of the factors above into an account, the electronic transition energy of two interacting molecules could be determined using the following equation:

$$\Delta E_{total} = \Delta E_1 + \Delta D \pm \beta \quad (2.33)$$

where ΔE_1 is an energy difference between excited and ground state, ΔD is the difference in stabilization of the excited and ground states. The magnitude of the resonance interaction (β) is a very important parameter that has a strong influence on the molecular photophysics.

In amorphous films and dilute solutions intramolecular distances are large which makes $\beta \sim 0$. Thus, in amorphous films chromophores often exhibit monomer-like absorption and

emission. When the resonance interaction β is about 100 meV, which is on the order of the reorganization energy but smaller than excited states energies, such interaction leads to physical dimer (or larger aggregates) formation. Dimer or aggregate formation is often observed when molecules adopt sandwich or herringbone arrangements in solid state. Dimer formation does not lead to a significant displacement between ground and excited state potential energy surfaces, which is illustrated on **Figure 2.11**. [4]

Figure 2.11. Schematic illustration of dimer and excimer potential energy surfaces: potential energy of ground and excited states of interacting molecules as a function of the intermolecular distance. Adopted from ref. [4]

In some cases, resonance energy interaction can force the molecules to reorient to optimize their interaction and cause an even larger energy stabilization. This situation could result in the formation of an excimer and is often observed for disk-shaped or planar elongated conjugated molecules. The excited state potential energy surface of an excimer is significantly shifted compared to ground state surface. Thus, absorption and emission occur at different intermolecular distances, as shown in **Figure 2.11**. Schematic illustration of dimer and excimer potential energy surfaces: potential energy of ground and excited states of interacting molecules as a function of the intermolecular distance. The emission occurs to a ground state with the significant repulsion energy (Q_0^{ES}) which forces the molecules to move apart and dissociate. This process occurs both in solution and in solid state. [4]

2.3.5 High mobility in organic solids

The energy difference between the HOMO and LUMO in organic crystals is comparable to that of silicon, therefore it is possible to apply organic molecules in transistors, solar cell and light emitting diodes. However, inorganic semiconductors possess a high charge carriers'

mobility, which is in the range of 10^3 - 10^4 $\text{cm}^2\text{V}^{-1}\text{s}^{-1}$. Whilst in organic semiconductors, mobilities range from only 10^{-5} to 10^{-2} $\text{cm}^2\text{V}^{-1}\text{s}^{-1}$ for amorphous materials, and up to 10 $\text{cm}^2\text{V}^{-1}\text{s}^{-1}$ or higher for crystalline materials. [4]

Inorganic and organic semiconductors have significantly different structures. This is due to different types of bonds involved. Organic molecules are weakly bound together by van der Waals forces, whilst inorganic semiconductors structures are formed by strong covalent bonds. For this reason, mobility mechanisms are different for these two types of materials. Most of organic solids are referred to as hole or electron transport materials, however, this classification is based on the ease of charge injection rather than actual ability of charge transport. [25]

The mobility arises when an external potential is applied to the material sandwiched between two electrodes and charge carriers (holes and electrons) begin to drift across the sample. The velocity of this movement can be described by the following equation:

$$v = \mu \cdot F \quad (2.34)$$

where v is the velocity of the charge carriers, F is electric field strength, μ is drift mobility constant *i.e.* the distance over which charge carriers are transported per second under the unit electric field (hence expressed in $\text{cm}^2\text{V}^{-1}\text{s}^{-1}$).

The exact nature of charge transport in organic solids is still heavily debated. However, it is clear that charge transport mechanism in disordered semiconductors (such as amorphous polymers) and in highly ordered crystalline semiconductors is different. [26]

Charge mobility in disordered materials is usually described by thermally activated hopping mechanism. This model suggests that the charges are strongly localized in potential wells. The transfer occurs due to hopping from one molecule to the neighbouring molecule. Transport can be enhanced by the increase of the temperature since it helps to overcome energy barriers created by energetic disorder. Therefore, the mobility dependence on the temperature can be expressed as:

$$\mu \propto \exp\left(-\frac{\Delta E_a}{k_B T}\right) \quad (2.35)$$

where ΔE_a is the activation energy. [25]

For highly organized thin films and organic crystals, mobility usually increases with decrease of temperature. Thus, it was assumed that charge carriers' mobility can be described in terms of band theory as for inorganic semiconductors. As a result of molecules interaction, the

HOMO and LUMO form valence and conduction bands (respectively) which allow hole and electron mobility. Consequently, the efficiency of charge mobility is dependent on the widths and shape of the bands. [27]

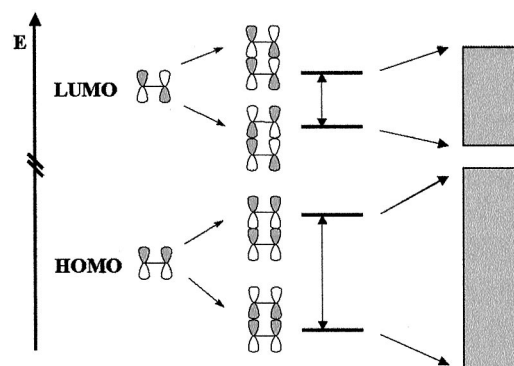


Figure 2.12. The bonding–antibonding interactions between the HOMO/LUMO levels of two ethylene molecules in a cofacial configuration and the valence and conduction bands formed as a result of interaction of many molecules. Reprinted from [27]. Copyright 2002, National Academy of Sciences.

This theory explains the decrease of charge mobility with increase of the temperature in crystals and ordered thin films. The decrease of mobility is due to a reduction of effective bandwidth by a phonon-scattering process.

However, facts which contradict this theory were also found. Namely, the free path of charge carriers at high temperatures (above 150 K) was found to be comparable with the size of crystal unit cell lattice parameters. [28]

Considering that it is very hard to obtain organic solids without defects and impurities and operation temperatures of electronic devices is usually reasonably high, the charge hopping model probably describes more adequately charge transport in organic solids.

There are two key parameters that determine charge transport: the interchain transfer integral and the reorganization energy. Interchain transfer integral (t) describes the ease of charge transfer between two interacting chains and refers to energy splitting between HOMO and LUMO, which is strongly influenced by π -overlap between neighbouring molecules. For efficient mobility the interchain transfer integral has to be maximized. According to theoretical calculations, transfer integral is significantly reduced when the π - π stacking distance and tilt angle between the molecules is increased (**Figure 2.13**).

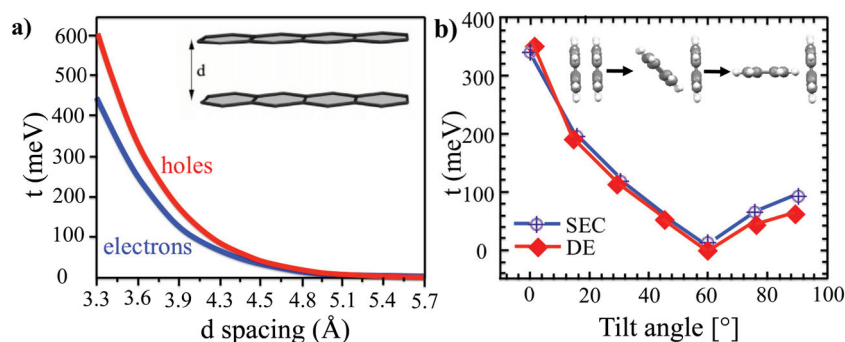


Figure 2.13. a) Dependence of transfer integral on the intramolecular distance between a tetracene cofacial dimer; b) Dependence of transfer integral for pentacene dimer on the tilt angle. Reprinted from [29]. Copyright 2013 WILEY-VCH Verlag GmbH & Co. KGaA, Weinheim.

In crystal cofacial displacement is often observed. This displacement also has great influence on the transfer integral. **Figure 2.14** indicates the effect of cofacial displacement on charge transfer integral. The decrease in transfer integral has an oscillating character and its periodicity is different for holes and electrons transport. Consequently, holes and electrons mobility is different for different degree of translation of one molecule along the other.[27][29]

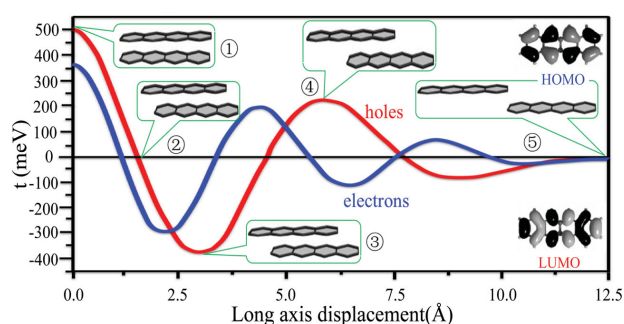
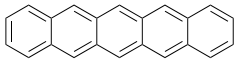
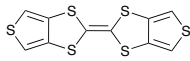


Figure 2.14. Effect of cofacial displacement on tetracene dimer. Reprinted from [29]. Copyright 2013 WILEY-VCH Verlag GmbH & Co. KGaA, Weinheim.

The reorganization energy (λ_{reorg}) represents the energy loss when a charge carrier passes through a molecule. It corresponds to the sum of relaxation energies for transformation of one molecule from the neutral state to the +1 charged state and, consequently, for a neighbouring molecule for transformation from the charged state back to the neutral state. (Possible contributions to reorganization energy from the molecular vibrations and medium polarization are neglected). To enable efficient charge carrier transport the reorganization energy must be low. **Table 2.3** represents reorganization energies for high mobility compounds: pentacene and dithiophene-tetrathiafulvalene (DT-TTF).

Table 2.3. λ_{reorg} values (eV) for Pentacene and DT-TTF (from [30]).

	<i>Pentacene</i>	<i>DT-TTF</i>
		
Isolated (boat geom.)		0.574
Isolated (planar geom.)	0.098	0.238
Embedded molecule	0.080 (0.32 e) ^a	0.042 (0.28 e) ^a
Mobility (cm²V⁻¹s⁻¹)	1.5 (ref. [31])	1.4 (ref. [32])

^aTotal charge on the charged embedded molecule.

An isolated DT-TTF molecule adopts a boat conformation. This conformation of DT-TTF has higher reorganization energy, because the molecule has planar conformation in a charged state and thus the transition energy from the boat conformation to planar conformation is high. Whilst the reorganization energy for planar geometry of DT-TTF (which is actually observed in DT-TTF crystals) is significantly lower. [30]

Therefore, the geometry and its intrinsic molecular packing mode has a large influence on the reorganization energy as well as on the transfer integral. Dense molecular packing with maximized π -orbital overlap is a basic requirement for achieving high mobility in organic solids.

2.3.6 Organic field effect transistors

Transistors are the main building blocks in modern electronic devices. Basically, transistors act as amplifiers and switchers in any electronic circuit. They are used in a number of applications, *e.g.* for operating individual pixels in an active matrix displays.

A transistor is constructed with three electrodes. The third electrode is used to control (switch or amplify) the current between two other electrodes (in the channel). A basic scheme of a field effect transistor (FET) is shown on **Figure 2.15**. In FETs the control electrode (gate) is separated from the channel by a layer of insulator. The gate electrode, insulating layer and the channel form a capacitor. The semiconducting layer in the channel acts as the second electrode in the capacitor. Therefore, a negative voltage V_g is applied to the gate electrode then the

associated electric field withdraws positive charges from the source electrode into a narrow ($\leq 5\text{nm}$) semiconductor region which borders the insulator layer (**Figure 2.15**). When negative voltage V_d is applied to the drain electrode, the current flow is enabled.

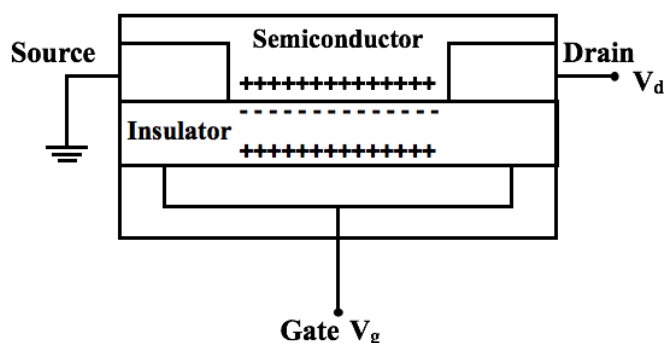


Figure 2.15. Basic scheme of field effect transistor. [4]

The interest in organic FETs is due to the possibility of processing them from solution, rather than using high temperature crystallization techniques as is required for silicon-based semiconductors. The main requirements for the organic molecules to enable their usage in FETs are: high charge carriers mobility, stability under ambient conditions and bias stress and processing from solution. [28]

In order to achieve a high mobility in OFETs, semiconducting molecules need to pack along the current direction in the conducting channel, because then, the dominant charge transport direction is parallel to the substrate (**Figure 2.16**).

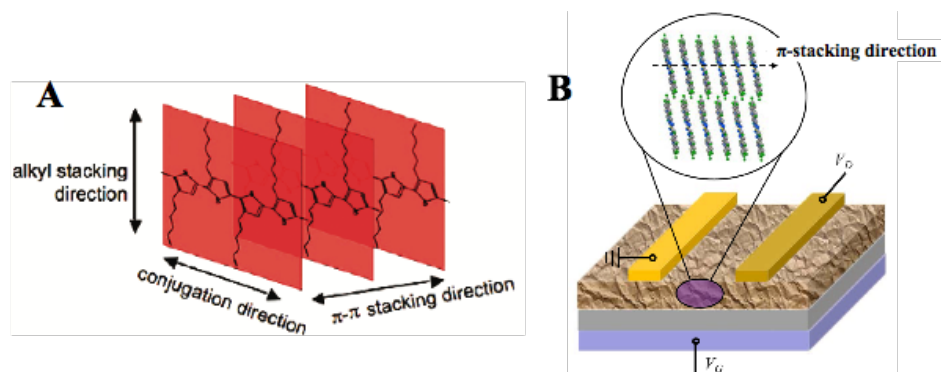


Figure 2.16. A - Intrachain transport, along the π -conjugation direction and interchain transport, along the π -stacking direction or alkyl stacking direction. B - edge-on orientation of the polymer molecules on the substrates. (A) - Reprinted with permission from [19]. Copyright 2012, American Chemical Society, (B) - reprinted with permission from [33]. Copyright 2015, American Chemical Society.

Single crystal transistors usually show better performance in OFETs due to their better molecular arrangement with no grain boundaries and minimized charge traps. However, well-

ordered thin films, especially in the crystalline state are of great interest due to the ease of processing. A lot of organic molecules have been investigated for application in OFETs. Among them fused acene systems (*e.g.* anthracene, tetracene, pentacene etc.) have attracted a lot of attention due to the efficient π -conjugation and good crystal packing. The mobility increases drastically with an increase of the conjugation length of the molecule. However, the oxidation stability and good solubility are equally important. Both of these factors cause problems in the application of large fused acenes in OFETs. The oxidation problem occurs due to high HOMO energy level of the organic material. Insertion of suitable substituents often helps to improve the stability as well as increase the solubility of the compounds. This approach was used for pentacene (**Figure 2.17a**), the triisopropylsilylethynyl solubilizing groups were introduced into 6 and 13 position (**Figure 2.17b**). The resulting hole mobility was reported to be up to $4.6 \text{ cm}^2\text{V}^{-1}\text{s}^{-1}$ in a strained film. [29]

The stabilizing effect also can be reached by introducing heteroatoms into fused rings systems. This is due to lower degree of aromaticity in heteroacene compounds. The DNTT molecule (**Figure 2.17c**), for example, is rather stable and exhibits reasonably high mobility up to $3.1 \text{ cm}^2\text{V}^{-1}\text{s}^{-1}$. Insertion of alkyl chains improves solubility and it can also alter the packing motifs of organic molecules. It has been recently reported that alkyl chains introduced into the long axis of the molecule could reduce its dynamic disorder in the solid state which improves the charge mobility. C8-BTBT molecule (**Figure 2.17d**) is one of the good examples of the influence of the alkyl chains on the mobility. [34] This molecule is suitable for inkjet printing and exhibits excellent stability and hole mobility up to $31.3 \text{ cm}^2\text{V}^{-1}\text{s}^{-1}$.

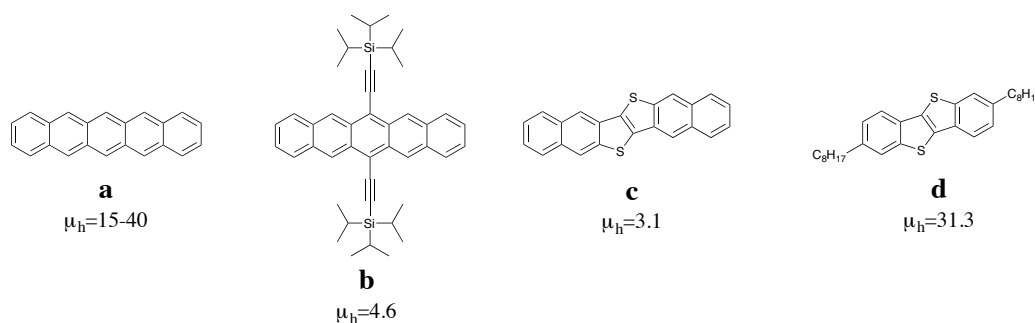


Figure 2.17. Structures and mobility values ($\text{cm}^2\text{V}^{-1}\text{s}^{-1}$) in of the organic molecules used in OFETs: a) pentacene [35]; b) TIPS- pentacene (strained film) [36]; c) DNTT (thin film)[37]; d) C8-BTBT (single crystal films produced by inkjet printing) [38].

3 Materials and Methods

This chapter contains information on synthesis and structural characterization of the organic molecules used in this thesis. It also describes general sample preparation methods and overviews the techniques that were used for photophysical characterization of the molecules, along with their basic operation principles.

3.1 Materials

All chemicals were obtained from commercial sources (Sigma Aldrich, Alfa Aesar, Fluorochem, Fisher Scientific, etc.) and used without further purification. Solvents were either used as received from commercial sources (HPLC grade) or obtained from the Grubbs solvent system located in the Department of Chemistry. Solvents for spectroscopy studies (such as THF, ethyl acetate, chloroform) were purchased in spectroscopic grade purity.

3.2 Characterization of organic compounds

3.2.1 Thin Layer Chromatography (TLC)

TLCs were performed on aluminium TLC plates purchased from Merck, silica gel 60 coated with fluorescent indicator F₂₅₄. Visualisation was performed using UV light.

3.2.2 Melting points (Mp)

Melting points were obtained using Gallenkamp Melting Point Apparatus. The obtained melting points were compared to the values reported in literature if this information was available.

3.2.3 Mass Spectrometry (MS)

GC-MS spectra were recorded on Perkin Elmer Turbomass mass or Agilent 7200 GC-MS QToF spectrometers equipped with Perkin Elmer PE-5MS Capillary column, using electron impact (EI+) or chemical ionisation (CI+) methods; the column was ramped from 60 °C to 360 °C at 20 °C min⁻¹ and then held at 300 °C for 20 mins. For some cases Bruker Reflex III MALDI-TOF and Waters LCT Premier Solids Probe Analysis mass spectrometers were used.

3.2.4 Fourier Transform Infrared spectroscopy (FT-IR)

FT-IR absorption spectra were recorded on Nicolet Model 205 FT-IR Spectrometer. All the samples were analysed using the ATR technique.

3.2.5 Nuclear magnetic resonance (NMR)

NMR spectra were recorded on Bruker AVII-250, Bruker AVII-400, Bruker AVIIIHD 500MHz or Bruker AV 400MHz spectrometers at 22°C. Samples were recorded in solutions of CDCl₃ or d₆-DMSO purchased from VMR Chemicals. Proton chemical shifts (δ) are reported in ppm downfield from tetramethylsilane (TMS).

3.2.6 Elemental analysis

Elemental analysis was performed using Vario MICRO cube CHN/S analyser. Precise quantity of the sample was catalytically combusted and reduced, producing N₂, CO₂, H₂O and SO₂. The proportion of these gasses is then detected and the % of each element can be calculated. Halogens content is determined using the Schoninger flask combustion method. In this case, the material is combusted in oxygen rich atmosphere, the resulting gasses. The detection limit of the analyser is 0.3%.

3.3 Materials characterization

3.3.1 Cyclic voltammetry (CV)

In the CV experiment forward and reverse linear potential scans are applied to materials in a concentrated electrolyte solution. The oxidation (or reduction) of a molecule in a solution can occur due to a heterogeneous electron transfer from the molecule to the electrode (or *vice versa*). Oxidation of a material is indicated by an anodic wave on the positive forward scan, whereas a cathodic wave (on the reverse scan) is a sign of reduction. [39][4]

CV experiments were conducted using a Princeton Applied Research Model 263A Potentiostat/Galvanostat at room temperature in degassed dichloromethane solutions of the investigated molecules (concentration: 1mM) using 0.1M n-Bu₄NClO₄ as a supporting electrolyte. The cell was equipped with a Pt working electrode, Pt rode as the counter electrode and an Ag/Ag⁺ reference electrode. The solutions of investigated materials were scanned at 50mV/s rate. The HOMO energy levels were calculated using the onset potentials corrected against the Ferrocene(Fc)/Ferrocene⁺ couple: $E_{\text{HOMO}} = - (4.8 + E_{\text{ox}} + \text{Fc correction})$ [eV]; LUMO

energy was calculated using the value of optical band gap (determined as an onset of absorption):

$$E_{\text{LUMO}} = E_{\text{HOMO}} + E_{\text{g}}.[40]$$

3.3.2 Thermogravimetric analysis (TGA)

TGA was used to establish the stability of the samples and the data presented in this thesis features the 5% decomposition temperature of the molecules.

The thermal stability of the molecules was tested by TGA using Pyris 1 Perkin Elmer TGA thermobalance. The experiments were carried out in nitrogen atmosphere (25 mL/min). Samples were subjected to thermal degradation between 25 and 800°C at heating rate 10°C/min.

3.3.3 Differential Scanning Calorimetry (DSC)

Our DSC is a heat flux-based device, which means the sample and the reference are directly connected through a low-resistance heat-flow path (metal disc). The temperature of the sample cell corresponds to the temperature of both the sample and the reference material. The temperature of the cell is varied (in our case from -30 to 250°C) and the temperature difference between the sample and the reference is recorded as a function of temperature. The data is presented as heat flow vs temperature. Heat flow represents ratio between unit of heat per unit time and is given in W/g. The measurement allows to establish thermal transitions (such as melting, crystallization and glass transitions) in materials of interest.

Calorimetric analysis was carried out on Pyris 1 Perkin Elmer thermal analyser. Samples (5-10 mg) were heated in nitrogen atmosphere (20 mL/min) with heating rate of 10 °C/min. Calorimeter was calibrated using indium standard (heat flow calibration) and indium-lead-zinc standard (temperature calibration).

3.3.4 X-Ray crystallography and diffraction

Single crystals for X-Ray diffraction were obtained by careful crystallization from THF : hexane solvent system. The molecules were placed in a small tube and dissolved in small amount of THF (~0.5 mL), the tube with this solution (not sealed) was then placed in a bigger tube filled with a couple of millilitres (~2-3 mL) of hexane. The larger tube was carefully sealed to prevent solvents evaporation. This system was left in a dark place at ambient temperature for 2 weeks. This approach allows for a slow solvent mixing and results in very slow crystallization. The polymorph 2 of C8-C-inin was crystallized from 30mM toluene solution, which has been

kept in the freezer for 6 months. The thin films XRD was obtained from polycrystalline evaporated films (80 nm) on Si/SiO₂ (300nm) substrate.

X-Ray crystallography and diffraction was performed by Dr. Craig Robertson, X-ray Crystallography Service Manager at Department of Chemistry, University of Sheffield.

Single Crystal XRD

Intensity data was collected at 100 K on either a Bruker SMART APEX-II CCD diffractometer operating with a MoK α sealed-tube X-ray source or a Bruker D8 Venture diffractometer equipped with a Photon 100 CMOS detector using a CuK α microfocus X-ray source. Crystals were mounted in fomblin oil on a MiTiGen microloop and cooled in a stream of cold N₂. Data were corrected for absorption using empirical methods (SADABS) based upon symmetry equivalent reflections combined with measurements at different azimuthal angles. The crystal structures were solved and refined against F₂ values using ShelXT for solution and ShelXL for refinement accessed via the Olex2 program. Non-hydrogen atoms were refined anisotropically. Hydrogen atoms were placed in calculated positions with idealized geometries and then refined by employing a riding model and isotropic displacement parameters.

Powder XRD

Samples were placed onto a zero-background silicon wafer in a sample holder. X-ray diffraction data were collected using Cu-K α ($\lambda = 1.541 \text{ \AA}$) radiation on a Bruker D8 ADVANCE X-ray powder diffractometer in Bragg-Brentano Geometry equipped with a high-resolution energy dispersive Lynxeye XE detector.

Interplanar distances were calculated where possible using Bragg's law:

$$n\lambda = 2d_{hkl}\sin\theta_{hkl} \quad (3.1)$$

where θ – is Bragg angle, d_{hkl} – interplanar distance, λ – radiation wavelength, n –order of reflection.

3.3.5 Grazing incidence X-ray scattering (GIWAXS)

GIWAXS was performed and analysed by Dr. Daniel Toolan at the Department of Chemistry, University of Sheffield. GIWAXS measurements were carried out on a Xeuss 2.0 instrument equipped with an Excillum MetalJet liquid gallium X-ray source. Films prepared on glass were collected for 900 s using collimating slits of $0.5 \times 0.6 \text{ mm}$ (“high flux” mode). Alignment was performed via three iterative height (z) and rocking curve (Ω) scans, with the

final grazing incidence angle set to $\Omega = 0.3^\circ$. Scattering patterns were recorded on a vertically-offset Pilatus 1M detector with a sample to detector distance of 385 mm, calibrated using a silver behenate standard to achieve a q-range of 0.035 – 2.0 Å⁻¹. Data reduction was performed using the instrument-specific Foxtrot software.

3.3.6 Atomic force microscopy (AFM)

Atomic force microscopy (AFM) was performed by Guy E Mayneord in the group of Dr Matthew Johnson, Department of Molecular Biology and Biotechnology. Peak Force – Quantitative Nanomechanical Mapping (PF-QNM) in air was used for imaging, maintaining a modulation frequency of 2kHz, and a peak force value no greater than 500pN and image size of 1024 pixels. Bruker™ SNL AFM probes were used for imaging. Imaging was performed in Nanoscope 9.2, and data analysis was performed in Nanoscope Analysis 1.8 and MATLAB 2017a.

3.4 Photophysics

3.4.1 Sample preparation for photophysics measurements

Solutions

Materials were dissolved in appropriate solvents. Materials that could not be dissolved in ambient conditions were sonicated with heating (20 mins, the temperature depended on the solvent boiling point). Polymer solutions were prepared in two stages, first a small amount of solvent was added to the solid polymer and the suspension was left soaking for 24 hours, then the concentrated polymer solution was diluted to a necessary concentration. Concentration of polymer solutions was 25 mg/mL, concentrations of materials varied from 10⁻⁴ to 10⁻⁶ M.

All the measurements were performed in quartz spectroscopic cuvettes or quartz NMR tubes. If necessary, solutions were degassed using a standard freeze-pump-thaw degassing technique. Some of the solutions were prepared in nitrogen atmosphere of glovebox.

Films

Films were either spin-coated or vacuum deposited on quartz substrates. Substrates were thoroughly cleaned before use. First of all, they were soaked in acid mixture (HCl₃:HNO₃) for 24 hours, then washed with water until neutral pH and then sonicated in isopropanol, followed by ozone cleaning for 20 mins.

Spin-coating

Spin-coating was conducted on a commercial apparatus. A 1×2 cm substrate was placed on spin-coater and fixed according to spin-coater manufacturer requirement, 50 μL of solution of suitable concentration was pipetted onto a substrate. Then, the substrate was spun at high speed (2000 rpm) for 60 seconds. The concentration of solution, solvent, speed and duration of spinning affect the thickness of the resulting film. These parameters will be given where relevant for each sample individually. The thickness of the films was determined using Bruker DekTak XT surface profiler.

Vacuum deposition

Evaporated films were made using Angstrom Evaporator commercial thermal evaporator. The thickness of the sample is controlled in the software of the device and was calibrated by DekTak XT measurements for the materials used in this thesis. The thickness of the films for optical measurements was 80nm, for thin film transistors 10-20nm.

3.4.2 UV-Visible absorption

Absorption spectra were measured using Agilent Technologies Cary 60 Spectrometer. The spectra were recorded at room temperature (25°C) and corrected against pure solvent or blank substrate. The efficiency of light absorption is characterized by absorption (A) or transmission (T):

$$A(\lambda) = \log \frac{I_{\lambda}^0}{I_{\lambda}} = -T(\lambda) \quad (3.2)$$

These values are related to molar absorption (extinction) coefficient. We used the Beer-Lambert law to determine extinction coefficients in solution:

$$A(\lambda) = \log \frac{I_{\lambda}^0}{I_{\lambda}} = \varepsilon(\lambda)lC \quad (3.3)$$

where A stands for absorbance, I_{λ}^0 and I_{λ} is the light intensities of the beam entering and leaving the absorbing medium, $\varepsilon(\lambda)$ is the molar absorption (extinction) coefficient ($\text{L mol}^{-1}\text{cm}^{-1}$), C is the molar concentration (mol L^{-1}), l is the absorption path length (cm). [3]

The absorption coefficient $a(\lambda)$ is absorbance divided by the optical pathlength:

$$a(\lambda) = \frac{A(\lambda)}{l} = \frac{1}{l} \log \frac{I_{\lambda}^0}{I_{\lambda}} \quad (3.4)$$

$$I_{\lambda} = I_0 10^{-a(\lambda)l} \quad (3.5)$$

Another way to describe the same process is through Napierian absorption coefficient:

$$\alpha(\lambda) = \frac{A(\lambda)}{l} = a(\lambda) \ln 10 = a(\lambda) \times 2.3 \quad (3.6)$$

Napierian absorption coefficient is directly related to absorption cross-section which can be calculated as follows:

$$\sigma = \frac{\alpha(\lambda)}{N} = 3.82 \times 10^{-21} \varepsilon(\lambda) \quad (3.7)$$

where σ stands for absorption cross section, N is a number of absorbing chromophores. Equation (3.7) also shows that the absorption cross section also relates to absorption (extinction) coefficient.

3.4.3 Steady state photoluminescence

Steady state fluorescence spectra were measured using Jobin Yvon Horiba Fluoromax4 (equipped with xenon arc lamp) or Agilent Technologies Cary Eclipse Fluorescence (equipped with xenon flash lamp) spectrofluorometers.

Phosphorescence spectra were measured on the Eclipse Cary spectrometer because it allows to have a time delay. Phosphorescence spectra were recorded at 77K using liquid nitrogen as a cooling media. Samples were placed in quartz NMR tubes and cooled down in a custom-made transparent quartz Dewar, thus allowing to maintain the sample temperature at 77K. Samples with low phosphorescence quantum yield could not be measured using Cary Eclipse, due to lack of sensitivity. In those cases, measurements were performed using laser excitation with ICCD detection. The excitation wavelengths were determined from UV-vis spectra and were specific to every sample.

3.4.4 Photoluminescence quantum yield (PLQY)

PLQY is a number of photons emitted relative to the number of photons absorbed.

Solutions

In solutions the quantum yields of fluorescence were determined by comparison of the emission spectra of material with emission from an optically matched solution of the reference.

This is standard procedure and was extensively described in literature. [41][42]

Quinine sulfate (0.1M in sulfuric acid) and 9,10-diphenylanthracene (in cyclohexane) were used as references. The optical density of the solutions was kept below 0.05 (which is approximately 1 μ M for studied materials and 10 μ M for quinine sulfate). To determine fluorescence quantum yield steady state absorption and emission of the reference and materials solutions were measured on the same day in the same cuvette. Absorption background was corrected using corresponding pure solvent. The data for PLQY for each compound was taken from 5 different solutions.

From the obtained data the PLQY was determined using the equation:

$$PLQY = PLQY_{ref} \cdot \frac{I}{I_{ref}} \cdot \frac{A_{ref}}{A} \cdot \frac{n^2}{n_{ref}^2} \quad (3.8)$$

where I – integrated intensity of emission from the sample, I_{ref} – integrated intensity of emission from the reference, A is the value of absorbance of the material at the excitation wavelength, A_{ref} – is the value of absorbance of the reference at the excitation wavelength, n – refractive index of the solvent of the material solution, n_{ref} – refractive index of the solvent of the reference solution, $PLQY_{ref}$ – photoluminescence quantum yield of the reference, taken from literature. [41]

Table 3.1. Photoluminescence quantum yields of the reference materials. [41]

Reference	Solvent	Excitation wavelength (nm)	PLQY
Quinine sulfate	0.1M H ₂ SO ₄	350	0.577
		366	0.53
9,10-Diphenylanthracene	cyclohexane	any	1.0

Films

PLQY of films were measured in an integrating sphere, which is a sphere that is coated with diffuse, uniformly reflective paint. To determine PLQY two spectra were collected: first

measurement - the blank substrate, and second measurement - the substrate with the sample. Each sample was measured 5 times. To calculate PLQY the following equation was used:

$$PLQY = \frac{P_c}{L_a - L_c} \quad (3.9)$$

L_a - is the integrated intensity of the excitation beam (number of photons in the excitation wavelength region) determined in the first measurement, L_c - is the integrated intensity of attenuated excitation beam (number of photons in the excitation wavelength region after the illumination of the sample) determined in the second measurement. P_c – integrated intensity of the sample emission (the number of photons emitted by the sample) determined in the second measurement. [43]

3.4.5 Triplet yields

Triplet states can interact with oxygen in ground state to produce singlet oxygen. It is a common practice to employ singlet oxygen emission to quantify the triplet yields in solution. However, due to technical limitation in our lab the UV excitation and precise detection of singlet emission (1275nm) wasn't possible. For this reason, we employ an indirect method of singlet oxygen detection. We use a solution of singlet oxygen sensor - 9,10-dimethylanthracene (DMA) to determine the quantity of the formed singlet oxygen. We monitor the change in absorbance of DMA as it reacts with the singlet oxygen over 1.5 hour.

Examined material was dissolved in toluene, concentration was adjusted to have optical density of material at excitation wavelength less than 0.1. To this solution a concentrated DMA solution (~1.6mM, 10-20 μ L) was added, the optical density of DMA was kept less than 0.6. The resulting solution was exposed to UV light (with stirring) for a fixed time period and then the absorption spectrum of the solution was measured. Exposure times were 0-90 minutes, with 5 mins time intervals. Pulsed laser was used as a UV-light source: 320 nm (1 kHz, 0.5 mW) – for C8-BTBT and n-BTBT, 355 nm (1 kHz, 0.4 mW) for diBT. Each compound was measured 5 times using 5 different solutions and these measurements were accompanied by the measurement of the reference solution in the same conditions. We used optically matched phenalenone solution as a reference ($\Phi_T = 100\%$). [44]

Therefore, in this experiment we excite the chromophore and generate singlet oxygen. Then singlet oxygen reacts with DMA which results in lowering of its absorbance. To quantify this process reliably, we measure decrease in absorbance as a function of time and hence we

obtain the rate of singlet oxygen reaction with DMA. We compare this effect caused by triplets of the compounds of interest with that using a well characterized standard molecule (phenalenone). We estimate the triplet yield using the following equation:

$$\Phi_T = \frac{\left(\frac{k}{1 - 10^A}\right)}{\left(\frac{k_{ref}}{1 - 10^{A_{ref}}}\right)} \cdot 100\% \quad (3.10)$$

where A is absorbance of the reference and a compound of interest at the excitation wavelength, k – is the slope on the graph of A_{DMA} vs exposure time. A_{DMA} was taken at 380 nm.

The obtained results were averaged, and the standard deviation was determined. The results should be treated with caution, because the singlet oxygen formation can be affected by the structural differences of the compounds, e.g. presence of the alkyl chains and their arrangement in solution.

3.4.6 Rate constants calculation

The rate constants were determined from the following equations [4]:

$$\tau_{rad} = \frac{1}{k_{rad} + k_{nr}} \quad (3.11)$$

$$k_{rad} = \frac{PLQY}{\tau_{rad}} \quad (3.12)$$

$$k_{ISC} = \frac{\text{Triplet yield}}{\tau_{rad}} \quad (3.13)$$

$$k_{nr} = k_{ISC} + k_{IC} \quad (3.14)$$

τ_{rad} – time-constant of singlet radiative decay

k_{rad} – radiative decay rate constant

k_{ISC} – intersystem crossing rate constant

k_{nr} – non-radiative decay rate constant

k_{IC} – internal conversion rate constant

3.4.7 Laser setup

The laser experiments were performed in the Lord Porter Laser Laboratory at the University of Sheffield, except where otherwise is stated.

Solstice

Solstice is an enclosed Titanium : Sapphire laser system with 800 nm fundamental wavelength, 120 fs pulse duration and 1 kHz frequency.

Nd:YAG laser

This is abbreviation for Neodymium-doped Yttrium–Aluminum garnet matrix laser with fundamental wavelength of 1064 nm and 500 ps pulse duration. We generate 355 nm pulses through frequency tripling using removable modules. The frequency of the pulses is 5 kHz when used with ICCD.

UV-light generation

We used the output of Solstice to obtain 320 nm excitation for spectroscopic study of BTBT derivatives. To obtain the UV excitation, the 800 nm beam was sent through a traveling-wave optical parametric amplifier of white light continuum (TOPAS). TOPAS output is a tuneable IR frequency beam. For our purposes, we chose 1280nm beam.

To generate 320 nm pulse, we used two sequential second harmonic generations (SHG). SHG is a nonlinear optical process that occurs when two photons of the same energy interact in nonlinear medium resulting in generation of a new photon with doubled energy. Thus, 1280 nm was sent through a β -barium borate (BBO, $\theta = 21.2^\circ$) giving 640nm beam. This output was then focused onto the BBO, $\theta = 42.3^\circ$ to give 320 nm light which was then collimated and used for all of the time-resolved experiments on BTBT derivatives.

3.4.8 Time resolved photoluminescence spectroscopy using Time Gated Intensified Charge-Couples Device (ICCD)

CCD is a type of very sensitive imaging detector that contain large number of small light-sensitive areas (pixels). When a pixel is exposed to light, it accumulates charge in proportion to total light exposure. Intensified CCDs uses gain to overcome the read noise limit. Besides a better signal to noise ratio, ICCD can have a fast gating time, which allows time-resolved measurements. Simple scheme of ICCD is presented on **Figure 3.1**. The amplification and gating occur in the image intensifier tube. The tube contains photocathode, microchannel plate (MCP) and a phosphor screen in vacuum. The interaction of photon with photocathode results in photoelectron emission. A high potential that is applied to MCP forces the photoelectron to travel towards MCP. As a result, it is forced to pass through one of the channels of MCP, where

secondary electrons are generated and accelerated. This amplified signal is then turned back to photons through the interaction with phosphor. This output is directed to CCD camera. The time resolution (gating) is achieved by reversing the voltage between photocathode and MCP. In our setup time-resolution is around 2ns. The output that we get from our ICCD is a whole emission spectrum. To obtain the kinetic profile of emission we take intensity of emission at selected spectral range (usually 10 nm or less) at different gating time. [45][46]

All of the experiments were performed on ICCD spectrometer (Andor Oxford Instruments) with instrument response of 2 ns. In all of the experiment, optical filters were used to protect ICCD camera and eliminate excitation peak. For all the experiments with 355nm excitation, the filter was GG395. Therefore, the PL spectral shape was affected in all of the experiments. The spectral shape was corrected where necessary using filter transmittance spectrum.

A background (electronic and room light) was subtracted from all of the obtained spectra. The background was recorded at the time-delay before the laser pulse. We also accomplished the control experiments where only solvent without the chromophore was measured.

Spectra were corrected for ICCD sensitivity using a correction spectrum, which was obtained by comparing the white light spectrum of a standard white light source with a well-characterized spectrum obtained using our experimental setup and the spectrum provided by the white light source manufacturer. Due to a small intensity of the white light of the source and poor quantum efficiency of our ICCD in the UV (below 400 nm) region, the resulting correction file was not able to fully correct the obtained intensities. Therefore, there would be some difference in the intensity between the spectra obtained using fluorimeters and the ICCD.

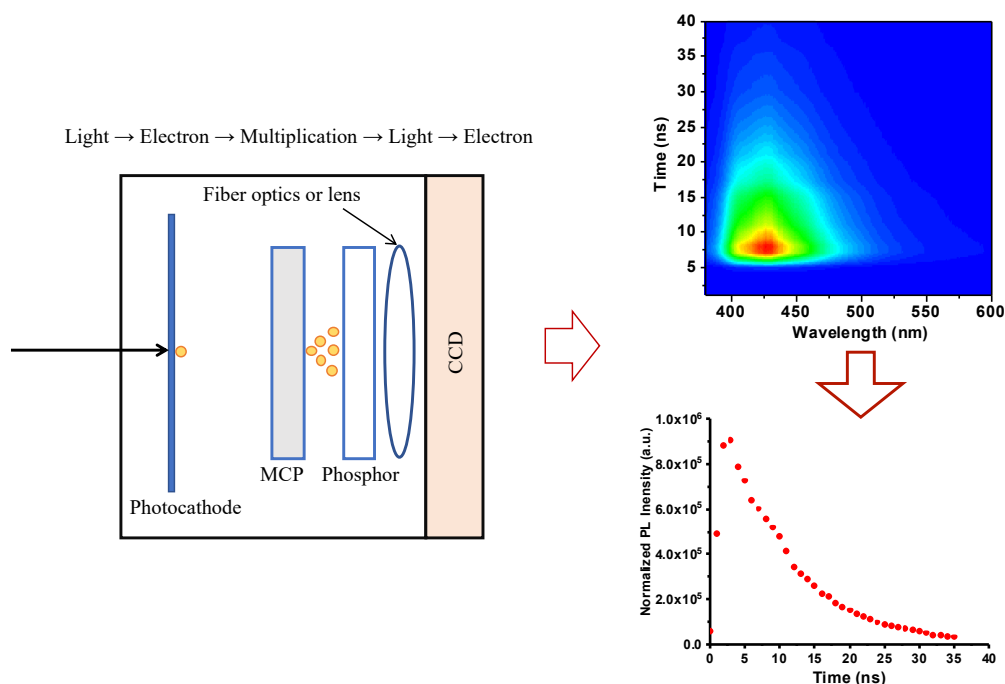


Figure 3.1. Basic working principle of a time-gated ICCD and the resulting data output.

3.4.9 Streak camera

Streak camera data was obtained by Dr. Sai Rajendran in the group of Prof. Ifor Samuel, School of Physics and Astronomy, University of St Andrews. The experiments were performed using Hamamatsu C10910 streak camera with temporal resolution of ~ 2 ps coupled to a Pharos femtosecond laser system (Light Conversion). Excitation pulses at 320 nm (180 fs) were generated using an Orpheus OPA.

3.4.10 Transient absorption (TA)

TA is a technique which allows to monitor excited states relaxation dynamics *via* measuring absorption of those states. This experiment requires two laser pulses: monochromatic high energy pulse (pump) which creates excited states and a weak broad pulse (probe - white light) which allows to monitor the dynamics. A simplified TA principle is shown in **Figure 3.2**.

In order to generate excited states, the energy of pump pulse must be on resonance with electronic transitions of the studied molecule. The probe pulse is passed through the same sample volume within certain time delay with respect to pump pulse (*e.g.* Δt_1 , Δt_2 , Δt_3). For each time delay, two signals need to be recorded: probe spectrum after interaction with the excited sample

(pump on) and probe spectrum after interaction with not excited sample (pump off). Then the difference between these two signals is analysed. [47]

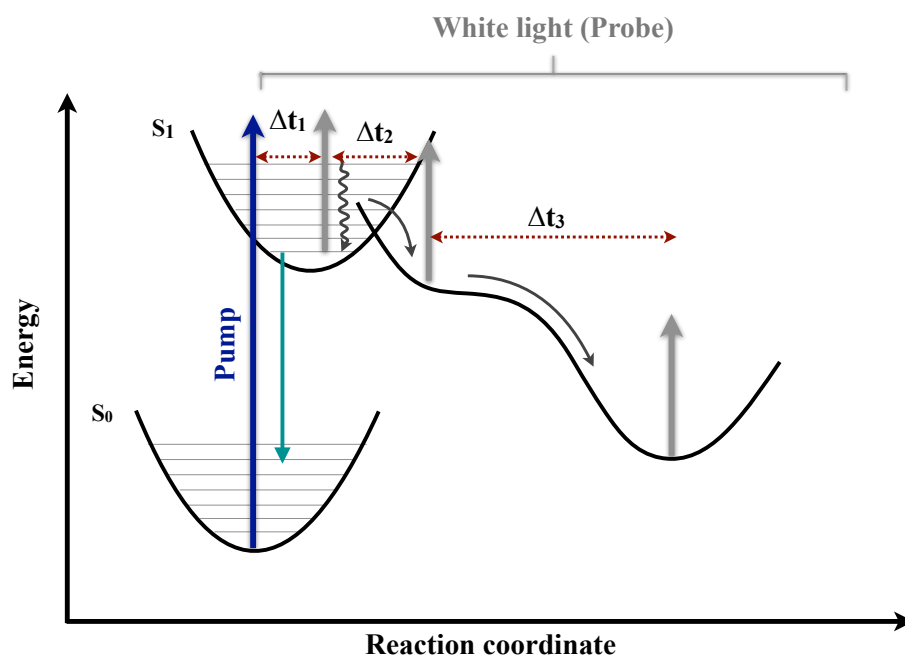


Figure 3.2. Basic principle of transient absorption.

In this thesis the data are presented in normalized difference transmission ($\Delta T/T$):

$$\frac{\Delta T}{T} = \frac{T_{pump\ on} - T_{pump\ off}}{T_{pump\ off}} \quad (3.15)$$

where T is transmission with pump on (signal) or off (the background). Division of the transmission difference by the transmission at pump off normalizes the spectral shape by the spectral shape of the probe pulse.

Normalized difference transmission ($\Delta T/T$) can be converted into difference of absorbance using the following equation:

$$\frac{\Delta T}{T} \div 2.3 = -\Delta A \quad (3.16)$$

There are three types of signals generated in transient absorption spectra (**Figure 3.3**):

- Ground state bleach (positive on $\Delta T/T$ scale). Occurs due to depopulation of the ground state as a result of pump pulse absorption. Consequently, less of the probe beam is absorbed compared to pump off spectrum.

- Stimulated emission (positive on $\Delta T/T$ scale). Occurs due to interaction of the singlet excited state with the specific energy range of probe beam resulting in relaxation of the singlet excited state through light emission. It has the roughly the same position as fluorescence spectra.
- Photoinduced absorption (negative on $\Delta T/T$ scale). Absorption of excited states. [47]

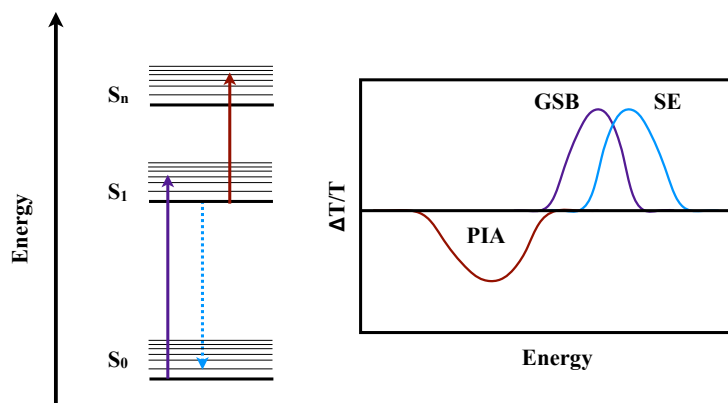


Figure 3.3. Schematic illustration of signals types in transient absorption.

All of the transient absorption data in this thesis were taken on Helios Transient Absorption spectrometer made by Ultrafast Systems aligned by Alexander J Auty (Prof. Julia Weinstein research group). Spectra Physics ~ 40 fs 10 KHz amplifier laser was used as a light source. The wavelengths required for the experiments were generated using TOPAS and will be stated individually next to the corresponding figures.

3.4.11 Resonance Raman spectroscopy

IR and Raman spectroscopy are types of vibrational spectroscopy, and thus, the energies that are detected are those required to cause nuclear motion. However, Raman greatly differs from IR spectroscopy. In IR, the sample is exposed to a range of frequencies. The sample absorbs the frequencies that match its intrinsic vibrational frequencies which results in promotion of the molecule into an excited state. The loss of frequency in initial radiation is then detected.

The process is very different in Raman spectroscopy. It is a technique based on light scattering rather than light absorption. In Raman scattering a single frequency radiation is used, this radiation is scattered from the sample. In this case, the light interacts with the molecule and polarizes the electron cloud around the nuclei to form a ‘virtual’ state. If no change in position

of nuclei occurs, then only elastic (Rayleigh) scattering will be observed (**Figure 3.4**). This means that the molecule is excited in ‘virtual’ state and then relaxes into original vibrational state.

However, if the nuclear motion occurred, the energy could be transferred from the incident photon to the molecule or vice versa (Raman scattering) and thus the molecule relaxes to a different vibrational state. Thus, the energy of the scattered photon will differ from the initial photon’s energy by one vibrational unit and this change will be detected.

For this thesis we used resonance Raman technique. In this technique, the excitation energy is chosen to be close to that of electronic transition. In our case it was 282 nm, which is a bit higher than S0-S2 electronic transition of BTBT derivatives. The lower energies were also tested; however, a significant fluorescence background was observed which resulted in poor quality of data.

The basic principle of resonance Raman is shown on **Figure 3.4**. The electron is first absorbed into the molecule and nuclei relax to the excited state equilibrium geometry. The scattering occurs not from a ‘virtual’ state but from the actual electronic excited state. A significant enhancement of the Raman signal occurs for the vibrations that are involved in the electronic transition resonant with excitation energy. [48]

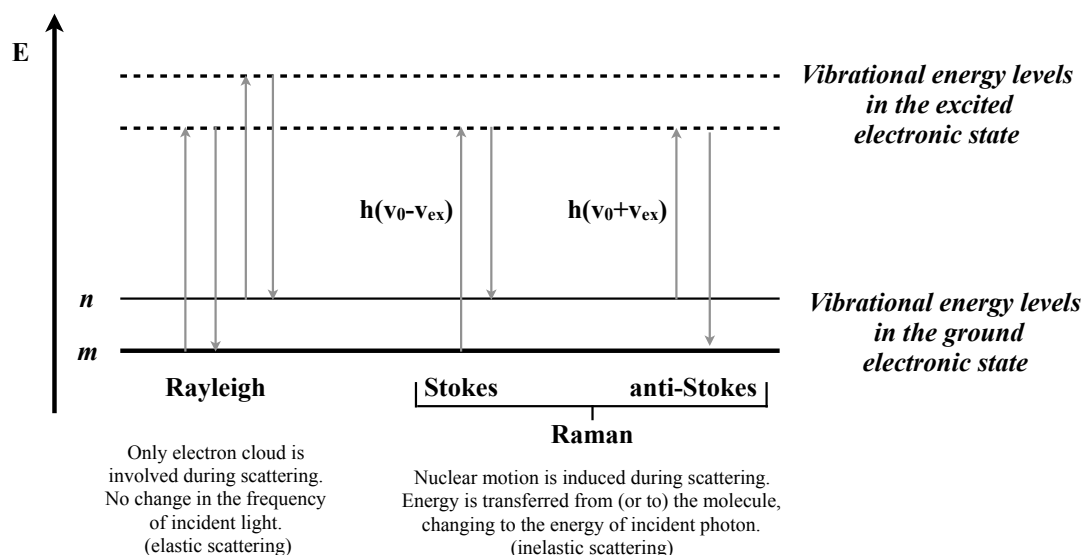


Figure 3.4. Resonance Raman theoretical principle [48].

The Raman cross sections were calculated from the following equation:

$$\frac{\sigma_s}{\sigma_{cxn}} = \frac{I_s \cdot c_{cxn} \cdot [(1 + 2\rho)/(1 + \rho)]_s}{I_{cxn} \cdot c_s \cdot [(1 + 2\rho)/(1 + \rho)]_{cxn}} \quad (3.17)$$

where σ_s and σ_{cxn} are Raman cross sections of the sample and cyclohexane, respectively; c is concentration in mol/L; I is the scattered intensity determined by integration of peak areas; ρ is depolarization ration, which for all of the studied samples was assumed to be 0.33.

All of the obtained Raman cross sections were corrected for self-absorption using the following equation:

$$\sigma_s^{cor} = \sigma_s \cdot \frac{\varepsilon_s + \varepsilon_0}{\varepsilon_r + \varepsilon_0} \quad (3.18)$$

where σ_s^{cor} - corrected Raman cross section; ε_s – extinction coefficient at scattered frequency; ε_0 – extinction coefficient at laser frequency; ε_r – extinction coefficient at the reference frequency (801 cm^{-1}).

Resonance Raman was performed in collaboration with Prof Sophia Hayes at the University of Cyprus.

3.5 Computational Methods

3.5.1 Molecular dynamics (MD) and spin-orbit coupling matrix element (SOCME)

Computations in Chapter 4 and Chapter 5 were performed by Dr. Theo Keane in the group of Prof Anthony Meijer at Department of Chemistry, University of Sheffield. The following methods were used: calculations were carried out using ORCA 4.1.0. Density functional theory (DFT) and linear-response Tamm-Dancoff approximated time-dependent DFT calculations were performed using the CAM-B3LYP exchange-correlation functional and the def2-TZVP basis set. Resolution-of-the-identity and the chain-of-spheres approximation was used in order to simplify the computation of some of the integrals, with the appropriate auxiliary basis sets. The solvent environment (toluene) was included implicitly in the calculations using the conductor-like polarizable continuum model (CPCM). The lowest 20 singlet and triplet excited states were sought, and the spin-orbit coupling matrix-elements between them evaluated using the seminumerical, mean-field approach, RI-SOMF(1X), of Neese. Numerical analysis was performed using Python 3, NumPy and SciPy.

Molecular dynamics calculations were performed by Dr. Daniel Cole (School of School of Natural and Environmental Sciences, University of Newcastle) and Lupeng Yang (University of Cambridge).

Computations in Chapter 7 were performed by Dr. Anna Stradomska at School of Chemistry, University of Glasgow. The following methods were used: all calculations performed with Gaussian09 rev. D01, using density functional theory with CAM-B3LYP functional and def2-TZVP basis set, in vacuum. Vertical excitation energies and oscillator strengths for singlets calculated with TDDFT, vertical triplet excitation energies with Δ SCF. Excited state geometry optimizations for S_1 performed with TDDFT, for T_1 with DFT.

3.5.2 Frank-Condon analysis

For Frank-Condon analysis a self-written Python script was used to simulate the measured spectra on the basis of the equation (2.13) using a mean vibrational energy. Details of equation are explained in section 2.2.3.

The fitting of the simulated function to the experimental data was accomplished using an open source package SciPy (Jones E, Oliphant E, Peterson P, et al. SciPy: Open Source Scientific Tools for Python, 2001, <http://www.scipy.org/>).

```
import numpy as np
import math
import matplotlib.pyplot as plt
from lmfit import Model
file = np.loadtxt("data.txt")
x=np.array(file[:,0])
y=np.array(file[:,1])
#Function:
def FCprogressionPL(x, huangrhys_parameter, energy_00, vibration_energy, broadening, scaling_factor):
    y1=0
    for i in range (10):
        franck_condon_factor = np.exp((1)*huangrhys_parameter)*(huangrhys_parameter**i)/math.factorial(i)
        gaussian = np.exp(-((x - energy_00 + i*vibration_energy)**2)/(2*broadening**2))
        y1+=franck_condon_factor*gaussian
    return scaling_factor*y1*(x**3)
#Fitting using specified function:
FC_model = Model(FCprogressionPL)
params = FC_model.make_params(huangrhys_parameter=1.24, energy_00=3.21, vibration_energy=0.19,
                              broadening=0.038, scaling_factor=0.065)
result = FC_model.fit(y, params, x=x)
#Plotting the result:
plt.plot(x, y, 'k-')
plt.plot(x, result.init_fit, 'b--')
plt.plot(x, result.best_fit, 'r-')
```

```
plt.show()
overall_fit=np.array([x,y,result.best_fit])
print(result.fit_report())
#Saving result:
with open('fit_result.txt', 'w') as fh:
    fh.write(result.fit_report())
np.savetxt("data.csv", np.transpose(overall_fit), delimiter=",")
```

A multimode Frank-Condon analysis was performed using a Python script that was written together with David Bossanyi, a PhD student at Dr. Jenny Clark's group. The script is now available online. [49]

3.6 Devices preparation and performance evaluation

3.6.1 OLEDs

We used patterned ITO glass OLED substrates with 3 mm x 1.5 mm (4.5 mm²) pixel size as a transparent anode purchased from Ossila Ltd. The substrates were cleaned according to recommendations from manufacturer. PEDOT:PSS (Ossila Ltd) was used as a hole-transporting layer. It was filtered (0.45µm PVDF filter) and spinned onto a clean substrate (5000 rpm, 30 sec, 50 µL). Then the layer was dried at 120°C for 15 mins. C8-C-inin film was spinned on top of dry PEDOT:PSS layer (12 mg/mL, 2000 rpm, 60 sec, 50 µL). This was followed by sequential vacuum thermal evaporation of TPBi (400 nm) which was used as electron transporting and hole blocking layer and LiF (3 nm)/Al (100 nm) as a bilayer cathode. The obtained devices were encapsulated with UV curable Encapsulation Epoxy E131 (Ossila) and a glass slide in an inert atmosphere. The active area of device was 4 mm². Current-voltage sweeps were performed using a Keithley 2602 source measure unit. The electroluminescence spectra were recorded using Andor Shamrock SR193i spectrograph.

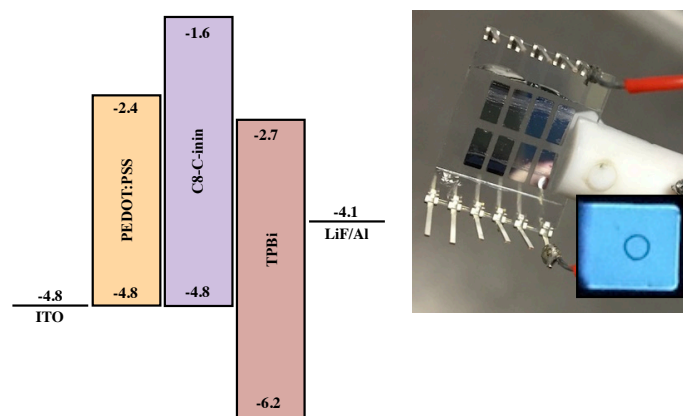


Figure 3.5. Schematic representation of the OLED architecture (left) and picture of fabricated device and pixel emission (right).

3.6.2 Organic Thin Film Transistors (OFETs)

The devices were fabricated (apart from organic semiconductor vacuum thermal evaporation) and evaluated by Zahrah Alqahtani, PhD student in Martin Grell's group at the Department of Physics and Astronomy, University of Sheffield.

Silicon substrates consisting of a heavily p-doped silicon gate electrode covered with a 300-nm thick thermally grown SiO₂ insulating layer (capacitance = 11 nFcm⁻²) were purchased from Ossila Ltd. The substrates were treated with a monolayer-forming substance: hexamethyldisilazane (HMDS) or CYTOP®, structures are shown on **Figure 3.6**. HMDS treatment was carried out by spraying 1 mL of HMDS into the air inlet of vacuum oven with a clean substrate inside at 80°C, the film was kept in this atmosphere for 2 h. CYTOP (35 μL) was spun on a substrate at 1000 rpm for 40 s.

On the treated (or untreated) substrates homogeneous thin films of organic semiconductors (20 nm) were thermally evaporated in vacuum with the rate of 0.2 Å/s. This was followed by vacuum thermal evaporation of gold source and drain electrodes (100 nm) through a shadow mask to create electrodes pattern. The dimensions of transistor channel were: width (W) = 1000 μm, length (L) = 30 μm; W/L = 33. General device structure of the obtained OFETs is shown on **Figure 3.7**.

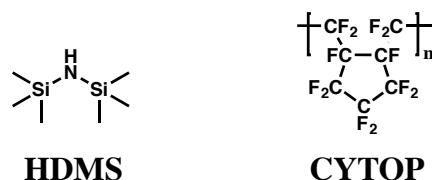


Figure 3.6. Chemical structure of substances used for monolayers.

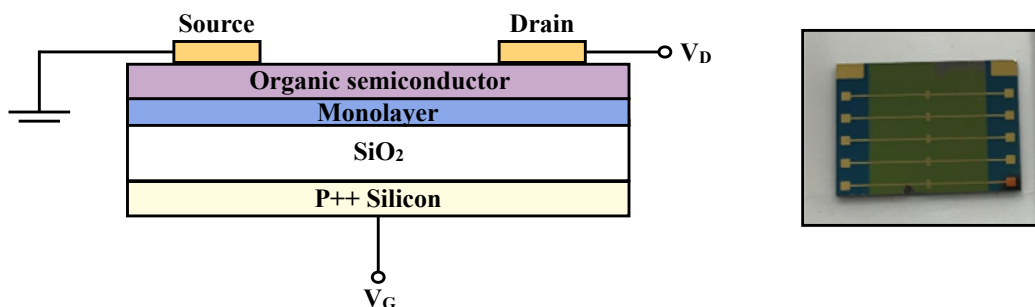


Figure 3.7. Schematic layout of thin film transistor (left) and a photo of fabricated device (5 transistors per substrate) (right).

The electrical measurements were performed using Keithley 2400 Source Meter. The output characteristics were evaluated by measuring a drain current (I_D) at gate voltages (V_G) of 0, -10, -20, -30, -40, -50, and -60 V while sweeping drain voltage V_D from 0 to -60 V. Transfer curves (I_D vs. V_G) were recorded by sweeping V_G from 0 to -60 V in step of 5 V at linear ($V_D = -10$ V) and saturation ($V_D = -60$ V) regimes.

Based on the obtained data, we evaluated the following parameters:

- The mobility (μ) in linear regime ($V_D \ll V_G - V_{Th}$) can be expressed as:

$$\mu_{lin} = \frac{L}{WC_i V_D} \left(\frac{\partial I_D}{\partial V_G} \right) \quad (3.19)$$

where C_i - insulator capacitance, W - channel width and L refers to the channel length (in our devices $W/L = 33$), I_D - drain current and V_G - gate voltage.

- In saturation regime ($V_D > V_G - V_{Th}$), the mobility is given by:

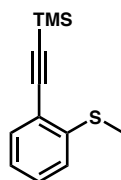
$$\mu_{sat} = \frac{2L}{WC_i} \left(\frac{\partial \sqrt{I_{D,sat}}}{\partial V_G} \right)^2 \quad (3.20)$$

- Threshold voltage (V_{th}): fit a straight line to the characteristics at high V_D and read the threshold as the intercept of that line with the V_G axis.
- On/Off Current ratio: ratio between I_D ($V_G = V_D = V$) and I_D ($V_D = 0, V_D = V$). It is important to have high ratio for low driving voltage and good signal to noise.

3.7 Synthetic procedures

3.7.1 Benzothieno[3,2-*b*]benzothiophene (BTBT) derivatives

2-[2-(Trimethylsilyl)ethynyl]thioanisole (1) [50]



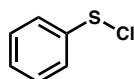
To a solution of 2-iodothioanisole (1.44 mL, 10.3 mmol), PdCl₂(PPh₃)₂ (0.1446 g, 2 mol %), and CuI (0.038 g, 2 mol %) in triethylamine (40 mL), 12.36 mmol of trimethylsilyl acetylene (1.2 eq, 1.75 mL, 12.36 mmol) in 10 mL of triethylamine was added dropwise. The reaction flask was evacuated and refilled with argon several times, and the mixture was stirred at room temperature for 2 hours. After completion of the reaction (TLC, eluent: petroleum ether), the reaction mixture was washed with 2M aq HCl solution and extracted with ethyl acetate. The combined organic layers were dried over MgSO₄ and concentrated under vacuum to yield the crude product. The product was purified by column chromatography on silica gel using petroleum ether as an eluent. 2-[2-(Trimethylsilyl)ethynyl]thioanisole was obtained as a yellow liquid, the yield was 2.2g (98%). ¹H and ¹³C NMR match the reported spectra. [50]

¹H NMR (CDCl₃) δ (ppm): 7.44 (1H, d, J=7.6 Hz), 7.31 (1H, m), 7.15 (1H, d, J=7.8 Hz), 7.08 (1H, td, J=7.5 Hz), 2.5 (3H, s), 0.31 (9H, s).

¹³C NMR (CDCl₃) δ (ppm): 142.0, 132.7, 129.0, 124.1, 123.9, 121.1, 102.1, 101.4, 15.0, 0.0.

MS (EI⁺): (m/z) 220.1 (calculated for C₁₂H₁₆SSi: 220.07).

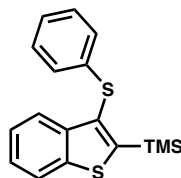
Phenylsulfenyl chloride (2) [51]



Under argon atmosphere, N-chlorosuccinimide (1.2 eq, 1.34g, 10 mmol) was dissolved in 40 mL of DCM. Thiophenol (0.828 mL, 8.1 mmol) was added dropwise at 0°C and the reaction mixture was stirred at the same temperature for 1 hour. Afterwards, the solvent was evaporated, and hexane was added to the residue. The solid phase was filtered off. The filtrate was evaporated,

and the crude product was used for the next step straight away without any purification and analysis.

3-Phenylthio-2-(trimethylsilyl)benzo[*b*]thiophene (3) [52]



Under argon atmosphere, a solution of phenylsulfenyl chloride (**2**) (1.5 eq, 1.1g, 7.3 mmol) in dichloromethane (30 mL) was added dropwise to a solution of 2-[2-(trimethylsilyl)ethynyl]thioanisole (**1**) (1.1 g, 4.9 mmol) in DCM (65 mL) at 0 °C. The reaction mixture was stirred at room temperature for 5 hours. After completion of reaction (TLC, eluent: hexane), the reaction mixture was washed with water. The organic layer was dried with MgSO₄ and concentrated in vacuum. The residue was purified by column chromatography on silica gel using petroleum ether as an eluent. The product was obtained as white crystals with the yield of 0.96g (62.4%). Mp = 78-80°C (lit. Mp = 82-84°C). ¹H and ¹³C NMR match the reported spectra. [52]

¹H NMR (CDCl₃) δ (ppm): 7.92 (1H, d, J=7.9 Hz), 7.77 (1H, d, J=7.4 Hz), 7.36 (2H, dt, J=15.1, 6.5 Hz), 7.18 (2H, t, J=7.5 Hz), 7.08 (1H, t, 7.3 Hz), 7.00 (2H, d, J=7.3 Hz), 0.45 (9H, s).

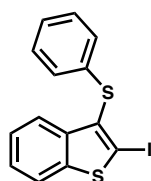
¹³C NMR (CDCl₃) δ (ppm): 149.4, 142.7, 141.7, 138.1, 129.2, 129.1, 128.8, 127.53, 126.0, 125.0, 124.8, 124.7, 123.1, 122.4, 0.2.

FT-IR (ATR): 3057.8 (w), 2960 (w), 1579.4 (m), 1475.8 (m), 1439 (m), 1438.4 (m), 1418.3 (w), 1320.5 (w), 1286 (w), 1248.6 (m), 1073.2 (m), 1009.9 (m), 900.58 (m), 834.42 (s), 756.8 (m), 733.8 (s), 690.6 (m), 638.8 (m).

MS (EI⁺): (m/z) 314.1 (calculated for C₁₇H₁₈S₂Si: 314.06).

Elemental Analysis (%): Calculated for C₁₇H₁₈S₂Si: C, 64.92; H, 5.77; S, 20.39. Found: C, 64.98; H, 5.82; S, 20.45.

2-Iodo-3-phenylthiobenzo[*b*]thiophene (4) [52]



A solution of ICl in dichloromethane (1.2 eq, 1 M, 0.76 mL, 0.762 mmol) was added to a solution of 3-phenylthio-2-(trimethylsilyl)benzo[b]thiophene (**3**) (0.2 g, 0.63 mmol) in 6 mL of DCM at -40°C . The mixture was stirred for 3 h at the same temperature. After completion of the reaction (TLC, eluent: petroleum ether), 3 mL of saturated aqueous solution of $\text{Na}_2\text{S}_2\text{O}_3$ was poured into the reaction mixture. The resulting mixture was extracted with DCM, and the combined organic layers were washed with water, dried with MgSO_4 , and concentrated in vacuum. The product was recrystallized from ethanol giving white crystals. The yield was 0.15g (65%). Mp = $84-86^{\circ}\text{C}$ (lit. Mp = $97-98^{\circ}\text{C}$). ^1H and ^{13}C NMR match the reported spectra. [52]

^1H NMR (CDCl_3) δ (ppm): 7.81 (2H, d, $J=8.0$ Hz), 7.34 (2H, m), 7.22 (2H, t, $J=7.4$ Hz), 7.14 (3H, m).

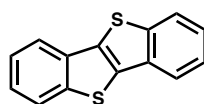
^{13}C NMR (CDCl_3) δ (ppm): 143.7, 138.8, 135.8, 131.3, 129.1, 127.1, 125.9, 125.3, 125.1, 123.8, 121.8, 95.3.

FT-IR (ATR): 3046.3 (w), 2931.3 (w), 1576.5 (m), 1478.7 (m), 1450 (m), 1435.6 (m), 1412.6 (m), 1329.2 (w), 1245.7 (m), 1150.8 (w), 1125 (w), 1081.8 (w), 1021.4 (m), 989.7 (m), 940 (w), 891.9 (m), 841 (w), 742.4 (s), 735 (s), 687.7 (s), 615.8 (w).

MS (EI⁺): (m/z) 367.9 (calculated for $\text{C}_{14}\text{H}_9\text{IS}_2$: 367.92).

Elemental Analysis (%): Calculated for $\text{C}_{14}\text{H}_9\text{IS}_2$: C, 45.66; H, 2.46; I, 34.46; S, 17.41. Found: C, 45.76; H, 2.67; I, 34.34; S, 17.47.

[1]Benzothieno[3,2-*b*][1]benzothiophene (**5**) [52]



2-iodo-3-phenylthiobenzo[b]thiophene (**4**) (0.69 g, 1.88 mmol), sodium acetate (2 eq, 0.31 g, 3.8 mmol) and $\text{PdCl}_2(\text{PPh}_3)_2$ (0.05 eq, 0.066g, 0.094mmol) were placed in a two-necked round-bottom flask. The flask was evacuated and refilled with argon several times. Afterwards, 25 mL of degassed *N,N*-dimethylacetamide were added. The mixture was heated at 140°C for 48 hours. After completion of the reaction (TLC: eluent hexane), HCl (aq) (1 M, 100 mL) was added to quench the reaction. The mixture was extracted with ethyl acetate, the organic layer was dried with MgSO_4 and the solvent was evaporated in vacuum. The residue was purified by column chromatography (eluent: hexane) and recrystallized from ethanol. The yield was 0.196 g (44%).

Mp could not be determined because the compound decomposes before melting. ^1H and ^{13}C NMR match the reported spectra. [52]

^1H NMR (CDCl_3) δ (ppm): 7.94 (4H, dd, $J=13.6, 7.9$ Hz), 7.46 (4H, dt, $J=13.8, 7.7$ Hz).

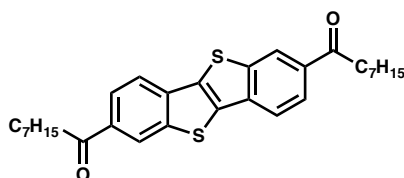
^{13}C NMR (CDCl_3) δ (ppm): 142.3, 133.5, 133.1, 125.0, 124.9, 124.1, 121.6.

FT-IR (ATR): 3053.5 (w), 1892.5 (w), 1865.9 (w), 1819.3 (w), 1782.7 (w), 1689.5 (w), 1553.1 (w), 1456.7 (w), 1433.4 (m), 1333.6 (m), 1297 (w), 1253.7 (m), 1150.5 (w), 1127.3 (w), 1057.4 (w), 1014.2 (w), 954.3 (w), 931 (w), 738.1 (s), 721.4 (s), 698.1 (s).

MS (EI+): (m/z) 240.0 (calculated for $\text{C}_{14}\text{H}_8\text{S}_2$: 240.34).

Elemental Analysis (%): Calculated for $\text{C}_{17}\text{H}_8\text{S}_2$: C, 69.96; H, 3.36; S, 26.68. Found: C, 69.64; H, 3.51; S, 26.59.

1,1'-[1]Benzothieno[3,2-*b*][1]benzothiophene-2,7-diyl dioctan-1-one (6) [53]



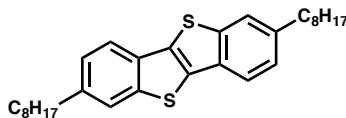
[1]Benzothieno[3,2-*b*][1]benzothiophene (0.26g, 1 mmol) was dissolved in dichloromethane (20 mL) and cooled down to -10 °C. At this temperature aluminium chloride (5.5 eq, 0.73 g, 5.5 mmol) was added. The solution was cooled to -78 °C. Then, octanoyl chloride (5 eq, 0.85 mL, 5 mmol) was added dropwise, and the mixture was stirred for 1h at the same temperature. The reaction mixture left stirring without cooling for 48 h at rt. The reaction was quenched with iced water and then it was diluted with methanol to give a precipitate. The precipitate was collected by filtration and washed consecutively with water and methanol. The crude solid was purified by recrystallization from toluene to give 1,1'-[1]benzothieno[3,2-*b*][1]benzothiophene-2,7-diyl dioctan-1-one as yellow crystals. The yield was 0.36 g (74%). Mp = 210-213 °C (lit. Mp = 250-251°C).

FT-IR (ATR): 2952.6 (m), 2916.8 (m), 2848 (m), 1905 (w), 1800.7 (w), 1766 (w), 1678.4 (s), 1583.4 (m), 1464.9 (m), 1455.5 (m), 1398.9 (m), 1372.3 (m), 1358.7 (m), 1343.5 (m), 1323 (m), 1296 (m), 1273.4 (m), 1248 (m), 1225.6 (m), 1191.6 (m), 1142.3 (w), 1075.9 (w), 1055.4 (w), 1013.8 (m), 984.8 (m), 954.9 (m), 901.9 (m), 840 (w), 812.4 (s), 789.4 (w), 770.7 (m).

MS (APCI+): (m/z) 492 (calculated for $\text{C}_{30}\text{H}_{36}\text{O}_2\text{S}_2$: 492.22).

Elemental Analysis (%): Calculated for C₃₀H₃₆O₂S₂: C, 73.13; H, 7.36; S, 13.01. Found: C, 72.98; H, 7.14; S, 12.87.

2,7-Dioctyl[1]benzothieno[3,2-*b*][1]benzothiophene (7) [53]



A mixture of 1,1'-[1]benzothieno[3,2-*b*][1]benzothiophene-2,7-diyldioctan-1-one (0.37g, 0.75 mmol), potassium hydroxide (5.5 eq, 0.23g, 4.1 mmol), hydrazine hydrate (25.5eq, 0.59 mL, 19 mmol) in diethylene glycol (35 mL) was heated to 100 °C for 1 h and then further heated at 210 °C for 5 h. The reaction mixture was cooled, and the resulting precipitate was collected by filtration, washed with water and methanol. The crude product was purified by column chromatography on silica gel eluted with petroleum ether. The obtained 2,7-dioctyl[1]benzothieno[3,2-*b*][1]benzothiophene was recrystallized from hexane to give white crystals. The yield was 0.12 g (34%). Mp = 113°C by DSC, which corresponds to the value reported in literature (111°C). ¹H and ¹³C NMR match the reported spectra. [53]

¹H NMR (CDCl₃) δ (ppm): 7.79 (2H, d, J=8.1 Hz), 7.73 (2H, s), 7.29 (2H, d, J=6.9 Hz), 7.78 (4H, m), 1.72 (4H, m), 1.33 (20H, m), 0.9 (6H, t, J=6.8 Hz).

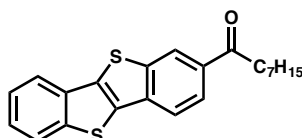
¹³C NMR (CDCl₃) δ (ppm): 142.4, 140.1, 132.5, 131.2, 125.8, 123.3, 121.1, 36.2, 31.9, 31.8, 29.5, 29.4, 29.2, 22.7, 14.2.

FT-IR (ATR): 3036.7 (w), 3018.5 (w), 2953.8 (m), 2917.7 (m), 2848.7 (m), 1884.1 (w), 1753.6 (w), 1733.8 (w), 1630 (w), 1598 (w), 1550.9 (w), 1458.7 (m), 1406.9 (w), 1371.1 (w), 1336.6 (w), 1305.9 (w), 1283 (w), 1255.9 (w), 1135.4 (w), 1121.5 (w), 1053.6 (w), 1004.8 (w), 951 (w), 879.2 (w), 870.9 (w), 813.8 (s), 791.6 (m).

MS (APCI+): (m/z) 464 (calculated for C₃₀H₄₀S₂: 464.26).

Elemental Analysis (%): Calculated for C₃₀H₄₀S₂: C, 77.52; H, 8.68; S, 13.8. Found: C, 77.55; H, 8.57; S, 13.69.

1,1'-[1]Benzothieno[3,2-*b*][1]benzothiophene-2-diyldioctan-1-one (8)



[1]Benzothieno[3,2-*b*][1]benzothiophene (0.48g, 2.0 mmol) was dissolved in dichloromethane (38 mL) and cooled down to $-10\text{ }^{\circ}\text{C}$. At this temperature aluminium chloride (2.5 eq, 0.66 g, 4.9 mmol) was added. The solution was cooled to $-78\text{ }^{\circ}\text{C}$. Then octanoyl chloride (1.1 eq, 0.36 mL, 2.2 mmol) was added dropwise, and the mixture was stirred for 1h at the same temperature. The reaction mixture left stirring without cooling for 48h at rt. The reaction was quenched with 10mL of iced water and then it was diluted with 20mL of methanol to give a precipitate. The precipitate was collected by filtration and washed thoroughly with water and methanol to give 1,1'-[1]benzothieno[3,2-*b*][1]benzothiophene-2,7-diyl dioctan-1-one as yellow solid. The crude solid was used in further reaction without purification. The yield was 0.46 g (66%). Mp= 159-163 $^{\circ}\text{C}$ (lit. Mp = 163 $^{\circ}\text{C}$). [54]

^1H NMR (CDCl_3) δ (ppm): 8.56 (1H, d, $J=1.1\text{ Hz}$), 8.07 (1H, dd, $J=8.3, 1.3\text{ Hz}$), 7.95 (3H, m), 7.49 (2H, pd, $J=7.2, 1.3\text{ Hz}$), 3.08 (2H, t, 7.4 Hz), 1.81 (2H, m), 1.39 (8H, m), 0.92(3H, t, $J=6.8\text{ Hz}$).

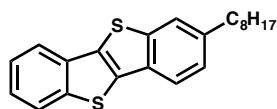
^{13}C NMR (CDCl_3) δ (ppm): 199.6, 142.8, 142.2, 136.9, 136.2, 133.6, 133.0, 132.75, 125.9, 125.1, 124.7, 124.6, 124.2, 122.1, 121.4, 38.8, 31.8, 29.4, 29.2, 24.5, 22.7, 14.1.

FT-IR (ATR): 3050.8 (w), 2915.0 (m), 2847.9 (m), 1676.8 (s), 1585.0 (m), 1553.9 (w), 1462.8 (m), 1425.5 (m), 1384.7 (s), 1340.8 (s), 1295.2 (m), 1273.1 (m), 1250.2 (m), 1225.7 (s), 1192.2 (s), 1130.6 (w), 1076.4 (w), 1056.0 (w), 1013.4 (m), 984.8 (w), 952.9 (m), 935.1 (w), 901.5 (m), 841.1 (w), 812.1 (s), 770.8 (s).

MS (+EI): (m/z) 366.1 (calculated for $\text{C}_{22}\text{H}_{22}\text{OS}_2$: 366.54).

Elemental Analysis (%): Calculated for $\text{C}_{22}\text{H}_{22}\text{OS}_2$: C, 72.09; H, 6.05; S, 17.49. Found: C, 72.1; H, 6.22; S, 17.09.

2-Octyl[1]benzothieno[3,2-*b*][1]benzothiophene (9)



A mixture of 1,1'-[1]benzothieno[3,2-*b*][1]benzothiophene-2,7-diyl dioctan-1-one (0.46 g, 1.3 mmol), potassium hydroxide (2.8 eq, 0.2 g, 3.5 mmol), hydrazine hydrate (13eq, 0.51 mL, 16 mmol) in diethylene glycol (35 mL) was heated to $100\text{ }^{\circ}\text{C}$ for 1 h and then further heated at $210\text{ }^{\circ}\text{C}$ for 5 h. The reaction mixture was cooled and extracted with ethyl acetate. The organic layer was dried over MgSO_4 and the solvent was evaporated. The crude product was purified by

column chromatography on silica gel eluted with petroleum ether. The obtained 2-dioctyl[1]benzothieno[3,2-*b*][1]benzothiophene was recrystallized from hexane to give white crystals. The yield was 0.2 g (45%). Mp = 117°C by DSC (lit. Mp = 112 °C). ¹H and ¹³C NMR match the reported spectra. [54]

¹H NMR (CDCl₃) δ (ppm): 7.93 (1H, d, J=7.9 Hz), 7.89 (1H, d, J=8.3 Hz), 7.81 (1H, d, J=8.1 Hz), 7.75 (1H, s), 7.48 (1H, t, J=7.5 Hz), 7.41 (1H, t, J=7.6 Hz), 7.31 (1H, d, J=8.1 Hz), 2.78 (2H, t, J=7.5 Hz), 1.72 (2H, m), 1.33 (10H, m), 0.9 (3H, t, J=6.8 Hz).

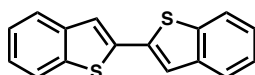
¹³C NMR (CDCl₃) δ (ppm): 142.6, 142.1, 140.4, 133.4, 133.3, 132.6, 131.0, 125.9, 124.8, 124.7, 124.0, 123.4, 121.4, 121.3, 32.6, 31.9, 31.7, 29.5, 29.4, 29.3, 22.7, 14.2.

FT-IR (ATR): 3047.2 (w), 2955.1 (w), 2917.2 (s), 2848.5 (s), 1934.7 (w), 1881.8 (w), 1865.3 (w), 1814.4 (w), 1778.2 (w), 1752.3 (w), 1683.2 (w), 1598.4 (w), 1552.5 (w), 1467.0 (s), 1450.3 (s), 1429.2 (s), 1336.2 (s), 1299.6 (m), 1255.1 (s), 1208.9 (w), 1164.4 (w), 1126.6 (m), 1094.3 (w), 1057.5 (m), 1015.7 (m), 952.2 (m), 929.2 (w), 889.8 (w), 877.0 (m), 866.5 (m), 854.1 (w), 812.0 (s), 799.1 (m).

MS (+EI): (m/z) 352.1 (calculated for C₂₂H₂₄S₂: 352.55).

Elemental Analysis (%): Calculated for C₂₂H₂₄S₂: C, 74.95; H, 6.86; S, 18.19. Found: C, 74.88; H, 6.85; S, 18.18.

2,2'-Bi(benzo[*b*]thiophene) (10) [55]



Benzo[*b*]thiophene (1 g, 7.5 mmol) was dissolved in 170mL of anhydrous diethyl ether in argon atmosphere. To this solution *n*-BuLi (1.2 eq, 9.2 mmol, 2.5 M, 4 mL) was added slowly dropwise at the room temperature. The reaction mixture was heated at reflux with stirring under argon for 6 hours. Afterwards the reaction mixture cooled to the room temperature and anhydrous CuCl₂ (1 eq, 7.5 mmol, 1 g) was added. This mixture was refluxed again for 4 h. The completion of reaction was checked by TLC (eluent: petroleum ether). The resulting reaction mixture was cooled to the room temperature and filtered through Celite® Hyflo Supercel plug. The precipitate was washed with diethyl ether. The filtrate was washed with 100mL 5% aq HCl solution. The combined organic layers were dried over MgSO₄ and then solvent was evaporated. The crude product was purified by silica gel column using gradient of the eluent polarity starting from petroleum ether and moving onto petroleum ether: ethyl acetate (10:1). The resulting product was

recrystallized from toluene giving white crystals. The yield was 40 mg (4%). Mp = 260 – 262 °C. ^1H and ^{13}C NMR match the reported spectra. [56]

^1H NMR (CDCl_3) δ (ppm): 7.81 (4H, m), 7.54 (2H, s), 7.38 (4H, m).

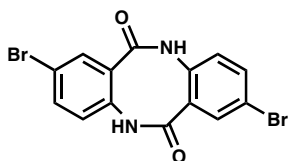
^{13}C NMR (CDCl_3) δ (ppm): 140.2, 139.5, 137.2, 125.0, 124.8, 123.7, 122.2, 121.4.

FT-IR (ATR): 3052 (w), 3027 (w), 1948 (w), 1907 (w), 1879 (w), 1834 (w), 1800 (w), 1692 (w), 1645 (w), 1588 (w), 1556 (w), 1496 (w), 1452 (w), 1423 (m), 1322 (w), 1284 (w), 1246 (w), 1177 (w), 1151 (w), 1123 (w), 1072 (w), 1006 (w), 968 (w), 940 (m), 886 (m), 854 (w), 816 (s), 738 (s), 721 (s), 658 (w).

MS (EI+): (m/z) 266.0 (calculated for: 266.38).

3.7.2 Indolo[3,2-*b*]indole (ININ) derivatives

2,8-Dibromo-dibenzo[*b,f*][1,5]diazocine-6,12(5H,11H)-dione (11) [57]



250 mL three-necked round-bottom flask equipped with a condenser, stirring bar and 50 mL dropping funnel was charged with 0.57g (23.8 mmol) of sodium hydride. The system was degassed and refilled with argon. Dry THF (50mL) was transferred into the flask through the metal cannula. Methyl 2-amino-5-bromobenzoate (2.74g, 11.9 mmol) was dissolved in 10 mL of dry THF in a separate flask under argon. The obtained solution was transferred into the dropping funnel. Methyl 2-amino-5-bromobenzoate solution was added dropwise into the flask. The mixture was refluxed for 3 days. After completion of the reaction (TLC: ethyl acetate: 40-60 petroleum ether, 1:2), the mixture was cooled down to the room temperature and poured into 200mL of cold aqueous 0.1 M HCl solution. The precipitate was filtered off, thoroughly washed with water and dried in vacuum. The product was obtained as fine beige powder with a yield of 86% (4.05 g). Mp = 298°C.

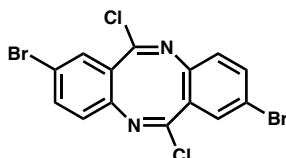
^1H NMR (DMSO-d_6) δ (ppm): 10.4 (2H, s), 7.58 (2H, dd, $J = 8.5, 2.4$ Hz), 7.51 (2H, d, $J = 2.3$ Hz), 7.06 (2H, d, $J = 8.5$ Hz).

^{13}C NMR (DMSO-d_6) δ (ppm): 172.6, 140.35, 139.1, 138.8, 135.9, 133.2, 125.1.

FT-IR (ATR): 3161 (w), 3046 (w), 2921 (w), 2853 (w), 1647 (s), 1595 (m), 1570 (m), 1507 (m), 1484 (m), 1416 (s), 1351 (s), 1293 (m), 1258 (m), 1229 (m), 1160 (w), 1104 (m), 1081 (m), 1066 (m), 960 (w), 923 (m), 887 (m), 826 (s).

MS (EI⁺): (m/z) 395.9 (calculated for C₁₄H₈Br₂N₂O₂: 396.04).

2,8-Dibromo-6,12-dichloro-dibenzo[b,f][1,5]diazocine (12) [57]



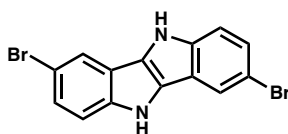
4.2g (10mmol) of the product **11** and 6.63g (31.8 mmol) of phosphorus pentachloride were mixed together in 500mL two-necked round-bottom flask equipped with a condenser and a stirring bar. The flask was degassed and refilled with argon. Then 200mL of dry chloroform were added using a metal cannula. The mixture was refluxed for 4 hours. The reaction was monitored by TLC using ethyl acetate: 40-60 petroleum ether (1:2) as an eluent. After the completion of reaction, the solvent was evaporated, and the product was used in the next step without further purification.

¹H NMR (CDCl₃) δ (ppm): 7.52 (2H, dd, J = 8.6, 2.2 Hz), 7.47 (2H, d, J = 2.1 Hz), 6.88 (2H, d, J = 8.6 Hz).

¹³C NMR (CDCl₃) δ (ppm): 155.2, 144.0, 135.0, 129.7, 127.3, 123.8, 118.8.

MS (EI⁺): (m/z) 431.8 (calculated for C₁₄H₆Br₂Cl₂N₂: 432.92).

3,8-Dibromo-5,10-dihydroindolo[3,2-b]indole (13) [57]



Product **12** in the 500mL round-bottom flask was sealed with a suba seal and dissolved in 250mL of dry THF under argon. 500mL three-necked round bottom flask equipped with a condenser, stirring bar and 50mL dropping funnel was charged with 7.9g (120mmol) of activated zinc powder. The solution of the product **12** was transferred into the reaction flask using a metal cannula. Trifluoroacetic acid (19mL, 240mmol) was added dropwise into the reaction mixture using a dropping funnel. The reaction was left stirring overnight. The completion of reaction was confirmed by TLC (ethyl acetate: 40-60 petroleum ether, 1:5). To stop the reaction zinc was

filtered off and the solvent was evaporated. The obtained liquid was transferred into a separation funnel, diluted with ethyl acetate and washed with 200 mL of saturated ammonium chloride solution, followed by washing with 200 mL saturated sodium carbonate solution. The collected organic layer was dried over MgSO_4 . Solvent was then evaporated. The obtained solid was dissolved in 10 mL of THF and precipitated into 200 mL of cold hexane. The precipitate was collected by filtration. The product was a yellow powder. Overall yield of two reactions was 69% (2.5 g). $\text{Mp} > 300^\circ\text{C}$, might be decomposing before melting.

$^1\text{H NMR}$ (DMSO-d_6) δ (ppm): 11.3 (2H, s), 7.90 (2H, d, $J = 1.9$ Hz), 7.50 (2H, d, $J = 8.7$ Hz), 7.31 (2H, dd, $J = 8.7, 2.0$ Hz).

$^{13}\text{C NMR}$ (DMSO-d_6) δ (ppm): 139.5, 125.9, 124.8, 120.4, 116.1, 114.7, 110.6.

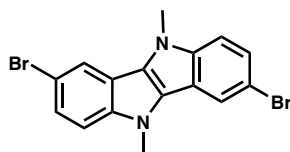
FT-IR (ATR): 3397 (m), 2959 (w), 2917 (w), 2855 (w), 1866 (w), 1718 (w), 1595 (w), 1560 (w), 1487 (w), 1452 (m), 1355 (m), 1306 (m), 1259 (w), 1247 (w), 1220 (w), 1158 (w), 1124 (w), 1092 (w), 1045 (m), 948 (m), 862 (m), 796 (s).

MS (EI^+): (m/z) 363.9 (calculated for $\text{C}_{14}\text{H}_8\text{Br}_2\text{N}_2$: 364.04).

Activated zinc

20 g of zinc fine powder was placed in the round bottom flask and mixed with 150 mL of 1 M HCl aqueous solution. The mixture was stirred for 30 minutes. The liquid was then decanted, and zinc powder was washed with ethanol, followed by diethyl ether. Then the obtained powder was dried in high vacuum at 120°C for an hour.

3,8-Dibromo-5,10-dimethylindolo[3,2-b]indole (14)



Product **13** (3.3 g, 9.1 mmol), sodium hydride (1.1 g, 46 mmol) were placed in 100 mL two-necked flask equipped with condenser and a stirring bar. The mixture was degassed, filled with argon and then 30 mL of dry DMF were added. The mixture was stirred for 10 minutes. Afterwards 2.8 mL (45 mmol) of methyl iodide were added. The reaction was heated to 50°C overnight. The completion of reaction was confirmed by TLC (ethyl acetate: 40-60 petroleum ether, 1:5). The reaction mixture was cooled down to a room temperature and poured into 300 mL of cold water. The precipitate was collected by filtration, washed with water and dried in a

vacuum oven. The product was obtained as a beige powder with a yield of 79% (2.8 g). Mp = 190-195°C.

^1H NMR (DMSO- d_6) δ (ppm): 8.22 (2H, d, J = 1.9 Hz), 7.60 (2H, d, J = 8.9 Hz), 7.41 (2H, dd, J = 8.8, 2.0 Hz), 4.10 (6H, s).

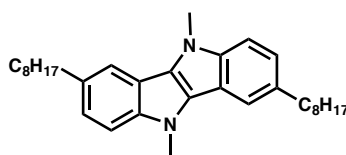
^{13}C NMR (DMSO- d_6) δ (ppm): 126.2, 125.0, 121.9, 120.5, 115.5, 112.7, 110.9, 32.00.

FT-IR (ATR): 2954 (w), 2923 (w), 2853 (w), 1656 (w), 1588 (w), 1560 (w), 1461 (m), 1420 (w), 1382 (m), 1329 (m), 1228 (m), 1146 (m), 1091 (m), 10521 (m), 969 (m), 928 (w), 880 (m), 862 (m), 794 (s).

MS (EI $^+$): (m/z) 391.9 (calculated for $\text{C}_{16}\text{H}_{12}\text{Br}_2\text{N}_2$: 392.09).

Elemental analysis (%): Calculated for $\text{C}_{16}\text{H}_{12}\text{Br}_2\text{N}_2$: C, 49.01; H, 3.08; N, 7.14; Br, 40.76. Found: C, 49.07; H, 3.32; N, 6.95; Br, 40.96.

3,8-Dioctyl-5,10-dimethylindolo[3,2-b]indole (15)



1.5 g (3.8 mmol) of product **14** and 0.1 g (5%, 0.19 mmol) of $\text{Ni}(\text{dppp})\text{Cl}_2$ were placed in two-necked 50 mL round-bottom flask equipped with condenser and a stirring bar. The flask was thoroughly degassed and refilled with argon. Dry THF (18 mL) was added using a syringe. The mixture was cooled to 0°C and 5.7 mL of octylmagnesium bromide (2 M in Et_2O) were added dropwise. The mixture was allowed to warm up to the room temperature and then heated to reflux. The mixture was refluxed for 3 days. The progress of reaction was monitored by TLC (40-60 petroleum ether). When the reaction was completed, the mixture was cooled down to a room temperature, transferred into a separating funnel, diluted with ethyl acetate and washed with 100 mL of 1 M aqueous HCl solution. The collected organic layer was dried over MgSO_4 and the solvent was evaporated. The obtained product was purified by silica gel column chromatography, using ethyl acetate: 40-60 petroleum ether (1:10) as an eluent. Then the product was recrystallized from hexane, giving white crystals with 12% (68 mg) yield. Mp = 153°C (DSC).

^1H NMR (CDCl_3) δ (ppm): 7.68 (2H, broad singlet), 7.35 (2H, d, $J = 7.8$ Hz), 7.14 (2H, broad singlet), 4.11 (6H, broad singlet), 2.89 – 2.67 (2H, m), 1.74 (4H, dt, $J = 15.4, 7.7$ Hz), 1.50 – 1.22 (20H, m), 0.91 (6H, t, $J = 6.8$ Hz).

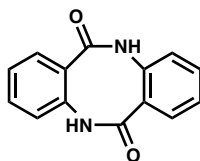
^{13}C NMR (CDCl_3) δ (ppm): 140.0, 132.6, 126.5, 122.4, 116.6, 115.1, 36.2, 32.5, 31.9, 31.7, 29.6, 29.5, 29.3, 22.7, 14.1.

FT-IR (ATR): 2954 (w), 2917 (m), 2868 (m), 2848 (m), 1843 (w), 1713 (w), 1615 (w), 1568 (w), 1489 (m), 1466 (m), 1423 (w), 1386 (m), 13489 (m), 1336 (w), 1294 (w), 1269 (w), 1258 (w), 1244 (m), 1171 (m), 1143 (w), 1117 (w), 1088 (w), 1004 (w), 986 (w), 937 (w), 917 (w), 890 (w), 864 (w), 805 (m), 788 (s), 755 (m).

MS (EI⁺): (m/z) 458 (calculated for $\text{C}_{32}\text{H}_{46}\text{N}_2$: 458.73).

Elemental analysis (%): Calculated for $\text{C}_{32}\text{H}_{46}\text{N}_2$: C, 83.79; H, 10.10; N, 6.11. Found: C, 83.14; H, 9.69; N, 5.91.

Dibenzo[b,f][1,5]diazocine-6,12(5H,11H)-dione (16) [57]



100mL three-necked round-bottom flask equipped with a condenser and stirring bar was charged with 0.79 g (33 mmol) of sodium hydride. The system was degassed and refilled with argon. Dry THF (40 mL) was transferred into the flask through the metal cannula. Methyl 2-aminobenzoate (2.5 g, 17 mmol) was added dropwise using a syringe. The mixture was refluxed for 3 days. After completion of the reaction (TLC: ethyl acetate: 40-60 petroleum ether, 1:2), the mixture was cooled down to the room temperature and poured into 200mL of cold aqueous 0.1M HCl solution. The precipitate was filtered off, thoroughly washed with water and dried in vacuum. The product was obtained as fine beige powder with a yield of 46% (1.81 g). Mp=324°C.

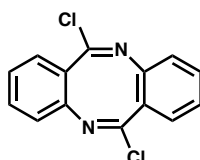
^1H NMR (DMSO-d_6) δ (ppm): 10.2 (2H, s), 7.38 – 7.28 (4H, m), 7.26 – 7.21 (2H, m), 7.07 (2H, d, $J = 7.9$ Hz).

^{13}C NMR (DMSO-d_6) δ (ppm): 170.0, 135.2, 134.0, 131.0, 128.6, 127.7, 126.1.

FT-IR (ATR): 3161 (w), 3029 (w), 2899 (w), 2854 (w), 1654 (s), 1638 (s), 1603 (m), 1577 (m), 1488 (m), 1439 (m), 1379 (s), 1296 (m), 1261 (m), 1236 (m), 1161 (w), 1139 (m), 1096 (w), 1041 (w), 989 (w), 954 (w), 928 (w), 900 (w), 837 (m), 794 (m).

MS (EI⁺): (m/z) 238.1 (calculated for C₁₄H₁₀N₂O₂: 238.25).

6,12-dichlorodibenzo[b,f][1,5]diazocine (17) [57]



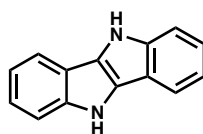
2 g (8.4 mmol) of the product **16** and 5.24 g (25 mmol) of phosphorus pentachloride were mixed together in 250 mL two-necked round-bottom flask equipped with a condenser and stirring bar. The flask was degassed and refilled with argon. Then 100 mL of dry chloroform were added using a metal cannula. The mixture was refluxed for 4 hours. The reaction was monitored by TLC using ethyl acetate: 40-60 petroleum ether (1:5) as an eluent. After the completion of reaction, the solvent was evaporated, and the product was used in the next step without further purification.

¹H NMR (CDCl₃) δ (ppm): 7.41 – 7.32 (4H, m), 7.19 – 7.13 (2H, m), 6.99 (2H, d, J = 8.6 Hz).

¹³C NMR (CDCl₃) δ (ppm): 156.3, 145.3, 131.6, 127.1, 126.1, 125.4, 122.0.

MS (EI⁺): (m/z) 274.0 (calculated for C₁₄H₈Cl₂N₂: 275.13).

5,10-dihydroindolo[3,2-b]indole (18) [57]



Product **17** in the 250 mL round-bottom flask was sealed with a suba seal and dissolved in 125 mL of dry THF under argon. 250 mL three-necked round bottom flask equipped with a condenser, stirring bar and 50 mL dropping funnel was charged with 6.5 g (101 mmol) of activated zinc powder. The solution of the product **17** was transferred into the reaction flask using a metal cannula. Trifluoroacetic acid (16 mL, 202 mmol) was added dropwise into the reaction mixture using a dropping funnel. The reaction was left stirring overnight. The completion of reaction was confirmed by TLC (ethyl acetate: 40-60 petroleum ether, 1:5). To stop the reaction zinc was

filtered off and the solvent was evaporated. The obtained liquid was transferred into a separation funnel, diluted with ethyl acetate and washed with 300 mL of saturated ammonium chloride solution, followed by washing with 200 mL saturated sodium carbonate solution. The collected organic layer was dried over MgSO_4 . Solvent was then evaporated. The obtained solid was dissolved in 15 mL of THF and precipitated into 250 mL of cold hexane. The precipitate was collected by filtration. The product was a yellow powder. Overall yield of two reactions was 88.5% (1.85 g). The material does not melt before decomposition.

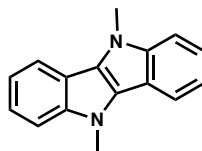
^1H NMR (DMSO- d_6) δ (ppm): 11.1 (2H, s), 7.72 (2H, d, $J = 7.8$ Hz), 7.47 (2H, d, $J = 8.1$ Hz), 7.19 – 7.13 (2H, m), 7.10 – 7.03 (2H, m).

^{13}C NMR (DMSO- d_6) δ (ppm): 140.8, 125.7, 121.8, 118.4, 117.9, 115.1, 112.6.

FT-IR (ATR): 3398 (m), 3050 (w), 2942 (w), 2866 (w), 1678 (m), 1501 (w), 1459 (m), 1404 (m), 1365 (w), 1322 (w), 1261 (m), 1192 (m), 1165 (m), 1136 (s), 1106 (m), 1009 (m), 925 (m), 846 (m), 800 (m).

MS (EI $^+$): (m/z) 206.1 (calculated for $\text{C}_{14}\text{H}_{10}\text{N}_2$: 206.25).

5,10-dimethylindolo[3,2-b]indole (19)



Product **18** (1 g, 4.9 mmol) and sodium hydride (0.58 g, 24 mmol) were placed in 50 mL two-necked flask equipped with condenser and a stirring bar. The mixture was degassed, filled with argon and then 10 mL of dry DMF were added. The mixture was stirred for 10 minutes. Afterwards 1.51 mL (24 mmol) of methyl iodide were added. The reaction was heated to 50°C overnight. The completion of reaction was confirmed by TLC (ethyl acetate: 40-60 petroleum ether, 1:10). The reaction mixture was cooled down to a room temperature and poured into 100 mL of cold water. The precipitate was collected by filtration, washed with water and dried in a vacuum oven. The product was purified by silica gel column chromatography using ethyl acetate: 40-60 petroleum ether (1:10) as an eluent. The purified product was recrystallized from methanol: THF mixture giving yellow crystals with a yield of 12% (137 mg). Mp could not be determined since compound decomposed before melting.

^1H NMR (CHCl_3) δ (ppm): 7.94 (2H, broad singlet), 7.47 (2H, d, $J = 8.4$ Hz), 7.34 (2H, broad singlet), 7.24 – 7.16 (2H, m), 4.16 (6H, broad singlet).

^1H NMR (DMSO-d_6) δ (ppm): 8.00 (2H, d, $J = 7.9$ Hz), 7.59 (2H, d, $J = 8.3$ Hz), 7.34 – 7.20 (2H, m), 7.13 (2H, t, $J = 7.9$ Hz), 4.11 (6H, s).

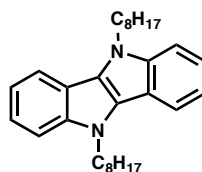
^{13}C NMR (DMSO-d_6) δ (ppm): 141.2, 126.1, 122.1, 118.5, 118.0, 114.6, 110.5, 31.9.

FT-IR (ATR): 3055 (w), 2914 (w), 2870 (w), 2836 (w), 2803 (w), 1905 (w), 1866 (w), 1831 (w), 1785 (w), 1748 (w), 1663 (w), 1603 (w), 1568 (w), 1500 (m), 1477 (m), 1429 (m), 1400 (m), 1366 (m), 1338 (m), 1269 (m), 1232 (m), 1151 (m), 1135 (m), 1113 (m), 1017 (m), 1006 (m), 918 (m), 843 (m), 769 (m).

MS (EI⁺): (m/z) 234.1 (calculated for $\text{C}_{16}\text{H}_{14}\text{N}_2$: 234.3).

Elemental analysis (%): Calculated for $\text{C}_{16}\text{H}_{14}\text{N}_2$: C, 82.02; H, 6.02; N, 11.96. Found: C, 80.92; H, 6.00; N, 11.70.

5,10-dioctylindolo[3,2-*b*]indole (20) [57]



100mL round bottom flask equipped with a stirring bar was charged with 2 g (9.7 mmol) of 5,10-dihydroindolo[3,2-*b*]indole and 0.62 g (1.9 mmol) of tetrabutylammonium bromide. The mixture was dissolved in 40mL of DMSO. Then 50% NaOH aqueous solution was added and the mixture was stirred for 10 minutes. Afterwards, 7.4 mL (49 mmol) of 1-octylbromide. The reaction mixture was left stirring at the room temperature for 2 hours. After completion of reaction, the reaction mixture was diluted with ethyl acetate and washed with 1L of distilled water. The organic layer was then collected and dried over MgSO_4 . The solvent was evaporated, and the product was purified by silica gel flash column using first 40-60 petroleum ether and then ethyl acetate: 40-60 petroleum ether (1:10) as eluent. The obtained product was then recrystallized from methanol, giving white crystals with a yield of 12% (0.5 g). Mp = 75°C (DSC).

^1H NMR (CDCl_3) δ (ppm): 7.86 (2H, d, $J = 7.8$ Hz), 7.49 (2H, d, $J = 8.3$ Hz), 7.32 (2H, t, $J = 7.5$ Hz), 7.20 (2H, t, $J = 7.5$ Hz), 4.51 (4H, t, $J = 6.9$ Hz), 2.05 – 1.90 (4H, m), 1.46 (4H, m), 1.3 (18H, m), 0.87 (6H, t, $J = 6.7$ Hz).

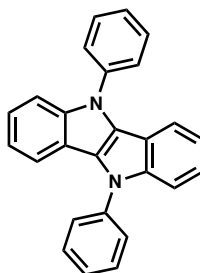
^{13}C NMR (CDCl_3) δ (ppm): 140.5, 125.8, 121.5, 117.9, 117.7, 114.5, 45.3, 31.8, 30.3, 29.4, 29.2, 27.2, 22.6, 14.1.

FT-IR (ATR): 2958 (w), 2921 (m), 2868 (w), 2847 (m), 1910 (w), 1875 (w), 1838 (w), 1788 (w), 1753 (w), 1658 (w), 1598 (w), 1575 (w), 1494 (m), 1474 (s), 1450 (m), 1344 (m), 1414 (m), 1344 (m), 1289 (w), 1268 (w), 1241 (w), 1222 (w), 1197 (m), 1184 (m), 1126 (m), 1072 (w), 1018 (m), 917 (w), 894 (w), 837 (w), 816 (w), 771 (w).

MS (EI⁺): (m/z) 430 (calculated for $\text{C}_{30}\text{H}_{42}\text{N}_2$: 430.68).

Elemental analysis (%): Calculated for $\text{C}_{30}\text{H}_{42}\text{N}_2$: C, 83.67; H, 9.83; N, 6.5. Found: C, 83.77; H, 9.88; N, 6.36.

5,10-dibenzodolo[3,2-b]indole (21) [58]



A mixture of 5,10-dihydroindolo[3,2-*b*]indole (0.8 g, 4 mmol), Cs_2CO_3 (3.11 g, 8 mmol), iodobenzene (3.6 mL, 10 mmol), and CuI (0.16 g, 20% mol) in DMF (20 mL) was heated in argon atmosphere to 150 °C for 48 hours. The termination of reaction was determined by TLC using 40-60 petroleum ether: ethyl acetate (5:1) as an eluent. The resulting mixture was cooled down to a room temperature. The mixture then was diluted with a saturated ammonium chloride solution (75 mL) and extracted into ethyl acetate. The organic layer was dried over MgSO_4 and then solvent was evaporated. The resulting oil was purified using a silica gel column using 40-60 petroleum ether: ethyl acetate (5:1) as an eluent. The product was recrystallized from toluene giving yellow crystals with a 17% (0.24 g). Mp could not be determined since compound decomposed before melting.

^1H NMR (CDCl_3) δ (ppm): 7.78 (4H, d, $J=8.4$ Hz), 7.67 (6H, t, $J=7.7$ Hz), 7.6 (2H, d, $J=7.8$ Hz), 7.49 (2H, t, 7.4 Hz), 7.28 (2H, m), 7.15 (2H, m).

^{13}C NMR (CDCl_3) δ (ppm): 140.8, 138.8, 129.7, 126.73, 126.68, 125.8, 122.7, 119.5, 118.5, 115.6, 110.9.

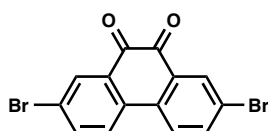
FT-IR (ATR): 3053 (w), 1594 (m), 1503 (m), 1487 (m), 1458 (s), 1399 (m), 1372 (w), 1326 (w), 1307 (w), 1286 (w), 1275 (w), 1226 (m), 1174 (w), 1160 (w), 1139 (m), 1097 (w), 1075 (w), 1064 (w), 1027 (w), 986 (w), 960 (w), 912 (w), 855 (w), 842 (w), 831 (w), 780 (w), 763 (w), 745 (w), 731 (s), 708 (s), 705 (s).

MS (AP+): (m/z) 359.4 (calculated for C₂₆H₁₈N₂: 358.4).

Elemental analysis (%): Calculated for C₂₆H₁₈N₂: C, 87.12; H, 5.06; N, 7.82. Found: C, 86.52; H, 5.18; N, 7.63.

3.7.3 Dicarbazolophenanthrene (DCP) derivatives

2,7-Dibromophenanthren-9,10-dione (22) [59]



5 g (24 mmol) of phenanthrene-9,10-dione were dissolved in 90 mL of 98% sulfuric acid. 9 g (50.6 mmol) of *N*-bromosuccinimide was added to this solution by small portions. The mixture was stirred at room temperature for 6 hours. Afterwards, the mixture was poured onto ice and filtered off. The crude product was recrystallized from DMSO. 2,7-Dibromophenanthren-9,10-dione was obtained as a deep orange solid with a quantitative yield of 8.3g (95%). Mp = 325-330°C, (lit. Mp = 331°C). [57]

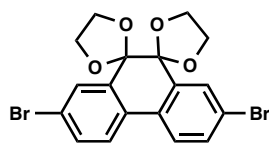
¹H NMR (CDCl₃) δ (ppm): 8.34 (2H, s), 7.87 (4H, s).

FT-IR (ATR): 3100 (w), 1673 (s), 1582 (s), 1458 (m), 1397 (m), 1287 (m), 1261 (m), 1200 (m), 1140 (m), 1077 (m), 996 (w), 905 (m), 828 (s), 774 (w), 701 (s).

MS (EI+): (m/z) 365.9 (calculated for C₁₄H₆Br₂O₂: 366.0).

Elemental analysis (%): Calculated for C₁₄H₆Br₂O₂: C, 45.94; H, 1.65; Br, 43.66. Found: C, 46.63; H, 2.19; Br, 43.06.

2,7-Dibromophenanthren-9,10-di(ethyleneglycol)ketal (23) [60]



In a round-bottom flask equipped with Dean-Stark apparatus, 0.5 g (1.4 mmol) of 2,7-dibromophenanthren-9,10-dione and 0.27 g (1.4 mmol) of p-toluenesulfonic acid monohydrate was dissolved in 60 mL of toluene. 3.5 mL (62.7 mmol) of ethylene glycol was added to the solution. The system was evacuated and refilled with argon. The solution was refluxed for 14 hours. The completion of the reaction was indicated by TLC (eluent: ethyl acetate: petroleum ether, 1:2). The resulting solution was cooled to room temperature, diluted with toluene and washed with water in an extraction funnel. The organic layer was dried with MgSO₄. The solvent was evaporated and the obtained solid was recrystallized from ethanol giving white crystals with a yield of 0.38 g (60%). Mp = 251-254°C, (lit. Mp = 263°C). [61]

¹H NMR (CDCl₃) δ (ppm): 7.91 (2H, s), 7.74 (2H, d, J = 8.5 Hz), 7.62 (2H, d, J = 8.4 Hz), 4.24 (4H, br s), 3.70 (4H, br s).

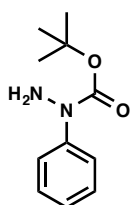
¹³C NMR (CDCl₃) δ (ppm): 134.8, 133.1, 131.2, 129.5, 125.5, 123.2, 92.1, 61.5.

FT-IR (ATR): 2861 (w), 1582 (w), 1456 (m), 1404 (w), 1266 (m), 1220 (m), 1188 (m) 1090 (s), 1039 (m), 981 (s), 964 (m), 901 (s), 817 (s), 705 (m), 613 (w).

MS (ESI⁺): (m/z) 454.9 (calculated for C₁₈H₁₄Br₂O₄: 454.1).

Elemental analysis (%): Calculated for C₁₈H₁₄Br₂O₄: C, 47.61; H, 3.11; Br, 35.19. Found: C, 47.88; H, 3.31; Br, 35.42.

1-Tert-Butoxycarbonyl-1-phenylhydrazine (24) [62]



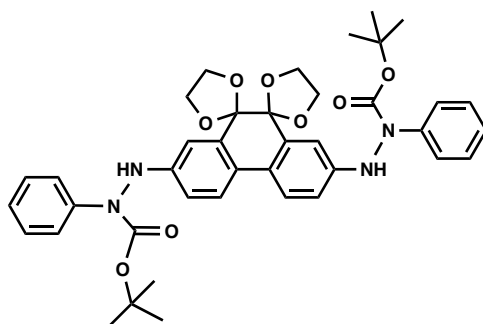
An oven-dried round-bottom flask was charged with CuI (5.7 mg, 0.03 mmol), 1,10-phenanthroline (54.1 mg, 0.3 mmol), Cs₂CO₃ (1.37g, 4.2 mmol), tert-butylcarbazate (0.476, 3.6 mmol), degassed and refilled with argon. Iodobenzene (0.33mL, 3 mmol) and DMF (3 mL) were added under argon. The reaction mixture was stirred at 80°C for 24 h. The resulting

suspension was cooled to room temperature and filtered through silica gel eluting with ethyl acetate. The filtrate was concentrated and purified by column chromatography (Ethyl acetate: Hexane, 1:5). The product is pale yellow oil. The yield was 0.49 g (70%).

^1H NMR (DMSO- d_6) δ (ppm): 7.43 (2H, d, $J = 7.9$ Hz), 7.27 (2H, t, 7.8 Hz), 7.04 (2H, t, $J = 7.6$ Hz), 5.04 (2H, br s), 1.43 (9H, s).

^{13}C NMR (CDCl_3) δ (ppm): 153.2, 143.1, 128.2, 124.7, 123.5, 81.8, 28.3.

Tert-butyl 2-{7'-[1-(tert-butoxycarbonyl)-2-phenylhydrazino]dispiro[1,3-dioxolane-2,9'-phenanthrene-10',2''-[1,3]dioxolan]-2'-yl}-1-phenylhydrazinecarboxylate (25)



A 50 mL round-bottom flask was charged with 0.3 g (0.66 mmol) of product **23**, 0.627 g (2.6 mmol) of 1-tert-butoxycarbonyl-1-phenylhydrazine, 0.645 g (2 mmol) of Cs_2CO_3 , 0.0444g (0.065mmol) of $\text{Pd}(\text{OAc})_2$ (trimer), 0.0574 g (0.19 mmol) of $\text{P}(\text{tBu})_3 \cdot \text{HBF}_4$. The flask was evacuated and refilled with argon several times. Afterwards, 10 mL of toluene and 4 mL of DMF were added. Mixture was heated at 110°C for 2 hours. After completion of reaction (TLC, Petroleum ether: Ethylacetate, 1:1), water was added into the reaction mixture and extracted into toluene. The solvent was evaporated, and the residue was precipitated into cold hexane. The precipitate was filtered off and washed with hexane. The target compound was light a brown powder with a yield of 0.25 g (53%). $\text{Mp} = 155\text{-}156^\circ\text{C}$.

^1H NMR (CDCl_3) δ (ppm): 7.69 (2H, d, $J = 8.6$ Hz), 7.61 (4H, d, $J = 7.8$ Hz), 7.34 (4H, t, $J = 8.0$ Hz), 7.19 (2H, s), 7.14 (2H, t, $J = 7.4$ Hz), 6.88 (2H, dd, $J = 8.5$ Hz, 2.5 Hz), 6.51 (2H, s), 4.16 (4H, br s), 3.66 (4H, br s), 1.43 (18H, s).

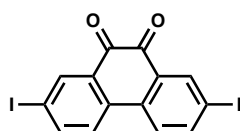
^{13}C NMR (CDCl_3) δ (ppm): 153.9, 147.9, 142.7, 133.1, 128.5, 126.3, 124.6, 124.4, 121.8, 114.2, 110.5, 92.8, 82.5, 61.4, 28.1.

FT-IR (ATR): 3331 (w), 2977 (w), 2934 (w), 2980 (w), 1706 (m), 1620 (m), 1600 (m), 1479 (m), 1306 (m), 1254 (m), 1154 (s), 1090 (s), 1044 (m), 1013 (m), 993 (m), 975 (m), 898 (w), 863 (w), 817 (w), 751 (s), 691 (s).

MS (MALDI): (m/z) 708.2 (calculated for C₄₀H₄₄N₄O₈: 708.8).

Exact mass (+ESI): (m/z) 731.3071 (MNa⁺) (calculated for C₄₀H₄₄N₄O₈: 731.3051).

2,7-Diiodophenanthren-9,10-dione (26) [63]



N-iodosuccinimide (6.48 g, 28.82 mmol) was added to a cold (0°C) 98% H₂SO₄ (90 mL), and the mixture was stirred for 25 min at 0°C. Afterwards, phenanthrene-9,10-dione (1.50 g, 7.20 mmol) was added, and the mixture was stirred for 24 hours at room temperature. The resulting solution was poured onto ice; the precipitate was filtered off, washed with water, and dried. Product was obtained as a dark-red powder with a yield of 2.4 g (73%). Mp > 250°C.

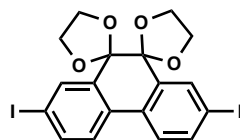
¹H NMR (DMSO-d₆) δ (ppm): 8.16 (6H, m).

FT-IR (ATR): 2920 (w), 1669 (m), 1574 (m), 1459 (m), 1392 (m), 1289 (m), 1263 (m), 1208 (m), 1148 (w), 1076 (m), 998 (w), 904 (w), 820 (s), 694 (s).

MS (+EI): (m/z) 459.8 (calculated for C₁₄H₆I₂O₂: 459.9).

Elemental analysis (%): Calculated for C₁₄H₆I₂O₂: C, 36.55; H, 1.31; I, 55.17. Found: C, 33.77; H, 1.54; I, 54.43.

2,7-Diiodophenanthren-9,10-di(ethyleneglycol)ketal (27) [64]



In a round-bottom flask equipped with Dean-Stark apparatus, 2,7-diiodophenanthren-9,10-dione (1 g, 2.2 mmol) and *p*-toluenesulfonic acid monohydrate (0.418 g, 2.2 mmol) were dissolved in 60 mL of toluene. 6.05 mL (110 mmol) of ethylene glycol were added to the solution. The system was evacuated and refilled with argon. The solution was refluxed for 20 hours. Upon cooling to room temperature, the resulting solution was diluted with toluene and washed with

water in an extraction funnel. The organic layer was dried with MgSO_4 . The solvent was evaporated. The obtained solid was recrystallized from ethanol giving pale yellow crystals with a yield of 0.8 g (66%). $\text{Mp} = 236\text{--}240^\circ\text{C}$ (lit. $\text{Mp} = 216\text{--}240^\circ\text{C}$). ^1H and ^{13}C NMR match the reported spectra. [64]

^1H NMR (CDCl_3) δ (ppm): 8.10 (2H, s), 7.82 (2H, d, $J = 8.3$ Hz), 7.60 (2H, d, $J = 8.3$ Hz), 4.23 (4H, br s), 3.68 (4H, br s).

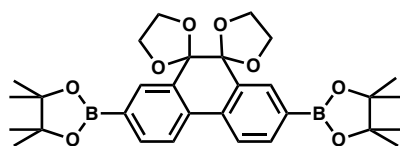
^{13}C NMR (CDCl_3) δ (ppm): 139.0, 135.3, 134.8, 131.9, 125.4, 94.7, 91.9, 61.5.

FT-IR (ATR): 2954 (w), 2854 (w), 1582 (w), 1450 (w), 1378 (w), 1269 (m), 1220 (m), 1185 (m), 1093 (s), 1039 (s), 981 (s), 961 (m), 901 (s), 814 (s), 694 (m), 610 (w).

MS (+ESI): (m/z) 548.9 (MH^+), 570.9 (MNa^+) (calculated for $\text{C}_{18}\text{H}_{14}\text{I}_2\text{O}_4$: 547.9).

Elemental analysis (%): Calculated for $\text{C}_{18}\text{H}_{14}\text{I}_2\text{O}_4$: C, 39.44, H, 2.57; I, 46.31. Found: C, 39.31; H, 2.75; I, 45.07.

2',7'-Bis(4,4,5,5-tetramethyl-1,3,2-dioxaborolan-2-yl)-phenanthren-9,10-di(ethylene-glycol)ketal (28)



A mixture of 2,7-dibromophenanthren-9,10-di(ethyleneglycol)ketal (1 g, 2.2 mmol), bis(pinacolato)diboron (1.68 g, 6.62 mmol), potassium acetate (1.294 g, 13.18 mmol) and [1,1'-bis(diphenylphosphino)ferracene]palladium(II) (3 mol%, 0.0544 g, 0.074 mmol) were degassed and refilled with argon several times. Afterwards, 16 mL of toluene was added. The mixture was stirred at 90°C under argon for 24 hours. After completion of the reaction (TLC, eluent: petroleum ether: ethyl acetate, 5:1), the reaction mixture was washed with water. The organic layer was dried over MgSO_4 and then the solvent was evaporated. The crude product was recrystallized from ethanol giving a brown powder. The yield was 0.48g (40%). $\text{Mp} = 292\text{--}293^\circ\text{C}$. ^1H and ^{13}C NMR match the reported spectra. [61]

^1H NMR (CDCl_3) δ (ppm): 8.22 (2H, s), 7.97 (2H, d, $J = 7.9$ Hz), 7.91 (2H, d, $J = 6.9$ Hz), 4.26 (4H, br s), 3.71 (4H, br s), 1.37 (24H, s).

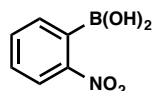
^{13}C NMR (CDCl_3) δ (ppm): 136.2, 135.5, 132.7, 132.4, 123.4, 92.7, 83.9, 61.4, 24.9.

FT-IR (ATR): 2974 (w), 2928 (w), 2877 (w), 1611 (m), 1490 (w), 1450 (w), 1415 (w), 1355 (s), 1332 (s), 1277 (m), 1234 (m), 1142 (s), 1090 (s), 1044 (m), 990 (m), 955 (s), 852 (s), 734 (m), 682 (s).

MS (ES⁺): (m/z) 549.4 (MH⁺), 571.3 (MNa⁺) (calculated for C₃₀H₃₈B₂O₈: 548.3).

Elemental analysis (%): Calculated for C₃₀H₃₈B₂O₈: C, 65.72, H, 6.99. Found: 64.10; H, 6.88.

(2-Nitrophenyl)boronic acid (29) [65]



A dry argon-flushed 100 mL round-bottomed flask equipped with a magnetic stirrer, and a septum was charged with 1-iodo-2-nitrobenzene (2 g, 8 mmol). Dry THF (12 mL) was added, and the resulting solution was cooled to -60°C using a dry ice/acetone bath. To this chilled solution PhMgCl (2 M in THF, 4.4 mL, 8.8 mmol) was added dropwise. The mixture was stirred at the same temperature for 15 min. Trimethyl borate (1.07 mL, 9.6 mmol) was added dropwise into the reaction solution. The reaction mixture was stirred for 1 hour at -60°C and then quenched with 2 M HCl (aq) (10 mL) at -20°C. The reaction was extracted with Et₂O, and the organic layers were combined, dried over MgSO₄, filtered, and concentrated in vacuo. The crude residue was precipitated into chloroform. The yield was 0.77 g (57.5%). Mp = 150-154°C.

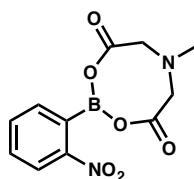
¹H and ¹³C NMR match the reported spectra. [66]

¹H NMR (DMSO-d₆) δ (ppm): 8.20 (2H, s), 8.14 (1H, d, J = 8.2 Hz), 7.76 (1H, t, J = 7.3 Hz), 7.58 (2H, m).

¹³C NMR (DMSO-d₆) δ (ppm): 150.4, 135.9, 134.6, 132.8, 129.6, 123.0.

FT-IR (ATR): 3213 (m), 1603 (w), 1560 (w), 1522 (s), 1479 (m), 1338 (s), 1280 (s), 1252 (s), 1145 (m), 1113 (m), 1067 (m), 993 (m), 972.5 (m), 855 (s), 971 (s), 745 (s), 696 (s), 627 (s).

6-Methyl-2-(2-nitrophenyl)-1,3,6,2-dioxazaborocane-4,8-dione (30)



In a 100 mL round-bottom flask equipped with Dean-Stark apparatus (2-nitrophenyl)boronic acid (0.5 g, 2.9 mmol) and methyliminodiacetic acid (0.529 g, 3.59 mmol) were dissolved in 30 mL of toluene and 6 mL of DMSO. The system was degassed and refilled with argon. The solution was refluxed for 14 hours. Upon cooling to room temperature, the residues of toluene were evaporated, and the resulting solution was precipitated into ethanol giving white crystals. The yield was 0.56 g (69%). Mp = 257-259°C.

^1H NMR (DMSO- d_6) δ (ppm): 7.77 (1H, d, $J = 7.8$ Hz), 7.70 (2H, m), 7.63 (1H, m), 4.46 (2H, d, $J = 17.4$ Hz), 4.26 (2H, d, $J = 17.4$ Hz), 2.84 (3H, s).

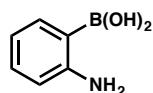
^{13}C NMR (DMSO- d_6) δ (ppm): 169.5, 155.4, 136.3, 132.2, 131.1, 123.7, 64.4, 49.9.

FT-IR (ATR): 3026 (w), 2980 (w), 1755 (s), 1608 (w), 1519 (s), 1453 (m), 1372 (m), 1341 (m), 1295 (s), 1252 (m), 1197 (s), 1093 (w), 1067 (w), 1047 (s), 1033 (s), 1004 (s), 964 (s), 892 (m), 875 (s), 849 (s), 788 (s), 751 (s), 728 (m), 702 (m), 688 (m), 636 (m), 607 (w).

MS (ESI $^+$): (m/z) 279.1(MH $^+$) (calculated for C $_{11}$ H $_{11}$ BN $_2$ O $_6$: 278.1).

Elemental analysis (%): Calculated for C $_{11}$ H $_{11}$ BN $_2$ O $_6$: C, 47.52; H, 3.99; N, 10.08. Found: C, 46.89; H, 4.05; N, 9.84.

2-Aminophenylboronic acid (31) [67]



A mixture of (2-nitrophenyl)boronic acid (1 g, 5.99 mmol) and 10% Pd/C (100 mg) in absolute ethanol (55 mL) was shaken under pressure (3.1 bar) overnight. The catalyst was filtered off, and the filtrate was evaporated in vacuum to give an orange oil. Recrystallization of this residue from MeOH-Hexane mixture afforded 0.49 mg of pure product as white crystals. The yield was 0.49 g (60%). The product is very unstable at room temperature and was stored in a freezer. ^1H and ^{13}C NMR match the reported spectra. [66]

^1H NMR (DMSO- d_6) δ (ppm): 8.98 (1H, s), 8.49 (1H, s), 7.72 (2H, dd, $J=17.1, 8.1$ Hz), 7.42 (1H, t, $J=8.4$ Hz), 7.23 (1H, d, $J=8.0$ Hz), 7.12 (1H, t, $J=7.6$ Hz), 6.94 (1H, t, $J=7.3$ Hz), 6.62 (1H, d, $J=8.1$ Hz), 6.54 (1H, t, $J=7.6$ Hz), 5.88 (2H, s).

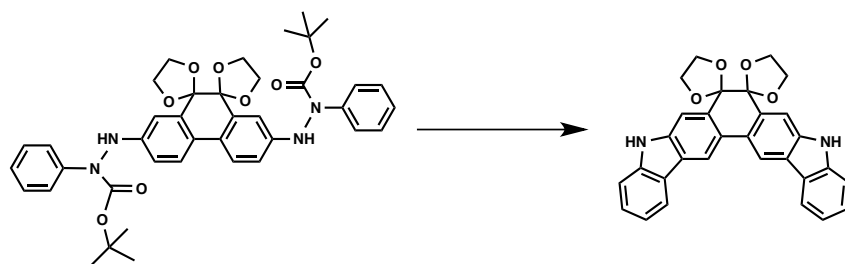
^{13}C NMR (DMSO- d_6) δ (ppm): 155.3, 151.2, 135.7, 133.9, 132.9, 132.0, 129.3, 120.4, 117.0, 115.5, 115.3, 114.3.

FT-IR (ATR): 3437(w), 3390 (w), 3315 (w), 3020 (w), 1606 (s), 1595 (m), 1462 (s), 1415 (s), 1383 (m), 1332 (m), 1250 (m), 1239 (m), 1149 (m), 1116 (m), 1088 (w), 1059 (m), 1034 (w), 994 (m), 936 (w), 864 (m), 796 (w), 757 (s), 649(s).

MS (ES⁺): (m/z) 138.0 (calculated for C₆H₈BNO₂: 137.1).

For easiness of the further synthesis this product was also purchased from Alfa Aesar.

General procedure for cyclization of (25):

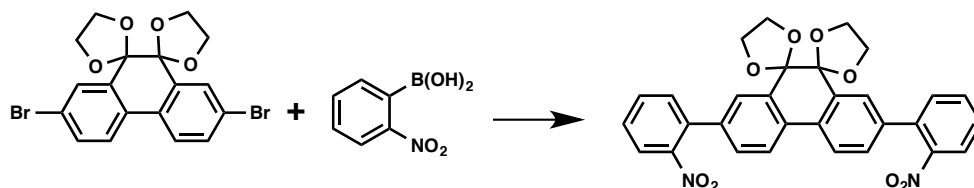


All the reactions were carried out under argon. To the solution of compound **25** in ethanol (or 1,4-dioxane), 3 drops of concentrated HCl was added. The mixtures were refluxed for different periods of time ranging from 4 to 24 hours. Afterwards, mixtures were neutralized and filtered. The products of reaction were separated by flash chromatography using different solvents (*e.g.* petroleum ether, ethyl acetate, chloroform). The obtained materials were analysed by NMR spectroscopy and mass spectrometry.

Example:

To the solution of 0.05 g (0.07 mmol) compound (**4**) in ethanol (3 mL), 3 drops of concentrated HCl was added. The mixture was refluxed for 4 hours. Afterwards, mixture was filtered off and precipitated was analysed by NMR. The rest of the reaction mixture was neutralized with saturated solution of NaHCO₃ and extracted in diethyl ether. Resulting solution was purified by flash chromatography using petroleum ether : ethyl acetate mixture as an eluent.

General procedure for Suzuki coupling:



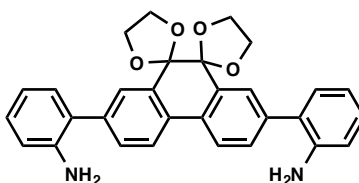
All Suzuki coupling reactions were carried out in argon atmosphere. All the solids were usually placed in the reaction flask and the flask was degassed and refilled with argon several times.

Afterwards, the liquids were added. Water was bubbled with argon for at least an hour prior to usage. All the organic solvents for reactions were taken from Grubbs system located in the Department of Chemistry. Reactions were generally carried at reflux temperatures of the solvents. All the reactions were monitored by TLC for 48 hours.

Example:

A 50 mL two-neck round-bottom flask was charged with 0.1 g (0.22 mmol) of 2,7-dibromophenanthren-9,10-di(ethyleneglycol)ketal, 0.15 g (0.88 mmol) of 2-nitrophenylboronic acid, 0.09 g (0.88 mmol) of Na₂CO₃, 5 mol % (0.007 g, 0.011 mmol) of Pd(OAc)₂ and 10% (0.009 g, 0.022 mmol) 2-Dicyclohexylphosphino-2',6'-dimethoxybiphenyl (SPhos). The flask was degassed and refilled with argon several times; afterwards, degassed water and toluene (1:3) were added. The mixture was degassed and refilled with argon twice. The reaction mixture was kept at 100°C for 48 hours. After completion of the reaction (TLC, eluent: ethyl acetate: petroleum ether, 1:3), the mixture was extracted with toluene. The collected organic layer was dried with MgSO₄ and then the solvent was evaporated. Reaction mixture was purified by column chromatography using petroleum ether : ethyl acetate (2:1) as an eluent.

2,7-Bis(2-aminophenyl)phenanthren-9,10-di(ethylene-glycol)ketal (33)



A 50 mL two-neck round-bottom flask equipped with a condenser and a magnetic stirring bar was charged with 0.5 g (1.1 mmol) of 2,7-dibromophenanthren-9,10-di(ethyleneglycol)ketal, 0.45 g (3.3 mmol) of 2-aminophenylboronic acid, 1.2 g (8.8 mmol) of K₂CO₃ and 10 mol % (0.154 g, 0.22 mmol) of PdCl₂(PPh₃)₂. The flask was degassed and refilled with argon several times; afterwards, degassed deionized water and DMF (1:5) were added. The mixture was degassed and refilled with argon twice. The reaction mixture was kept at 80°C for 48 hours. After completion of the reaction (TLC, eluent: ethyl acetate: petroleum ether, 1:3), the mixture was extracted with ethyl acetate. The collected organic layer was dried over MgSO₄ and then the solvent was evaporated. The crude product was precipitated into hexane and filtered off giving 0.5 g of clean compound (**12**). The yield was 95%. Mp = 176-180°C.

^1H NMR (CDCl_3) δ (ppm): 8.03 (2H, d, $J=8.1$ Hz), 7.91 (2H, s), 7.66 (2H, d, $J=6.2$ Hz), 7.22 (4H, dd, $J=16.8, 7.6$ Hz), 6.88 (2H, t, $J=7.9$ Hz), 6.82 (2H, d, $J=8.0$ Hz), 4.24 (4H, br s), 3.84 (4H, br s), 3.74 (4H, br s).

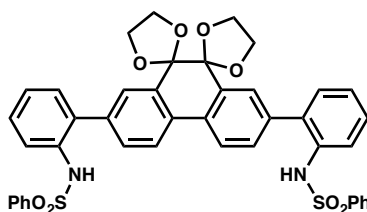
^{13}C NMR (CDCl_3) δ (ppm): 143.6, 140.0, 133.4, 132.2, 131.6, 130.5, 128.8, 126.9, 126.8, 124.4, 118.8, 115.8, 92.8, 61.5.

FT-IR (ATR): 3348 (w), 2945 (w), 2872 (w), 1667 (w), 1615 (m), 1476 (m), 1450 (m), 1407 (m), 1282 (w), 1259 (w), 1217 (w), 1186 (m), 1159 (w), 1090 (s), 1043 (w), 1025 (m), 1001 (w), 960 (m), 984 (m), 921 (w), 888 (w), 828 (w), 746 (s), 695 (w), 663 (w).

MS (ES $^+$): (m/z) 479.2 (calculated for $\text{C}_{30}\text{H}_{26}\text{N}_2\text{O}_4$: 478.2).

Exact mass (+ESI): (m/z) 479.1987 (MH^+) (calculated for $\text{C}_{30}\text{H}_{26}\text{N}_2\text{O}_4$: 479.1965).

2,7-Bis-(2-(benzenesulfonamide)phenyl)-phenanthren-9,10-di(ethylene-glycol)ketal (34)



A 100 mL two-necked flask was charged with 0.55 g (1.2 mmol) of 2,7-bis(2-aminophenyl)-phenanthren-9,10-di(ethylene-glycol)ketal (**12**). The flask was degassed and refilled with argon. The compound was dissolved in dry dichloromethane (33 mL). Then benzenesulfonyl chloride (0.39 mL, 2.9 mmol) and pyridine (0.61 mL, 7.5 mmol) were added. The mixture was stirred for 18 hours at the room temperature. Completion of the reaction was indicated by TLC using petroleum ether: ethyl acetate (2:1) as an eluent. Reaction mixture was diluted with chloroform, washed with 30 mL of 1 M HCl aqueous solution and 200 mL of deionized water. The organic layer was dried over MgSO_4 and then solvent was evaporated. The residue was dissolved in 5 mL of chloroform and precipitated in cold hexane and filtered off giving 0.69 g of compound (**13**). The yield was 79%. $\text{Mp} = 140\text{-}142^\circ\text{C}$.

^1H NMR (CDCl_3) δ (ppm): 7.91 (2H, d, $J=8.1$ Hz), 7.74 (6H, d, $J=7.4$ Hz), 7.59 (4H, m), 7.47 (4H, t, $J=7.8$ Hz), 7.38 (2H, m), 7.22 (4H, m), 7.07 (2H, dd, $J=8.0, 1.8$ Hz), 6.77 (2H, s), 4.27 (4H, br s), 3.72 (4H, br s).

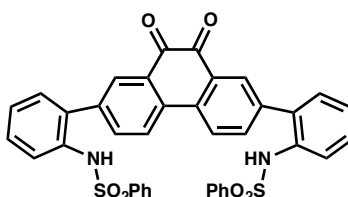
^{13}C NMR (CDCl_3) δ (ppm): 139.2, 138, 134, 133.7, 133, 132.2, 130.6, 130.5, 129.1, 129, 127.3, 127.1, 125.1, 124.8, 121.3, 92.4, 61.4.

FT-IR (ATR): 2876 (w), 1702 (w), 1578 (w), 1475 (m), 1447 (m), 1397 (w), 1331 (m), 1262 (w), 1223 (w), 1158 (s), 1090 (s), 1048 (w), 1030 (w), 1001 (w), 985 (m), 961 (m), 913 (m), 830 (w), 753 (s), 719 (m), 687 (s), 667 (w), 628 (w).

MS (ES⁺): (m/z) 759.2 (MH⁺) (calculated for C₄₂H₃₄N₂O₈S₂: 758.2).

Exact mass (ESI⁺): (m/z) 759.1833 (MH⁺) (calculated for C₄₂H₃₄N₂O₈S₂: 758.1829).

2,7-Bis-(2-(benzenesulfonamide)phenyl)-phenanthren-9,10-diketone (**35**)



A mixture of compound (**13**) (0.68 g, 0.89 mmol) and p-toluenesulfonic acid (8.52 g, 44.8 mmol) was refluxed overnight in a mixture of solvents: DCM (18 mL), water (12 mL), acetonitrile (36 mL). The resulting mixture was cooled to room temperature and extracted into DCM. The organic layer was dried over MgSO₄ and solvent was removed. The residue was dissolved in 5 mL of chloroform and precipitated into cold hexane giving compound **14** as a red powder (0.55 g). The yield was 92%. Mp = 131-135°C.

¹H NMR (DMSO-d₆) δ (ppm): 9.86 (2H, s), 8.34 (2H, d, J=8.4 Hz), 7.92 (2H, d, J=1.9 Hz), 7.75 (2H, dd, J=8.2, 1.9 Hz), 7.56 (6H, m), 7.39 (10H, m), 7.02 (2H, d, J=7.6 Hz).

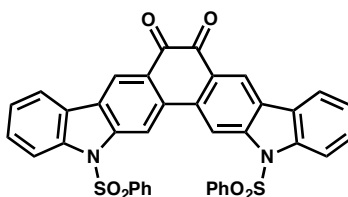
¹³C NMR (DMSO-d₆) δ (ppm): 179.6, 140.9, 140.3, 138.2, 136.8, 134.4, 133.7, 132.9, 131.2, 131.1, 130.4, 129.5, 129.3, 128.3, 128.0, 126.9, 125.0.

FT-IR (ATR): 2941 (w), 1671 (m), 1598 (m), 1472 (m), 1447 (m), 1401 (m), 1310 (m), 1155 (s), 1090 (s), 1010 (w), 907 (w), 857 (m), 837 (m), 753 (s), 713 (w), 690 (s), 661 (w), 628 (m).

MS (ES⁺): (m/z) 671.1 (MH⁺) (calculated for C₃₈H₂₆N₂O₆S₂: 670.1).

Exact mass (ESI⁺): (m/z) 671.1309 (MH⁺) (calculated for C₃₈H₂₆N₂O₆S₂: 670.1305).

13,17-Di-(2-(benzenesulfonamide)phenyl)benzo-5,6-diketone-[1,2-a;4,3-a']dicarbazole (36)



A 50 mL two-necked round bottom flask was charged with compound **14** (0.54 g, 0.8 mmol), Cu(OTf)₂ (0.029 g, 0.08 mmol). The flask was carefully degassed and refilled with argon. The solids were dissolved in 4 mL of dry dichloroethylene. (Diacetoxyiodo)benzene (1.03 g, 3.2 mmol) was dissolved in 8 mL of dry dichloroethylene in argon atmosphere. The obtained solution was added dropwise to the previously obtained mixture. The obtained reaction mixture was heated to 50°C and stirred at the same temperature for 24 hours. The completion of reaction was indicated by TLC (eluent: ethyl acetate: petroleum ether, 1:1). The reaction mixture was extracted into DCM and the organic layer was dried over MgSO₄. The solvent was evaporated, the residue was dissolved in 5 mL of chloroform and precipitated into cold hexane (200 mL) giving brown-red powder. The yield was 78%. Mp = 126-130°C.

¹H NMR (CDCl₃) δ (ppm): 8.38 (2H, d, J=10.3 Hz), 8.22 (2H, s, J=1.9 Hz), 7.98 (2H, t, J=8.5 Hz), 7.72 (2H, dd, J=8.2, 1.9 Hz), 7.63 (2H, m), 7.54 (4H, t, J=7.6Hz), 6.86 (4H, m).

¹³C NMR (CDCl₃) δ (ppm): 185.5, 179.1, 163.0, 147.6, 139.5, 136.5, 135.8, 135.6, 135.1, 133.8, 133.76, 132.1, 130.9, 130.6, 129.2, 127.4, 124.3.

FT-IR (ATR): 3070 (w), 1679 (m), 1648 (m), 1622 (m), 1599 (m), 1544 (m), 1476 (w), 1447 (w), 1411 (w), 1309 (s), 1288 (s), 1227 (w), 1180 (w), 1155 (s), 1114 (m), 1088 (s), 1026 (m), 901 (m), 869 (s), 834 (s), 756 (m), 731 (s), 686 (s), 657 (w), 630 (s).

MS could not be obtained.

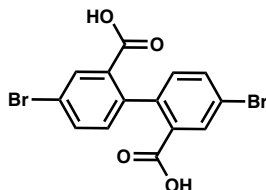
Elemental analysis (%): Calculated for C₃₈H₂₂N₂O₆S₂: C, 68.46; H, 3.33; N, 4.2; S, 9.62. Found: C, 62.12; H, 3.69; N, 3.58; S, 8.29.

General procedure of condensation of diketones with *o*-phenelenediamine:

Product **35** or **36** and *o*-phenelenediamine (1.1 eq) were dissolved in ethanol (or other solvent, ~50 mM). Then the catalyst was added (*p*-toluene sulfonic acid, hydrochloric acid, acetic acid).

The mixture was refluxed for 12 hours. To terminate the reaction, the reaction mixture was allowed to cool down, followed by filtration and extraction (ethyl acetate : water).

4,4'-Dibromobiphenyl-2,2'-dicarboxylic acid (38) [68]



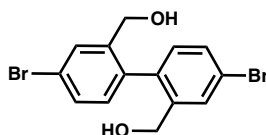
Diphenic acid (2 g, 8.25 mmol) was dissolved in 64 mL of concentrated H₂SO₄ and cooled down to 0°C in an ice bath. Dibromoisocyanuric acid (1.02 eq, 2.41 g, 8.4 mmol) was added to the reaction mixture in 4 portions. The reaction mixture was allowed to warm up to room temperature and was left stirring overnight. Afterwards the reaction mixture was poured onto 400 mL of ice. The precipitate was filtered off and washed with water, followed by a small amount of cold methanol. The product was used in further synthesis without additional purification. Crude yield was 3.29 g (99.6%). Mp = 235°C (lit. Mp = 246 – 250°C).

¹H NMR (CDCl₃) δ (ppm): 12.91 (2H, s), 8.01 (2H, d, J=2.2 Hz), 7.77 (2H, dd, J=8.2, 2.2 Hz), 7.15 (2H, d, J=8.2 Hz).

FT-IR (ATR): 3085 (m), 2981 (m), 2812 (m), 2656 (m), 2533 (m), 1686 (s), 1586 (w), 1557 (w), 1497 (w), 1473 (w), 1412 (m), 1382 (w), 1297 (s), 1279 (s), 1245 (s), 1155 (w), 1094 (m), 1002 (w), 929 (w), 899 (w), 823 (s), 780 (w), 759 (w).

MS (ES⁻): (m/z) 399 (M-H⁺) (calculated for C₁₄H₈Br₂O₄: 400.02)

4,4'-Dibromobiphenyl-2,2'-dimethanol (39) [69]



4,4'-Dibromobiphenyl-2,2'-dicarboxylic acid (0.5 g, 1.25 mmol) was dissolved in dry THF (6 mL) in argon atmosphere. NaBH₄ (3 eq, 0.14 g, 3.75 mmol) were added in portions. The mixture was stirred at room temperature for an hour. Then BF₃•Et₂O (4.6 eq, 0.71 mL, 5.75 mmol) was added dropwise into the reaction mixture. The mixture was stirred overnight at room temperature. Termination of reaction was determined by TLC using ethyl acetate: hexane (1:1) as an eluent. The reaction was quenched with 5% aqueous HCl solution and then diluted with

ethyl acetate. The mixture was then filtered through Celite® Hyflo Supercel plug. The filtrate was washed with saturated Na₂CO₃, followed by saturated NaCl solution. The combined organic layers were dried over MgSO₄ and then solvent was evaporated. The crude product was purified by column chromatography using ethyl acetate: petroleum ether (1:2.5) as an eluent. After the column material was recrystallized from ethanol: hexane mixture giving white crystals with 37% yield. Mp =139-140°C (lit. Mp = 133-134°C). [66] ¹H and ¹³C NMR match the reported spectra. [68]

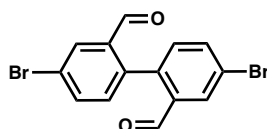
¹H NMR (DMSO-d₆) δ (ppm): 7.71 (2H, d, J=2.0 Hz), 7.49 (2H, dd, J=8.1, 2.1 Hz), 7.04 (2H, d, J=8.1 Hz), 5.27 (2H, t, J=5.4 Hz), 4.12 (4H, ddd, J=40.2, 14.2, 5.4 Hz).

¹³C NMR (DMSO-d₆) δ (ppm): 143.0, 136.4, 131.5, 130.0, 129.7, 121.6, 60.6.

FT-IR (ATR): 3307 (w), 3203 (w), 2949 (w), 2919 (w), 2859 (w), 1689 (w), 1588 (w), 1560 (w), 1467 (w), 1423 (w), 1392 (w), 1335(w), 1246 (w), 1186 (w), 1112 (w), 1088 (m), 1038 (s), 1002 (m), 886 (w), 839 (m), 810 (s).

MS (EI⁺): (m/z) 371.9 (calculated for C₁₄H₁₂Br₂O₂: 372.06).

4,4'-dibromo-2,2'-diformyl-1,1'-biphenyl (40) [68]



A three-necked flask containing 2 M oxalyl chloride solution in dichloromethane (2.7 eq, 5.3 mmol, 2.6 mL) was diluted with 10 mL of dry dichloromethane and cooled down to -78°C. DMSO (3.8 eq, 7.5 mmol, 0.53 mL) was added to the mixture dropwise. 4,4'-Dibromobiphenyl-2,2'-dimethanol (0.73 g, 2 mmol) was dissolved in 13 mL of dry dichloromethane and added to the reaction mixture dropwise. The mixture was stirred at the same temperature for 2 hours. Afterwards, triethylamine (6.16 eq, 12.1 mmol, 1.69 mL) was added to the reaction mixture. The mixture was allowed to warm up to the room temperature. Termination of reaction was determined by TLC using ethyl acetate: petroleum ether (1:5) as an eluent. The reaction mixture was then transferred into separating funnel and washed with 5% HCl and Na₂CO₃ until neutral pH and then the mixture was washed with brine. The organic layer was dried over MgSO₄ and the solvent was then removed under reduced pressure. 4,4'-dibromo-2,2'-diformyl-1,1'-biphenyl was obtained as a white solid with 97% (0.7 g) yield. The product was used in further synthesis

without additional purification. Mp = 126-136°C (lit. Mp = 144-146°C). [61] ¹H and ¹³C NMR match the reported spectra. [68]

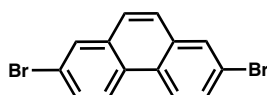
¹H NMR (DMSO-d₆) δ (ppm): 9.70 (2H, s), 8.12 (2H, d, J=2.1 Hz), 7.95 (2H, dd, J=8.2, 2.2 Hz), 7.39 (2H, d, J=8.2 Hz).

¹³C NMR (DMSO-d₆) δ (ppm): 191.1, 138.9, 136.5, 136.0, 134.3, 132.4, 122.7.

FT-IR (ATR): 3088 (w), 3061(w), 2917 (w), 2850 (w), 2758 (w), 1749 (w), 1691 (s), 1680 (s), 1582 (s), 1559 (w), 1457 (m), 1388 (m), 1285 (w), 1255 (w), 1236 (w), 1176 (s), 1117 (w), 1085 (m), 1037 (w), 1011 (w), 1001 (m), 983 (w), 964 (w), 917 (w), 904 (w), 876 (m), 844 (w), 830 (s), 764 (m), 736 (w), 677 (s), 640 (m), 561 (m), 491 (w), 473 (w), 450 (m).

MS (EI⁺): (m/z) 367.9 (calculated for C₁₄H₈Br₂O₂: 368.02).

2,7-Dibromophenanthrene (41) [68]



4,4'-dibromo-2,2'-diformyl-1,1'-biphenyl (1.49 g, 4 mmol) was dissolved in 35 mL of glacial acetic acid and heated to reflux. Hydrazine monohydrate (1.4 eq, 0.27 mL, 5.6 mmol) in 5 mL of glacial acetic acid was added to the boiling reaction mixture dropwise. The reaction mixture was stirred for 1.5 hours. Termination of reaction was determined by TLC using ethyl acetate: petroleum ether (1:4) as an eluent. The reaction mixture was allowed to cool down to the room temperature and then was poured over 400 mL of ice. The precipitate was then filtered off, washed with water and dried in vacuum oven. The product was obtained as brown powder with a yield of 74% (1 g). Mp = 180°C. ¹H and ¹³C NMR match the reported spectra. [68]

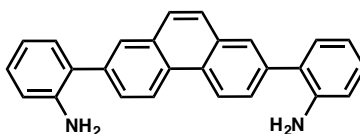
¹H NMR (DMSO-d₆) δ (ppm): 8.79 (2H, d, J=8.9 Hz), 8.3 (2H, s), 7.9 (2H, s), 7.85 (2H, d, J=8.7 Hz).

¹³C NMR (DMSO-d₆) δ (ppm): 133.6, 131.0, 130.5, 128.7, 127.6, 125.9, 121.0.

FT-IR (ATR): 3063 (w), 3032 (w), 2958 (w), 2919 (w), 2853 (w), 1742 (w), 1708 (w), 1664 (w), 1600 (w), 1561 (w), 1478 (w), 1452 (m), 1387 (w), 1334 (w), 1294 (w), 1260 (w), 1238 (w), 1211 (w), 1171 (w), 1148 (w), 1072 (m), 998 (m), 879 (s), 807 (m), 793 (s), 772 (m), 758 (w), 698 (s), 647 (w), 534 (w), 523 (w), 498 (w), 462 (w).

MS (EI⁺): (m/z) 335.9 (calculated for C₁₄H₈Br₂: 336.03)

2,7-Bis(2-aminophenyl)phenanthrene (42)



2,7-Dibromophenanthrene (0.15g, 0.45 mmol), 2-aminophenylboronic acid (3 eq, 1.33 mmol, 0.183 g), PdCl₂(PPh₃)₂ (10 %mol, 0.089 mmol, 0.063g), K₂CO₃ (8 eq, 3.6 mmol, 0.49 g) was placed in two-necked round bottom flask. The flask was evacuated and refilled with argon 5 times. The mixture of degassed DMF and water (5:1, 3 mL: 0.6 mL) was added to the mixture of solids. The resulting reaction mixture was stirred at 80°C for 2 days. After termination of reaction (TLC, ethyl acetate: petroleum ether (1:2)), the reaction mixture was extracted using ethyl acetate and water. The organic layer was dried over MgSO₄ and then solvent was evaporated. The resulting brown liquid was dissolved in 5 mL of THF and precipitated into 75 mL of cold hexane. The precipitate was filtered off and washed with hexane. The product was obtained as beige coloured powder, 0.13 g (80%). Mp =257-260°C.

¹H NMR (DMSO-d₆) δ (ppm): 8.9 (2H, d, J=8.6 Hz), 8.05 (2H, s), 7.91 (2H, s), 7.78 (2H, dd, J=8.48, 1.86 Hz), 7.17 (2H, d, J=7.5 Hz), 7.11 (2H, t, J=7.6 Hz), 6.84 (2H, d, J=7.6 Hz), 6.71 (2H, t, J=7.3 Hz), 4.95 (4H, s).

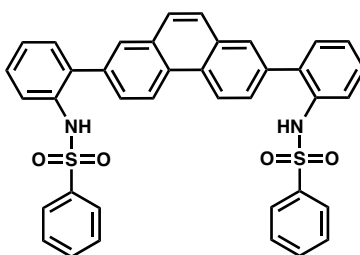
¹³C NMR (DMSO-d₆) δ (ppm): 145.8, 138.5, 132.4, 130.8, 128.9, 128.8, 128.5, 128.2, 127.7, 125.8, 123.8, 117.3, 115.9.

FT-IR (ATR): 3454 (w), 3370 (w), 3066 (w), 3024 (w), 1664 (w), 1612 (m), 1571 (w), 1496 (m), 1478 (w), 1470 (m), 1452 (w), 1437 (w), 1312 (w), 1297 (w), 1261 (w), 1158 (w), 1142 (w), 1119 (w), 1094 (w), 1056 (w), 1022 (w), 997 (w), 897 (w), 826 (m), 743 (s), 693 (m), 574 (w).

MS (EI⁺): (m/z) 360.2 (calculated for C₂₆H₂₀N₂: 360.46).

Exact mass (EI⁺): (m/z) 361.1713 (MH⁺) (calculated for C₂₆H₂₀N₂: 361.1699).

2,7-Bis-(2-(benzenesulfonamide)phenyl)-phenanthrene (43)



Product 42 (0.34 g, 0.94 mmol) was dissolved in 18 mL of dry dichloromethane under argon. To this solution benzenesulfonyl chloride (2.6 eq, 0.32 mL, 2.5 mmol), followed by pyridine (6.5 eq, 0.5 mL, 6.1 mmol) were added. The reaction mixture was stirred at room temperature overnight. After completion of the reaction (TLC, ethyl acetate: petroleum ether (1:2)), the mixture was washed with 30 mL of 1M aqueous HCl solution. The organic layer was then separated and dried over MgSO₄. The solvent was then evaporated. The resulting brown liquid was dissolved in 20 mL of THF and precipitated into cold hexane (150 mL). The precipitated was filtered off and washed with hexane. The product was obtained as light pink powder, 0.51 g (85%). Mp = 244-246°C.

¹H NMR (DMSO-d₆) δ (ppm): 9.73 (2H, s), 8.83 (2H, d, J=8.6 Hz), 7.82 (4H, s), 7.59 (8H, m), 7.4 (10H, m), 7.14 (2H, d, J=8.7 Hz).

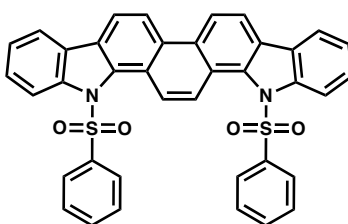
¹³C NMR (DMSO-d₆) δ (ppm): 141.2, 138.7, 137.5, 134.0, 133.0, 132.0, 131.7, 129.5, 129.3, 129.0, 128.7, 127.6, 127.3, 127.0, 126.9, 123.2.

FT-IR (ATR): 3259 (w), 3068 (w), 1701 (w), 1605 (w), 1578 (w), 1498 (w), 1468(w), 1447 (w), 1395 (w), 1332 (m), 1214 (w), 1159 (s), 1092 (m), 1070 (w), 1034 (w), 997 (w), 929 (w), 905 (w), 822 (w), 756 (s), 719 (m), 687 (s), 634 (w), 603 (w), 585 (s), 553 (s).

MS (AP⁺): (m/z) 640.2 (calculated for C₃₈H₂₈N₂O₄S₂: 640.77)

Exact mass (ESI⁺): (m/z) 641.1574 (MH⁺) (calculated for C₃₈H₂₈N₂O₄S₂: 641.1563)

13,16-Di-(2-(benzenesulfonamide)phenyl)benzo[1,2-a;4,3-a']dicarbazole (44)



Product 43 (0.51 g, 0.8 mmol) and Cu(OTf)₂ (10 %mol, 0.08 mmol, 0.029 g) were dissolved in the anhydrous dichloroethylene (4 mL) under argon. (Diacetoxyiodo)benzene (3 eq, 2.4 mmol, 0.77g) was dissolved in 4 mL of anhydrous dichloroethylene and added to the reaction mixture dropwise. The reaction mixture was heated to 50°C and stirred overnight. After completion of the reaction (TLC, ethyl acetate: petroleum ether (1:2)), the reaction mixture was washed with water and extracted into DCM. The organic layer was dried with MgSO₄ and then solvent was eliminated. The resulting brown liquid was dissolved in 20 mL of THF and precipitated into 150

Chapter 3: Materials and Methods

mL of cold hexane. The precipitate was filtered off and washed with hexane. The product was obtained as brown powder, 0.41 g (80 %). Mp =142-145°C.

^1H NMR (CDCl_3) δ (ppm): 9.11 (2H, s), 8.80 (2H, d, $J=8.6$ Hz), 8.39 (2H, d, $J=8.2$ Hz), 7.99 (2H, d, $J=8.5$ Hz), 7.77 (2H, d, $J=7.4$ Hz), 7.52 (2H, m), 7.40 (2H, m Hz), 7.26 (2H, m), 7.01 (8H, m).

FT-IR (ATR): 3063 (w), 1696 (w), 1654 (w), 1610 (w), 1586 (w), 1478 (w), 1447 (m), 1368 (m), 1334 (m), 1292 (w), 1168 (s), 1124 (w), 1090 (m), 1029 (w), 1000 (w), 887 (w), 824 (w), 754 (s) 722 (s), 686 (s), 574 (s).

MS (AP⁺): (m/z) 636.2 (calculated for $\text{C}_{38}\text{H}_{24}\text{N}_2\text{O}_4\text{S}_2$).

Exact mass (ES⁺): (m/z) 659.1098 (Na^+) (calculated for $\text{C}_{38}\text{H}_{24}\text{N}_2\text{O}_4\text{S}_2$: 659.1075).

4 Intersystem crossing in benzo[*b*]thiophene derivatives

*This chapter describes synthesis and photophysics of planar derivatives of benzo[*b*]thiophene, including a state of art hole transporting material – C8-BTBT. These molecules demonstrate a sub-nanosecond intersystem crossing (ISC), which cannot be explained by any available theoretical model when the molecule is considered to be in its equilibrium excited-state geometry. Our results can only be explained by considering the ensemble of molecular geometries in the excited state. These results demonstrate the need to take molecular dynamics into account when considering spin-orbit coupling and ISC. We also discuss the issue of correct approximation of the Frank-Condon weighted density of states for ISC rate calculation.*

*The qualitative steady state and time-resolved spectroscopy of benzothieno[3,2-*b*]benzothiophene derivatives was performed together with Jozra Garrido Velasco at the University of Sheffield. Streak camera data was obtained at the University of St Andrews together with Dr. Sai Rajendran. Resonance Raman spectroscopy was performed at the University of Cyprus together with Eirini Lariou under supervision of Prof. Sophia Hayes. All of the quantum calculations were performed by Dr. Theo Kean at the University of Sheffield. MD calculations were performed by Lupeng Yang at the University of Cambridge and Dr. Daniel Cole at the University of Newcastle. Multimode Frank-Condon analysis script was written together with David Bossanyi at the University of Sheffield.*

4.1 Intersystem crossing in planar organic molecules

Intersystem crossing is a transition between electronic states of different multiplicity. Due to the reasons discussed in Chapter 2, singlet states are emissive short-lived states, whereas the emission of triplets (as well as their formation upon optical excitation) is quantum mechanically forbidden, and, thus, the states are usually long-lived. These fundamental properties of the excitons are crucial for application of organic molecules in electronic devices. The rate of ISC process determines the efficiency of OLEDs based on thermally activated delayed fluorescence. ISC is a limiting factor for creating electrically pumped organic lasers.

Thus, controlling intersystem crossing becomes a very important issue because it has a direct effect on the efficiency of light-driven devices. A huge number of research has been reported on intersystem crossing in organic molecules. Regular rate of ISC in purely organic semiconductors is on nanosecond scale, but there are exceptions (**Table 4.1**).

The reasons for fast (picosecond) and ultrafast (femtosecond) ISC are all based on the preservation of angular momentum in one way or another. For example, ISC in carbonyl containing and nitroaromatic compounds occurs according to El-Sayed's rule, *e.g.* the singlet is located on orbital that has a $\pi-\pi^*$ nature and triplet on $n-\pi^*$ orbital. In this case, the transition is enhanced due to a change in orbital angular momentum because these orbitals are orthogonal to each other. [17] Apart from El-Sayed's rule, preservation of total angular momentum can be achieved by coupling to out-of-plane vibrations. This explains fast ISC in non-planar thiophene derivatives and oligothiophenes. However, out-of-plane vibrations have been suggested to facilitate ISC even in small planar molecules such as benzene [70], base-free porphyrin and, surprisingly, large perylene derivatives. [71]

Despite the fact that coupling to out-of-plane vibrations is not exactly a new phenomenon and it has been readily employed to explain the rate of ISC in various molecules, the exact design rule to achieve a control over out-of-plane vibrations and ISC process have not been reported. In this chapter I will discuss our step forward to vibrationally controlled ISC in planar highly conjugated thiophene derivatives.

Thiophene derivatives attracted a lot of research interest due to their stability, ease of synthesis, high charge carrier mobility and interest for application in transistor and organic solar cells. Oligothiophenes is a class of molecules that is one of the most commonly used for organic electronic purposes. Over the years of research, nearly all imaginable properties of

these molecules have been studied and applied in OLEDs, solar cells, photodynamic therapy, sensors, lasers etc.

Photophysical properties of thiophene itself have been studied experimentally and theoretically and it was concluded that the relaxation dynamics of the initial singlet state (S_1) is dominated by internal conversion to the ground state (S_0). However, bithiophene exhibits drastically different dynamics. The photoexcitation of this molecule is followed by fast (12 ps) intersystem crossing to triplet manifold. [72] The mechanism of this process has been studied computationally by Kölle *et al.* [73] Interestingly, they found that SOC between first singlet state equilibrium geometry is nearly zero suggesting that fast ISC should not be observed. Further investigation showed that the value of SOC can be influenced and significantly enhanced by vibrational relaxation of the excited state with out-of-plane vibrations being crucial for this process. [73] The visual representation of the process is shown in **Figure 4.1** (left). In the case of oligothiophenes, relaxation of Frank-Condon geometry is accompanied by change of the torsional angle between thiophene units. It is these movements that allow angular momentum conservation as the change in spin of the system is accompanied by the change in angular momentum. Different type of out-of-plane vibration was found to contribute to fast ISC in 2-methyl-5-phenylthiophene (**Figure 4.1, right**). It was found that not only the torsion between thiophene and phenyl but also a significant elongation of C-S bond contribute to promotion of ISC rate resulting in 135 ps triplet formation. [74]

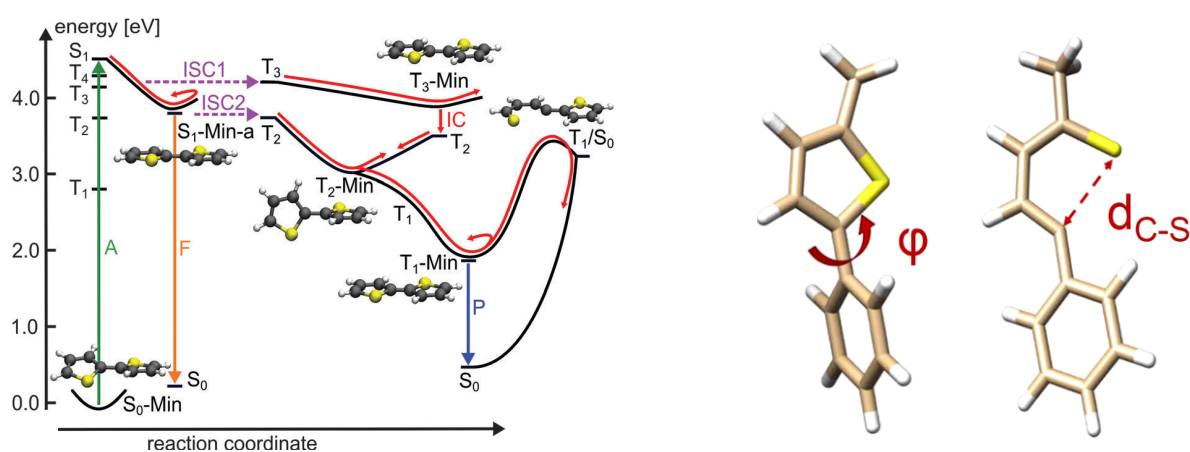


Figure 4.1. Mechanisms of excited state relaxation in thiophene derivatives: bithiophene [73] **and 2-methyl-5-phenylthiophene** (Adapted with permission from [74]. Copyright 2016, American Chemical Society).

The mechanism of out-of-plane vibration influence on ISC relies on mixing between π and σ orbitals. This is why it is easy to explain high PLQYs in planar aromatic compounds and

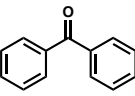
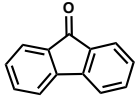
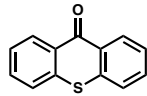
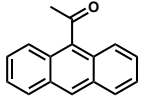
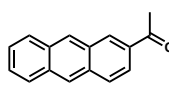
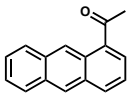
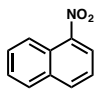
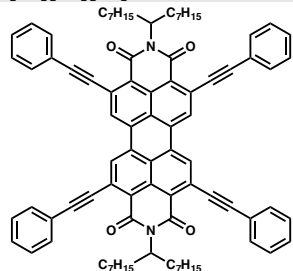
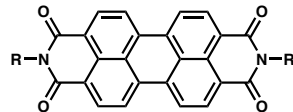
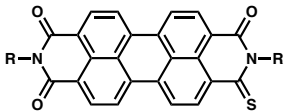
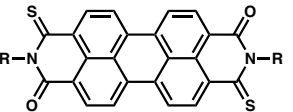
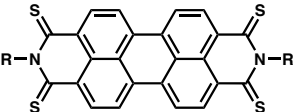
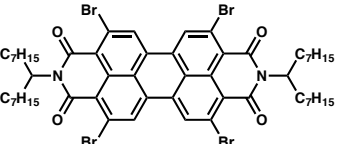
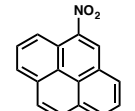
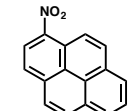
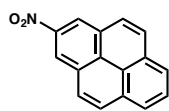
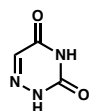
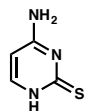
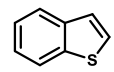
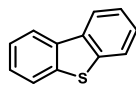
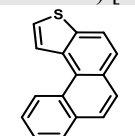
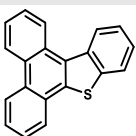
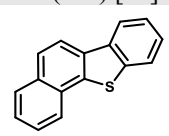
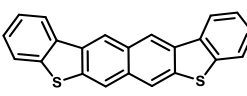
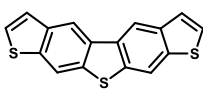
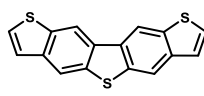
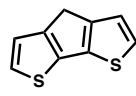
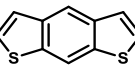
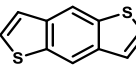
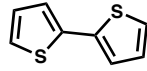
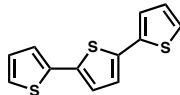
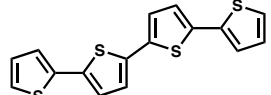
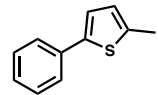
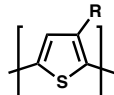
their slow rate of ISC rates. This was convincingly demonstrated in the study of small heavy atom free aromatic molecules by Nijegorodov *et. al.* which revealed that the rate of ISC decreases when the planarity of the molecules increases. [75] The same explanation was applied to explain ISC in oligothiophene family, where ISC rate decreases with the increase in conjugation length, from 12 ps in bithiophene to 1.2 ns in P3OT and P3HT. [76] This phenomenon is rationalised by reduced access to σ orbitals in highly conjugated systems. [77] Interestingly, this paper also suggests the design rule for highly fluorescent derivatives. They suggest that highly delocalized conjugated structures with planar skeletons would reduce spin-orbit coupling and intersystem crossing. [77] This suggestion is in line with the study of conjugated thiophene containing heteroacenes [78][79], which found reasonably high PLQY and slow ISC for all of the studied derivatives (rows 4-5 in **Table 4.1**).

For our study we selected planar sulfur-containing molecules, derivatives of benzothieno[3,2-*b*]benzothiophene. These molecules have been extensively studied in field effect transistors, showing one of the highest reported charge carrier mobilities to date (C8-BTBT $31.3 \text{ cm}^2\text{V}^{-1}\text{s}^{-1}$). [53][38] This, of course, is the consequence of their planarity and tight crystal packing.

Recently, these molecules were suggested as promising materials for spintronic applications. Spintronics requires stable spin of the molecule as well as a high charge carrier mobility. [80] In the paper by Schott *et al.*, it was demonstrated that gyromagnetic coupling tensor shifts (Δg) is determined by effective spin-orbit coupling. The authors suggest that it is possible to predict SOC using a simple EPR measurement. [81][55] It was also discussed how addition of alkyl chains can influence the spin density on the molecules. In the case of C8-BTBT and its non-alkylated derivative SOC would be smaller for C8-BTBT, because of spin-leak into the alkyl chains. [82]

We studied the photophysics of benzothieno[3,2-*b*]benzothiophene derivatives (**Figure 4.2**) using steady state and time-resolved spectroscopic techniques in order to learn about excited state relaxation processes. Surprisingly, we found that the excited state relaxation of these molecules in low concentration solutions is dominated by fast ISC to the triplet manifold. In the following text we will demonstrate the experiments that lead us to this conclusion, our attempt to explain this phenomenon. Our findings contradict previous reports suggesting that planar molecules and planar benzothiophene derivatives cannot have fast ISC. We also found that alkylated benzothieno[3,2-*b*]benzothiophene (C8-BTBT) has faster ISC and, hence, larger SOC than its non-alkylated derivative.

Table 4.1. Intersystem crossing rates and structures of different organic molecules [ps].

						
0.2-1.7 [83][84][85]	12195 [85]*	4 [86]	0.29[87]	29750 [87]*	3300 [87]*	0.1-0.4 [87]
						
278 [88]	3.15 [88]	0.59 [88]	0.97 (cis) 0.81 (trans) [88]	0.94 [88]	714 [88]	
						
400 in AcCN (4.4 in cxn) [89]	3 [89]	1200 (AcCN) 10 (cxn) [89]	5.2 [90]	0.25 [91]	286 [78] or 833 [79]*	1087 [78] or 3333 [79]*
						
3448 [78]*	24390 [78]*	2083 [78]*	1190 [78]*	1018 [79]*	25000 [79]*	3.2 [72]
						
10000 [79]*	12500 [79]*	12-50 [72][77]	188 [77]	538 [77]	135 [74]	P3OT and P3HT 1200 [76]

*Calculated from available data using the equations: $k_{ISC} = \frac{\phi_T}{\tau_F}$; $\tau_{ISC} = \frac{1}{k_{ISC}}$.

4.2 Results and Discussion

4.2.1 Synthesis of benzothieno[3,2-*b*]benzothiophene

This section describes synthesis of the compounds that were further used to study intersystem crossing in conjugated benzothiophene derivatives. All of the compounds were previously reported in the literature [52][92], however to our knowledge, their photophysical properties have not been studied. The structures are presented on **Figure 4.2**.

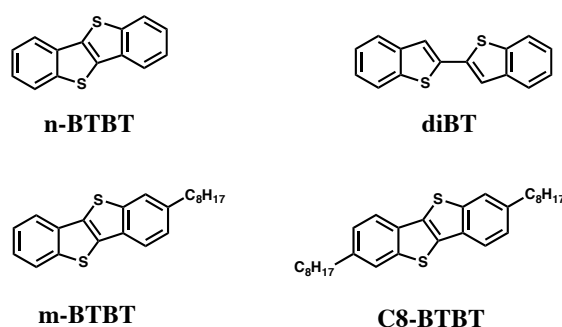
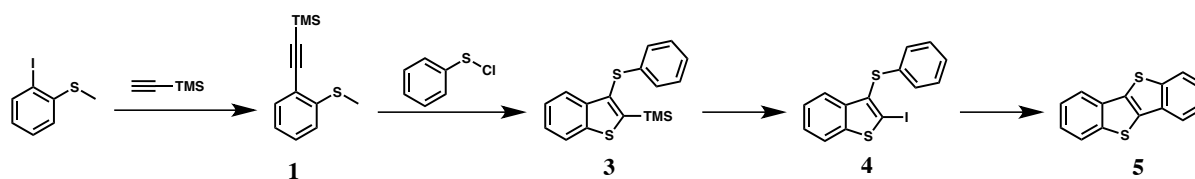


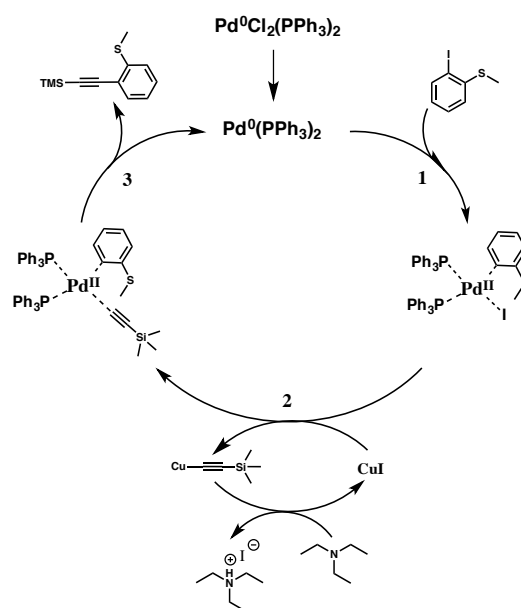
Figure 4.2. Structures of studied compounds.

The strategy for the synthesis of benzothieno[3,2-*b*]benzothiophene (BTBT) framework was reported by T. Mori *et al.* [52]. It is based on two consecutive thiophene-annulation reactions. The full scheme of the synthesis is presented below:



Scheme 4.1. Synthetic route to obtain BTBT framework

2-[2-(Trimethylsilyl)ethynyl]thioanisole (**2**) was synthesised through Sonogashira coupling reaction of terminal alkyne with 2-iodothiobenzene. This reaction is catalysed by Pd (0) complexes and proceeds with the proposed catalytic cycle described in the following scheme:

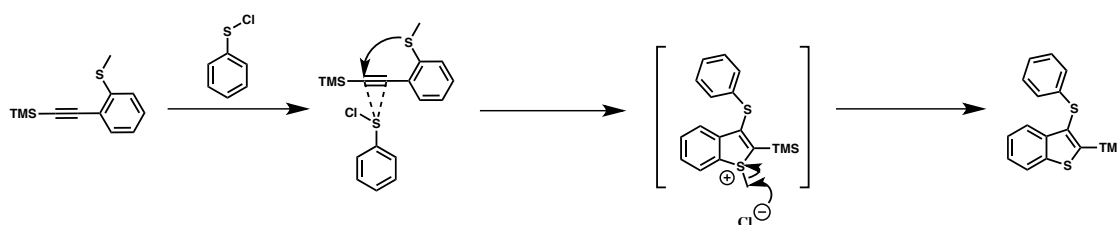


Scheme 4.2. Catalytic cycle of Sonogashira coupling reaction.

The first step in Sonogashira coupling is oxidative addition of halogenated compound to Pd (0) complex (1). This step is followed by transmetalation with alkynyl copper (2), which is formed from a terminal triple bond of trimethylsilyl acetylene after its interaction with the base and CuI. [93] The reaction terminates with reductive elimination (3) of the coupled compound and regeneration of the initial palladium complex. The Sonogashira coupling reaction proceeds with very high yield without formation of by-products. [94]

The obtained product (2) was used in the reaction with phenylsulfenyl chloride, which is an electrophile. [95] The electrophilic cyclization is a very efficient way to obtain heterocyclic structures. This reaction requires good leaving group attached to nucleophile. Methyl group was reported to be good enough leaving group for this type of cyclization.

The mechanism of this reaction is the following:

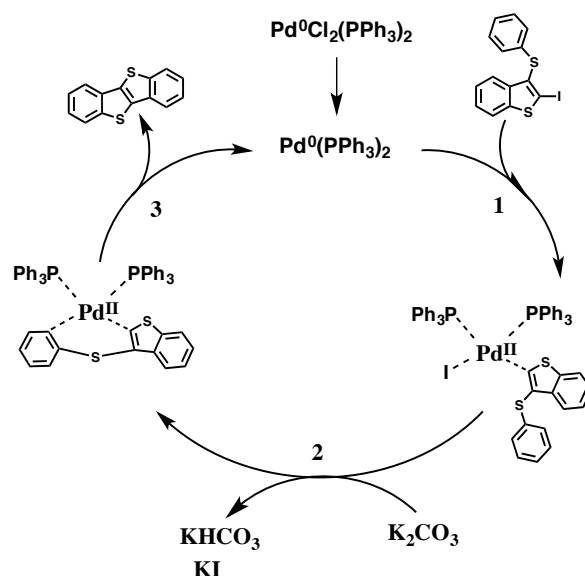


Scheme 4.3. Mechanism of electrophilic thiophene ring closer.

This reaction starts with attack of the alkyne triple bond by the electrophile (phenylsulfenyl chloride) and sulfur of the methyl sulfide group. In the result of this attack a

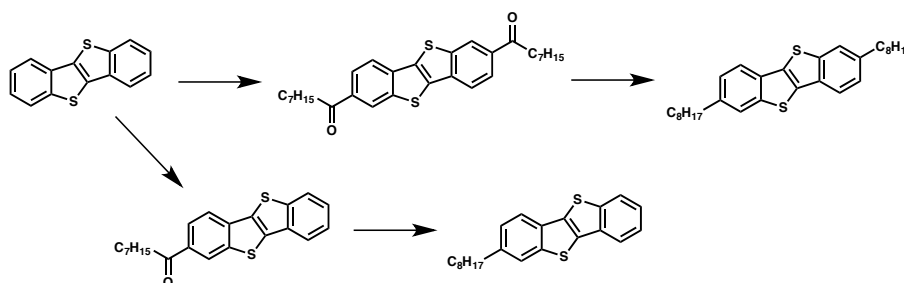
cationic intermediate is formed. The methyl group is removed *via* S_N2 displacement by a nucleophile from the reaction mixture, such as chloride anion. [96]

The product of the ring closure (**3**) contains all the carbon and sulfur atoms which are essential for the construction of the BTBT core. The α -TMS group in (**3**) was converted into the iodide to give product (**4**). This compound was then cyclized via the intramolecular direct arylation catalysed by palladium. [97] This reaction has the following mechanism:



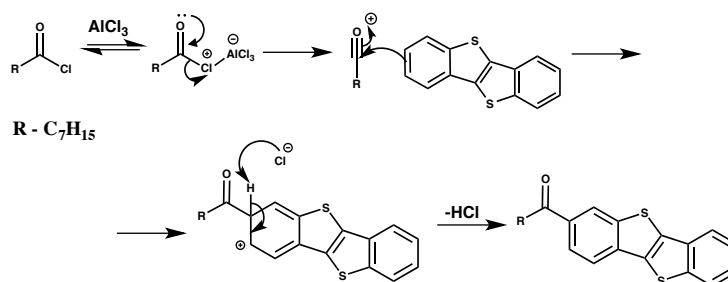
Scheme 4.4. Catalytic cycle of direct arylation ring closure.

This reaction involves three steps; it starts with oxidative addition of aryl iodide to the palladium complex (step 1). Afterwards, one proton and iodine are removed from the complex by the base (step 2). The final step is reductive elimination of BTBT (**5**). [97] The obtained heterocyclic compound was further functionalized with alkyl chains as previously reported [53]:



Scheme 4.5. Functionalization of BTBT core.

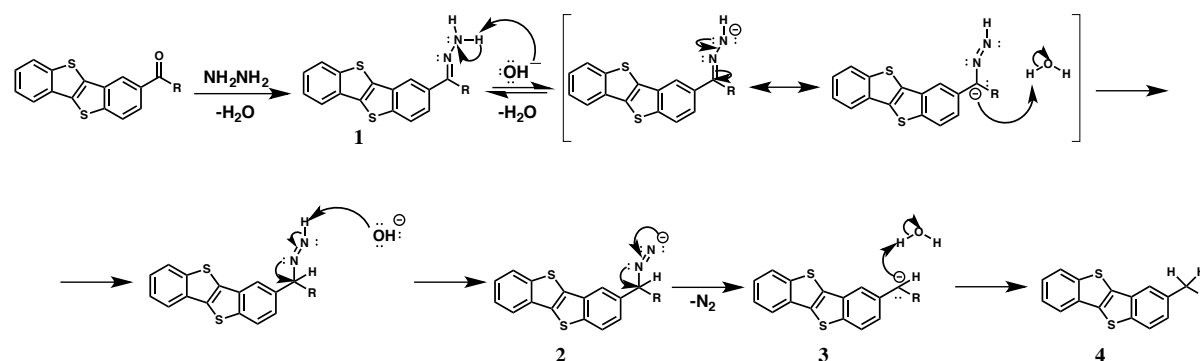
This was accomplished through two step transformations, the first step was a simple Friedel-Crafts acylation reaction with the following mechanism:



Scheme 4.6. Friedel-Crafts acylation of benzothieno[3,2-*b*]benzothiophene core.

In this reaction AlCl₃ removes chlorine from the acid chloride which results in a formation of a reactive acylium ion. This ion can attack one of the benzene rings of BTBT, which leads to formation of an aromatic ketone. Depending on the stoichiometry of the reagents in the reaction mixture, this nucleophilic attack can be repeated on the other side of BTBT, which would result in diketone formation. [93]

The final step of the synthesis was the reduction of the ketone to saturated hydrocarbon chain. This was accomplished using Wolff-Kishner reduction procedure with the following mechanism:

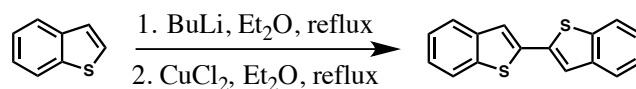


Scheme 4.7. Mechanism of Wolff-Kishner reduction.

This reaction begins by condensation of hydrazine with the keto-group which results in hydrazone (1) formation. The hydrazone is then deprotonated by a base (often potassium hydroxide is used). This is a rate limiting step and leads to formation of diimide anion (2). The diimide anion is then transformed into the alkyl anion (3) due to thermodynamically facilitated elimination of N₂. This step is followed by protonation of the anion by solvent which results in formation of the desired reduced product (4). [93]

The synthesis of diBT molecule was previously reported as part of a synthetic procedure for materials for TFT applications. [55] **Scheme 4.8** shows the synthetic procedure, which was

accomplished as a one-pot reaction that involved two stages. First, standard lithiation of benzo[*b*]thiophene and then reductive coupling using copper (II) chloride.



Scheme 4.8. Synthesis of diBT.

Despite the ease of synthesis, the overall yield of the molecule after purification was very poor, due to huge losses in silica gel column chromatography purification.

4.2.2 Photophysics of benzo[*b*]thiophene derivatives

4.2.2.1 Steady state absorption spectra and DFT calculations

In this section we discuss basic steady state optical properties of benzo[*b*]thiophene derivatives, since they have not previously been reported in literature.

The absorption, steady state fluorescence and phosphorescence are compared in **Figure 4.3**. Let's first consider absorption spectra of C8-BTBT. The spectrum exhibits vibronic structure with three well defined maxima at 3.75, 3.85 and 2.95 eV. This vibronic progression is independent of solvent polarity and concentration (**Figure 4.4** and the values are collected in **Table 4.2**). To understand the origin of this progression, we performed DFT calculations that are summarized on the bottom panel of **Figure 4.3**. We can conclude from the calculations that the first peak in the absorption spectrum corresponds to first singlet excited state (S_1) and second peak is the second excited state (S_2). The rest of the peaks are simply the vibronic replicas of these two states.

There is a quite obvious change of the shape of absorption spectra between the three BTBT derivatives. This change can be explained by DFT calculation results; the energy splitting between S_1 and S_2 states increases for the less alkylated molecules (**Table 4.4**). That is why for n-BTBT the S_2 state peak simply merges with the S_1 -(0-1)-transition. However, a very minor S_1 peak position shift is observed. The presence of the alkyl chains also influences the oscillator strength and extinction coefficients. The values of oscillator strength suggest that the S_0 - S_1 is an allowed transition and is of π - π^* nature [4]. The peak position values and extinction coefficients for all of the molecules are collected in **Table 4.3**.

The absorption spectrum of diBT is redshifted compared to BTBT derivatives and has a different vibronic progression. The redshift is due to larger conjugation in this molecule. The change in vibronic structures is probably due to a forbidden nature of S₂ transition, which, therefore, cannot contribute to the spectrum to the same extent as it is observed in BTBT derivatives.

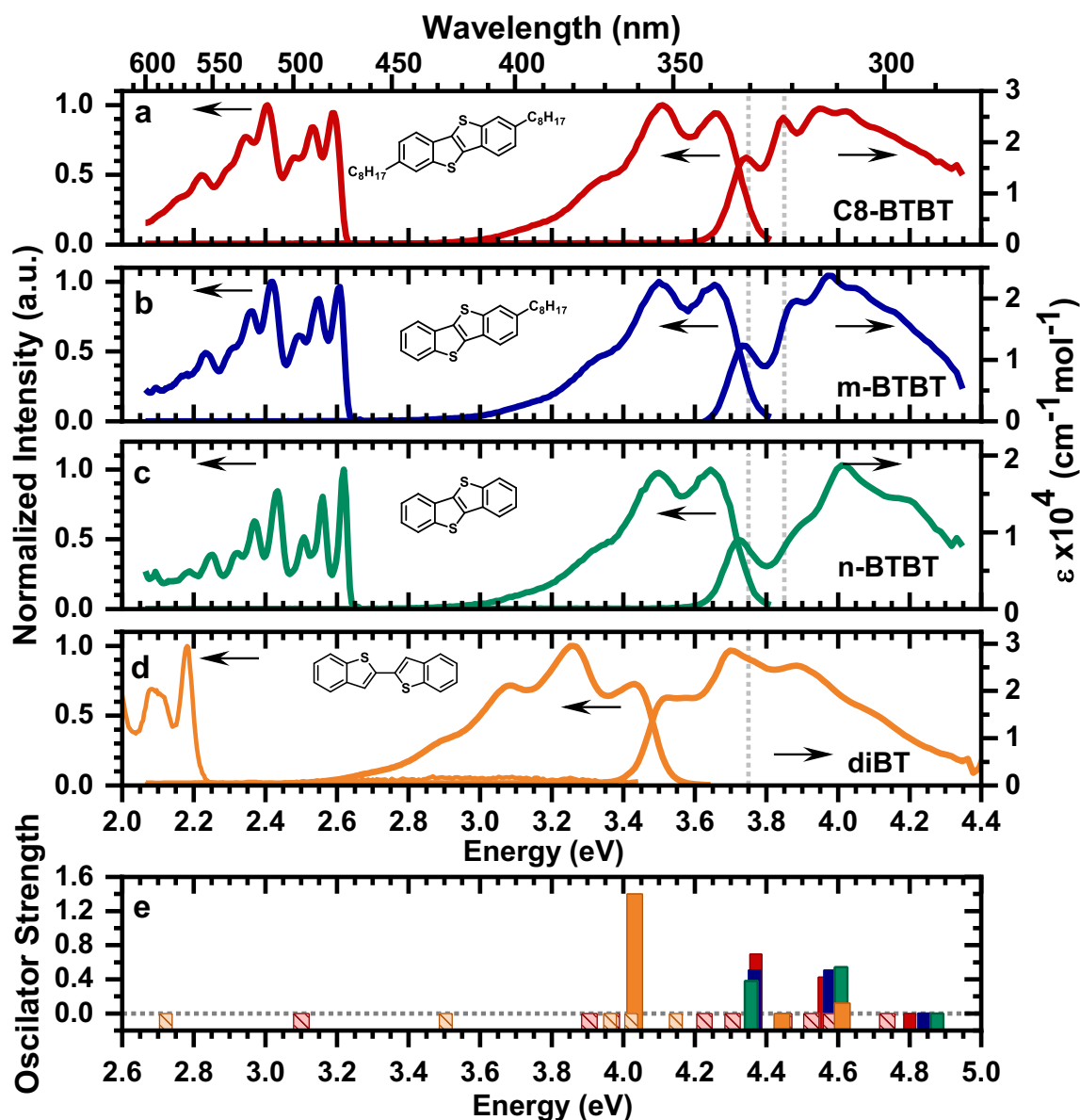


Figure 4.3. Steady state photophysical properties and DFT calculations of benzo[*b*]thiophene derivatives. Room temperature measurements were performed in 10 μ M solutions in toluene. Phosphorescence was recorded at 77 K in a glass solution (toluene:ethanol:diethyl ether, 1:1:2). The bottom panel represents results of DFT calculations: singlet excited states are presented as simple coloured bars, triplets – bars with stripes.

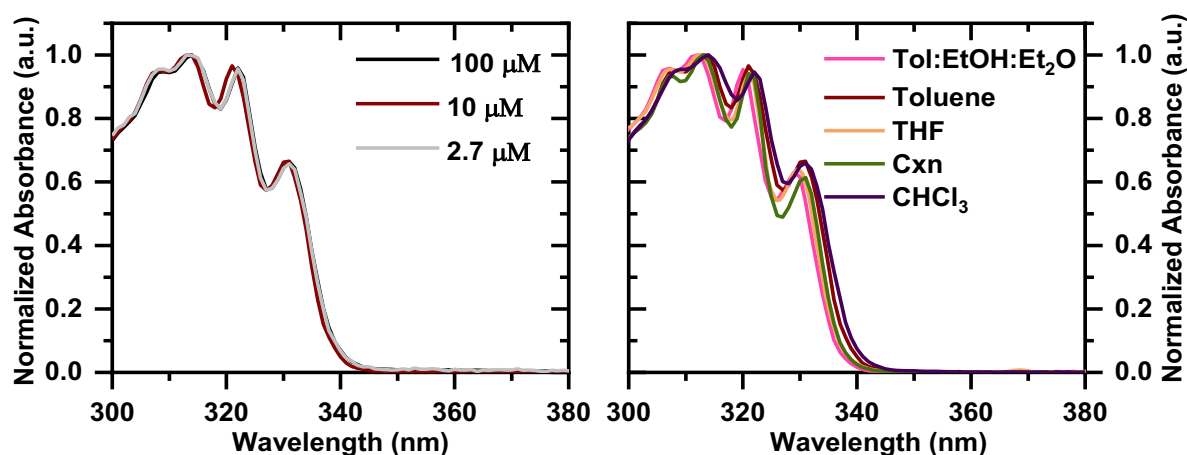


Figure 4.4. Absorption spectra of C8-BTBT in toluene solutions of different concentration (left) and in solvents of different polarity (10 μM).

Table 4.2. Steady state absorption and fluorescence of C8-BTBT in different solvents.

	S_1 , eV	ϵ (at 330nm), $\text{cm}^{-1}\text{M}^{-1}$	PL($\lambda_{\text{ex}}=320\text{nm}$), eV	Stokes shift, eV
Cyclohexane	3.74	19920	3.67	0.07
Toluene	3.74	17010	3.65	0.09
THF	3.76	18115	3.69	0.07
Chloroform	3.74	11360	3.65	0.09

Table 4.3. Steady state characteristics of benzo[*b*]thiophene derivatives in 10 μM toluene solutions.

	S_1 , eV	ϵ (of S_1-S_0)* in toluene, $\text{cm}^{-1}\text{M}^{-1}$	ϵ (of S_1-S_0)* in cxn, $\text{cm}^{-1}\text{M}^{-1}$	PL ($\lambda=320\text{nm}$), eV	Stokes shift, eV	Fluorescence quantum yields**, %	Triplet yields**, %
C8-BTBT	3.75	17020 \pm 640	19775 \pm 2460	3.66	0.09	3.4 \pm 0.7	51 \pm 7
m-BTBT	3.74	12340 \pm 1180	12640 \pm 130	3.65	0.09	3.4	-
n-BTBT	3.73	7300 \pm 30	17090 \pm 480	3.64	0.09	3.8 \pm 0.7	63 \pm 8
diBT	3.52	17580	15990 \pm 950	3.44	0.08	29 \pm 4	52 \pm 4

*Extinction coefficients values were determined from three different solutions (10 μM).

**PLQY and triplet yields were determined from five different solutions. The mean values with standard deviation are stated.

Table 4.4. Quantitative results of DFT calculations.

	C8-BTBT		m-BTBT		n-BTBT		DiBT	
	Energy, eV	Oscillator strength	Energy, eV	Oscillator strength	Energy, eV	Oscillator strength	Energy, eV	Oscillator strength
S₁	4.37	0.6955	4.37	0.5090	4.36	0.3790	4.03	1.3990
S₂	4.56	0.4250	4.58	0.5090	4.61	0.5410	4.44	0
S₃	4.80	0	4.84	0.0035	4.88	0	4.61	0.1180
ΔS_1-S_2	<i>0.19</i>		<i>0.21</i>		<i>0.25</i>		<i>0.41</i>	
T₁	3.10	0	3.10	0	3.11	0	2.72	0
T₂	3.91	0	3.88	0	3.86	0	3.50	0
T₃	3.97	0	3.97	0	3.97	0	3.96	0
T₄	4.23	0	4.23	0	4.23	0	4.02	0
T₅	4.31	0	4.37	0	4.42	0	4.15	0
T₆	4.45	0	4.52	0	4.55	0	4.36	0
T₇	4.53	0	4.56	0	4.64	0	4.56	0

4.2.2.2 Steady state fluorescence spectra

S_0 - S_1 is an allowed transition and we attribute emission as coming from the first (S_1) excited state. Emission is independent of solvent polarity and excitation wavelength, and concentration quenching is obvious only at 100 μM (**Figure 4.5**). The concentration quenching is due to a small Stokes shift of the molecules, which is 90 meV for BTBT derivatives and 80 meV for diBT. The values (**Table 4.3**) are reasonable for planar heterocyclic molecules and are in line with Stokes shifts reported for similar planar molecules. [98]

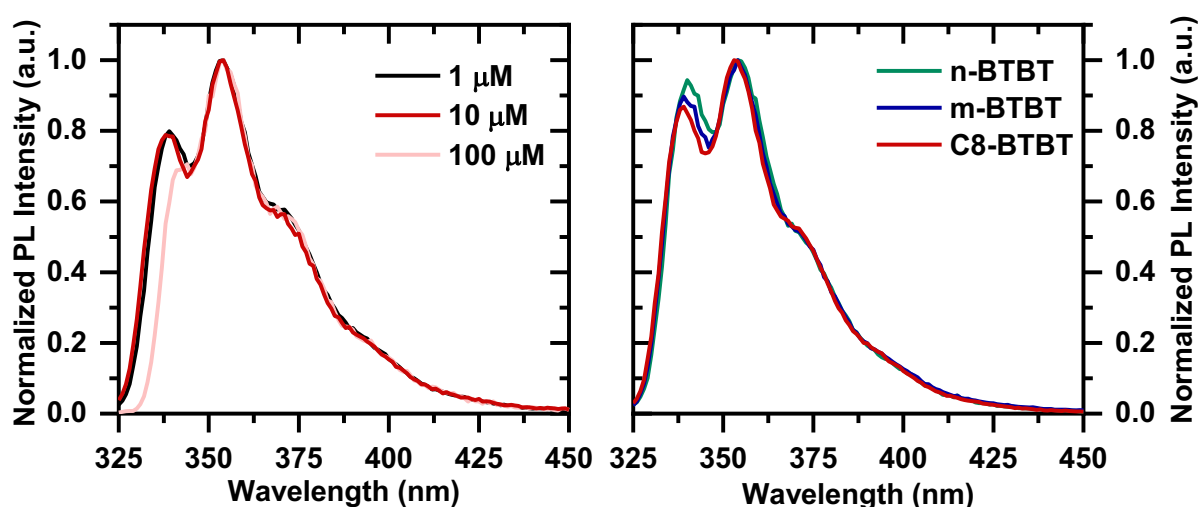


Figure 4.5. Fluorescence of different concentration C8-BTBT in toluene (left) and all of the molecules in 10 μM in toluene (right), $\lambda=320\text{nm}$.

Interestingly the splitting between the 0-0 and 0-1 vibronic peaks increases for alkylated BTBT derivatives (**Figure 4.5, right**). This is also accompanied by redistribution of 0-0 and 0-1 intensity, which suggests a different alignment of excited and ground state potential energy surfaces and different intrinsic reorganization energy.

4.2.2.3 Resonance Raman spectroscopy

To determine which modes couple to fluorescence (S_1 - S_0) transition, we performed resonance Raman on the solutions of these molecules in cyclohexane. The results are presented in **Figure 4.6**. The quantitative analysis of the spectra was performed to obtain Raman cross sections, the results are collected in **Table 4.5**.

The assignment of Raman shifts was accomplished with the aid of DFT calculations (**Table 4.6**). In the obtained resonance Raman spectra of all of the compounds, only in-plane

vibrations were found, which confirms the planar structure of the excited singlet state. BTBT derivatives exhibit strong Raman shifts at approximately 1600 and 1560 cm^{-1} , which correspond to C=C symmetric in-plane stretch along the long axis of the molecule. Small shifts of the signals are probably due to contribution of side chains to these vibrations. The Raman shift around 1474 cm^{-1} for C8-BTBT is due to C=C between thiophenes and side chain C-H in-plane scissoring. A similar Raman shift is also observed in m-BTBT (1478 cm^{-1}), however, in this case we can see that there are actually two signals in this region with shift values of 1478 and 1487 cm^{-1} . The peak at 1487 cm^{-1} is almost 3 times more intense than the 1478 cm^{-1} . We can assume that the lower energy vibration involves the alkyl chain and in the case of the C8-BTBT it would be more intense. We can also assume that in the C8-BTBT spectra these vibrations could be merged together. This lower energy shift is not found in the n-BTBT Raman spectrum.

For n-BTBT a reasonably strong signal is observed at 1415 cm^{-1} , it corresponds to C=C stretch between sulfur atoms and C-H symmetric rocking. Similar vibrations are observed for m-BTBT and C8-BTBT derivatives at 1396 and 1388 cm^{-1} . The difference in energy between this Raman shift is probably due to a larger contribution of aromatic C-H rocking in the case of n-BTBT.

1177 cm^{-1} is another strong Raman shift that is observed for all of the molecules. It takes its origin from C=C in-plane bending and side chains C-H rocking. However, in the case of non-alkylated derivatives the contribution of bending to this vibration is probably much higher.

DiBT resonance Raman spectrum possesses a different set of signals. The strongest vibration appears at 1574 cm^{-1} , it corresponds to symmetric in-plane C=C stretch along the short axis of the molecule and C-H rocking. In general, the observed vibrations are similar to those of BTBT derivatives. However, there is a contribution of stretching of C-C between benzo[b]thiophenes.

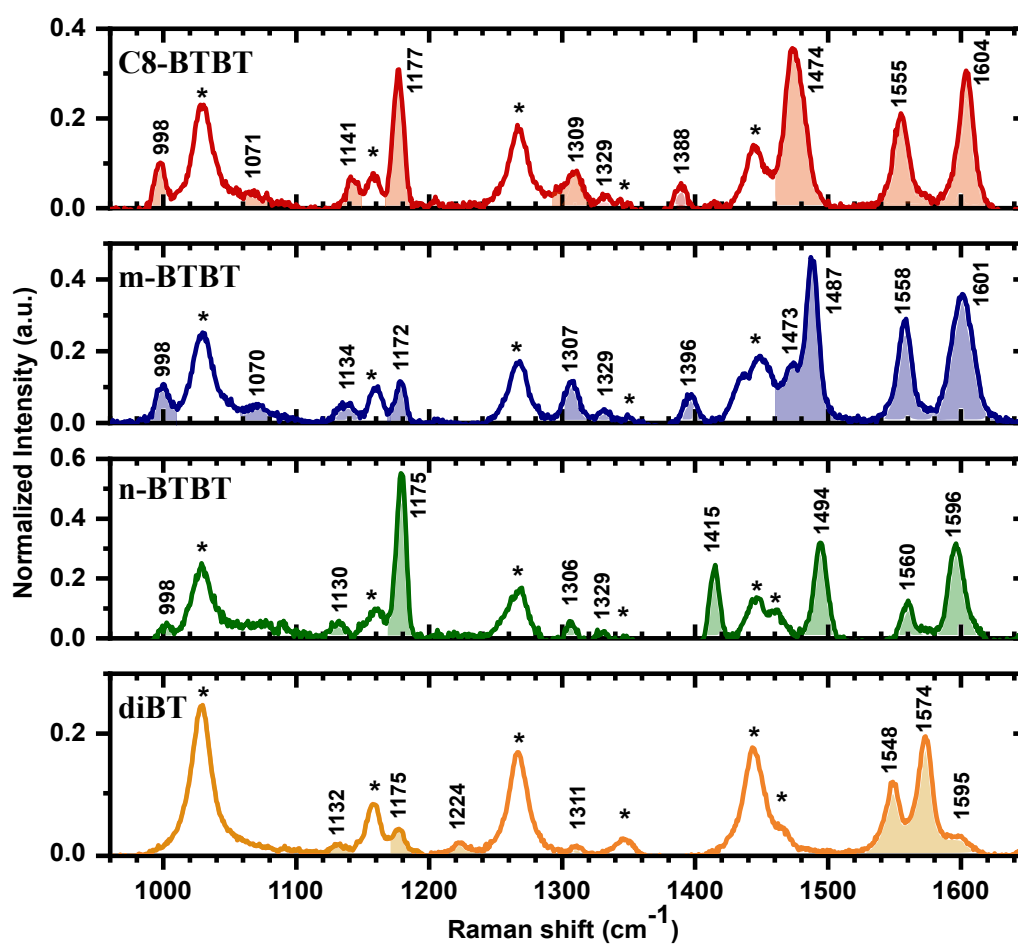


Figure 4.6. Resonance Raman spectra of benzo[*b*]thiophene derivatives in cyclohexane solutions ($\lambda = 282 \text{ nm}$). Starred peaks correspond to Raman shifts of cyclohexane.

Table 4.5. Raman shifts and cross sections of benzo[*b*]thiophene derivatives.

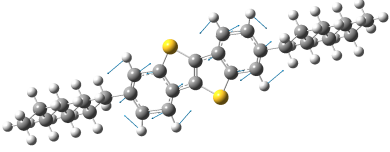
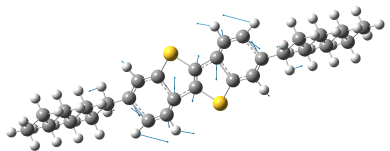
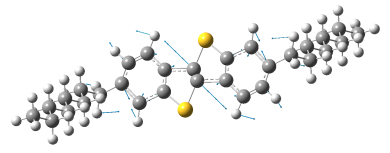
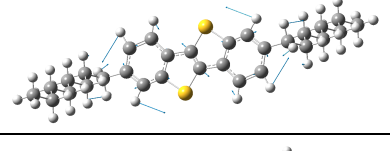
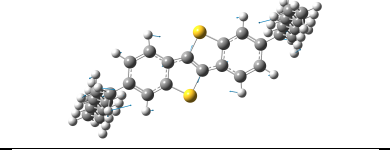
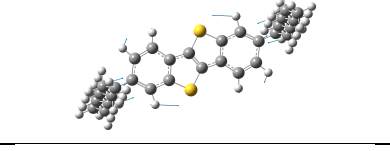
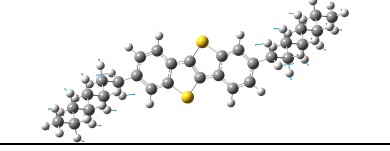
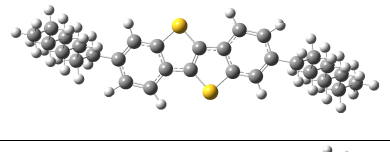
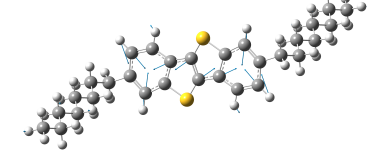
<i>C8-BTBT</i>			<i>m-BTBT</i>			<i>n-BTBT</i>			<i>diBT</i>		
Raman Shift (cm ⁻¹)	Energy (eV)	Cross section (*10 ⁷)	Raman Shift (cm ⁻¹)	Energy (eV)	Cross section (*10 ⁷)	Raman Shift (cm ⁻¹)	Energy (eV)	Cross section (*10 ⁷)	Raman Shift (cm ⁻¹)	Energy (eV)	Cross section (*10 ⁷)
1604	0.199	4.16	1601	0.1985	4.74	1596	0.1979	7.37	1595	0.1978	1.02
1555	0.1928	2.96	1558	0.1932	2.47	1560	0.1934	2.52	1574	0.1952	4.24
			1487	0.1844	3.3	1494	0.1852	5.94	1548	0.1919	3.01
1474	0.1830	6.29	1473	0.1826	0.98	1415	0.1754	3.14			
1388	0.1720	0.45	1396	0.1731	0.53						
			1329	0.1648	-	1329	0.1648	0.68	1224	0.1518	0.41
1309	0.1623	0.91	1307	0.1621	0.96	1306	0.1619	0.53	1311	0.1625	0.13
1177	0.1459	2.51	1172	0.1453	0.60	1175	0.1457	6.35	1175	0.1457	0.73
1141	0.1415	0.53	1134	0.1406	0.47	1130	0.1401	0.80	1132	0.1404	0.43
1071	0.1328		1070	0.1327							
998	0.1237	0.74	998	0.1237	0.6	998	0.1237	-			

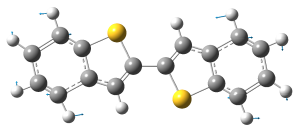
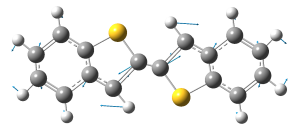
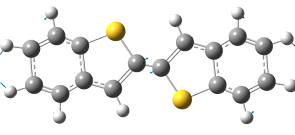
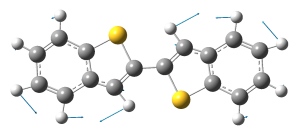
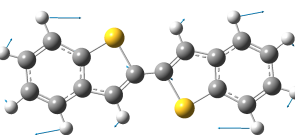
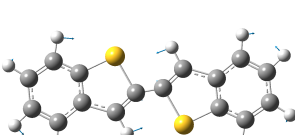
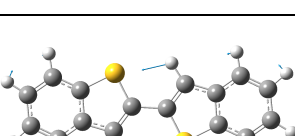
Blue – largest Raman cross sections

* - could not determine the cross sections due to poor integration of the peak

+

Table 4.6. Calculated and measured Raman shifts, visualisation and description of corresponding vibrations.

Calculated Raman Shift (cm ⁻¹)	Experimental Raman Shift (cm ⁻¹)	Vibration visualization	Vibration description
C8-BTBT			
1680	1604		<i>C=C symmetric in-plane stretch along the long axis of the molecule.</i>
1626	1555		<i>C=C asymmetric stretch along the short axis of the molecule</i>
1541	1474		<i>In-plane C=C between thiophenes and side chain C-H in-plane scissoring.</i>
1441	1388		<i>C-H in-plane rocking in phenyl rings and side chains.</i>
1385	1309		<i>C-H rocking of side chains and deformation of thiophene rings.</i>
1245	1177		<i>C=C in-plane bending and side chains C-H rocking.</i>
1219	1141		<i>Side chains C-H rocking.</i>
1178	1071		<i>Symmetric C-H scissoring in the phenyl ring, side chains and deformation of thiophene rings.</i>
1031	998		<i>Phenyl ring breathing mode and side chains C-H twisting.</i>

DiBT			
1672	1595		<i>Symmetric in-plane C=C stretch along the long axis of the molecule and C-H rocking.</i>
1651	1574		<i>Asymmetric in-plane C=C stretch along the short axis of the molecule and C-H rocking.</i>
1619	1548		<i>Symmetric in-plane C=C stretch along the short axis of the molecule and C-H rocking.</i>
1385	1311		<i>C-H rocking of side chains and C=C stretch in thiophene rings.</i>
1309	1224		<i>Asymmetric in-plane deformation of thiophene rings. C-C stretch between thiophene rings, C-H rocking.</i>
1261	1175		<i>Symmetric in-plane deformation of thiophene rings. C-C stretch between thiophene rings. C-H scissoring.</i>
1206	1132		<i>Symmetric in-plane deformation of thiophene rings. C-C stretch between thiophene rings. C-H scissoring.</i>

4.2.2.4 Photoluminescence quantum yield (PLQY)

Finally, we evaluated the PLQY and the obtained values for these molecules are collected in **Table 4.3**. The values are 3-4% for BTBT derivatives and 29% for diBT. The low PLQY values are quite unusual for planar molecules with an allowed S_1 - S_0 transition.

Such low PLQY can be explained by efficient non-radiative decay of a singlet state. This can be caused by multiple reasons:

- Aggregation
- Small HOMO-LUMO gap and efficient internal conversion to ground state
- Efficient ISC.

From the information shown above we know that these molecules do not form aggregates, at least this is true for the concentrations and solvents that we used for our experiments.

The value of the band gap is 3.65 eV (determined as an onset of the absorption spectra), which is very large compared to most of the other molecules. According to energy gap law (section 2.2.4.1), non-radiative transitions between states with such large energy separation will be quite inefficient. Therefore, low PLQY cannot be explained by efficient internal conversion to ground state.

Thus, we conclude that low PLQY must be due to efficient ISC. We indeed have previously observed phosphorescence in frozen solutions (**Figure 4.3**). To quantify the triplet yields we used an indirect method of singlet oxygen yield estimation (section 3.4.5). The triplet yields are summarised in **Table 4.3**. We find that the yields of triplets are high (around 60% for n-BTBT, the value is close to triplet yields of palladium complexes). [99]

4.2.2.5 Time-resolved spectroscopy

To investigate singlet-triplet transition dynamics, we used transient absorption spectroscopy (TA). The TA spectra and kinetics of triplet formation are collected in the **Figure 4.7**. All of the time constants values extracted from the TA data and auxiliary experiments are collected in **Table 4.7**.

The positive bands in all of the spectra correspond to stimulated emission. Due to the limitations of our probe spectrum, we could not see the ground state bleach. The negative signals in the spectra corresponds to photoinduced absorption (PIA), *i.e.* absorption of the excited states. To determine the origins of the PIA signals we used a streak camera which allows PL measurements on picosecond scale (the time constants are collected in **Table 4.7**). Therefore, using a streak camera we can determine the singlet state lifetime. The decay time constant that we get from steak camera measurement approximately matches the constant obtained in the TA. Thus, we assign PIA with maximums around 2.2 – 2.4 eV to S₁-S_n absorption. The second positive signal in TA we assign to triplet excited state absorption. This

assumption is based on the fact that this signal does not decay within TA experiment (7 ns). To confirm this assignment, we perform nanosecond time-resolved emission experiment, where all of the fluorescence was filtered using a GG435 filter. The experiment shows that at 4 ns time delay we already have an emission from triplet states (**Figure 4.8**).

Table 4.7. Time constants of the excited states decay and generation determined by transient absorption and streak camera measurements in toluene and Me-THF.

	TA (in toluene)			Streak Camera (in Me-THF)	
	τ (S ₁ -S _n), ps at RT	τ (T ₁ -T _n)*, ps at RT	τ (T ₁ -T _n)*, ps at 60°C	τ (S ₁ -S ₀), ps at RT	τ (S ₁ -S ₀), ps at 77 K
C8-BTBT	120±2 (toluene)/ 174±8 (Me-THF)	124±2 (toluene)/ 110±6 (Me-THF)	112±13	113±4 (toluene) /174±1.5 (Me-THF)	285±2
m-BTBT	148±2	174±3	136±13	-	-
n-BTBT	197±3	211±4	161±5	213±0.6	374±2
diBT	421±16	452±7	-	421±3	685±9

* rise time of triplet PIA.

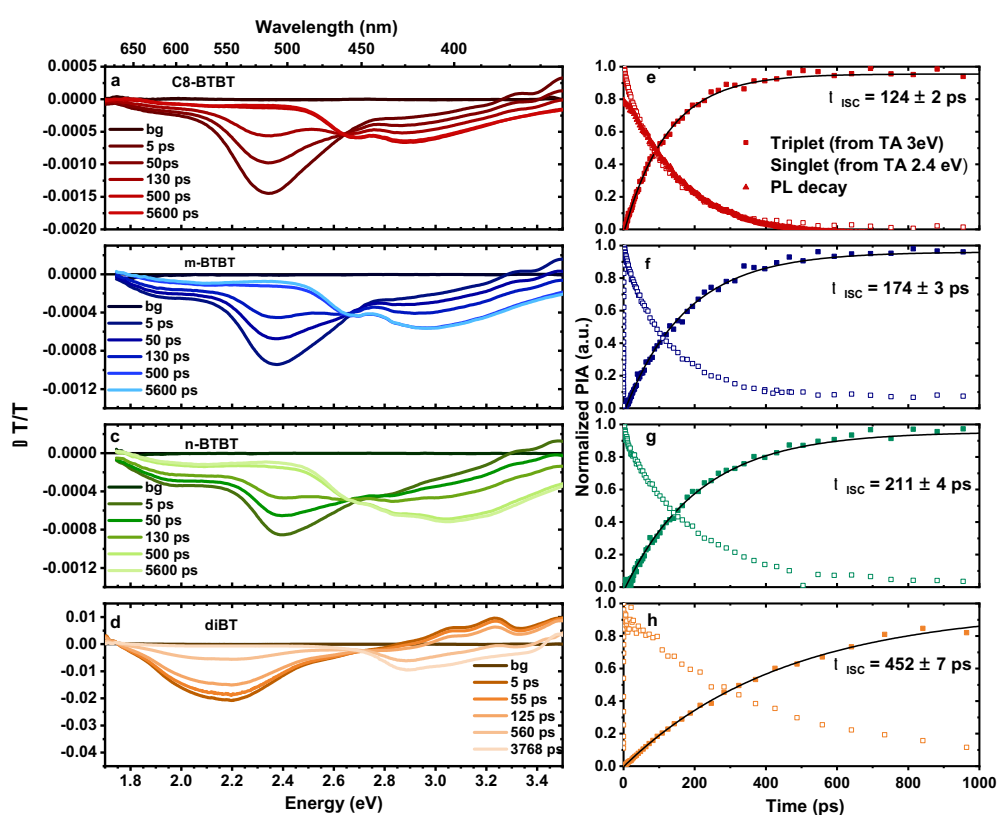


Figure 4.7. Transient absorption spectra of benzo[*b*]thiophene derivatives in toluene solutions at $\lambda = 330$ nm.

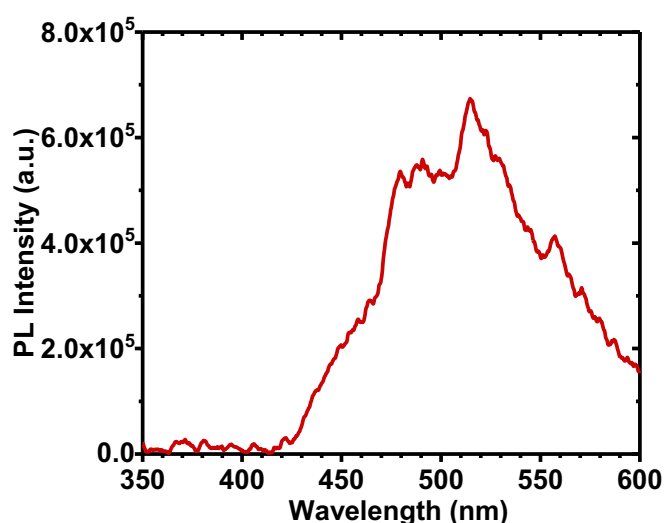


Figure 4.8. Triplet emission spectrum of C8-BTBT in toluene:ethanol:diethyl ether (1:1:2) mixture at 4 ns time delay at 77 K (not corrected for the filter effect).

The rise time constant of the triplet PIA signal is around 124 ps for C8-BTBT, which is very fast for a planar molecule. All of the TA spectra exhibit an isosbestic point, this indicates one-to-one conversion of singlet into triplet states. Dialkylated C8-BTBT molecule exhibits faster ISC than mono and non-alkylated derivatives. These results are solution density, wavelength and excitation power independent. [100] The results of our photophysical studies are summarised in **Table 4.8** (energies) and **Table 4.9** (rate constants).

Therefore, our time-resolved study shows that all benzo[*b*]thiophene derivatives have a sub-nanosecond ISC. This is highly unusual for planar molecules since similar benzothiophene derivatives tend to have ISC on nanosecond scale (**Table 4.1**). To rationalize this phenomenon and to explain the trends within the molecular derivatives (*i.e.* faster ISC in alkylated derivatives), we employ molecular dynamics simulations and quantum mechanics calculations in order to figure out spin-orbit coupling matrix element values in these molecules.

Table 4.8. Energies of singlet and triplet states of BTBT derivatives at 77 K in Ethanol:Toluene:Diethyl Ether (1:2:1).

Compound	Singlet, eV	Triplet, eV	S-T, eV
C8-BTBT	3.76	2.59	1.17
m-BTBT	3.76	2.61	1.15
n-BTBT	3.75	2.62	1.13
DiBT	3.44	2.18	1.26

Table 4.9. Rate constants of excited state relaxation processes in BTBT derivatives.

Sample	$k_r \cdot 10^{-8}$, s	$k_{nr} \cdot 10^{-9}$, s	$k_{ISC} \cdot 10^{-9}$, s	$k_{IC} \cdot 10^{-9}$, s	$k_{ISC}(\text{nBTBT})/$ $k_{ISC}(\text{diBT})$	$k_{ISC}(\text{n-BTBT})/$ $k_{ISC}(\text{diBT})$ (assuming triplet yield is equal)
C8-BTBT	2.83 ± 0.23	8.05 ± 0.02	4.11 ± 0.57	3.94 ± 0.57		
m-BTBT	2.30	6.53	-	-	2.55	2.14
n-BTBT	1.93 ± 0.16	4.88 ± 0.02	2.94 ± 0.38	1.94 ± 0.38		
DiBT	6.89 ± 1.38	1.69 ± 0.14	1.15 ± 0.89	0.54 ± 0.21		

4.2.2.6 Molecular dynamics (MD) simulations and SOCME calculations

To rationalize the ISC mechanism of studied molecules, we have performed MD and DFT calculations (details in section 3.5.1) on n-BTBT, C8-BTBT and diBT. As it was mentioned in section 2.2.5.2, the rate of ISC (k_{ISC}) between n-th singlet state (S_n) and m-th triplet state (T_m) can be expressed by Fermi's golden rule approximation:

$$k_{ISC} = \frac{2\pi}{\hbar} \langle \Psi_{T_m} | \widehat{H}_{SOC} | \Psi_{S_n} \rangle^2 \times \rho$$

ρ – is Frank-Condon weighted density of states (FCWD). The element in brackets is called spin-orbit coupling matrix element (SOCME). Therefore, there are two important factors for evaluation of the rates of ISC: value of SOCME and the Frank-Condon density of states. We are going to account for the FCWD by dividing the SOCME by the energy difference between the state. Therefore, we assume that the intrinsic reorganization energy of the molecules during transition between singlet and triplet state is low. To evaluate the mixing between the states of different multiplicity and access the rate of ISC we use the following parameter:

$$\lambda_{S_1}^{T_n} = \frac{\langle \Psi_{T_n} | \widehat{H}_{SOC} | \Psi_{S_1} \rangle^2}{E_{S_1} - E_{T_n}} \quad (4.1)$$

E_{S_1} – energy of first excited singlet state, E_{T_n} – energies of triplet states.

The time constant of ISC in BTBT derivatives implies that ISC happens not from the Frank-Condon geometry, because IC should occur on femtosecond time scale due to energy gap law. Therefore, we first of all assumed that ISC happens from the relaxed equilibrium geometry of the singlet excited state.

We used DFT to estimate spin-orbit coupling matrix element values between equilibrium geometry of the excited singlet state and all triplet states that have $E_{S_1} - E_{T_n} > 0$. The results of all the calculations are collected in **Table 4.10**. We find that the SOCMEs are very small (smaller than 0.1 cm^{-1}) between S_1 in the equilibrium geometry and all of the triplet states that are energetically lower than S_1 (columns **a** in **Table 4.10**). Therefore, we conclude that the direct electronic mechanism of ISC in BTBT derivatives cannot explain our observations.

It is often suggested that coupling within triplet manifold (vibronic coupling) can increase SOC between singlet and triplet states of interest. However, even including all the triplet states into SOCME calculation does not give a value large enough to explain a sub-nanosecond ISC (sum of column **a** in **Table 4.10**).

An indirect mechanism of ISC through spin-vibronic coupling has been reported for several planar molecules. [71] To explore the possibility of spin-vibronic ISC in BTBT derivatives, we employ molecular dynamics simulations to obtain all possible geometries of BTBT derivatives in singlet state. We then use these conformations to calculate SOCMEs and state mixing parameters ($\langle \lambda \rangle$ - for ensembles).

To understand how geometry alters the properties of the molecules, ensembles of geometries are constructed by sampling 400 times from MD simulations of the two molecules, BTBT and diBT, in both their S_0 and S_1 states. By performing the above calculations on each ensemble of geometries, we are able to investigate how:

- Changes in equilibrium geometry between the electronic states of a molecule alter its properties;
- Vibrational motion alters a molecules' properties.

We compare ratios between n-BTBT and diBT states coupling parameters (λ) and ratios between n-BTBT and diBT rate constants that were obtained experimentally. The experimental ratios are collected in **Table 4.9**.

Table 4.10. SOCME and states coupling elements (λ) based on relaxed singlet state (S_1) geometries obtained by MD simulations on n-BTBT and diBT.

Column index		<i>a</i>	<i>b</i>	<i>c</i>	<i>d</i>	<i>e</i>	<i>f</i>	<i>g</i>	<i>h</i>		
S₁, eV	T₁, eV	$\Delta ST, \text{cm}^{-1}$	SOCME, cm⁻¹	<SOCME>, cm⁻¹	λ, cm^{-1}	<λ>, cm⁻¹	<λ>/λ	<SOC>/SOC	$\lambda(\text{n-BTBT})$ /$\lambda(\text{diBT})$	<λ>(n-BTBT)/ <λ>(diBT)	
n-BTBT											
S₁-T₁	4.36	3.11	10082	0.06	1.13	3.57E-07	1.27E-04	355	18.8	47.2	2.02
S₁-T₂		3.86	4033	0.1	1.93	2.48E-06	9.24E-04	373	19.3	-	2.70
S₁-T₃		3.97	3145	0	1.95	0	1.21E-03	-	-	0	0.55
S₁-T₄		4.23	1049	0.01	2.10	9.54E-08	4.21E-03	44100	210.0	-	0.94
S₁-T₅		4.42	-484	0	2.41						
S₁-T₆		4.55	-1532	0	2.61						
S₁-T₇		4.64		0	2.60						
Sum				0.17		2.93E-06	6.47E-03	2205		0.42	0.91
diBT											
S₁-T₁	4.03	2.72	13227	0.01	0.91	7.56E-09	6.26E-05	8281	91.0		
S₁-T₂		3.5	6936	0	1.54	0	3.42E-04	-	-		
S₁-T₃		3.96	3226	0.15	2.66	6.97E-06	2.19E-03	315	17.7		
S₁-T₄		4.02	2742	0	3.51	0	4.49E-03	-	-		
S₁-T₅		4.15	1694	0.07	2.49						
S₁-T₆		4.36	0	0	2.85						
S₁-T₇		4.56	-1613	0.1	2.50						
Sum				0.33		6.98E-06	7.09E-03				

SOCME - spin-orbit coupling matrix element between the states in equilibrium geometries

<*SOCME*> - spin-orbit coupling matrix element in ensemble geometries

Including the geometry sampling results in a significant increase in SOCME (columns *b* in **Table 4.10**). This, of course, transfers into even larger increase (by at least 354) in states mixing element (λ), which to first approximation is directly proportional to the ISC rate constant (columns *d* in **Table 4.10**). This shows the importance of taking the molecular vibrations into account even when considering planar molecules.

However, even with this approach we are not able to match the experimental ratio between rate constants for the molecules. Namely, the experimental ratio between n-BTBT and diBT is 2.14 or 2.55 (**Table 4.9**), the calculated ratio based on summed SOCME is 0.91 (**Table 4.10**).

If we take into account only the coupling between the states involved in transition, *e.g.* between T_1 and S_1 etc, then the closest to experiment would be the paths S_1-T_1 or S_1-T_2 . However, this is still very irregular result because this suggests that the ISC in this case does not obey the energy gap law.

4.2.2.7 Effect of temperature on ISC

To test our theory further, we calculate SOCME at 77 K and perform low temperature PL experiment using a streak camera. The results of calculations and predicted SOCMEs are presented on **Figure 4.9**. The results of low temperature measurements are shown on **Figure 4.10** and the fitting results are collected in **Table 4.7**. The decay of the singlet state at 77 K slows down by approximately 20% comparing to room temperature.

The theoretical difference between 77 K and room temperature (333 K) for n-BTBT is 4.4 and for diBT is 5.4 (**Table 4.11**). What we find from the experiment is different, for n-BTBT it is 1.76 and for diBT is 1.52, which is much smaller than calculated. For the calculation of the experimental ratio, we assumed that the yield of triplets remains the same at 77 K and room temperature, however, this is not necessarily correct. We, therefore, also compare the ratio between experimentally determined ISC rates at 77 K of n-BTBT and diBT ($\tau_{ISC}(n-BTBT)/\tau_{ISC}(diBT)$). It is 1.83, whereas the theoretical ratio is 2.29 (**Table 4.11**).

At 60°C, the values of ISC time constant remain approximately the same for C8-BTBT but change by slightly more than 20% at 60°C for n-BTBT (**Figure 4.11**). Interestingly, the TA spectral shape also changes slightly comparing to the spectra obtained at room temperature. The

loss of structure could be due to a change in the mechanism of the ISC or due to a change in vibrations that govern the process.

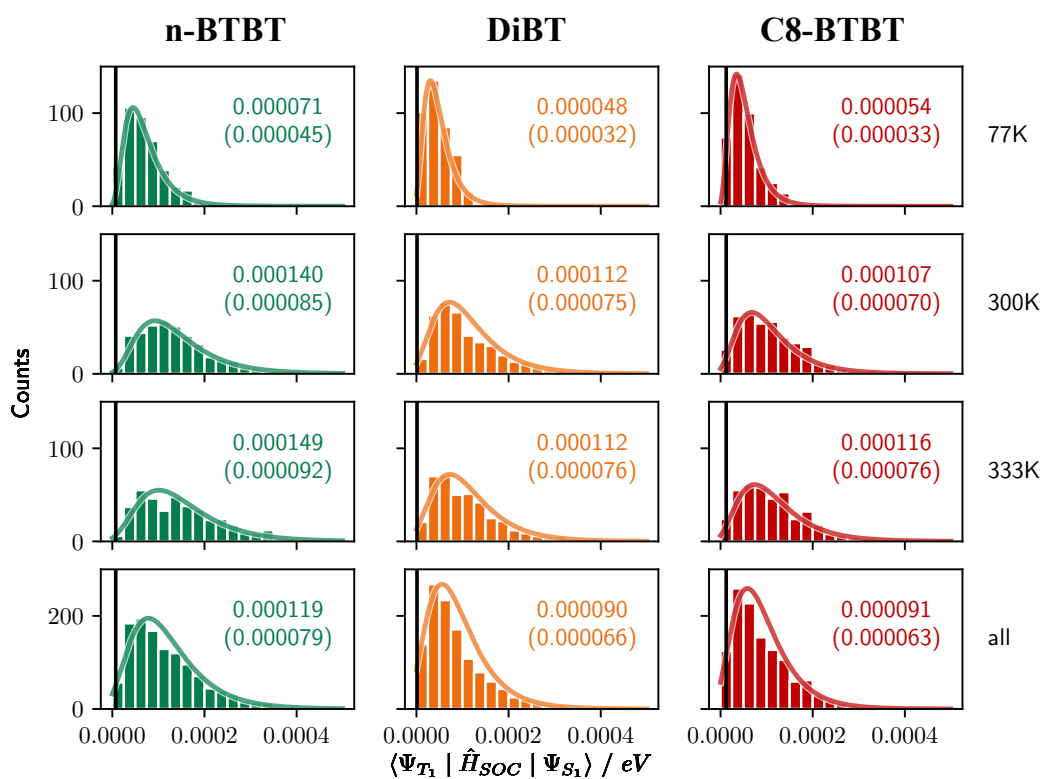


Figure 4.9. Spin-orbit couplings of BTBT derivatives at different temperatures, the number on each graph corresponds an overall SOC.

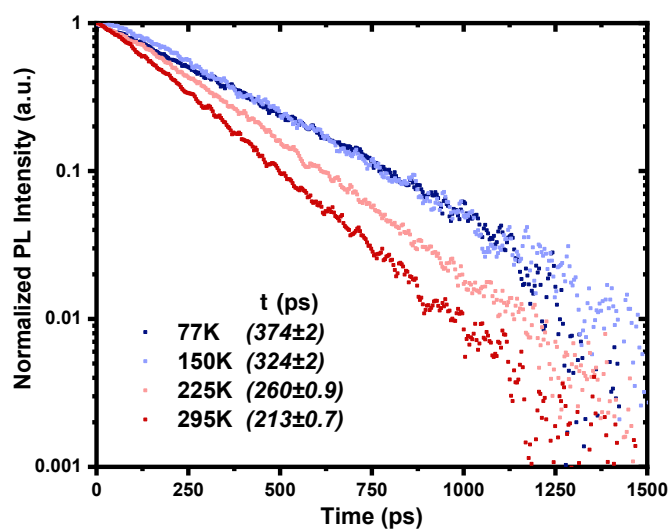
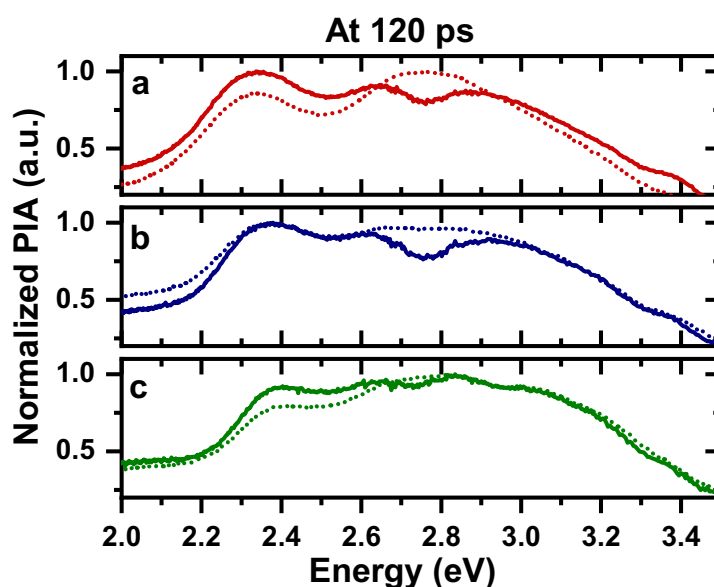


Figure 4.10. Photoluminescence decay kinetics of n-BTBT in Me-THF recorded at different temperatures using streak camera $\lambda = 330\text{ nm}$.

Table 4.11. SOCME and states coupling elements (λ) based on geometries obtained by MD simulations on n-BTBT and diBT at different temperatures.

	77 K		RT (333 K)		$\langle\lambda\rangle(\text{RT})/\langle\lambda\rangle(77\text{ K})$	$\langle\lambda\rangle(\text{n-BTBT})/\langle\lambda\rangle(\text{diBT})$ at 77 K	$k_{\text{isc}}(\text{RT})/ k_{\text{isc}}(77\text{ K})$	$k_{\text{isc}}(\text{n-BTBT})/ k_{\text{isc}}(\text{diBT})$ at 77 K
	$\langle\text{SOCME}\rangle, \text{cm}^{-1}$	$\langle\lambda\rangle^* 10^7, \text{cm}^{-1}$	$\langle\text{SOCME}\rangle, \text{cm}^{-1}$	$\langle\lambda\rangle^* 10^7, \text{cm}^{-1}$	Theory		Experiment	
C8-BTBT	0.00054	2.3	0.000116	0.11	0.05	2.29	1.64	1.83
n-BTBT	0.000071	0.04	0.000149	0.18	4.40		1.76	
DiBT	0.000048	0.018	0.000112	0.09 5	5.44		1.52	

**Figure 4.11. Transient absorption spectra of BTBT derivatives (a – C8-BTBT, b – m-BTBT, c – n-BTBT) in toluene at room temperature (solid line) and 60°C (dotted line) at $\lambda = 330\text{nm}$.**

Therefore, we conclude that our calculations cannot correctly predict the ISC dynamics. This is most likely to be due to Frank-Condon weighted density of states parameter. We assumed that the reorganization energy in the transition from singlet to triplet does not change significantly for the studied derivatives. A better way to evaluate the FCWD is using Marcus-Levich-Jortner (MLJ) theory, in which the FCWD is expressed as follows:

$$FCWD = \frac{1}{\sqrt{4\pi\lambda k_B T}} \sum_{n=0}^{\infty} \exp(-S) \frac{S^n}{n!} \exp\left[-\frac{(\Delta E + n\hbar\omega + \lambda^2)}{4\pi\lambda k_B T}\right] \quad (4.2)$$

where λ is the Marcus reorganization energy due to intramolecular low-frequency vibrations (λ_L) and intermolecular solvent-induced relaxation (λ_S), $\hbar\omega$ is the energy of an effective high energy vibrational mode involved in the transition, S is a Huang-Rhys parameter associated with the effective vibration, ΔE is the energy difference between the states at the equilibrium geometry. [12] To account for a possible change in reorganization energy, we need to know Huang-Rhys parameter and the vibrational mode related to the ISC.

4.2.2.8 Frank-Condon analysis

Frank-Condon analysis allows to calculate the Huang-Rhys parameter and, hence, to estimate potential energy surfaces displacement (section 2.2.3). We started evaluation from the simplest case – single vibrational mode analysis. Therefore, we assume that only one (mean) vibrational mode is coupled to a transition between the electronic states.

It is much easier to use luminescence spectra for FC analysis rather than absorption. This is because in luminescence we only see the vibrational replicas of a single electronic state, whereas in absorption electronic states can be close in energy which would result in vibrational peaks overlap.

Analysing the room temperature fluorescence spectra (**Figure 4.12**), we found that the fluorescence spectra of all four derivatives are governed by a similar mean vibration, ~ 164 meV for BTBT and 173 meV for diBT. The Huang-Rhys parameter was found to decrease for less alkylated BTBT derivatives, indicating lower coupling to vibrations. This effect of alkyl chains on excited state relaxation is different to what was reported for other conjugated molecules, e.g. 2,3,9,10-tetramethyl-pentacene, where the reorganization energy remains the same as for unsubstituted pentacene. [101][11] The largest values of Huang-Rhys parameter and the corresponding reorganization energy were found for diBT, which can be rationalized by transition from non-planar ground state to quinoid singlet state.

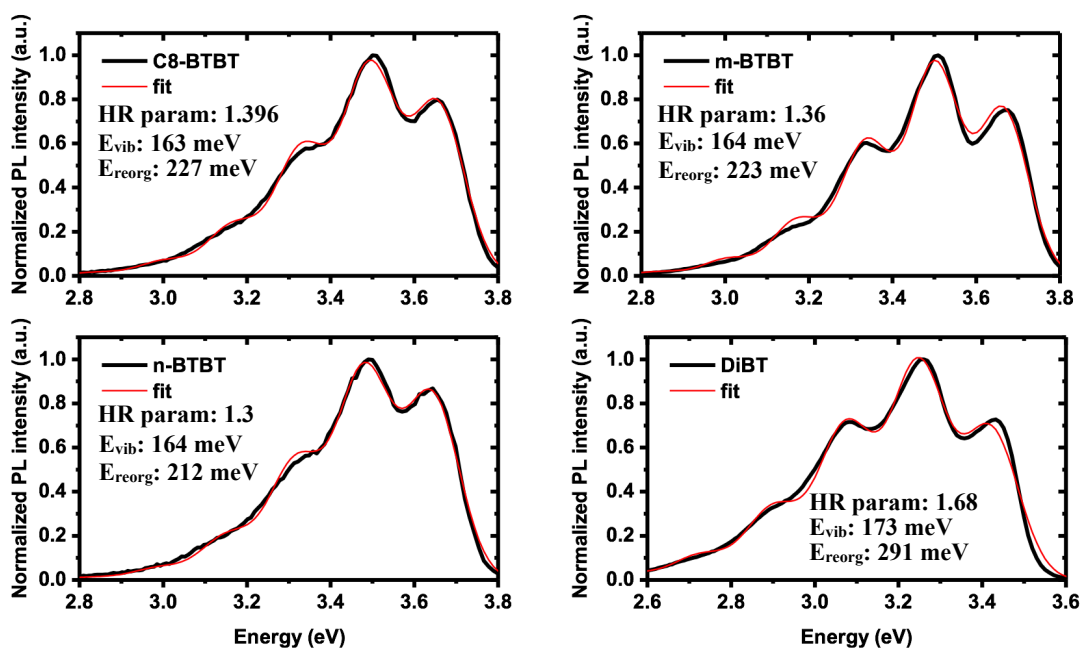


Figure 4.12. Single-mode Frank-Condon fitting results for benzo[*b*]thiophene derivatives fluorescence in 10 μ M toluene solutions.

To evaluate the reorganization energy of the singlet to triplet transition, we performed Frank-Condon analysis on fluorescence and phosphorescence spectra at 77 K. The resulting reorganization energy of the fluorescence transition is very similar to what is obtained at room temperature. However, at 77 K the inhomogeneous broadening (related to λ) is much smaller and this allows us to distinguish between low and high energy vibrations. Fitting the phosphorescence spectra allows us to evaluate which vibrations are involved in this transition and access the difference between the singlet and the triplet state.

We used a multi-mode Frank-Condon model (equation (2.16)). This approach allowed us to fit C8-BTBT luminescence data obtained at 77 K (**Figure 4.13**). The fluorescence spectra at 77 K exhibits sharp peaks with at least two kinds of vibronic replicas. In order to fit this spectrum with the fewest free parameters, we used the resonance Raman data. In resonance Raman vibrations that are involved in fluorescence are significantly enhanced. The description of resonance Raman results is given in the section 4.2.2.3. We used the vibrations found in resonance Raman for a more informed and precise fitting.

To fit C8-BTBT fluorescence spectrum, we fixed two of the vibrational energies to the vibrations that were obtained from resonance Raman (189 and 138 meV) using an effective model where modes are grouped by frequency and the effective mode is a weighted average based on Raman cross section. The rest of the parameters were allowed to vary. The obtained

vibrations and Huang-Rhys parameters also fit the fluorescence at room temperature giving the same values of Huang-Rhys parameter as previously shown in single mode analysis, however with a different broadening value. To fit the phosphorescence at 77 K, we allowed all of the parameters to vary, this approach yields a very good fit to the experimental data. The results of the fitting are shown in **Figure 4.13**. We compared the change between in the vibrational modes of fluorescence and phosphorescence transition in **Table 4.12**. Both phosphorescence and fluorescence are coupled to ~ 190 meV effective vibration (HR parameter ~ 1), which corresponds to in-plane C=C stretching. Both phosphorescence and fluorescence are also coupled to a low frequency effective mode at ~ 60 meV, however with a significantly different HR parameter. This vibration probably corresponds to an in-plane phenyl breathing mode. Finally, the most significant change (in both the vibrational energy and the Huang-Rhys parameter) is observed in the mid-frequency mode: from 138 meV in fluorescence to 102 meV in phosphorescence with a Huang-Rhys parameter twice as large in phosphorescence compared with fluorescence. These changes mean that S_1 and T_1 have different conformations. A positive change in Huang-Rhys parameters suggests a higher distortion of the molecule in the triplet state.

We fit fluorescence and phosphorescence spectra of all of the studied molecules and find that the vibrations that all of them have similar vibrations coupled to these transitions. We were not able to obtain a good quality fluorescence fit for n-BTBT, due to the presence of a significant scattering background.

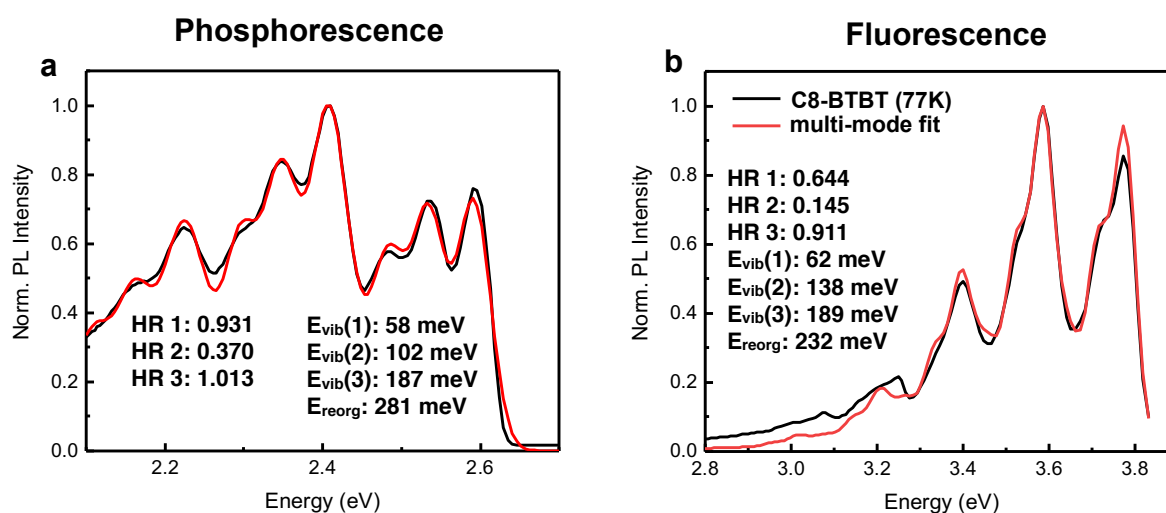


Figure 4.13. Multi-mode Frank-Condon fitting results for solutions of C8-BTBT in $10\mu\text{M}$ toluene:ethanol:diethyl ether (1:1:2) at 77 K.

Table 4.12. Results of FC analysis of luminescence at 77 K.

	S ₁ -S ₀			T ₁ -S ₀			% change in E _{vib}
	E _{vib} , meV	E _{vib} , cm ⁻¹	HR parameter	E _{vib} , meV	E _{vib} , cm ⁻¹	HR parameter	
C8-BTBT	62	500	0.664	58	468	0.931	7
	138	1113	0.145	102	823	0.370	30
	189	1524	0.911	187	1508	1.013	1
m-BTBT	66	532	0.578	57	460	0.961	14
	135	1089	0.236	100	807	0.362	26
	192	1549	0.741	188	1516	1.065	2
n-BTBT	-	-	-	59	477	0.938	-
	-	-	-	102	823	0.441	-
	-	-	-	190	1532	1.057	-
DiBT	76	613	0.436	59	477	0.7	22
	144	1161	0.409	98	790	0.776	32
	194	1565	1.117	191	1541	0.862	2

The obtained information allows us to estimate the HR parameter of S₁-T_n transition, assuming that all of the triplet states have a similar conformation to the T₁ state. The HR parameter is related to potential energy surfaces displacement. This can be related to the change in potential energy surface position between the singlet and triplet electronic states as follows:

$$(\Delta Q_{S_1-T_1})^2 = (\Delta Q_{S_1-S_0} \pm \Delta Q_{T_1-S_0})^2 \quad (4.3)$$

where $\Delta Q_{S_1-T_1}$ is nuclear coordinates displacement during transition from singlet to triplet state, $\Delta Q_{S_1-S_0}$ is nuclear coordinates displacement of fluorescence, $\Delta Q_{T_1-S_0}$ is nuclear coordinates displacement of phosphorescence transition. **Figure 4.14** summarizes the equation (4.3) and shows four principle cases of potential energy surfaces arrangement that involves one ground state, one singlet and one triplet state. The case **c** on **Figure 4.14** corresponds to vibration at ~190 meV, because it has a HR parameter of ~ 1 before and after ISC and, thus, no change in potential energy surfaces arrangement is observed. The case **d** on **Figure 4.14** corresponds to the vibration at ~138 meV, as it is only present in the singlet state. Based on the equation (4.3) and the data obtained by FC analysis, we estimate HR parameters of the ISC for each vibrational mode found in our FC analysis. The results are summarized in **Table 4.13**.

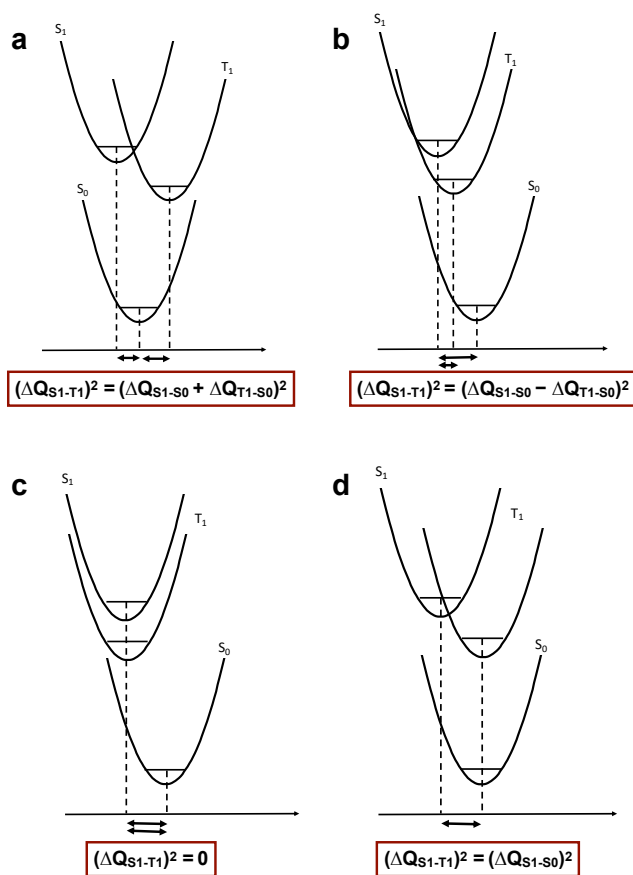


Figure 4.14. Possible potential energy surfaces arrangements that involve one ground state, one singlet and one triplet state and the corresponding $(\Delta Q_{S_1-T_1})^2$.

Table 4.13. Huang-Rhys parameters of S_1-T_1 transition for vibrational modes coupled to fluorescence and phosphorescence in C8-BTBT and diBT at 77K.

E_{vib} (eV)	C8-BTBT		diBT	
	S+	S-	S+	S-
~60	3	0.03	2.3	0.03
~100	0.37	0.37	0.78	0.78
138	0.145	0.145	0.41	0.41
~190	4	0	3.9	0.02
$\sum_i s_i$	7.515	0.543	7.39	1.24

Total Huang-Rhys parameter of ISC is unlikely to be ~ 7 . Thus, we take S_1 values of Huang-Rhys parameters for FCWD calculations. For further calculations, we will use a single effective vibration of $E_{vib}^{eff} = \frac{\sum_i S_i E_{vib,i}}{\sum_i S_i}$, which is 108 meV for BTBT and 113 meV for diBT (calculated from values in **Table 4.13**). For simplicity, we will use 110 meV for both of them in our further calculations. The Huang-Rhys parameters for this vibration will be taken as a sum of Huang-Rhys parameters in **Table 4.13**, which for ~ 0.5 for BTBT and ~ 1 for diBT. Therefore, the reorganization energy is ~ 55 meV for S_1 - T_1 transition in BTBT, which matches the value that we get from theoretical computations (~ 50 - 53 meV).

Using the equation (4.2) and taking a range of “classical” reorganization energies (due to low-energy intramolecular modes or solvent reorganization), we obtain the FCWD for four different classical reorganization energies (**Figure 4.15**). We calculate the ISC rate constant based on the calculated *ensemble* geometries and corresponding spin-orbit coupling matrix elements and the corrected FCWD. The ratio of calculated and experimental rate constants of ISC are compared in **Figure 4.16**. This allows us to conclude that our theory is able to predict the ratio between the rate constants of two studied molecules. However, the calculated values of the ISC rate constant were determined to be roughly 8-9x smaller than experimental. The reorganization energy of 0.2 eV yields the most accurate correlation between the theoretical and experimental rates. However, we note that this value, although reasonable [12], is rather large for a non-charged planar molecule. From **Figure 4.15** (for reorganization energy of 0.2 eV) we see that FCWD is negligible between S_1 and T_5 , T_4 and T_1 for BTBT; and between S_1 and T_4 and T_1 for diBT. Therefore, only the sum of ISC rate constants from S_1 to T_2 , T_3 , T_4 (for BTBT), and S_1 to T_2 , T_3 for diBT needs to be considered when comparing the theory with the experiment.

This model still does not explain all of the experimental observables, *e.g.* the temperature dependence; however, it is significantly improved compared to direct mechanism or when ISC is considered between *ensemble* geometries with FCWD estimated using just the singlet-triplet splitting.

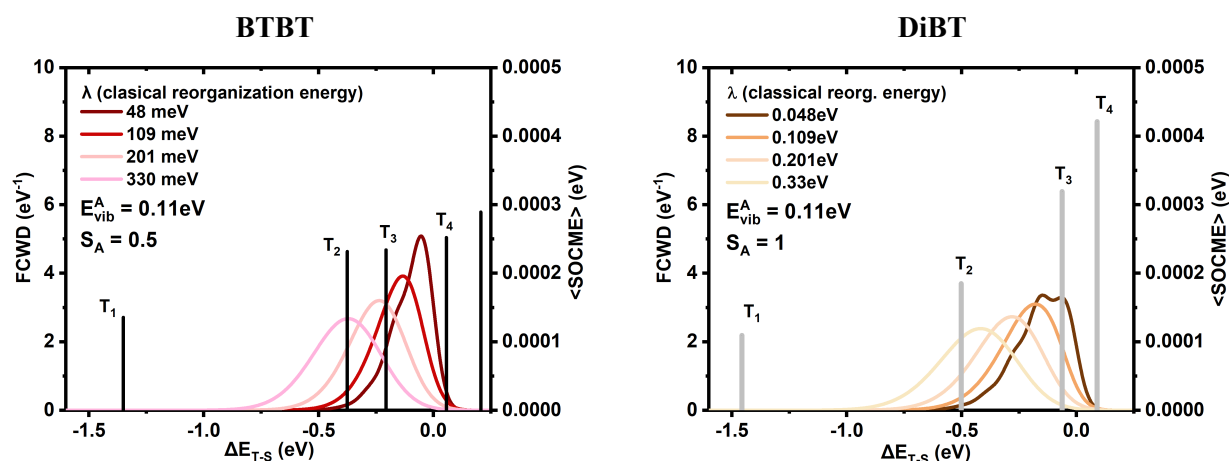


Figure 4.15. Calculated spin-orbit coupling matrix elements between S_1 - T_n (right y-axis, values are represented as length of the sticks) vs the energy gap between the involved states (x-axis) vs calculated Frank-Condon weighted density of states (left, represented as coloured curves, where each curve was obtained with different value of classical reorganization energy).

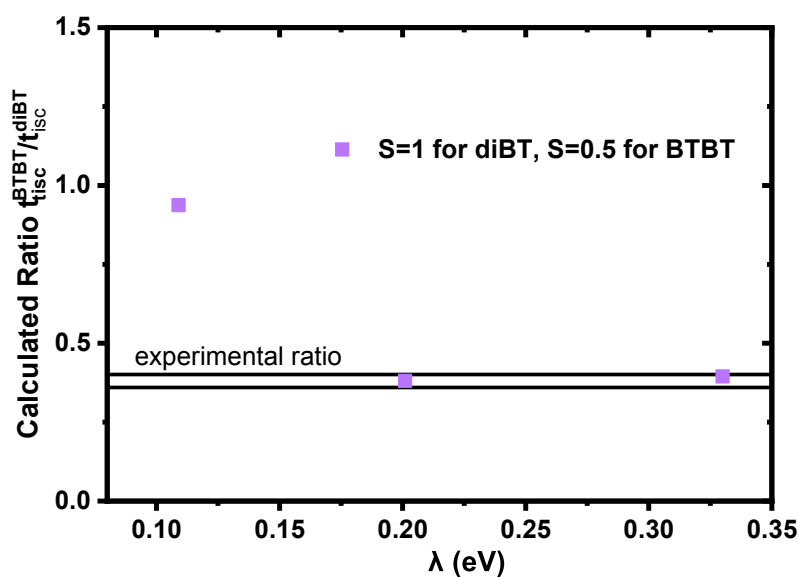


Figure 4.16. Comparing calculated and experimental ISC in benzo[*b*]thiophene derivatives. On x-axis plotted “classical” (induced by the environment) reorganization energy, S is Huang-Rhys parameter of the 0.11 eV effective vibrational mode (or “quantum” part of reorganization energy).

4.2.2.9 ISC in extended C8-BTBT analogue: C8-DNTT

C8-DNTT is an extended in conjugation derivative of C8-BTBT. This molecule exhibits higher conjugation length. Therefore, we assume that it would be more rigid and have less vibrations involved in the optical transitions. The optical properties of this molecule are presented on **Figure 4.17**. Interestingly, S_1 and S_2 transitions are separated in energy by 0.8 eV (**Figure 4.17, a**), suggesting that no character mixing of these two states should be observed. The photoluminescence spectrum is dominated by 0-0 transition, which implies more rigid structure and smaller reorganization energy. This is confirmed by Frank-Condon analysis (**Figure 4.18**): the Huang-Rhys parameter is 0.81 and the reorganization energy is 132 meV, both of these values are significantly lower than those found for C8-BTBT.

Transient absorption spectroscopy (**Figure 4.18, b**) shows a structured positive signal at 3-3.5 eV, which we assign to ground state bleach as it matches the vibronic structure of C8-DNTT absorption. The second signal observed in TA is broad negative signal at 2-3 eV that changes its shape over the time of experiment. In addition, we observe the change in the sign of the signal at 3-3.5 eV. We suggest that these changes are due to triplet state formation and ISC. Therefore, initial broad negative signal (2-3 eV) corresponds to the singlet state and the following structured negative spectra (see **Figure 4.18, b** 3071 ps) corresponds to the excited triplet state absorption. The kinetics of the singlet decay and ISC is shown on **Figure 4.18, c**. ISC in C8-DNTT occurs with the time constant of 2 ns which is almost 20 times slower than in C8-BTBT.

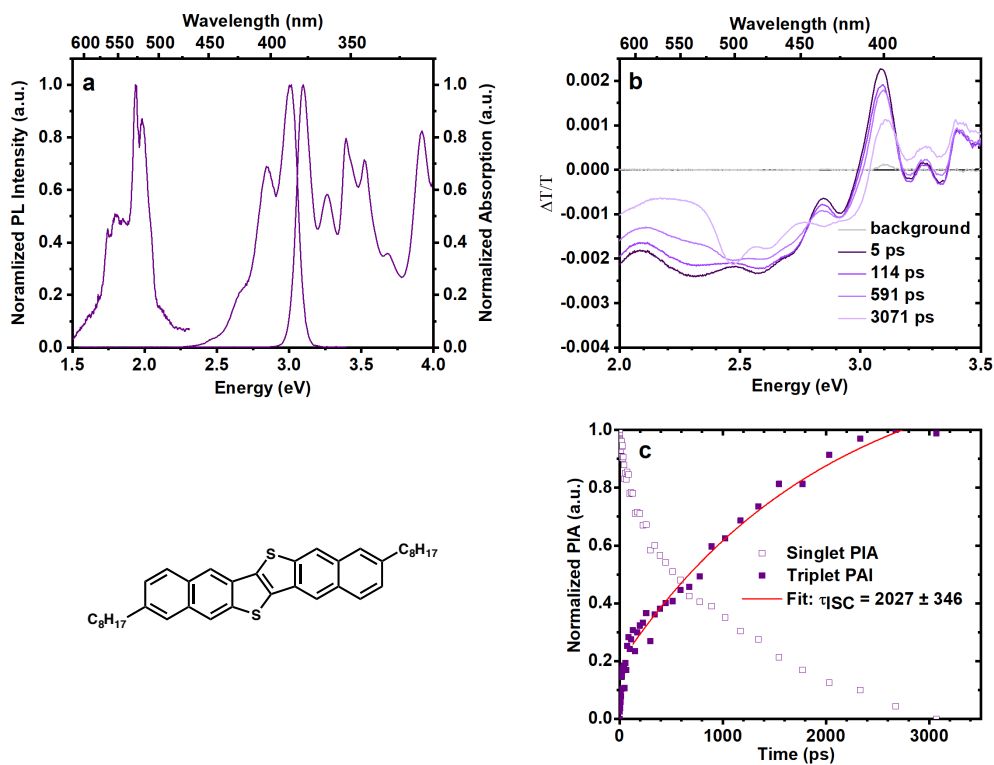


Figure 4.17. Steady state absorption and PL of C8-DNTT (a), transient absorption (330nm) (b), kinetics of PAI signals of singlet (600-610nm) and triplet (435-335) states (c).

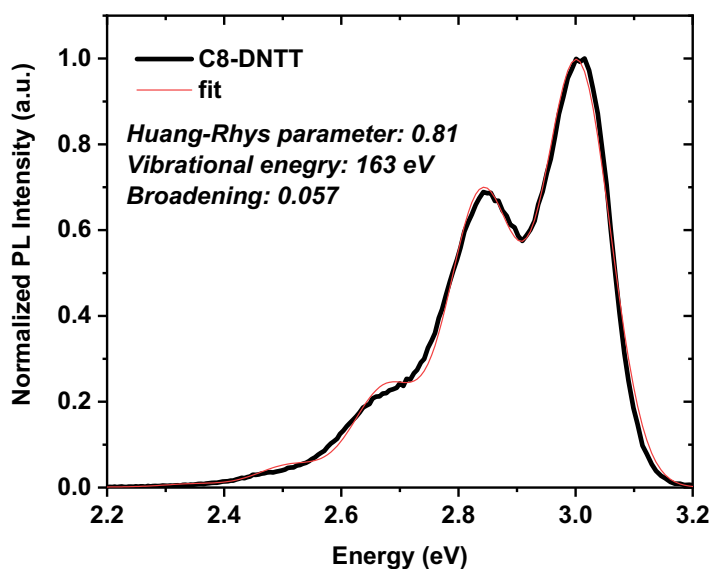


Figure 4.18. Single-mode Frank-Condon fitting results for solution of C8-DNTT in THF.

4.3 Conclusions

We find surprisingly fast ISC in planar benzo[*b*]thiophene derivatives. A picosecond rate of ISC in planar molecules is very irregular because ISC requires conservation of total angular momentum of the system. This is very hard to achieve in planar systems due to limited possibility of out-of-plane motion and, hence, limited σ and π orbital mixing.

Despite the common belief that ISC is faster in non-planar molecules, our study finds slower ISC in slightly twisted more flexible benzo[*b*]thiophene (diBT) compared to planar BTBT derivatives. We also find that alkyl chains have an influence on the rate of ISC, thus, demonstrating faster ISC for dialkylated (C8-BTBT) molecule.

We find that the rate of ISC in these molecules cannot be explained by simple electronic mechanism of ISC, for which SOCME is calculated between singlet's equilibrium geometry and one of the isoenergetic triplet state. Our calculations demonstrate the importance of taking into account molecular dynamics even when considering planar aromatic molecules. We find that inclusion of the molecular vibrations results in 20-fold increase in SOCME and more than 300x increase in states coupling element. Based on our calculations, we conclude that ISC in benzo[*b*]thiophene derivatives occurs through S_1/T_3 or S_1/T_2 path.

We, however, were not able to quantitatively predict the ISC rate and temperature dependence using our theory methods. This suggests that our assumptions are still too restrictive: the FCWD that we used is rather crude and a full time-dependent quantum approach might be necessary.

5 Synthesis and spectroscopy of indolo[3,2-*b*]indoles

*In this chapter we discuss synthesis and photophysics of indolo[3,2-*b*]indole derivatives. These molecules are sulfur-free analogues of the molecules discussed in the previous chapter. They exhibit unity photoluminescence quantum efficiency in solution due to much slower intersystem crossing (~ 10 ns). Unexpectedly, the singlet state emission of these molecules persists for up to 5 μ s. This delayed fluorescence does not follow the kinetics of triplets, instead showing a power-law dependence. We study the origin of the long-lived emission and come to the conclusion that delayed emission is a result of electron ejection from the molecules, similar to what has been reported for indole derivatives.*

All of the quantum calculations were performed by Dr Theo Keane at the University of Sheffield. Ph-N-inin was synthesised by Chloe Coulson under my supervision as a part of her master's degree. DOSY and temperature dependent NMR was performed by Dr Sandra van Meurs at the University of Sheffield.

5.1 From indole to indolo[3,2-*b*]indoles and derivatives

In this chapter we discuss spectroscopy of indolo[3,2-*b*]indole (ININ) derivatives (**Figure 5.1**). These molecules are structurally similar to BTBT derivatives (Chapter 4); however, substitution of sulfur to nitrogen changes optical and the charge transporting properties. The differences in optical properties arise from the reduction in spin-orbit coupling matrix element (SOCME) due to the lower molecular weight of nitrogen. In addition, pyrrole, pyrrolo[3,2-*b*]pyrrole and indole are suggested to be more aromatic than the corresponding sulfur-containing derivatives. [102][103] This could result in better exciton and charge delocalization in ININ compared to BTBT molecules.

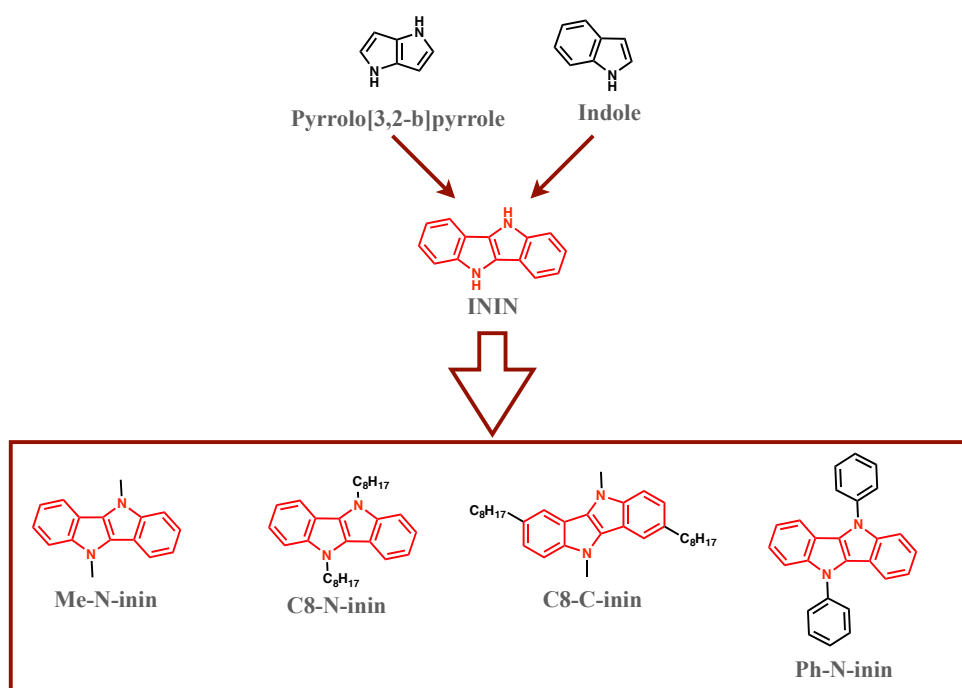


Figure 5.1. Structures of nitrogen containing heterocycles.

ININ is an extended analogue of indole chromophore. Indole itself is a very important moiety because it is a basic component of a biological chromophore tryptophan. Consequently, spectroscopy of indole, tryptophan and derivatives have been a topic of many scientific reports. [104][105][106] Multiple puzzling phenomena were reported for these systems, *e.g.* solvent polarity dependent emission of indole [105][107], one/two photon photoionization [108][109][110][111], delayed luminescence [112][113], etc. Thus, it would be interesting to establish if ININ derivatives (ININs) exhibit some of the intriguing properties of indole moiety, and if we could find use for them in organic electronic devices.

The similarity of ININ aromatic core to indole is not the only intriguing feature of these molecules. Pyrrole is known to be a stronger electron donor compared to thiophene. Pyrrolo[3,2-*b*]pyrrole was suggested to have a significantly lower ionization potential (7.27 eV) in comparison to other electron-rich heterocycles with similar structure, *e.g.* thieno[3,2-*b*]thiophene (8.1 eV). It means that this moiety is a more efficient π -electron donor. [114] The electron donating ability of organic semiconductors is related to their hole transporting properties; thus making pyrrolo[3,2-*b*]pyrrole, and its extended derivative ININ particularly interesting for applications in organic semiconductors. [115]

The interest in ININ derivatives as hole transporting materials is based not only on its electron-donating ability. Due to a smaller radii of the nitrogen atom, planar ININ derivatives could be able to form a more concise intermolecular assembly in films compared to BTBT derivatives. [115][116] This could improve both charge transfer integral and reorganization energy values. [29] The hole transporting properties of unsubstituted ININ and the derivatives have been tested in transistors [117][118][119], but the reported charge carrier mobilities were not found as good as for BTBT derivatives.

Electron donating ability is also related to the oxidation of compounds and, therefore, it would affect the stability of the molecules and their ionization potential. Both of the properties are important, and will be reflected in optical properties of the molecules and their performance in electronic devices. However, the ININ core has been suggested as a promising emitter for organic electronics applications [57], and it has also found application as a good electron donor moiety for TADF emitters [120] and organic donor-acceptor polymers for solar cells applications. [121][122]

ININ derivatives were predicted to form stable radical cations which is due to strong delocalization of an electron. [123] This property of ININ derivatives might be useful for applications in polaronic ferromagnets, and, in fact, a high spin-density was found in doped polymers that contained ININ moiety. [124] Spectroscopic studies of indole suggest formation of radical cations after photoexcitation; hence we naturally wondered if this mechanism is possible in ININ derivatives. Stable radicals are of interest because they have recently found application in OLEDs due to their potential to increase the EQE of the devices due to having a reduced triplet formation. [125][126][127]

Only some aspects of the optical spectroscopy of ININ derivatives have been reported [57][128][129]. However, to our knowledge to date, there is no comprehensive study of the ININ

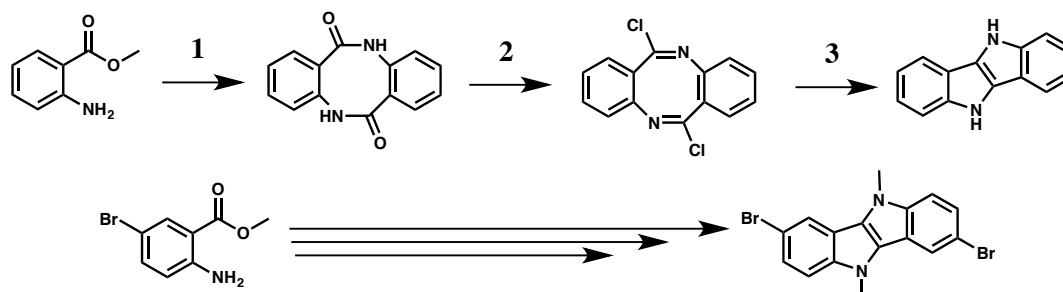
chromophore in solution and films using time-resolved techniques. We designed our derivatives to have different “inert” substituents that do not influence the nature of emissive states greatly; however, would have a significant impact on solid state arrangement of the molecules allowing for in depth investigation of optical and charge transporting properties. C8-C-inin is especially interesting compound due to the location of its alkyl chains at the long axis of the molecule. According to a report by Illig *et. al.* [34] such molecular design reduces the dynamic disorder in films; thus allowing for high charge carrier mobility. We shall discuss spectroscopy and mobility of the synthesised derivatives in thin films in Chapter 6. In this chapter we discuss the synthesis and optical properties of isolated ININ derivatives in different conditions in solutions.

5.2 Results and discussion

5.2.1 Synthesis of ININ derivatives

The synthesis of indole-containing compounds has received a lot of attention due to the importance of this moiety for biomedical applications and drug discovery. [130][131][106][132][133] The particular ININ heterocycle was first reported in 1917 by P. Ruggli where he synthesised ININ using *o,o'*-dinitrotolan as a starting compound. [134] Several other methods were developed over the years of research on indole-based heterocycles allowing for much better yields and shorter synthetic paths. [57][135] [136] [137]

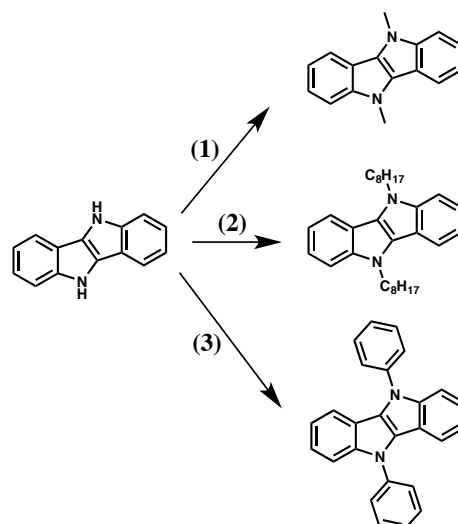
We choose to follow the procedure that was optimized by Qiu *et. al.* (Scheme 5.1) where the yield of the unsubstituted ININ core after the three steps synthesis was reported to be ~34%, which is reasonably high. [57]



Scheme 5.1. Synthetic route to ININ heterocyclic core: (1) – NaH, THF, reflux; (2) – PCl₅, CHCl₃, reflux; (3) – Zn, CF₃COOH, THF. [57]

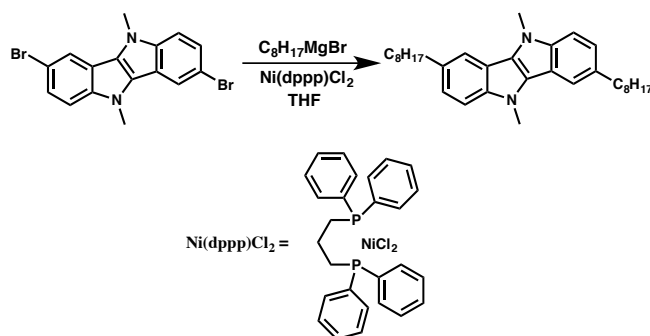
We used methyl 2-aminobenzoate (or methyl 2-amino-5-bromobenzoate) as a starting material for nucleophilic cyclization reaction (**1**) to form eight-membered cyclic dilactams. [138] We obtained cyclic dilactams with reasonably high yield of 86 % for brominated and 46 % for non-brominated starting compounds. The product of reaction **1** (**Scheme 5.1**) was isolated from reaction mixture by precipitation into water followed by thorough drying, and then it was used in the next step without further purification. The step **2** (**Scheme 5.1**) of the procedure involved chlorination of the dilactam using PCl_5 in a dry chloroform solution, the reaction had quantitative yields. The diimidoyl chlorides obtained in this reaction are prone to hydrolysis which results in formation of original dilactams; thus diimidoyl chlorides were used for transannulation without additional purification with minimal exposure to ambient atmosphere. [57] The final step in core preparation was the reductive transannulation reaction which was first reported in 1966 by Metlesics *et al.* [139] They utilized a mixture of zinc and acetic acid as a reducing agent. We followed a similar procedure reported by Qui *et al.* [57] using activated zinc with trifluoroacetic acid. The procedure was very efficient and allowed for 89% yield in case of non-brominated derivative and 69% for the brominated one.

Further derivatives of the ININ core are shown on **Scheme 5.2**. The brominated compound (bottom line on (**Scheme 5.1**)) was also subjected to *N*-methylation reaction using the same procedure **1** (**Scheme 5.2**) as for non-brominated derivative. Formation of phenyl substituted derivative (**3** on **Scheme 5.2**) was accomplished using Goldberg reaction. [140] All of the compounds after the functionalization were purified by column chromatography on silica gel and recrystallization. Unfortunately, the yields of the compounds after purification were very low (~10-20%).



Scheme 5.2. Functionalization of ININ core: (1) – NaH, DMF, MeI, (2) – NaOH, C₈H₁₇Br, DMSO, H₂O, TBAB; (3) – CuI, Cs₂CO₃, PhI, DMF.

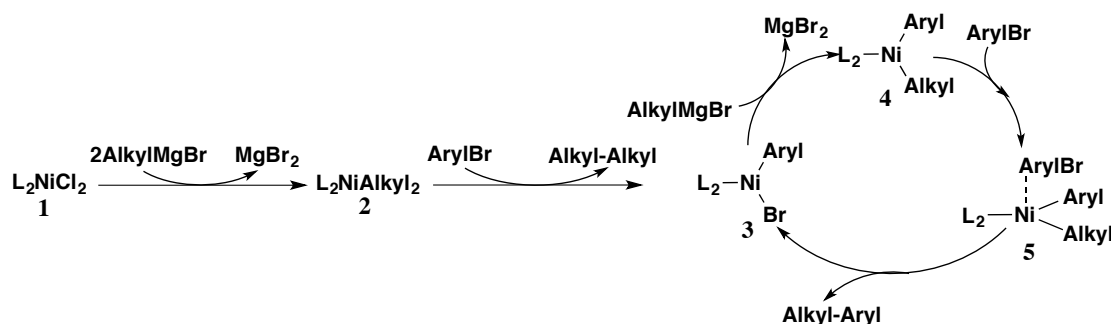
C8-C-inin was synthesised from dibrominated ININ using the **Scheme 5.3**. The reaction was performed using nickel-catalysed Kumada coupling, which was first reported by Kiso *et al.* [141] This reaction allows formation of carbon-carbon σ -bonds *via* reaction of aromatic halides with aliphatic Grignard reagents (or *vice versa*).



Scheme 5.3. Synthesis of C8-C-inin.

We used Ni(dppp)Cl₂ complex as a catalyst in this reaction as it was previously reported to be successful for a similar type of reactants. [142] The catalytic cycle for this reaction was proposed by M. Kumada [143], and is shown on the **Scheme 5.4**. The first step is reaction of dihalodiphosphenickel (1) with a Grignard reagent to form complex 2 which is then converted into complex 3 *via* reaction with aryl bromide. The nickel catalytic cycle in this reaction is slightly different from Pd catalytic cycle (demonstrated in the section 4.2.1). However, some of the steps are similar, *e.g.* transmetalation of the intermediate complex 3 into complex 4. The cross-coupling product is produced from intermediate 4 *via* attack of organic halide and

formation of pentacoordinated complex. The reductive elimination from complex 5 could also yield the Aryl-Aryl compound, but this process is thermodynamically unfavourable with an appropriate catalysts. [144] Nonetheless, the mechanism depicted on **Scheme 5.4** is not necessarily absolutely correct since there is still a debate about nickel oxidation state transitions during the reaction. [144][143]



Scheme 5.4. Kumada cross-coupling reaction mechanism. [143]

For our synthesis we used THF as a solvent due to poor solubility of brominated ININ derivative in diethyl ether. We observed full conversion of starting material into di-alkylated derivatives and a small amount of mono-alkylated compound (determined by TLC). We tested several methods for purification of C8-C-inin; however, the yield after purification was always low (~12%). We believe that low yields of ININ derivatives after purification could be due to light sensitivity of the molecule on silica gel. The majority of the material that was put on the column was visibly oxidized and retained by a column; thus, only small portion of the necessary compound could be separated. We tried purifying the material on basic alumina column, however, this didn't result in good separation of mono- and di-substituted derivatives. We have also tested sublimating this compound; however, the attempts were unsuccessful. After purification of C8-C-inin on a silica gel column, we used recrystallization to obtain the material that was further used for the experiments. Interestingly, the crystallization from different solvents resulted in formation of different polymorphs which will be discussed in Chapter 6.

5.2.2 Photophysics of ININ derivatives in solutions

5.2.2.1 Steady state spectroscopy, DFT calculations and Frank-Condon analysis

We started studying photophysics of ININ derivatives by using steady state absorption and photoluminescence. **Figure 5.2** collects absorption and emission spectra of ININ derivatives. The absorption spectra exhibit fine structure due to overlap of several close lying excited states, according to DFT calculations (details in section 3.5). The spectral values and results of DFT

calculation are summarized in **Table 5.1** and **Table 5.2**, respectively. The relative values of oscillator strength are in a good agreement with experimentally determined extinction coefficients. Oscillator strength of S_0 - S_1 transitions are between 0.28 – 0.48 suggesting that the S_0 - S_1 transition has π - π^* nature. The S_0 - S_1 and S_0 - S_2 transitions have approximately the same energy in all the molecules. Thus, alkyl chains have no significant influence on the excited state energies. Substitution of ININ core with phenyl moiety results in a blueshift in Ph-N-inin absorption and emission spectra. Phenyl substituents of Ph-N-inin have a poor orbital overlap with ININ core in solution, which would prevent it from significantly influencing absorption and emission spectra, unlike in the case of alkyl substituents. The difference in the shape of the absorption spectra between alkylated derivatives and Ph-N-inin is due to a change of the oscillator strength distribution between S_0 - S_1 and S_0 - S_2 transitions. For C8-C-inin, the oscillator strength of S_0 - S_2 transition is almost twice higher than S_0 - S_1 , whereas in Ph-N-inin these values are equal.

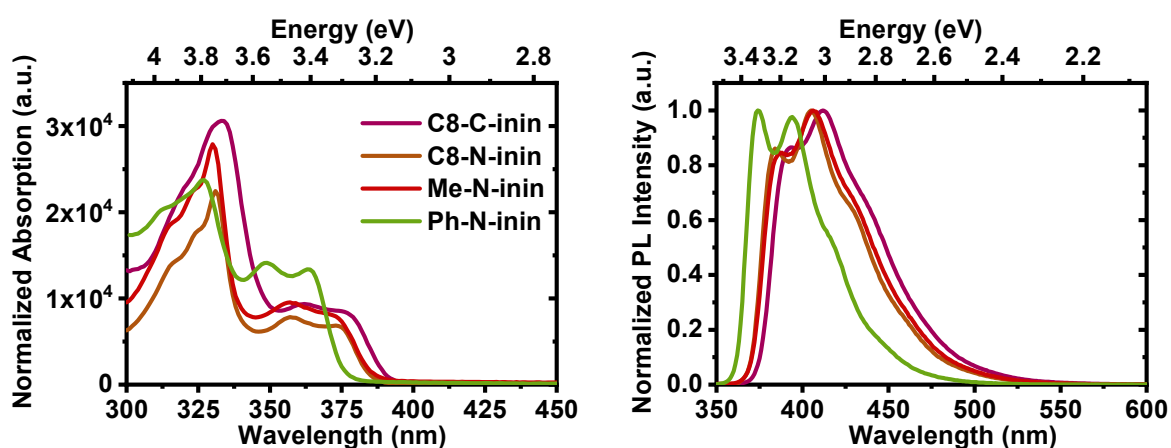


Figure 5.2. Absorption (left) and steady state photoluminescence spectra ($\lambda_{\text{ex}} = 330 \text{ nm}$) (right) of ININ derivatives in toluene ($10 \mu\text{M}$).

Absorption and emission are not dependent on solvent polarity (**Figure 5.3**) and they are not affected by concentration of the molecules in any of the tested solvents in the range of concentrations from 1 to $100 \mu\text{M}$ (**Figure 5.4**). This agrees with DOSY NMR results on C8-N-inin in toluene, monitoring the peak at 7.01 ppm allowed us to conclude that the value of diffusion coefficient is $2 \cdot 10^{-9} \text{ m}^2/\text{s}$ and it is the same in $10 \mu\text{M}$ and 9 mM solutions.

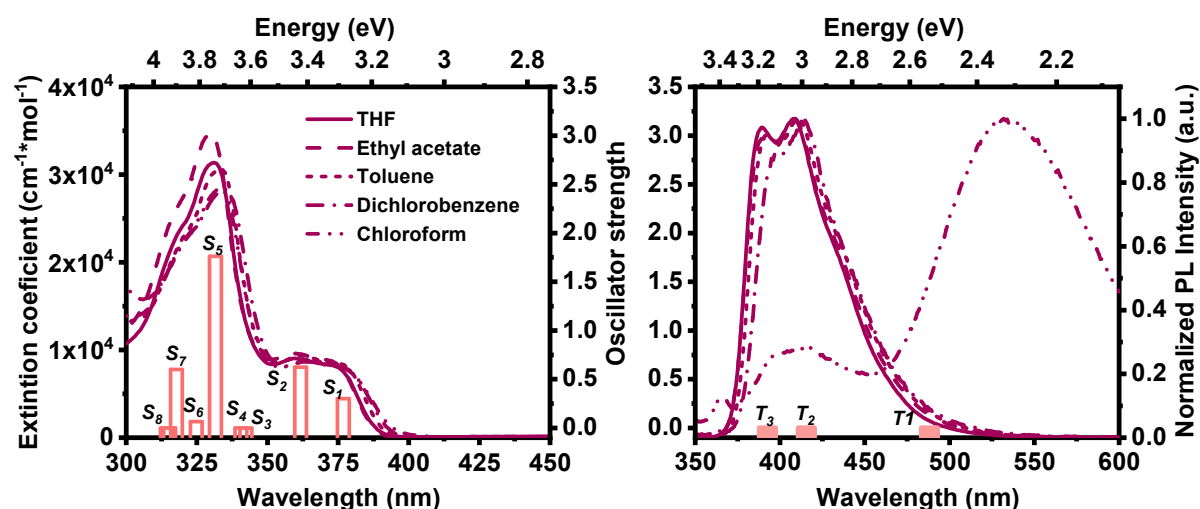


Figure 5.3. Absorption (left) and room temperature steady state fluorescence (right) of C8-C-inin in different solvents, $\lambda_{\text{ex}}=330\text{nm}$. Bars represent results of DFT calculations, the results were shifted by +70 nm.

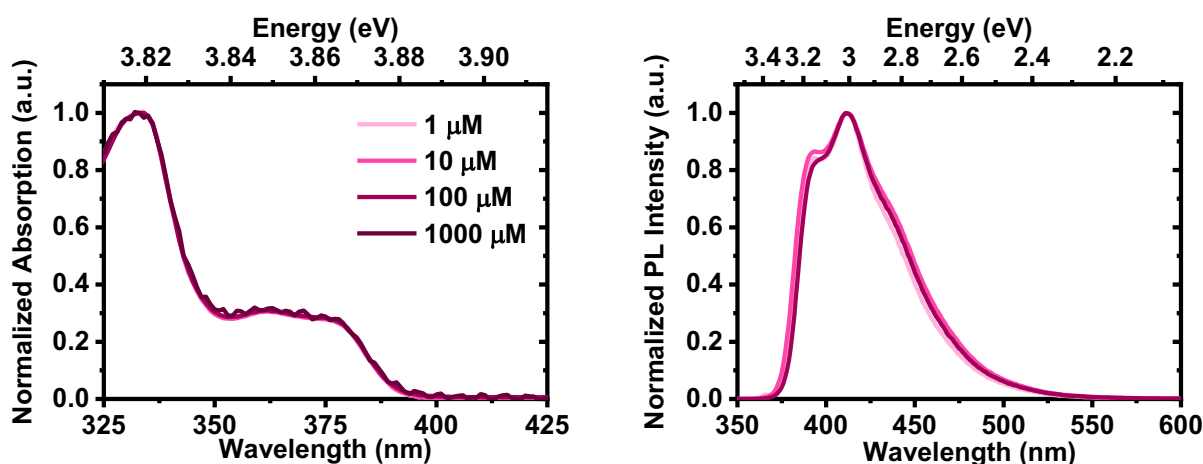


Figure 5.4. Concentration effects on absorption and steady state PL of C8-C-inin in toluene.

The fluorescence is excitation wavelength independent and originates from the lowest lying S_1 excited state (Figure 5.5). The energy of emission does not change significantly with solvent polarity (except in chloroform, which will be discussed separately). The efficiency of emission (Table 5.3) is high in all the molecules, with no dependence on presence of air that can be determined beyond the error of the measurement. The Stokes shift is very small (0.13 – 0.14 eV), which suggests very small change in the geometry between ground and excited states of the molecules. This should also be reflected in reorganization energy. To estimate the reorganization energy, we performed Frank-Condon analysis using a single effective (mean) vibration. The results are presented in the Table 5.4. The fit of Frank-Condon function,

equation (2.13), is shown in **Figure 5.6**. Huang-Rhys parameter of the alkylated ININ derivatives was found to be slightly higher than that of Ph-N-inin, suggesting a slightly stronger coupling to vibrations and higher reorganization energy in alkylated derivatives. The reorganization energy is related to a displacement of potential energy surfaces during relaxation of excited states (section 2.2.3). Therefore, this displacement is smaller for Ph-N-inin. The emission spectrum of Ph-N-inin is dominated by 0-0 vibrational peak, whereas in the case of alkylated derivatives transition to higher vibrational level is more pronounced. The values of the reorganization energies are in the range of those that are usually found for similar heteroacene molecules in solutions. [98] Interestingly, the reorganization energy values are lower than those found for BTBT derivatives (220-289 meV) suggesting more rigid internal structure of the molecules.

Table 5.1. Results of DFT calculations on ININ molecules in toluene.

State	C8-C-inin		C8-N-inin		Me-N-inin		Ph-N-inin	
	Energy (eV)	Oscillator strength	Energy (eV)	Oscillator strength	Energy (eV)	Oscillator strength	Energy (eV)	Oscillator strength
S1	4.02	0.3000	4.05	0.2900	4.05	0.2960	4.10	0.4750
S2	4.38	0.6230	4.45	0.4440	4.46	0.4640	4.45	0.4750
S3	4.94	0	4.90	0	4.96	0	4.56	0.0010
S4	5.00	0	5.07	0	5.09	0	4.75	0.2750
S5	5.33	1.7610	5.32	1.6170	5.34	1.6690	4.86	0.0160
S6	5.60	0.0650	5.74	0.0240	5.68	0.0370	4.90	0.0460
S7	5.91	0.6010	5.99	0.4860	6.01	0.4670	5.05	0
S8	6.03	0	6.04	0	6.13	0	5.29	0.0020
T1	2.96	0	2.98	0	2.98	0	3.02	0
T2	3.59	0	3.71	0	3.72	0	3.75	0
T3	3.84	0	3.87	0	3.89	0	3.83	0
T4	4.24	0	4.28	0	4.29	0	3.95	0
T5	4.33	0	4.43	0	4.45	0	4.02	0
T6	4.53	0	4.60	0	4.61	0	4.34	0
T7	4.64	0	4.61	0	4.61	0	4.43	0
T8	4.76	0	4.75	0	4.74	0	4.45	0

Table 5.2. Photophysical characterization of C8-C-inin in different solvents (onsets values).

Solvents	S_0-S_1 , eV	ϵ (max), $\text{cm}^{-1}\text{M}^{-1}$	ϵ (S_0-S_1) $\text{cm}^{-1}\text{M}^{-1}$	S_1-S_0 , eV ($\lambda_{\text{ex}} = 330$ nm or 3.75 eV)	Stokes shifts, eV
Ethyl Acetate	3.19	34520	8660	3.32	0.13
THF	3.19	31380	8140	3.33	0.14
Toluene	3.17	30560	8450	3.31	0.14
DCB	3.14	28300	7980	3.28	0.14
CHCl_3	3.14	28320	8040	-	-

S_0 – ground state, S_1 – first singlet state

ϵ – extinction coefficient

λ_{ex} – excitation wavelength

Stokes shift – determined as a difference between the 0-0 vibronic peaks.

Table 5.3. Photophysical characterization of ININ derivatives in toluene (10 μM).

Molecule	S_0-S_1 , eV	ϵ (S_0-S_1) $\text{cm}^{-1}\text{M}^{-1}$	S_1-S_0 , eV ($\lambda_{\text{ex}} = 330$ nm or 3.75 eV)	Stokes shifts, eV	PLQY ($\lambda_{\text{ex}} = 350$ nm or 3.54 eV), %	PLQY deoxygenated, %
C8-C-inin	3.17	8430	3.31	0.14	102±20	87±11
C8-N-inin	3.21	6850	3.36	0.15	58±10	62±23
Me-N-inin	3.20	8080	3.35	0.15	100±20	91±15
Ph-N-inin	3.30	13320	3.43	0.13	100±16	93±16

Table 5.4. Frank-Condon analysis results (using equation (2.13)).

Molecule	Huang-Rhys parameter	Vibration, meV	Broadening	Reorganization energy, meV
C8-C-inin	1.27	171	0.074	217
C8-N-inin	1.27	170	0.069	216
Me-N-inin	1.29	171	0.073	221
Ph-N-inin	1.07	168	0.065	180

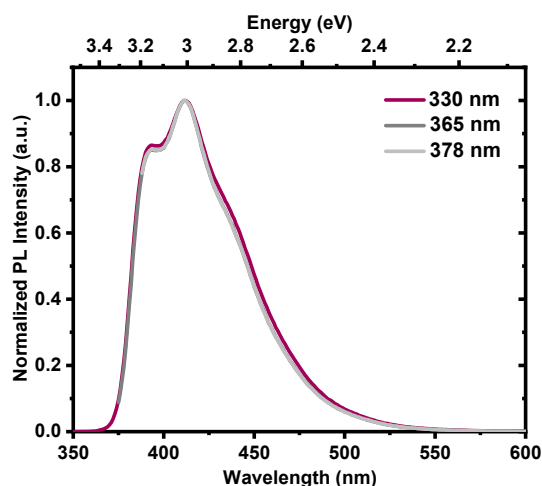


Figure 5.5. Steady state emission of C8-C-inin (10 μ M) in toluene excited at different wavelengths.

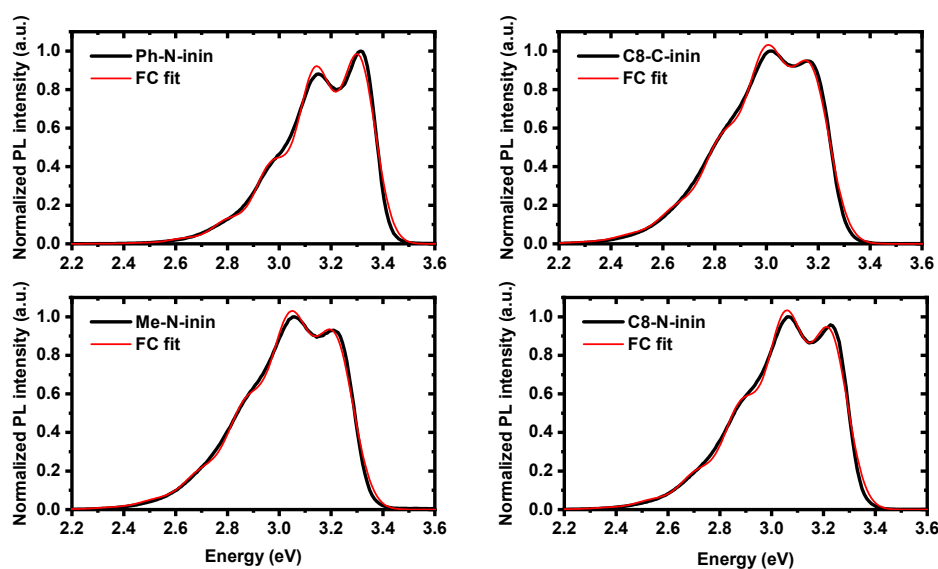


Figure 5.6. Frank-Condon fitting results for ININ derivatives in 10 μ M toluene solutions.

5.2.2.2 Cyclic voltammetry

To estimate HOMO and LUMO energy levels of these molecules we performed CV experiments, and the results are presented in **Figure 5.7** and **Table 5.5**. Details of the experiment and calculations of HOMO and LUMO are presented in section 3.3.1. The CV results suggest that ININ derivatives undergo two sequential oxidation processes. The oxidation occurs on the forward positive sweep and correlates with HOMO energies of the molecules. This process is not fully reversible in ININ derivatives, because the ratio of the anodic to cathodic current is less than 1. However, this could also be due to adsorption of the material to the surface of the working electrode. The second peak on the forward sweep corresponds to a second oxidation and this process is irreversible for all ININ derivatives.

We determined the oxidation potential of the molecules using the onsets of oxidation waves. The oxidation potentials provide an information on the electron donating abilities of the molecules. We conclude that C8-C-inin is the most easily oxidized and, hence, it has the shallowest HOMO energy. This is due to presence of two additional alkyl chains in the structure of the C8-C-inin, which evidently have electron donating effect to aromatic core that results in increase in HOMO level. C8-N-inin and Me-N-inin have the same HOMO energy, which suggests that the second (and further) carbon atom in the alkyl chain have no effect on the aromatic system. Ph-N-inin has the lowest HOMO out of all the ININ derivatives. This is in line with the blueshift that is observed in steady state absorption and emission.

Finally, the LUMO energy can be estimated, which, of course, is a significant assumption considering we have to use optical bandgap. Since the optical bandgap value also includes an exciton binding energy, the obtained LUMO energy values can hardly be treated as absolute. However, they could be discussed relative to each other. Thus, Ph-N-inin has the lowest LUMO, and the alkylated derivatives have roughly the same LUMO energy.

Overall, we conclude that all of these heterocycles are electron-rich, and are good candidates for hole transporting materials. C8-C-inin is, probably, the most promising molecule for such applications due to the shallowest HOMO level.

Table 5.5. Cyclic voltammetry results and estimation of HOMO/LUMO energy levels of ININ derivatives.

Compound	E_{ox} , V	E_g optical, eV	HOMO, eV	LUMO, eV
1st oxidation potential				
Me-N-inin	0.260	3.18	-4.86	-1.69
C8-C-inin	0.182	3.14	-4.76	-1.63
C8-N-inin	0.260	3.17	-4.84	-1.67
Ph-N-inin	0.345	3.30	-5.03	-1.73
2nd oxidation potential				
Me-N-inin	0.850		-5.45	
C8-C-inin	0.860		-5.44	
C8-N-inin	0.959		-5.54	
Ph-N-inin	0.975		-5.65	

E_{ox} – onset of an oxidation wave

E_g – optical band gap

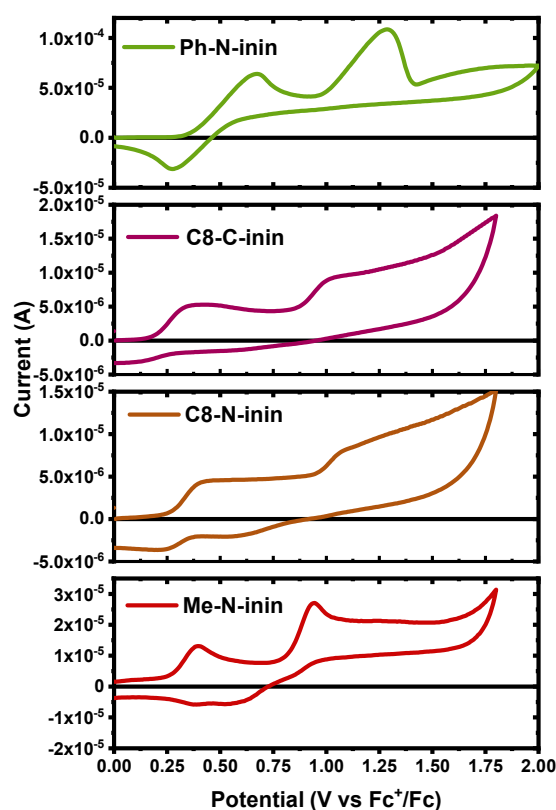


Figure 5.7. Cyclic voltammogram of ININ derivatives taken with scan rate 50 mV/s.

5.2.2.3 Fluorescence and phosphorescence at 77 K

To characterize triplet states of the molecules, we performed photoluminescence experiments at 77 K. At 77 K the non-radiative decay processes become less efficient and, thus, it is possible to observe phosphorescence. Unfortunately, we could not observe phosphorescence of these molecules using the phosphorescence mode available on fluorimeters. This is why we used a gated ICCD camera; spectra were recorded at large time delay ($\sim 100 \mu\text{s}$) after excitation using large gate time ($\sim 750 \text{ ns}$) and exposure ($\sim 1 \text{ s}$). The results of experiments at 77 K are collected in **Figure 5.8**. Panels on the left show absorption spectra of ININ derivatives in ethanol:diethyl ether (1:1) at the room temperature. This solvent mixture was chosen because it freezes into transparent glass. The fluorescence spectra at 77 K are collected in the middle panels, we can see that vibronic structure becomes more pronounced at 77 K.

The panels on the right show phosphorescence spectra of the molecules. The S-T gap was determined from these spectral data using onsets of the fluorescence and phosphorescence. The results are presented in **Table 5.6**. The values of singlet-triplet splitting are larger than 0.7 eV for all the molecules.

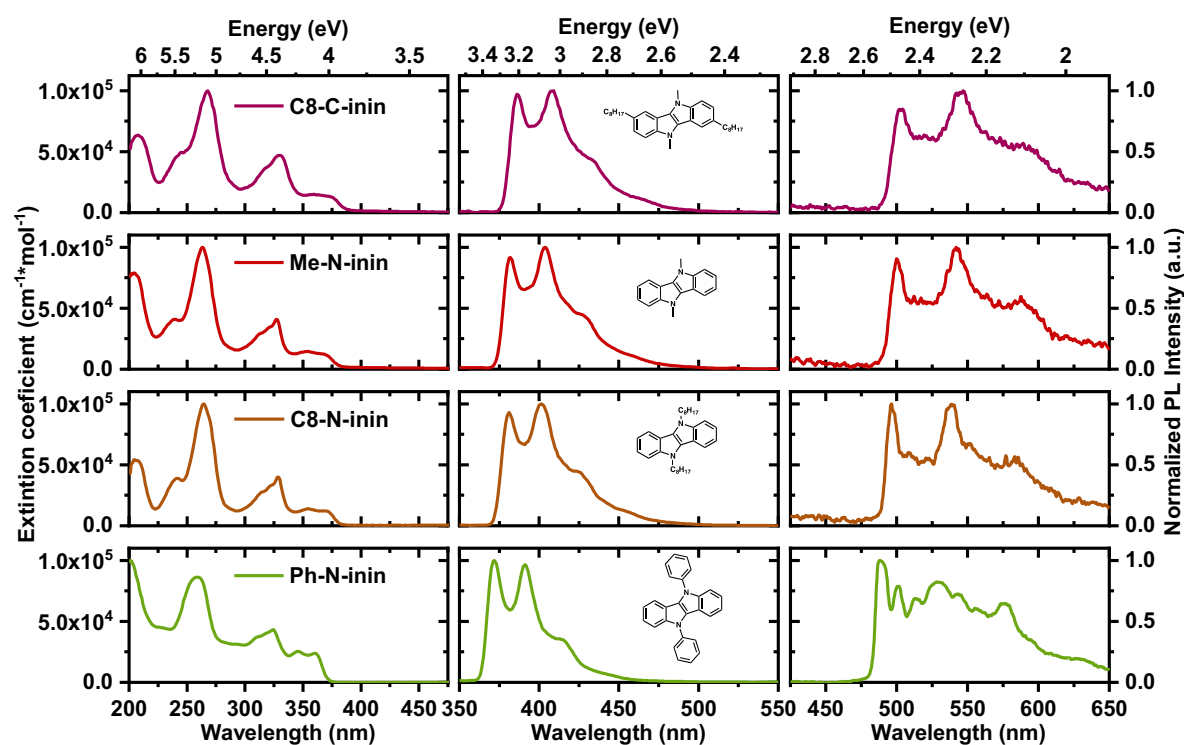


Figure 5.8. Absorption (left), fluorescence (middle) and phosphorescence (right) at 77 K of 100 μ M solutions in ethanol : diethyl ether (1:1), $\lambda_{\text{ex}} = 330\text{nm}$.

Table 5.6. Photophysical characterization of ININ derivatives in ethanol : diethyl ether (onset values).

Molecule	S_0 - S_1 , eV	ϵ (S_0 - S_1) $\text{cm}^{-1}\text{M}^{-1}$	S_1 - S_0 , eV ($\lambda_{\text{ex}} = 330\text{ nm}$)	Stokes shift, eV	T_1 , eV	S_1 - T_1 , eV
C8-C-inin	3.19	13565	3.29	0.1	2.53	0.76
C8-N-inin	3.25	12445	3.33	0.08	2.54	0.79
Me-N-inin	3.24	12342	3.31	0.07	2.53	0.78
Ph-N-inin	3.32	23514	3.41	0.09	2.57	0.84
Br-C-inin	3.10	9456	3.2	0.1	2.49	0.71

5.2.2.4 Time-resolved spectroscopy

The next step in our study was to characterize kinetics of singlet decay and ISC rate. We know that fast rate of ISC in BTBT derivatives is not due to “heavy atom effect”, but rather because of the structural properties of these molecules. Giving the similar structure of ININ molecules we naturally wondered if that would result in rapid ISC in ININ derivatives.

The kinetic profiles of ININ derivatives' emission monitored at 420 – 430 nm (2.88 – 2.95 eV) are collected in **Figure 5.9**. All numeric results of kinetic studies are collected in **Table 5.7**. The decay has two components: prompt and delayed. Prompt emission decay is mono exponential and has time constant of 3 – 9 ns (depending on measurement conditions, *e.g.* degassed / non-degassed). We assign this decay to singlet excited state relaxation.

Interestingly, the prompt component decay rate of Ph-N-inin is higher than for the rest of the derivatives. This is due to a faster rate of ISC which was confirmed by transient absorption (TA) (**Figure 5.10**). After excitation of Ph-N-inin in TA spectra we observe two signals: stimulated emission (positive peak at 3.1 eV) and singlet photoinduced absorption (broad negative signal with maximum at 2.6 eV). Both of these signals decay with monoexponential kinetics, this is followed by evolution of negative peak at 3.1 eV with isosbestic point at 3 eV. We assign this peak to triplet state photoinduced absorption (PIA), the presence of isosbestic point indicates one-to-one conversions between singlet and triplet states. We confirm singlet signal assignment by comparing the decay time constant of the peak at 2.6 eV with the prompt component decay obtained by ICCD (**Table 5.7**).

Thus, we conclude that faster decay of prompt singlet emission in Ph-N-inin is due to faster ISC compared to the rest ININ derivatives. To explain this difference and to further understand the excited state behaviour of the ININ derivatives, we performed the computational excited state analysis (using DFT, details in 3.5.1) to determine how exactly the electron density on the molecule changes upon excitation. The results of analysis are summarised in **Figure 5.11** and **Figure 5.12**.

From the **Figure 5.12**, we can conclude that the ISC in Ph-N-inin probably occurs between the first singlet state S_1 at 4.11 eV (calculated value) and a degenerate triplet state at 4.02 eV (calculated value). From the DFT calculations (computational excited state analysis **Figure 5.12**), we understand that in Ph-N-inin electron density of S_1 state is mostly located on the perimeter of the molecule, whereas the triplet electron (T_5 , 4.02eV) density is mostly located on phenyl substituent. Thus, they are located on different parts of the molecule, unlike in the rest of ININ derivatives, where singlet and triplet electron density are located on the same parts of the molecules. During ISC in Ph-N-inin a significant change in orbital angular momentum occurs as well as the change of spin. Thus, resulting in efficient preservation of total angular momentum and rapid rate of ISC, which we observe in TA.

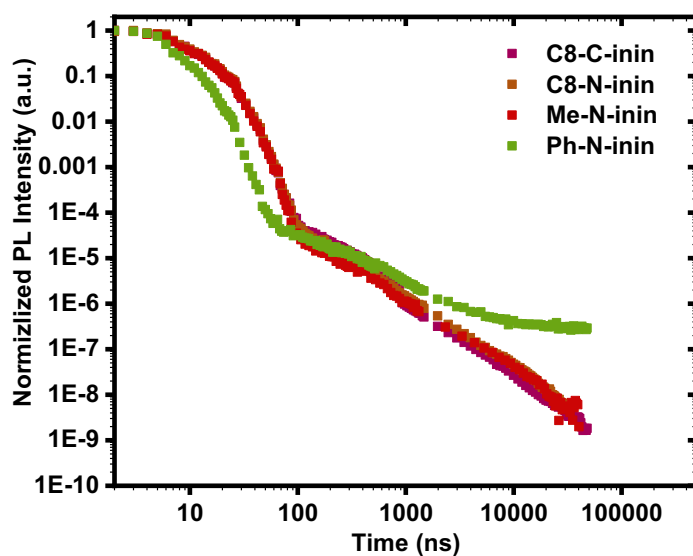


Figure 5.9. Kinetic profile of the emission detected at 420-430nm in ethanol:diethyl ether (1:1), $\lambda_{\text{ex}} = 355\text{nm}$. Instrument response is 2 ns.

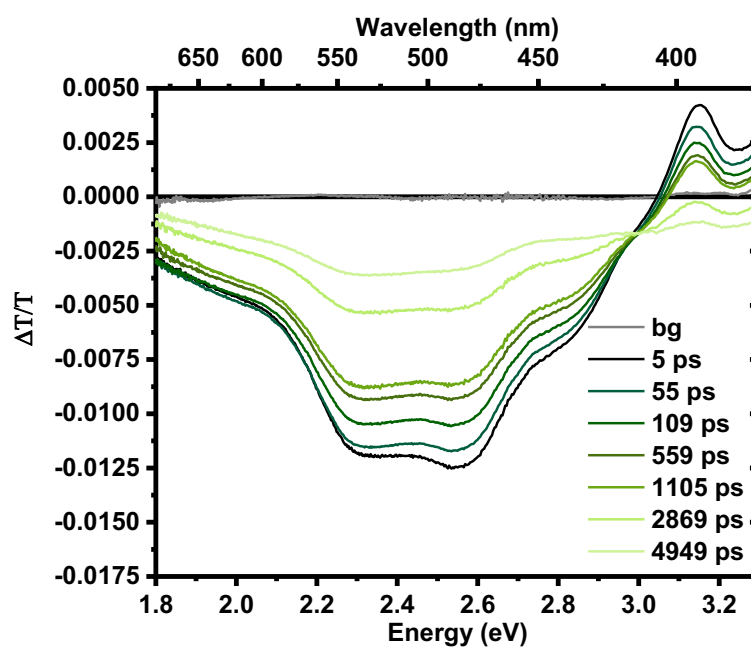


Figure 5.10. Transient absorption spectra of Ph-N-inin in toluene, $\lambda_{\text{ex}} = 355\text{ nm}$. bg stands for background.

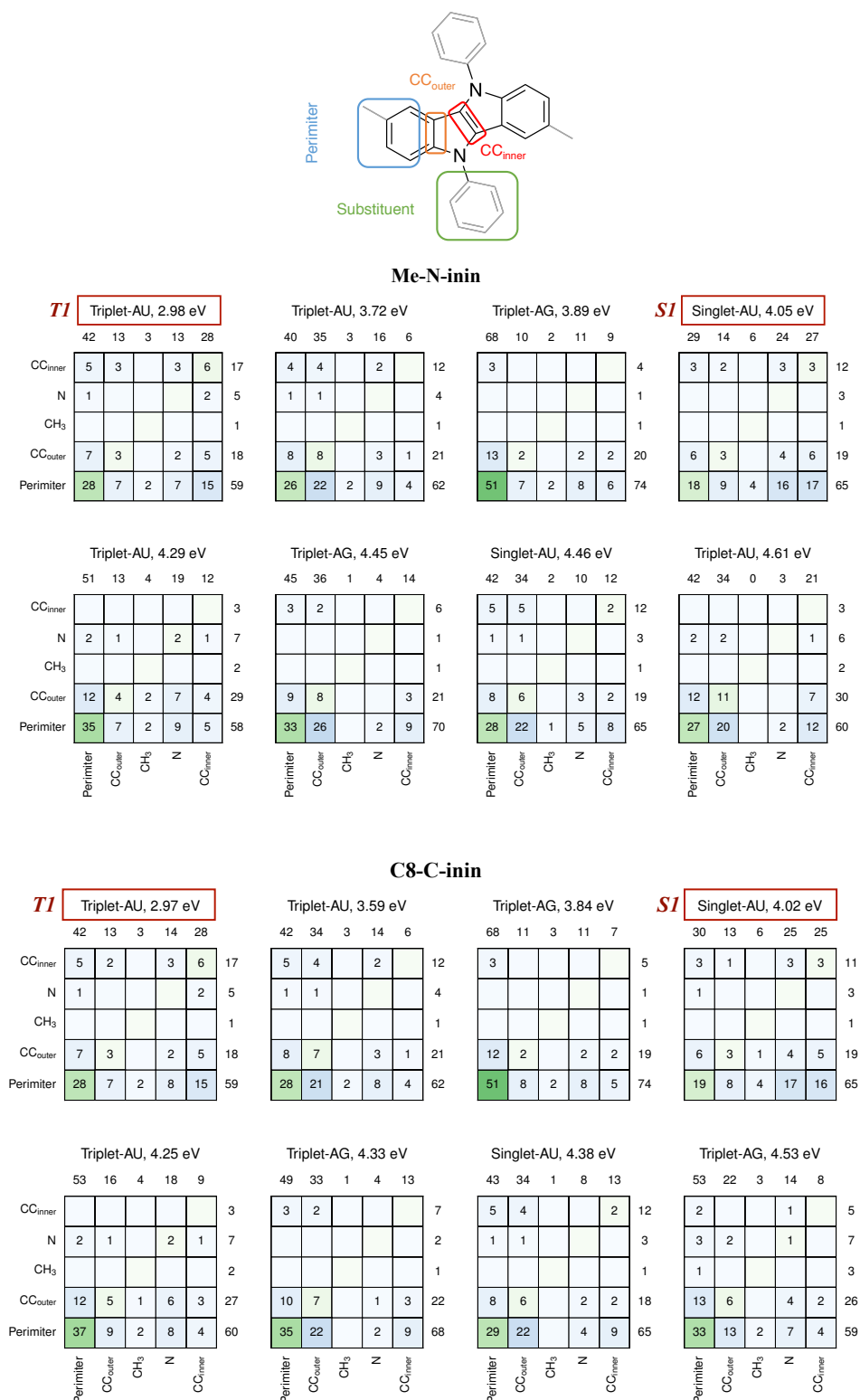


Figure 5.11. Part 1. Computational excited state analysis. The diagrams can be read as follows: The x axis indicates the location that the electron came from (i.e. the hole). The y axis indicates the electron goes to. The numbers show the percentage contribution of that hole-electron pair to the total excitation. The numbers at the end of the rows/columns are the sums of those rows/columns.

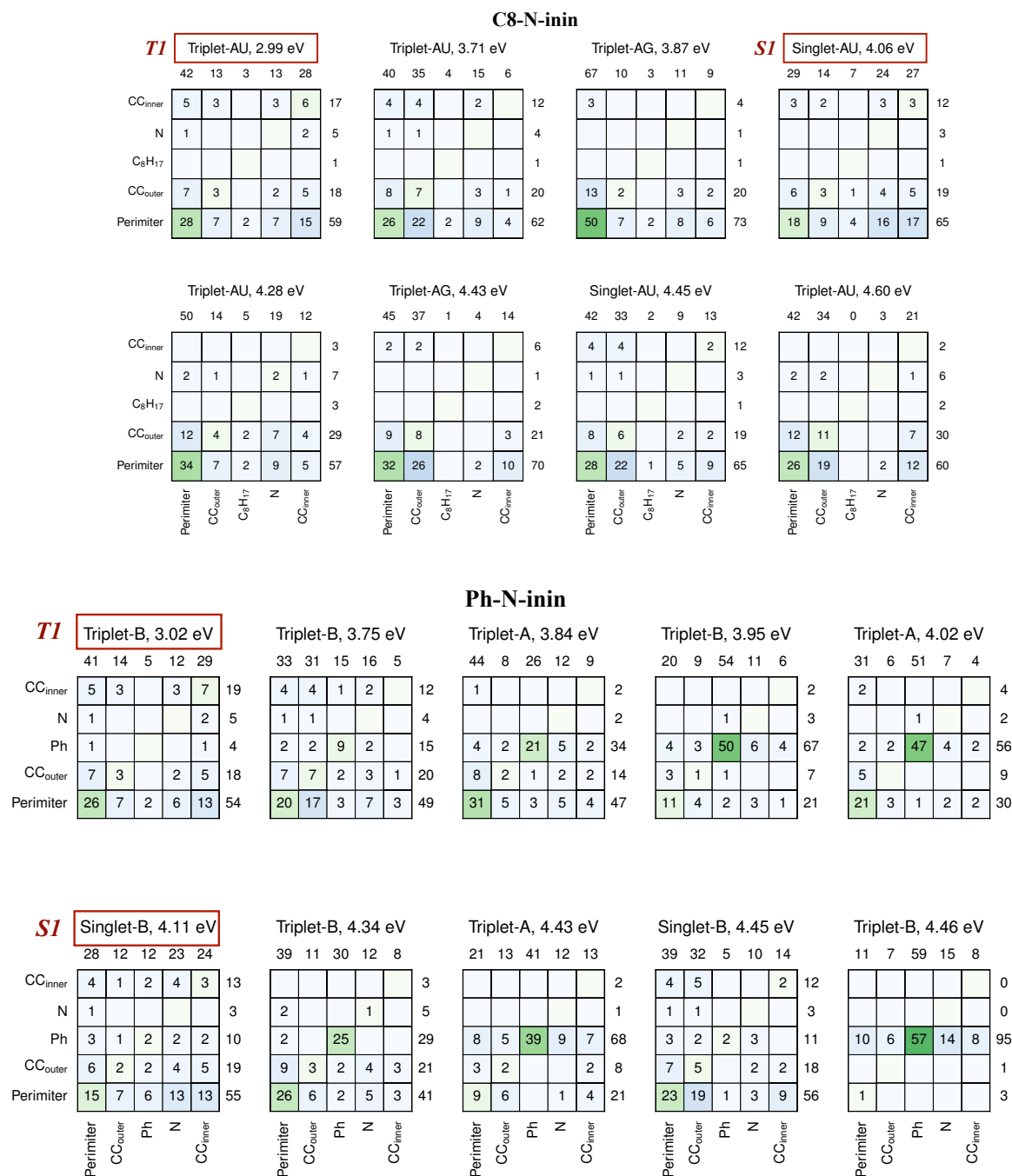


Figure 5.12. Part 2. Computational excited state analysis. The diagrams can be read as follows: The x axis indicates the location that the electron came from (i.e. the hole). The y axis indicates the electron goes to. The numbers show the percentage contribution of that hole-electron pair to the total excitation. The numbers at the end of the rows/columns are the sums of those rows/columns.

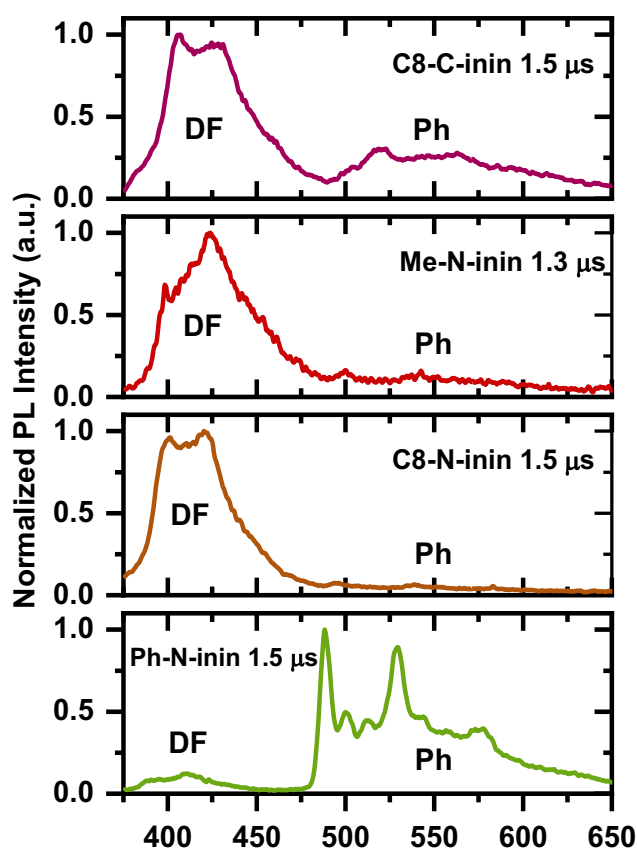


Figure 5.13. Spectra of ININ series in ethanol:diethyl ether (1:1) at 77 K taken at time period of 1.3-1.5 μ s, $\lambda_{ex} = 355$ nm. DF -delayed fluorescence, Ph – phosphorescence. Only Ph-N-inin exhibits meaningful phosphorescence at 1.5 μ s

The explanation of second (delayed) component of emission (**Figure 5.9**) is not straightforward. This emission in all the studied molecules has a complex kinetics that cannot be described by an exponential function.

Figure 5.13 shows spectra of ININ derivatives emission at 1.3 – 1.5 μ s after excitation. It is clear that delayed emission does not correspond to phosphorescence as they are well separated in energy. In alkylated derivatives, emission spectra at 1.3 – 1.5 μ s is dominated by emission at 375 – 450 nm, whereas in Ph-N-inin it is dominated by phosphorescence (due to faster rate of ISC). **Figure 5.14** compares the spectra of prompt and delayed luminescence in C8-N-inin solutions. The delayed emission has the same energy as initial singlet state emission at both 77 K and room temperature; however, it is narrower than prompt emission spectra. At 77 K the delayed spectrum exhibits vibronic progression, suggesting the localized nature of the excited state.

It is quite unusual for a singlet state emission to be observed on microsecond time scale, because singlet states normally decay with a time constant of less than ~ 10 ns. For delayed emission to be observed singlet state must be populated from a different much longer-lived state, *e.g.* triplet state. Further, we discuss possible origins of delayed emission and describe our effort to identify the cause of the delayed emission in ININ derivatives.

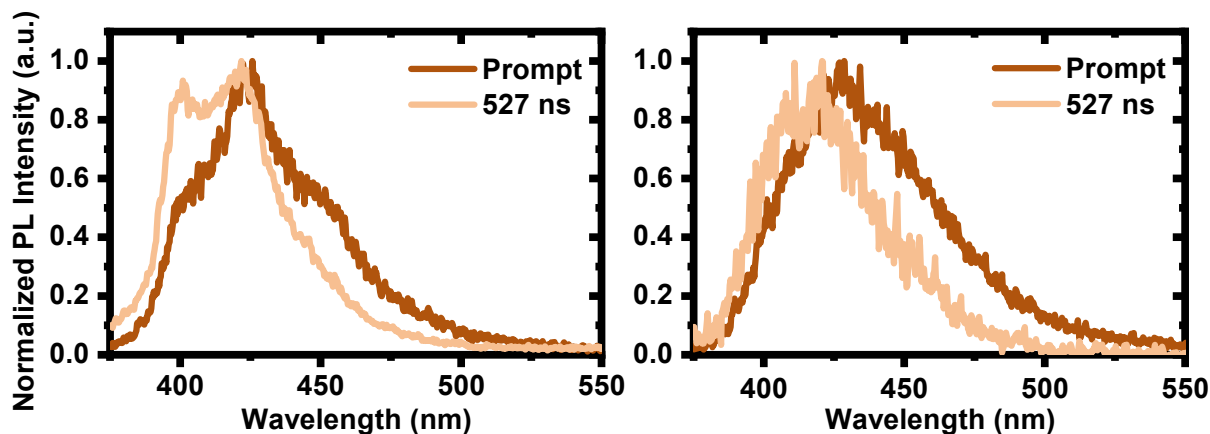


Figure 5.14. Prompt and delayed luminescence spectra of C8-N-inin (100 μM) at 77 K (left) and at room temperature (right).

Delayed emission is not a unique phenomenon. It has been observed in many systems, and can be efficiently utilized in organic electronic devices, *e.g.* in OLEDs. [120][145][146] From the literature we know that delayed emission can have several origins:

- Triplet-related delayed emission:
 - Thermally activated delayed fluorescence (TADF) [147][148]
 - Upper state crossing [149][150][151]
 - Triplet-triplet annihilation. [152][153]
- Photoinduced electron transfer (formation of excimer or exciplex) and delayed emission as a result of electron and radical ion (or two charged moieties with an opposite charge) recombination. [112][113][154][155]

5.2.2.5 Power dependence

The dependence of the delayed emission on the excitation power could indicate the information on origin of the delayed emission, *i.e.* if it is a result of the recombination of two excited states (quadratic power dependence) or it is a result of intrinsic dynamics of a single excited state (linear power dependence). The result of the test is presented on **Figure 5.15**. We

can see that the dependence is linear. This means that delayed emission cannot be attributed to triplet-triplet annihilation, which would require two excited states to recombine.

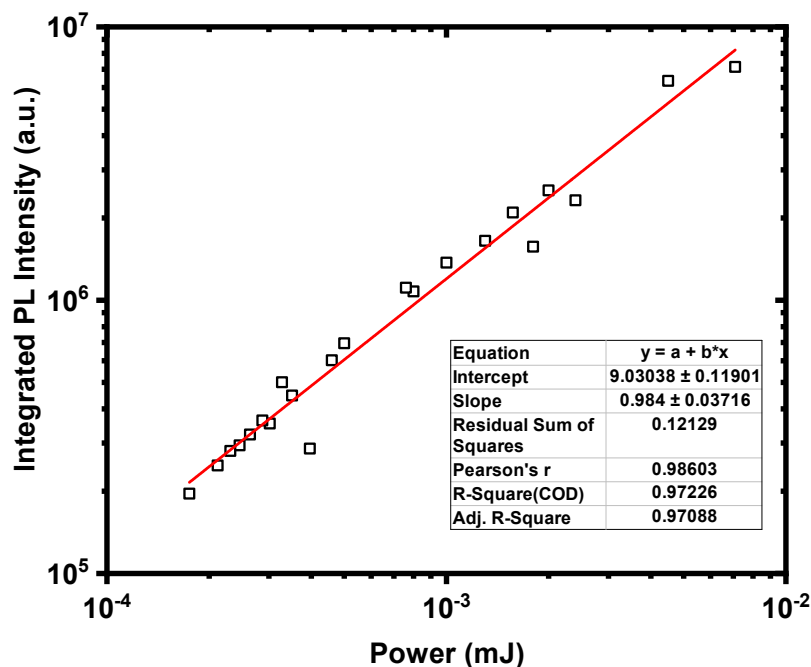


Figure 5.15. Power dependence of integrated delayed emission (collected at time-delay 200 ns) of C8-N-inin in deoxygenated solution at room temperature (no phosphorescence is observed), $\lambda = 355$ nm.

5.2.2.6 Is population transfer from triplet to singlet state possible in ININ derivatives?

The next step was to determine if the delayed emission originates from triplet states, *e.g.* be some sort of thermally activated delayed fluorescence (TADF) or hot-triplet state delayed fluorescence. Both of these processes have linear power dependence. TADF mechanism requires small energy gap between first singlet and first triplet states, as well as strong spin-vibronic coupling between the states. [147] In the case of ININ derivatives, a direct TADF mechanism is probably not possible because of the large singlet-triplet gap of ~ 0.7 eV. However, alternative mechanism that involves higher lying triplet state and first singlet state is feasible. [149][150][151] This mechanism does not require small singlet-triplet energy gap, but a strong coupling within the triplet manifold is essential. [156] It has also been shown to occur between states that do not have charge-transfer character. [150] Therefore, it could possibly be the cause of the delayed emission in ININ derivatives.

To test if singlet delayed emission is related to triplet state, we compared emission in presence of oxygen and in deoxygenated solution. Oxygen is efficient triplet quencher, the interaction of triplet state and ground state oxygen results in formation of a collision complex. This complex follows either non-radiative decay path or facilitates singlet oxygen formation, both of these processes result in triplet state deactivation. Thus, if the delayed luminescence takes its origin from triplet state, interaction with oxygen should decrease its lifetime. The experiment was performed on C8-C-inin in toluene solution (**Figure 5.16**). We can see that the delayed emission is not significantly affected (although, normalized intensity is somewhat lower than in degassed solution). However, the prompt part becomes shorter lived by approximately 46%.

Both singlet and triplet state can interact with oxygen. Interaction of a singlet (or triplet) with oxygen can follow two principle pathways: energy transfer to produce singlet oxygen (reaction with singlet oxygen can cause photooxidation) or spin-catalysed ISC. The possibility of energy transfer would depend on the energy splitting between singlet and triplet state (ΔST or the $T_1 - T_0$ energy gap) of the excited molecule. If these energy gaps are smaller than the energy gap between ground and excited state of oxygen (1.04 eV), energy transfer cannot occur, and the singlet oxygen cannot be formed.

Thus, we can conclude that the reduction in singlet state lifetime in the case of ININ derivatives is either due to energy transfer to oxygen and formation of ground state ININ derivative or due to oxygen spin-catalysed ISC to form a triplet state on the ININ molecule and a ground state oxygen.

The lack of the oxygen dependence on delayed emission and the fact that the delayed emission has a shorter lifetime compared to phosphorescence suggests that is unlikely to be related to triplet states. [5][157]

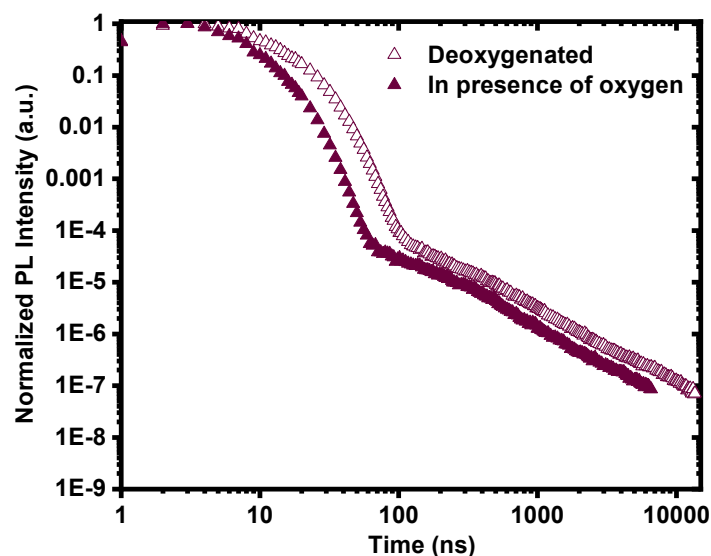


Figure 5.16. C8-C-inin in ethyl acetate (100 μM) taken at 420 – 430 nm, $\lambda_{\text{ex}} = 355\text{nm}$.

Instrument response is 2 ns.

To confirm our conclusion that the delayed emission is not related to ISC, we used one of the intermediate compounds Br-C-inin. This molecule has two bromines attached to the ININ aromatic system (**Figure 5.17**). The presence of the bromines in the proximity to the core and to the main site of electron density that is involved in transitions (“perimeter” from the excited state analysis, **Figure 5.11**) could speed up the ISC. If triplet states are involved in delayed emission, we would see a change in the kinetics of the delayed emission. We studied the photoluminescence and transient absorption of this molecule (**Figure 5.18** and **Figure 5.19**). With the same aim we performed transient absorption and photoluminescence study of Me-N-inin in iodobenzene (**Figure 5.20** and **Figure 5.22**). In this case iodobenzene creates an external “heavy atom effect” that can also influence ISC and triplet lifetime.

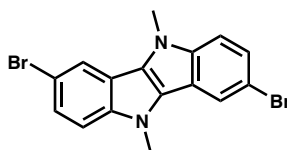


Figure 5.17. Chemical structure of Br-C-inin.

Let’s first consider the transient absorption of Br-C-inin in toluene (**Figure 5.18**). Excitation of the Br-C-inin solution is followed by rise of two signals in TA with peaks around 2.25 eV (negative) and 3 eV (initially positive). The peak at 3 eV corresponds to stimulated emission as it is at the same position as the fluorescence of Br-C-inin. We assign the negative peak at 2.25 eV to singlet excited state absorption; the decay time constant is 1.2 ns. As the singlet decays, we observe the change in the sign of the signal at 3 eV, which is due to ISC and the

emerging triplet excited state absorption. The transition exhibits an isosbestic point suggesting a one-to-one conversion of singlet to triplet states. The ISC time constant was determined to be 1.3 ns.

To confirm the signals assignment and to test the effect of heavy atom on delayed emission, we performed TRPL experiment (**Figure 5.19**). In **Figure 5.19** we compare decay of the singlet states of Br-C-inin and Me-N-inin (a close non-brominated analogue). We confirm the assignment of singlet excited state absorption in TA by comparing the decay constant of supposed singlet from TA with the prompt fluorescence decay obtained from TRPL (**Table 5.7**). The constants are 1.3 ns and 1.5 ns, respectively. Taking into account that time-response of our ICCD is 2 ns, we consider this result to be close enough to confirm the assignment.

From TRPL we can conclude that although the prompt PL decays significantly faster in Br-C-inin (1.5 ns) than in Me-N-inin (8.7 ns) (deoxygenated solutions), the delayed emission is still present and does not seem to be significantly affected.

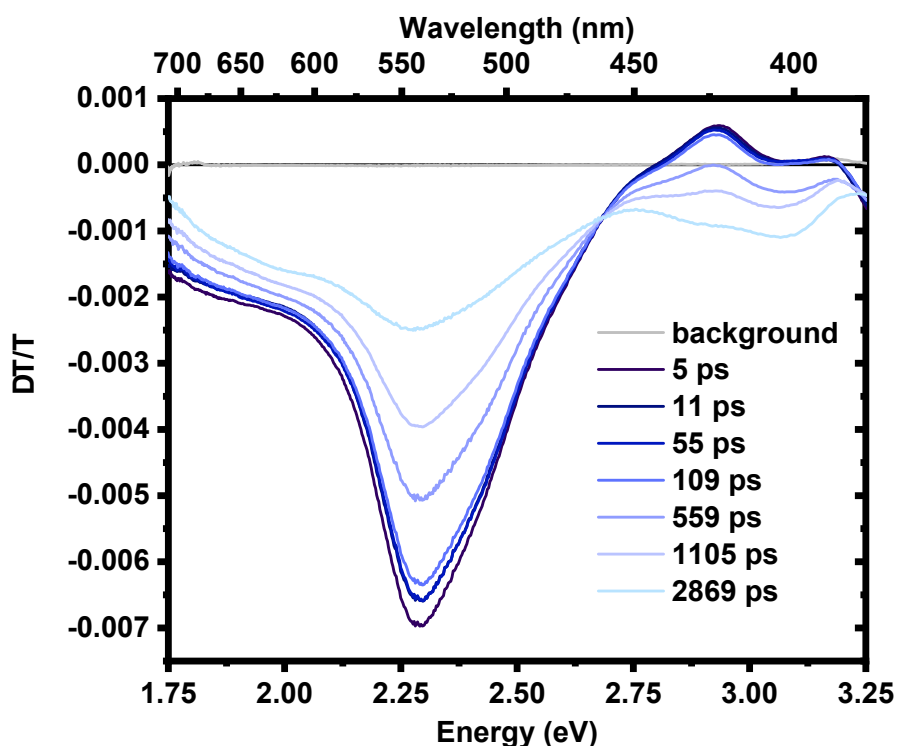


Figure 5.18. Transient absorption spectral evolution of Br-C-inin in toluene, $\lambda = 355$ nm.

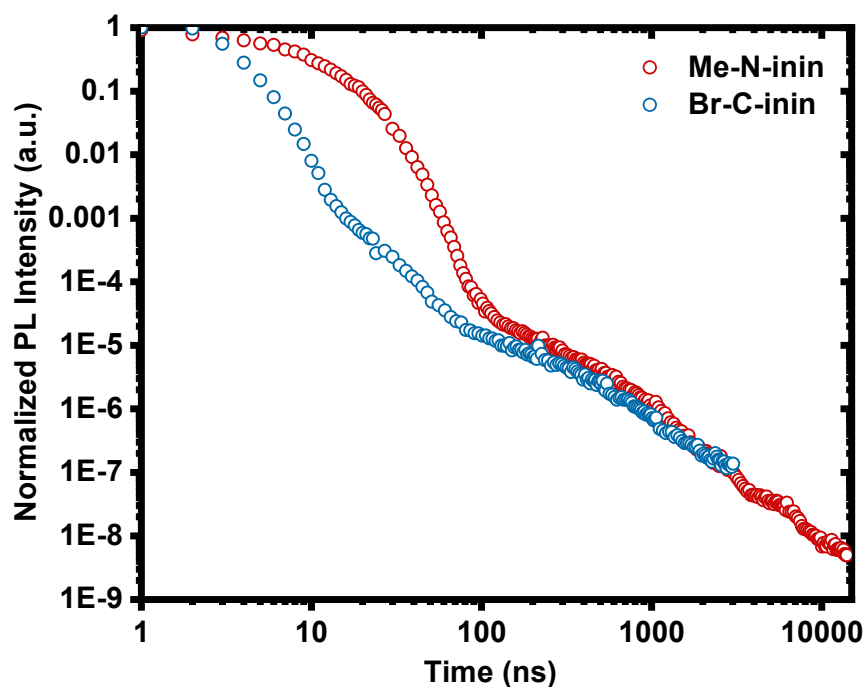


Figure 5.19. Kinetics of Br-C-inin and Me-N-inin in toluene taken at 420-430 nm, $\lambda_{\text{ex}} = 355$ nm.

Table 5.7. Transient absorption and photoluminescence results.

	TA		ICCD	
	τ (S ₁ -S _n), ns	τ (T ₁ -T _n), ns	τ (S ₁ -S ₀), ns	τ (S ₁ -S ₀) in argon, ns
Br-C-inin	1.2±0.1*	1.3±0.1*	1.5±0.1*	1.6±0.1*
Me-N-inin	5.9±2.4 ^{†*}	-	5.8±0.1 [‡]	8.4±0.1* 9.1±0.1 [†]
C8-N-inin	4.0±0.3*	-	5.4±0.1 [‡] 5.27±0.0*	8.1±0.1 [‡] 8.8±0.1 [†]
C8-C-inin	-	-	5.0±0.03 [‡]	9.1±0.0 [‡] 8.67±0.1 [†]
Ph-N-inin	3.3±0.1*	3.1±0.5*	-	5.04±0.1 [‡]

* in toluene

[‡] in toluene under argon

[†] at 77K

Next, we examine the TA of Me-N-inin in iodobenzene solution (Figure 5.20). The top panel of Figure 5.20 shows TA of Me-N-inin in toluene. There are only two signals in TA: 2.35 eV (negative), which we assign to the singlet excited state absorption and the positive signal

at 3 eV, which we assign to stimulated emission. No triplet formation was observed up to 6 ns (maximum available delay time on our setup).

Drastically different spectral evolution is observed in TA of Me-N-inin in iodobenzene solution. In this case there is no positive signal of stimulated emission, instead there is a very broad excited state absorption signal. The peak at 2.35 eV can be assigned to singlet state, which decays significantly faster than in toluene. The negative signal at 3 eV might indicate rapid triplet state formation. This is also supported by very low emission intensity of Me-N-inin in iodobenzene, which is demonstrated in **Figure 5.21**. The PL intensity of Me-N-inin in **Figure 5.21** is normalized but the actual intensity of PL in iodobenzene is hundred times lower compared to toluene solution, which is why the spectra in iodobenzene is very noisy. Therefore, iodobenzene creates heavy atom environment for Me-N-inin which results in enhancement of ISC.

To test the external heavy atom effect on delayed emission, we used our TRPL setup (**Figure 5.22**). The results confirm that singlet decays significantly faster in iodobenzene than in toluene (**Figure 5.22, left**). Interestingly, the kinetics is not monoexponential.

The right panel of the **Figure 5.22** shows the spectral evolution of the singlet state decay of Me-N-inin in iodobenzene. We can see that the initial spectra at 1 - 2 ns has the same energy as observed in steady state PL. The emission is redshifted and has no vibronic structure, which might be because of an exciplex formation between Me-N-inin and iodobenzene. We found that there was a spectral change in absorption spectra (**Figure 5.23**) after prolonged photoexcitation, which could mean that the formation of exciplex is followed by photoreaction with non-emissive photoproducts. The spectrum at 10-11 ns is positioned at the same wavelength as a delayed emission observed in other solvents (*e.g.* diethyl ether : ethanol) and the slope of kinetics in iodobenzene looks similar to delayed kinetics in any other solvent. Therefore, we conclude that the delayed emission is still observed in iodobenzene and it is detectable at earlier times, which could be due to low PLQY of singlet state emission. Delayed emission reaches our detection limit earlier (~100 ns) than in experiments in other solvents, this allows us to conclude that the population of the state that gives a rise to delayed emission is smaller. This conclusion also agrees with kinetics of Ph-N-inin delayed emission. Ph-N-inin has faster ISC and the delayed emission reaches the detection limit earlier (kinetics is flat after ~ 5000 ns, **Figure 5.9**) than in alkylated ININ derivatives.

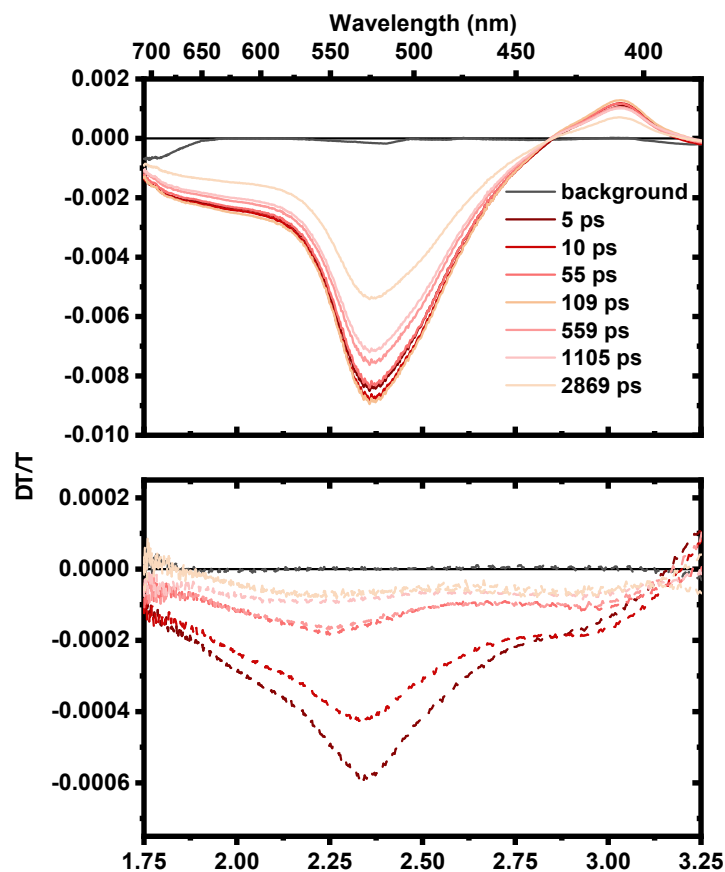


Figure 5.20. Transient absorption of Me-N-inin in toluene (top) and iodobenzene (bottom), $\lambda_{\text{ex}} = 355$ nm.

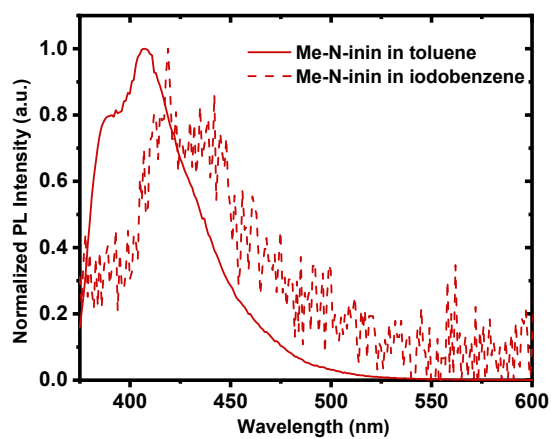


Figure 5.21. Normalized steady state photoluminescence of Me-N-inin ($10 \mu\text{M}$) in toluene and iodobenzene solutions. $\lambda_{\text{ex}} = 355$ nm.

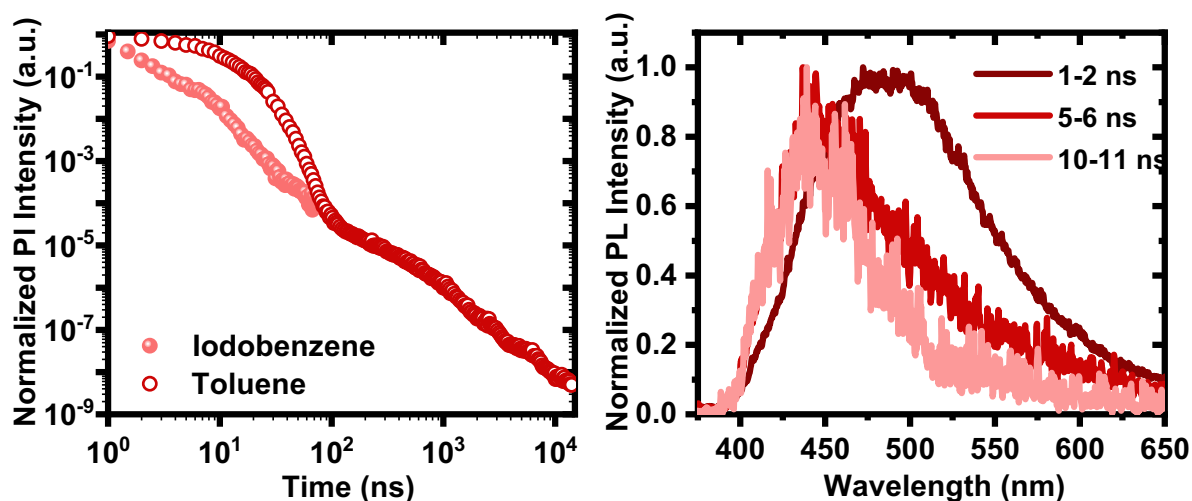


Figure 5.22. Kinetics of Me-N-inin in toluene and iodobenzene degassed solutions taken at 420-430 nm (left) and spectral evolution of emission in iodobenzene (right), $\lambda_{\text{ex}} = 355\text{nm}$.

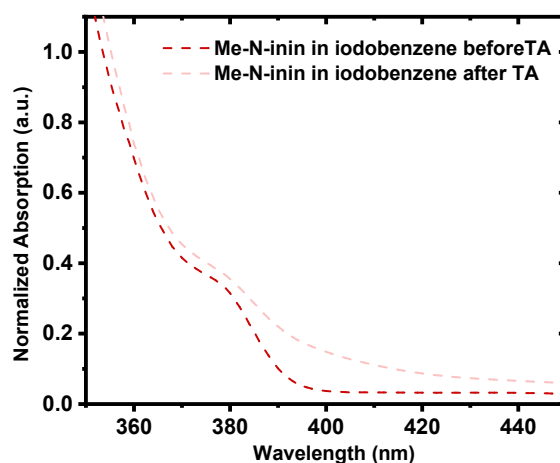


Figure 5.23. Normalized absorption of Me-N-inin (600 μM) in iodobenzene before and after TA experiment.

All the experiments described so far allowed us to confidently conclude that delayed emission does not come from triplet state population, because it is present in oxygenated solution and is only mildly affected by heavy atoms. However, faster ISC seems to decrease the population of the emissive state involved in the process. This means, that the state that yields the delayed emission is directly populated from singlet state.

5.2.2.7 Background on electron transfer

Alternatively, the delayed emission can be a result of electron transfer and charged radicals recombination. In this section we will explore this possibility. Electron transfer in the excited state causes charge separation and creates a radical ion pair. Due to the charged character

its photophysical characteristics will depend on polarity of the medium. The general mechanistic picture of electron transfer from an excited state is shown on **Figure 5.24**. Electron transfer occurs either through electron exchange interactions (requires the orbitals overlap) or through the “trivial” mechanism.

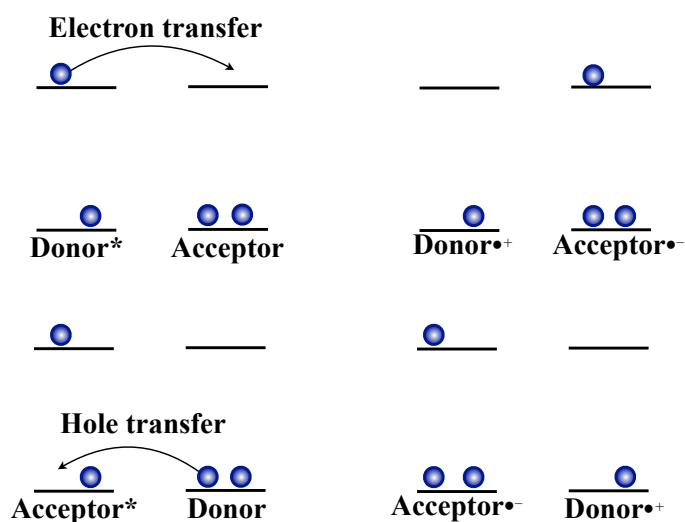


Figure 5.24. Schematic representation of electron transfer process. [5]

“Trivial” mechanism of electron transfer occurs even when there are no electronic interactions. In this process a donor molecule ejects an electron, due to presence of solvent this electron becomes solvated and then gets reabsorbed by an acceptor molecule. This mechanism is suggested to explain electron transfer as a result of two photon ionisation in pyrene and acridine. [158][159] The basic mechanism of “trivial” electron transfer in acridine solution is shown on **Figure 5.25**. [5]

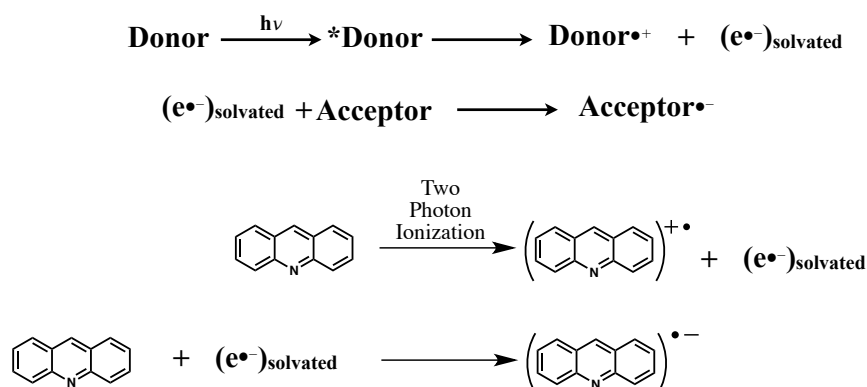


Figure 5.25. "Trivial" mechanism of electron transfer and its application to explain photophysics of acridine. [5]

Another mechanism of electron transfer requires actual interaction of the donor and acceptor orbitals. In an excited state a molecule is a better oxidizing and reducing agent and, therefore, electron transfer is more energetically favourable. The electron transfer can be visualized in two ways: occurring from excited state complex (exciplex) (path A, **Figure 5.26**) or occurring from ground charge transfer state (path B, **Figure 5.26**). Both of these processes would be diffusion controlled. In both of the cases, the product of electron transfer is contact radical ion pair (CRIP). This is electronically excited state that can emit photon (however, with low probability). In path A the diffusion has to happen within the excited state lifetime. In path B, the fact that there can be a ground-state complex implies that it does not have a formation time-limit, and, thus, it should result in a much more efficient CRIP formation. Anything that quenches the isolated-molecule S_1 state in path B would have no effect on the reaction, while in path A it would. [5] The recombination of CRIP depends on solvent polarity and is generally slower in polar solvents. The dissociation of the CRIP into free radicals occurs though formation of solvent separate radical ion pair and this process is diffusion controlled.

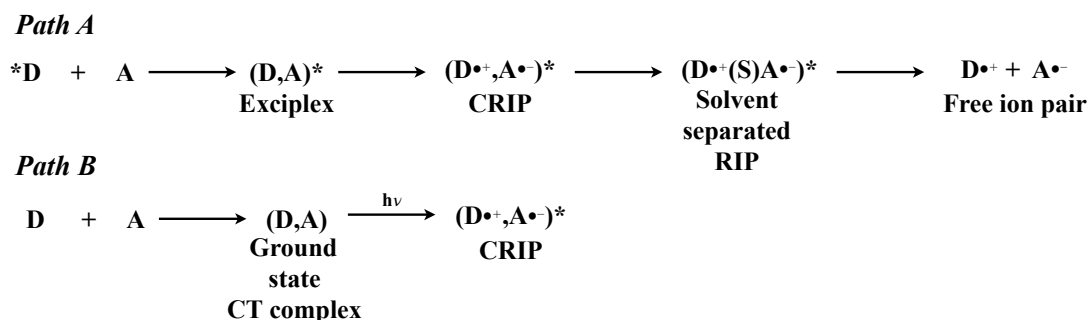


Figure 5.26. Electron transfer as a result of exciplex (path A) or ground state charge transfer state formation (path B). [5]

5.2.2.8 Photoinduced electron transfer (formation of excimer or exciplex excited species) and delayed emission as a result of radical ions recombination.

The delayed emission known as long persistent luminescence is a result of electron transfer from donor to acceptor molecules and formation of an exciplex. The lifetime of this emission can be on order of seconds (and even hours). The decay kinetics has power law dependence. [155] Thus, it is feasible to consider this phenomenon as an explanation for the delayed emission of ININ derivatives, especially taking into account that ININ derivatives were reported to form very stable radical-cations. [123] A similar process has previously been reported to occur in solutions on shorter time scales, *e.g.* lifetimes of cation radicals are 1.03 μ s for indole, 6 μ s for Me-indole, and 1.1 μ s tryptophan. [5][160]

We first consider the “trivial” mechanism of electron transfer and its feasibility to explain delayed emission of ININ derivatives as a result of excimer formation (similar to **Figure 5.25**). ININ derivatives are electron rich and, thus, electron ejection could be possible. However, the concentrations that were used for our experiments were very low, and the possibility for reabsorption of a solvated electron by another chromophore molecule would also be low, but not negligible. For the delayed luminescence to happen the radical anion and cation (one of them has to be in the excited state) need to participate in electron transfer event again which would result in formation of a neutral excited state and emission of photon.

Another option to explain the delayed emission through the electron transfer is formation of contact radical ion (as depicted in **Figure 5.26**), and then its recombination (after or before its dissociation). For the delayed luminescence to happen, the radical anion and cation need to

collide to produce a charge transfer state that can then recombine with emission of photon. In this case, the direct contact of donor and acceptor molecules is required.

For both of these theories, two physical parameters are important: viscosity and polarity of the medium. The kinetics of the recombination should be different in solvents of different polarity due to stronger stabilization of charges in polar solvents. Excited state complexes are formed upon collision of an excited molecule with the molecule in ground state. Therefore, the kinetics should be different when changing the viscosity of the solution. Thus, to test the idea of electron transfer induced delayed emission, we tested emission in solvents of different polarity and different viscosity mediums.

The results of the kinetic study in solutions of different polarity was performed on C8-N-inin. **Figure 5.27** shows kinetics of the singlet decay of C8-N-inin in ethyl acetate and toluene. These solvents have dielectric constants of 6.05 and 2.38, respectively. [161] The solvent with higher dielectric constant has higher polarity and, thus, better ability to stabilize the charges. This experiment allowed us to conclude that the delayed emission does not depend on the solvents of different polarity.

Next, we took the kinetics in a medium with high viscosity (PMMA solution, 25mg/mL). In viscous medium diffusion is slowed down; thus the kinetics would be affected. We performed TRPL experiments in viscous polymer solution. Our results suggest that there is no dependence on the viscosity of the medium (**Figure 5.28**).

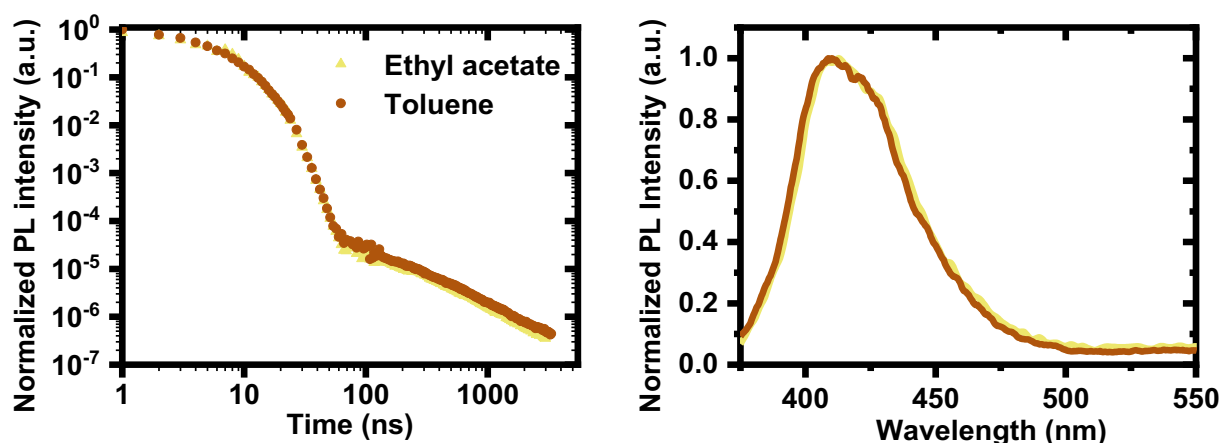


Figure 5.27. Kinetics (left) and delayed emission spectra (right) in solutions of C8-N-inin (10 μ M), $\lambda_{\text{ex}} = 355\text{nm}$.

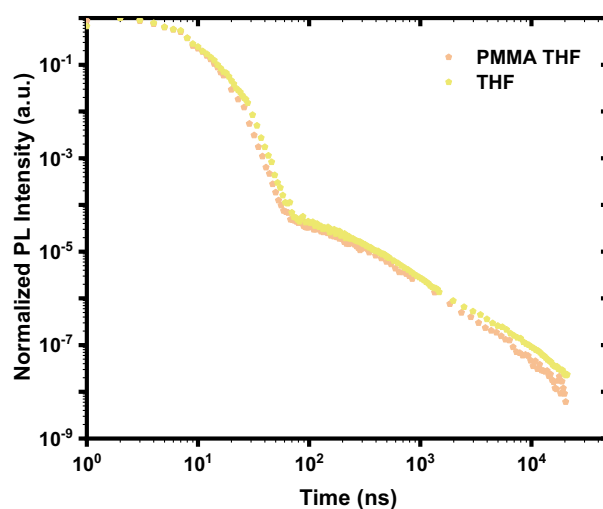


Figure 5.28. Kinetics of photoluminescence decay of C8-N-inin (10 μ M) in THF and PMMA THF solutions, $\lambda_{\text{ex}} = 355\text{nm}$.

Finally, we tested the emission of ININ derivatives in polymer films. The films with C8-N-inin content of about 10% were prepared by spin-coating (2000 rpm, 60 sec, 50 μ L per film, static spin-coating). Absorption spectra have the same energy as in solutions suggesting that no aggregate formation (**Figure 5.29**). The kinetic study of ININ in polymer films is presented in **Figure 5.30**. Polymers were chosen based on their dielectric constants, which were 3.0 for PMMA, 2.5 for PS and 2.3 for zeonex. Therefore, the polarity of the medium was different in different polymer films. We see the reduction in emission lifetime in polymer films of higher polarity. We can also conclude that singlet decay in films cannot be described by single exponential function. Instead, we can see that prompt decay is accompanied by additional component decay that is very long lived (**Figure 5.30, left**).

The spectral evolution of this delayed emission in films is more complex than in solution. **Figure 5.30 (right)** shows spectral evolution of C8-N-inin in polystyrene matrix. We can see that after first 20 ns of decay the spectra start to broaden and the maximum shifts to lower energies. This behaviour could be indicative of excimer formation, nonetheless, the delayed emission that has same energy as the singlet state is observed at later times (404 ns). This might mean that the excimer emission is a main relaxation pathway of the singlet state in polymer films. However, the long-lived component is still present but less intense.

The kinetics profiles of solutions and films are slightly different (**Figure 5.31**). We rationalize this difference by the overlap of the excimer emission with the delayed component at

higher energy. The lifetime of delayed emission in films is different compared to solution, however formation of an excimer suggests that there might be additional interactions in the films. Summarising the result of this experiment, we conclude that the delayed emission is also observed in polymer films of ININs; however, the obtained kinetics cannot be used to assign the origin of the delayed emission, due to additional solid state effects.

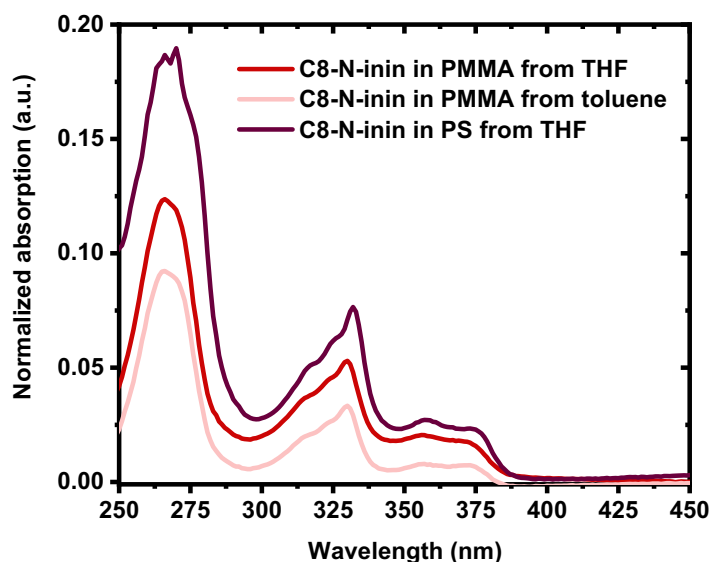


Figure 5.29. Absorption of C8-N-inin in polymer films, thickness of the films varied: PMMA/THF – 146 nm; PMMA/toluene – 101 nm; PS/THF – 234 nm; zeonex/THF – 557 nm (absorption could not be measured due to high reflectivity), $\lambda_{\text{ex}} = 355$ nm.

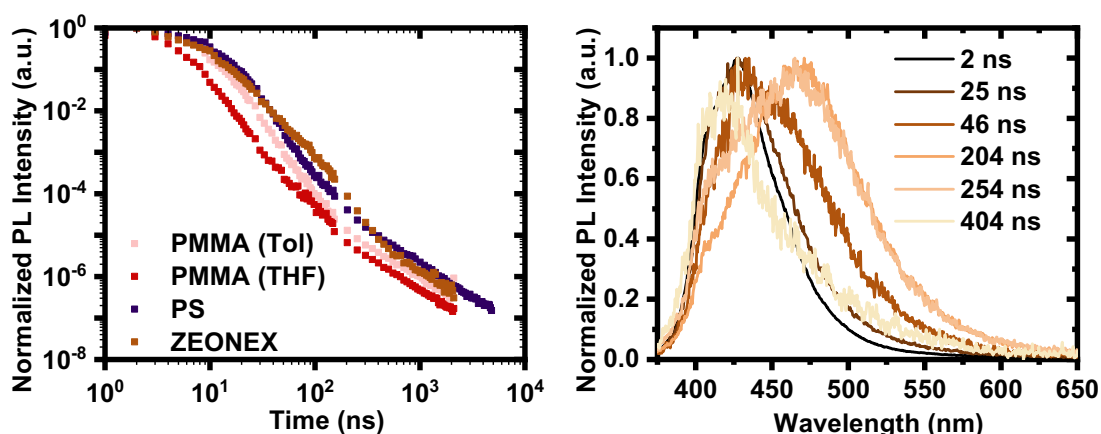


Figure 5.30. Kinetics of C8-N-inin in polymer films taken at 420-430nm (left) and spectral evolution of C8-N-inin in polystyrene film, $\lambda_{\text{ex}} = 355$ nm.

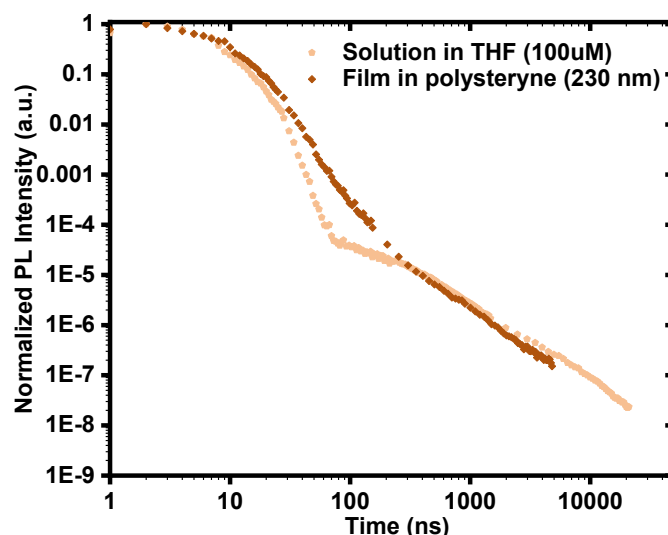


Figure 5.31. Comparison of kinetics of C8-N-inin in polystyrene film and THF solution taken at 420-430nm, $\lambda_{\text{ex}} = 355 \text{ nm}$.

5.2.2.9 Delayed emission as a result of recombination of radical cation and an ejected electron.

Apart from formation of excimers, electron transfer can result in solely electron ejection producing a stable radical cation and ejected solvated electron. This moiety has been extensively spectrally characterized in aqueous solutions [162], however there are reports of solvated electrons formation in non-aqueous solutions.[108][158][163] Electron transfer with solvated electron formation in indole and tryptophan chromophores has been reported. [160] This process was previously considered to be a cause of delayed emission in indole solutions at 77 K. [108][110][112] This suggests that it is a feasible model for the case of ININ derivatives; however, the mechanism of it is rather mysterious.

The study of photoexcitation of pyrene and anthracene suggested that quenching of lowest excited state by oxygen and methyl iodide does not impact the yield of radical cations. [164][165] The experiments reported by Hopkins *et. al* suggested that electron-donating substituents increase ejected electron yields. They also mention the possibility of existence of a metastable state that would consist of partially solvated electron held in close proximity to the cation radical (caged-electron state). This state can decay by complete electron ejection or by recombination. [109] In addition, it has been shown that indolyl cation radical can be in equilibrium with the neutral radical. [160] All of these studies point to possibility of similar mechanism of electron ejection in ININ derivatives.

As it was mentioned earlier another option of explaining this delayed emission would be some sort of radiative recombination of either charged radical ions or radical species. Due to the radical nature of the delayed emission some papers report quenching of the delayed emission when strong electron scavengers are used. [112]

In the report by Mazhul *et al.* it is suggested that due to the radical origin of emission, it can be quenched with radical quenchers like cysteine and glutathione. [113] To check if that would be the case for ININ derivatives, we tested several radical quenchers (**Figure 5.32**), the results of our study are depicted on **Figure 5.33**. L-glutathione and L-cysteine are not soluble in organic solvents; hence, to solubilize both ININ molecule and the quencher we had to use a 1:9 mixture of water and THF. The electron transfer requires orbital overlap and we think that it might not have been achieved. This might be because ININ derivative and the quencher would have been in slightly different solvated environments, which might have been not compatible. The experiment with BHT as a scavenger was performed in neat THF solution; however, it also has not resulted in quenching of the delayed emission. This might be due to bulky substituents on BHT or due to non-radical character or the ININ delayed emission.

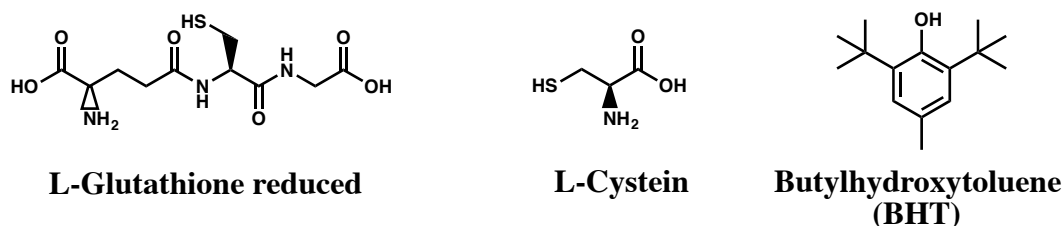


Figure 5.32. Radical quenchers structures.

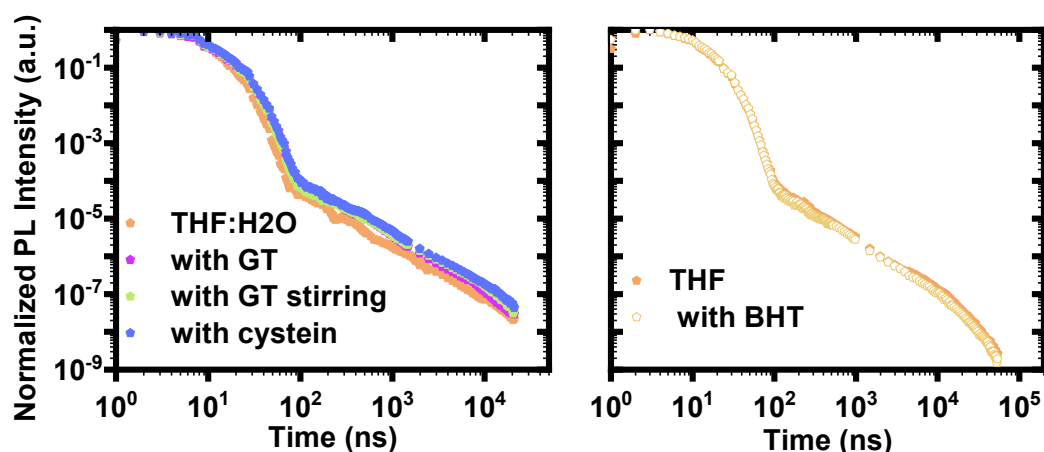
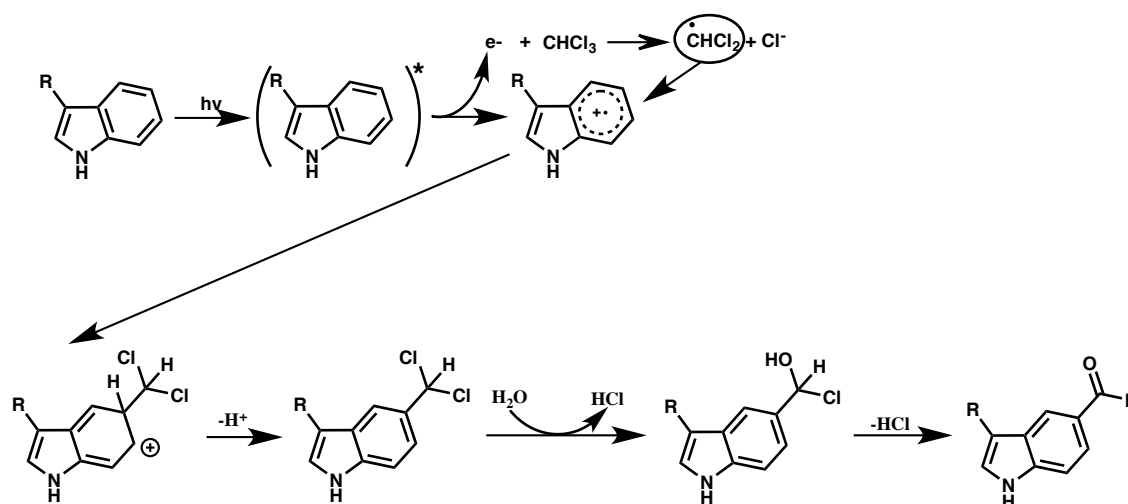


Figure 5.33. Kinetics of C8-N-inin with different emission quenchers, $\lambda_{\text{ex}} = 355 \text{ nm}$.

From literature we know that chloroform can react with solvated electron. We decided to test this reaction as a possible quenching mechanism for the delayed emission. The reaction of chloroform with solvated electron can be visualized as follows [158]:



Therefore, in a molecule that can generate solvated electron upon excitation, this electron would immediately react with chloroform. In the case of pyrene such reaction reduces the yield of excited singlet state, but not its lifetime. [158] Interestingly, there are reports of photoexcited reaction of tryptophan and derivatives with chloroform. [166][167] The report by Edwards *et al.* suggests that photoexcitation of tryptophan derivative could cause the reaction between tryptophan and chloroform in an aqueous buffer solution through the following path:



Scheme 5.5. Mechanism of photoinitiated reaction of indole with chloroform. [167]

The resulting radical cation can then participate in the reaction with $\bullet\text{CHCl}_2$ radical which in aqueous solution would result in formation of aldehyde. This mechanism requires water to participate in the last stage of aldehyde formation. This process can be monitored by fluorescence spectroscopy as the natural emission of tryptophan shifts from 360 nm to 500 – 550 nm as reported by Lander *et al.* [166]

However, the generated chlorine ion can also interact with aromatic molecules. It is known that halogen radicals can form complexes with aromatic molecules. For example, this is observed for bromonaphtalene in the process of photolysis where the C-Br bond cleavage results in formation of Br-radical which then forms a complex with benzene ring. This complex is reported to have a signal in transient absorption at around 550 nm. [168]

As we mentioned in the beginning of this chapter, we tested absorption and PL of ININ in chloroform. We know that absorption of ININs in chloroform looks similar to other solvents (**Figure 5.3**), however, the emission is quite different (**Figure 5.34**). The emission has two components: a high energy weakly emissive component that matches the position of the emission in other solvents and the low energy component (broad with no fine structure) with much stronger emission. Interestingly, the peak maximum of this new band corresponds to what has been reported in the paper by Ladner *et al.* [166] The excitation spectra of the emissions in THF and CHCl_3 are compared in **Figure 5.34 (right)**; this shows significant redshift and formation of new structureless band with maximum at 425 nm. Unfortunately, the excitation spectra from 400nm emission in chloroform could not be detected due to low signal. The excitation spectra from 400nm emission in THF matches the absorption. This suggests that there is some sort of photoreaction or charge transfer complex formation in excited state of the molecule specifically in CHCl_3 . Moreover, there must be a significant electronic interaction present (in some molecules) in the ground state.

Figure 5.35 shows the spectral evolution of ININ emission in chloroform solution. There is a difference in spectral evolution between the solution that were prepared in air and in inert atmosphere. We can see that in deoxygenated solution, in the first nanoseconds after excitation, the decay is dominated by the emission from S_1 state with maximum around 450 nm. However, the decay of S_1 state is very rapid (faster than instrument resolution), and it is followed by evolution of the broad emission band with maximum at 525 nm. We assign this process to electron transfer, and subsequent decay of the photoproduct emission. As we can see there is no delayed luminescence observed. The difference in spectral evolution in oxygenated and deoxygenated solution is a very interesting phenomenon and might suggest that in addition to this photoreaction there is an interaction with oxygen that causes the change in singlet state behaviour.

The photoproduct might be a superoxide (unlikely), an aldehyde (unlikely) or a charge transfer complex between aromatic molecule and chloroform derivative (chloroform radical, chlorine anion etc). As it was mentioned above, water is essential for aldehyde formation. In our system we do not have water in the quantity required (equimolar quantity, which means at least 10 μM) for the full conversion. Therefore, we suggest that this is not what happens in our system. Superoxide formation is unlikely due to energetics, because for electron transfer to happen between the ININ and oxygen the singlet-triplet energy gap must be larger than that of oxygen. However, it might be some sort of chloroform mediated process.

The photoreaction with chloroform is a reversible process. We show this by a simple experiment, for which we kept chloroform solution of the C8-C-inin for a week in an ambient atmosphere (daylight), and then we dried the chloroform. The resulting solid was dissolved in toluene to yield the same concentration that we previously had in chloroform. The PL of this solution was recorded and then the solution was dried again, the solid was dissolved in chloroform, and the PL was recorded. The results of this experiment are shown in **Figure 5.36**. This experiment shows that the molecule that was exposed to chloroform, actually has normal singlet state steady state emission when chloroform is eliminated. The shift in redshifted emission in **Figure 5.36** (the re-dissolved material at 330 nm excitation) could be because of a changed balance between the red- and blue-emitting species.

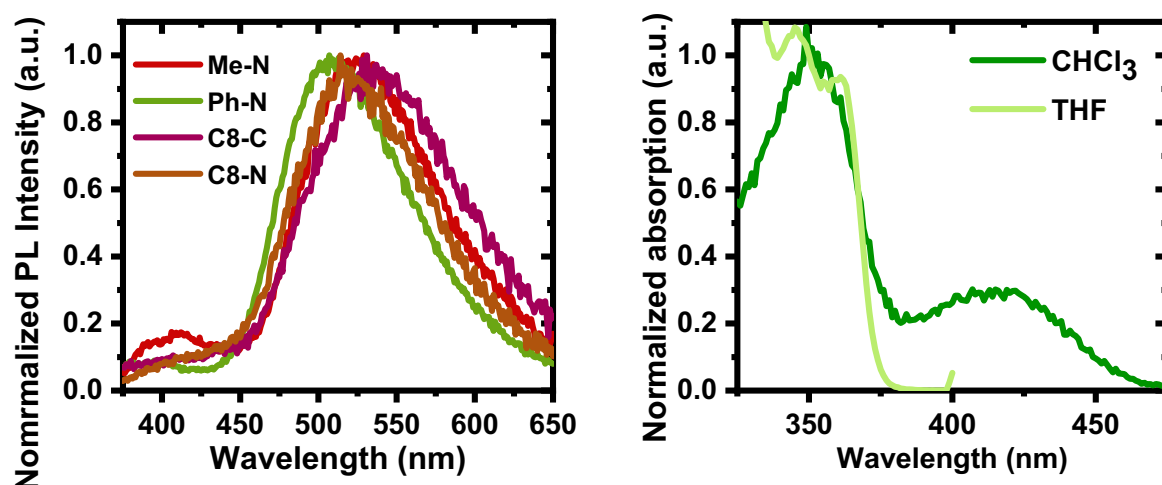


Figure 5.34. ININ derivatives in chloroform (10 μ M), $\lambda = 330$ nm (left) and excitation scans of Ph-N-inin in THF (400 nm) and CHCl₃ (510 nm).

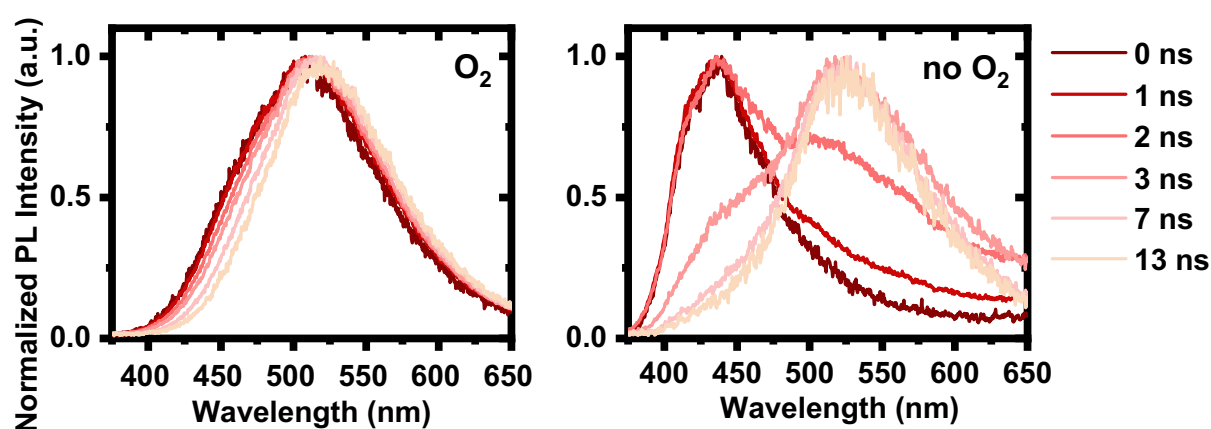


Figure 5.35. Difference in spectral evolution of Me-N-inin solution in chloroform when prepared in oxygen and nitrogen atmosphere, $\lambda_{\text{ex}} = 355$ nm.

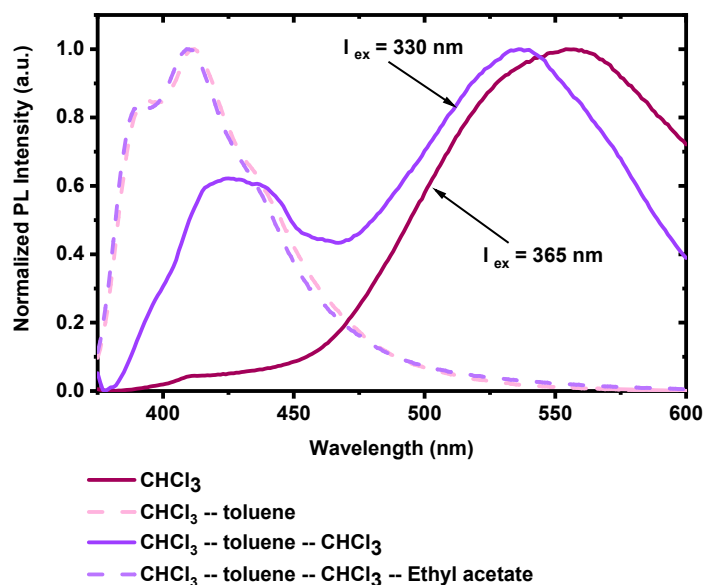


Figure 5.36. Chloroform to other solvents transitions of Me-N-inin (10 μM) solutions.

After consulting the literature and analysing all the data presented above, we conclude that there is most likely electron transfer occurring in chloroform. Therefore, there would be a radical species in solution as a result of an electron transfer. We confirm this by using a radical scavenger in chloroform solutions of ININ. **Figure 5.37** shows the difference in steady state emission in presence of electron scavenger. We can see that the singlet emission is quenched not to the same extent (**Figure 5.37, left**), and the evolution of the band at 550 nm is not observed (**Figure 5.37, right**) in solution with electron scavenger. **Figure 5.38** shows the effect of electron scavenger on emission of solution that was subjected to higher energy irradiation (low intensity LED light, 254 nm). We can see that the intensity of the photoproduct emission is much stronger in the solution that did not have the quencher in (**Figure 5.38, left**). **Figure 5.38 (right)** shows that a “loss” of a chromophore is observed (similar to excitation spectra, **Figure 5.34**), because absorbance is significantly decreased after irradiation, and there is a new band at 400 nm. A mild effect of radical scavenger can be also seen in decay kinetics of the new emission band (**Figure 5.39**). Sensitivity of the emission characteristics in chloroform to the presence of radical scavenger suggests the involvement of the solvated electron in the emissive state. Absence of delayed emission quenching in other solvents with a radical scavenger (**Figure 5.33**) might not be indicative of the absence of quenching since the effect might be very small.

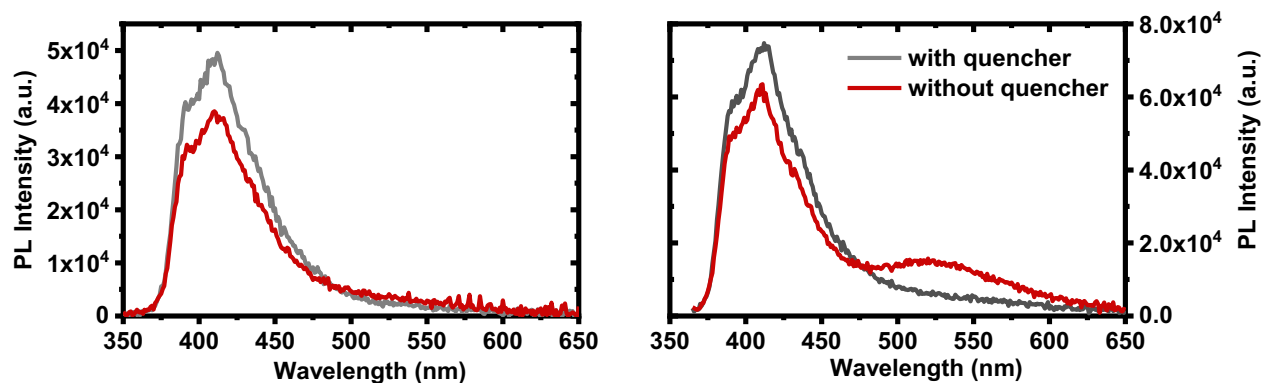


Figure 5.37. Me-N-inin in CHCl_3 ($10 \mu\text{M}$) with and without radical scavenger (BHT) at $\lambda = 330\text{nm}$ (left) and $\lambda = 355\text{nm}$ (right), inert atmosphere.

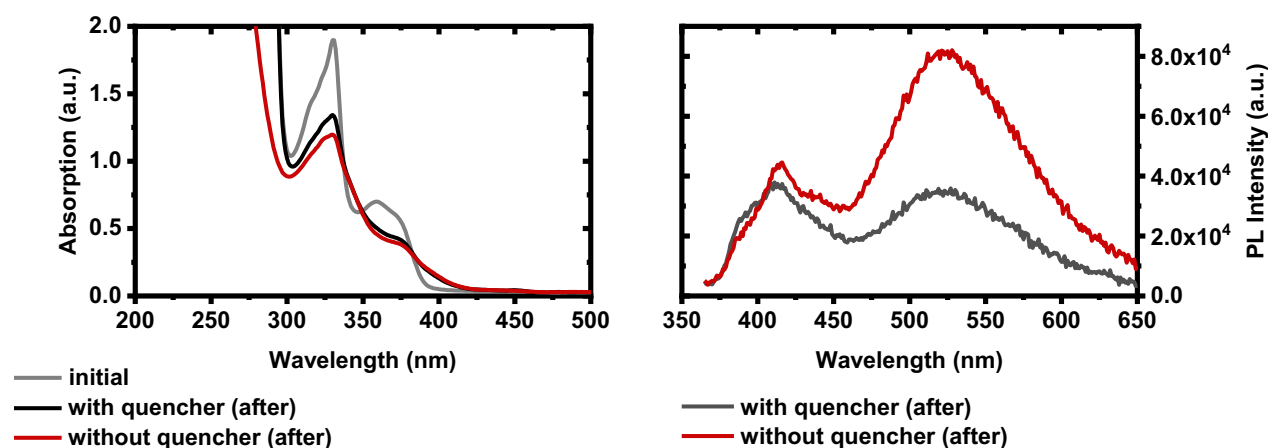


Figure 5.38. Absorption of Me-N-inin (left) and steady state emission of Me-N-inin in chloroform ($10 \mu\text{M}$, degassed) with and without radical scavenger (BHT), $\lambda = 355\text{nm}$. The solutions were irradiated with 254 nm light prior this measurement.

Finally, we compare effect of irradiation on inert and oxygenated solution. The solution was prepared in inert atmosphere in a sealed cuvette, and then irradiated with low intensity 254 nm for 20 mins, then the PL spectrum with $\lambda_{\text{ex}}=355\text{nm}$ was measured. **Figure 5.40 (left)** shows the result of this experiment. We observe a new redshifted emission band with a peak maximum at 450 nm , the band is structureless, which suggests a charge transfer origin. Then the cuvette with solution was exposed to both air and light (254 nm) for 20 mins. This resulted in another shift in emission maximum, yielding a band with maximum at 475 nm . Interestingly, in both cases irradiation at 254 nm resulted in an increase in emission intensity, this was also confirmed when solution was again irradiated (total exposure to 254 nm light was 50 mins).

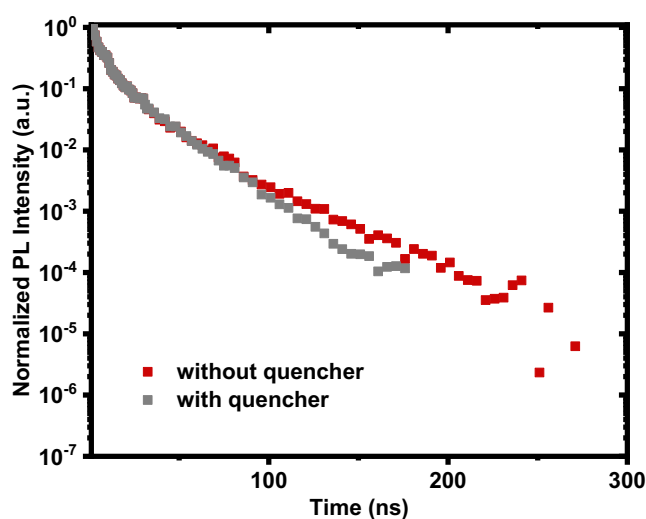


Figure 5.39. Kinetics of Me-N-inin luminescence decay in chloroform, $\lambda=355\text{nm}$.

Comparing emission of solution that was kept in air with the one that was initially oxygen-free, confirms the involvement of oxygen in the process (**Figure 5.40, right**). This can be rationalized either by photoproducts being slightly different or, as mentioned previously, by a change in the balance between the same red- and blue-emitting species. We, therefore, conclude that the process in chloroform is radical-based, and it interferes with delayed emission.

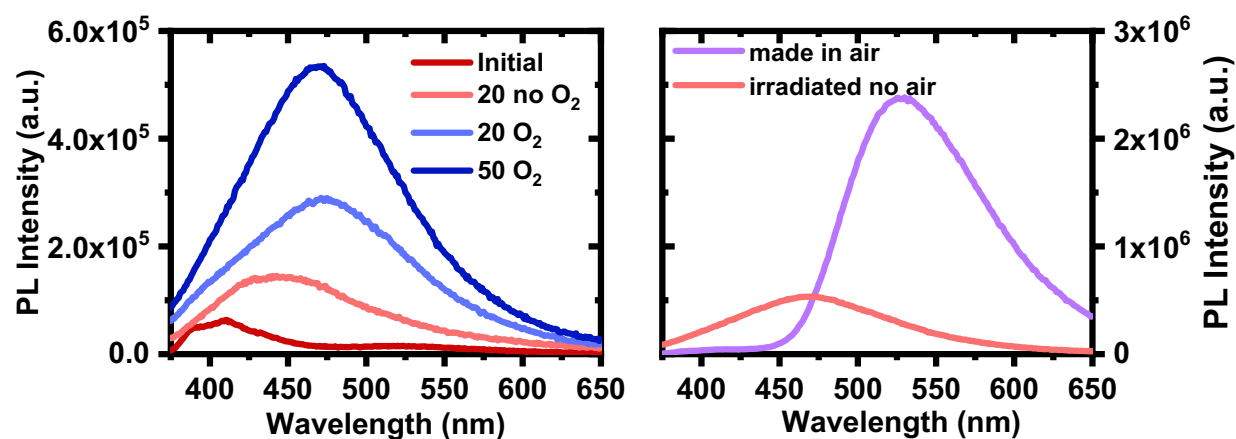
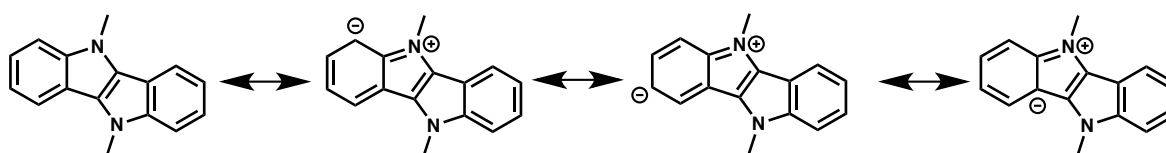


Figure 5.40. Me-N-inin solution in CHCl_3 irradiated with 254 nm lamp for 20 mins without air, then 20mins with air and 50 mins with air (left) and Me-N-inin solution in CHCl_3 made in air and after irradiation with no air.

5.2.2.10 Effect of chloroform on NMR spectra

Interestingly, we see the interaction of the ININ derivatives with deuterated chloroform in NMR. Essentially, we observe broadening of some NMR signals, which could be a ground state interaction, or it could be initiated by ambient light (**Figure 5.41**). It is well known that radicals have broad signals or even that they are not detectable in NMR. However, in this case all of the signals should be broad, whereas in our case only some signals are affected. [169] From steady state spectroscopy of ININs in chloroform, we know that they form ground state complex with chloroform (as we could see it in the excitation spectrum, **Figure 5.34**). The broadening of NMR signals could be a result of dynamic interaction of ININs with chloroform-d (possibly, ground state CT state formation), and these interactions would affect only protons with high electron density according to resonance structures on **Scheme 5.6**.



Scheme 5.6. Scheme of ININ core conjugation.

Figure 5.41 shows the difference in NMR spectra when CDCl_3 and DMSO-d_6 are used as a solvent, only 3 peaks are broadened. To confirm that the broadening is indeed due to the dynamic exchange nature that occurs in the analysed compounds, we performed NMR at low temperature. The results are shown on the **Figure 5.42**. We can see that all of the peaks become narrower at -60°C compared to -10°C . This suggest that slowing down the molecular motion at low temperature slows down the dynamic exchange. However, if the broadening in NMR was due to the radical nature of the species, NMR at low temperature would also show the narrowing of the peaks. Therefore, we cannot exclude this explanation.

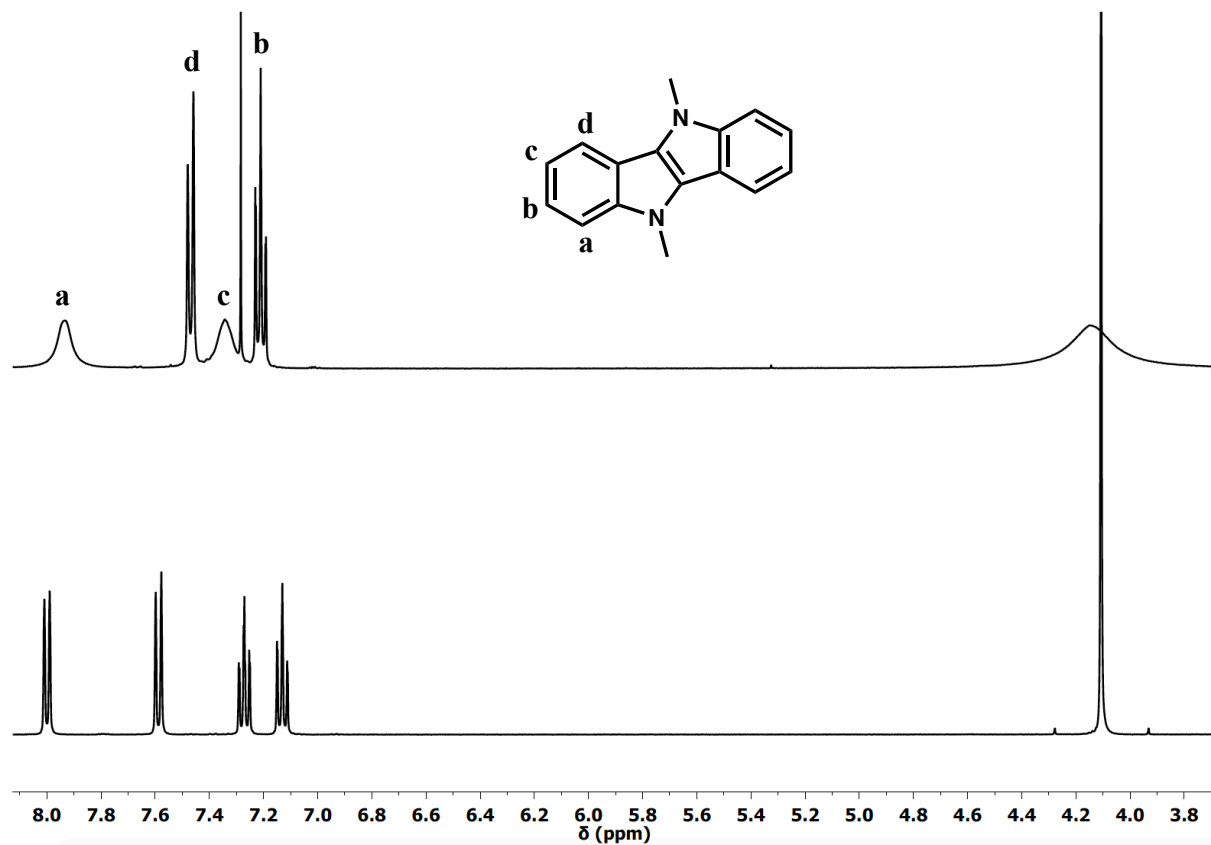


Figure 5.41. NMR spectra of Me-N-inin in chloroform-d (top) and DMSO-d6 (bottom).

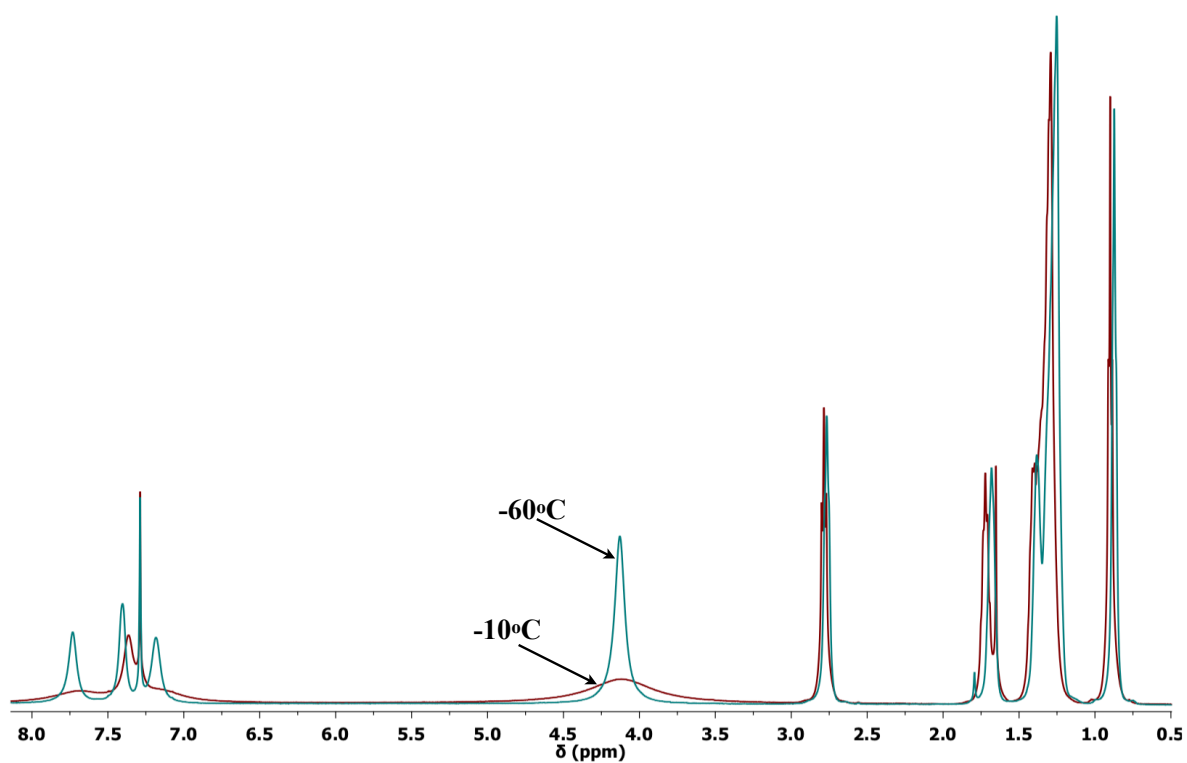


Figure 5.42. NMR spectra of C8-C-inin in CDCl3 at -10°C and -60°C.

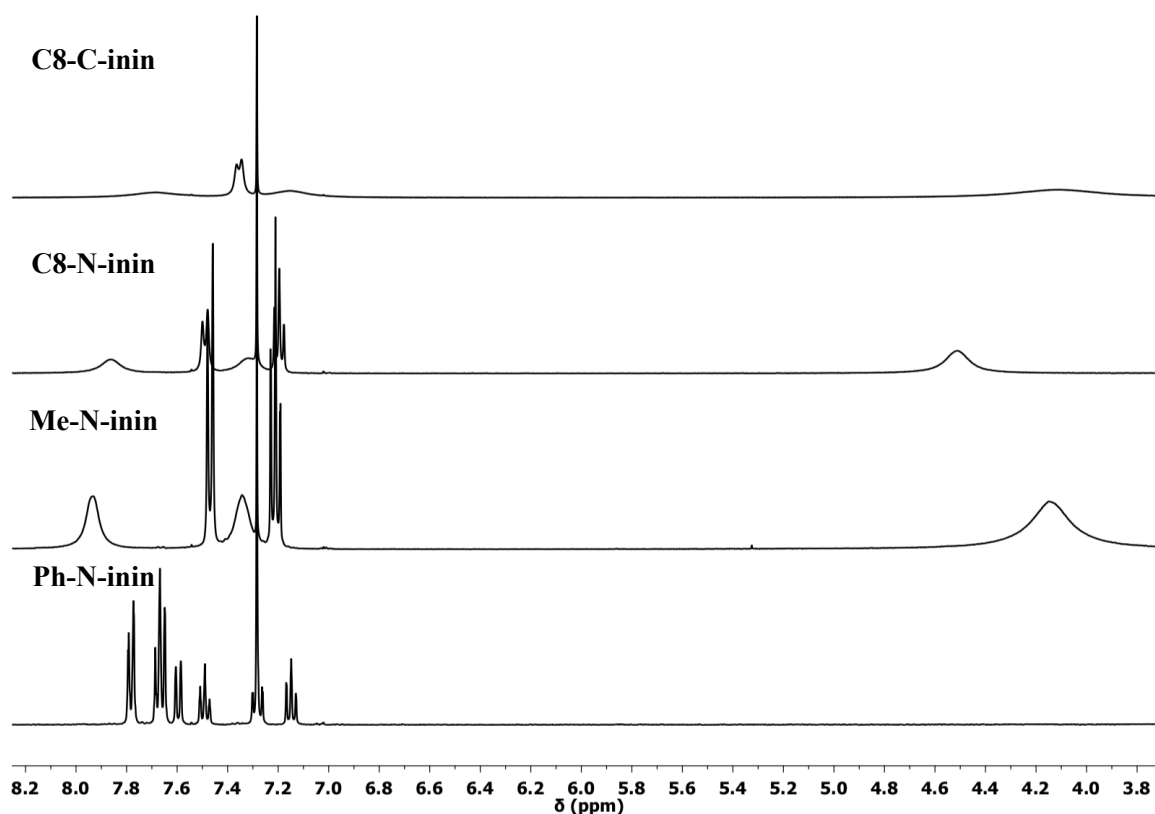
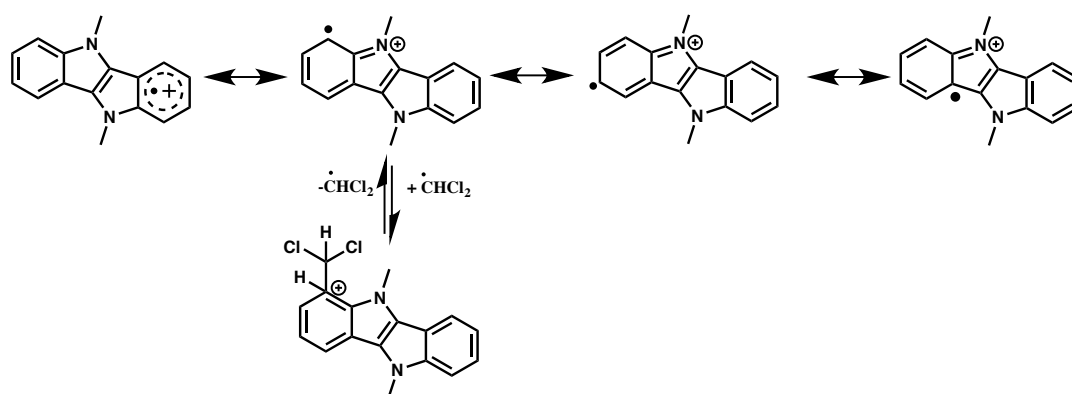


Figure 5.43. NMR spectra of ININ derivatives in CDCl₃.

5.2.2.11 Mechanism of delayed emission in ININ derivatives

The ground state interaction with chloroform would be preserved in the excited state forming a full charge transfer complex with chloroform radical. Because both of the species that participate in this reaction are radicals and would react with radical scavenger resulting in significant reduction in photoproduct as demonstrated above. Analysing the affected NMR peaks of different ININ derivatives (**Figure 5.43**), we suggest the following radical cation structure and the structure of the dynamic complex:



Scheme 5.7. Scheme of cation-radical conjugation and its reaction with chloroform (both ortho and para positions with respect to nitrogen will be affected).

It is likely that this complex in the excited state gives rise to a redshifted emission. The redshifted emission has a redshifted excitation spectra (**Figure 5.34**), which suggests a ground state charge transfer complex formation (**Figure 5.26**). This is supported by NMR, because we should be seeing only the ground state of the molecule, as not many molecules in solution could be excited with ambient light. Evidently, not all of the molecules form the ground state complex, some still undergo electron transfer from the excited state, because we see a emission at 400 nm in deoxygenated solution (**Figure 5.35**). The ground state complex of Ph-N-inin with chloroform might be weaker as we do not see the broadening in NMR, however, we do see it in the excitation spectrum. This is due to weaker electron-donating character of Ph-N-inin.

The complex of chlorine anion and aromatics is feasible; however, its formation should not be affected by electron scavenger. It is possible that both of the complexes form at the same time, because the formation of the adduct with chloroform radical results in a positively charged moiety. This would require stabilization with chlorine anion, which might also coordinate to aromatic system. Coordination of halogen anion to aromatic core would also explain redshifted emission in iodobenzene, if iodobenzene acts as an electron acceptor in the electron transfer reaction (**Figure 5.22**).

Summarizing all of the experiments describes so far, we can conclude:

- We observed delayed emission in ININ derivatives in all of the solvents, except for chloroform. This emission is related to an excited singlet state. We demonstrate that this emission cannot be explained as a triplet-related phenomena (sections 5.2.2.5 and 5.2.2.6).
- We observe electron ejection in chloroform, whilst the delayed emission is not present.

- We suggest that the ejected electron might be the cause of delayed emission in the rest of the solvents and, thus, when the ejected electron is used for the reaction with chloroform, the delayed emission cannot occur.

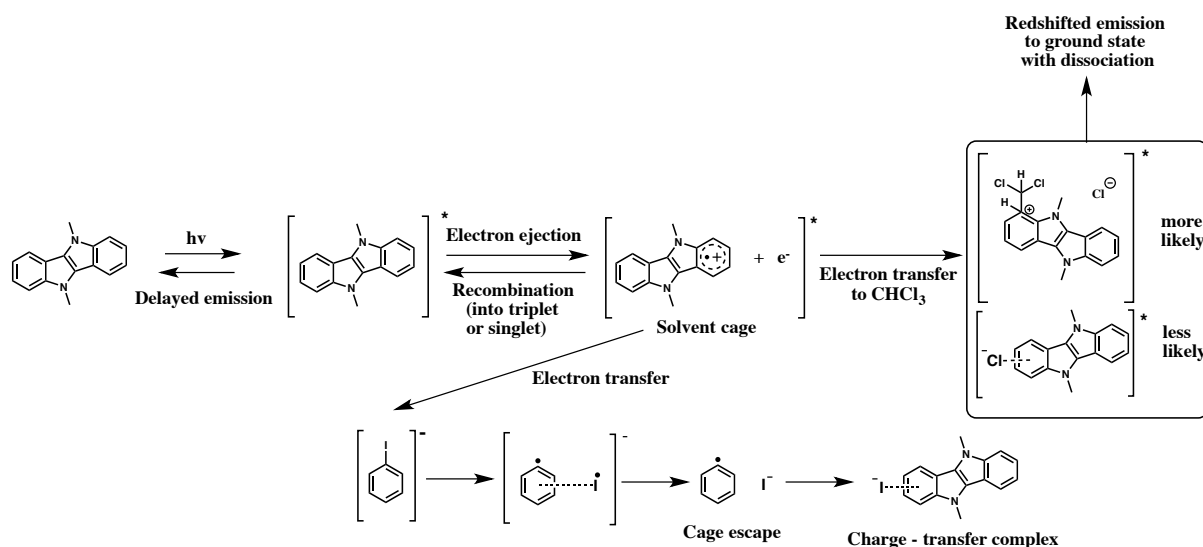
There is a debate in the literature concerning the conditions required for electron ejection: two or one photon ionization [108][109][111][163] as well as an exact mechanism of this process. [109][164][165][170] We know that in the case of ININ derivatives this process requires only one-photon. Despite having the ionization potential of 4.88 eV, we believe that in the excited state this value would be significantly reduced yielding pre-dissociative or even fully ejected electron with a radical-cation. This is in line with previous reports on photoionization and delayed emission in indole and derivatives. [113][111][109][158]

Another way to explain the delayed emission would be the complete photodissociation of the ININ derivatives with C-C bond cleavage. A study by Tseng *et al.* showed that photodissociation of N-methylindole and N-methylpyrrole is one photon process which occurs at the range of wavelengths yielding methyl and indolyl (pyrrole) radical as a product. [111] Therefore, a photodissociation followed by radical recombination into a singlet excited state cannot be discarded as a potential explanation of delayed emission in ININ derivatives.

The experiments described above allowed us to conclude that delayed emission originates from the recombination of cation radical with ejected electron that has been somehow stabilized by the solvent. The recombination of two neutral radicals is also possible. However, it is unclear why the radical species cannot be quenched with a radical quencher. We can speculatively offer a couple of explanations: a solvent cage “protects” these radical species from radical scavenger or that the mechanism of radical quenching is slower than the recombination.

The mechanism of the recombination determines the kinetics of the delayed emission. An electron and a cation-radical form a two particles system that can generate singlet and triplet excited states in 1:3 proportion (according to spin statistics described in section 2.1.2). The smaller intensity of the delayed emission in presence of heavy atoms can be rationalized by ISC crossing induced by heavy atom in “newly” formed excited singlet state. In the case of

iodobenzene, there might be formation of charge transfer complex between molecules and iodine. All of the processes are summarised on **Scheme 5.8**.



Scheme 5.8. Proposed mechanism of delayed emission and charge-transfer complex formation between ININ and iodine and chlorine ions.

5.3 Conclusions

We report synthesis and photophysics of electron - donating ININ derivatives. We find that the steady state absorption and emission of ININ derivatives do not depend on solvent polarity. The reorganization energy of these processes in ININs is lower (180 - 217 meV) than for BTBT (220 - 289 meV) derivatives, which suggest more rigid structure of the nitrogen-containing chromophore. ISC in ININ derivatives occurs on the time scales of 3 - 8 ns, which is significantly slower than in BTBT derivatives. The emission comes from the lowest lying singlet state and has high PLQY.

We use time-resolved absorption and photoluminescence to study excited state evolution and decay dynamics. We observe a delayed emission that has the same energy as prompt fluorescence. Its decay cannot be described by exponential function; however, it has a linear excitation power dependence. We conclude that delayed emission originates from the recombination of cation radical with ejected electron that has been somehow stabilized by the solvent cage. However, there also remains a possibility of photoionization with formation of two neutral radicals (which we think is less likely), the recombination of these radicals could also lead to delayed emission.

We show that delayed emission does not occur in chloroform due to electron transfer from the molecule to chloroform. We suggest that ININ derivatives form ground state charge transfer complex with chloroform which then gets excited, and its deactivation results in redshifted emission. This conclusion is based on the fact of broadening of some signals in NMR and redshifted excitation spectra.

Delayed emission was previously observed in many systems due to triplet-related, charges or radical-ions recombination reasons. We find the latter to be true for delayed emission in ININ derivatives. In this case the emission is a one-photon process that initiates formation of radical-cation and ejected electron and their subsequent recombination, as it was previously reported for indole derivatives. The materials reported here are stable towards oxidation and do not require high excitation power to observe the delayed emission, which makes them good candidates for applications in organic light emitting devices. Similar materials exhibiting long persistent luminescence are used as “glow in dark” paints that slowly release the energy obtained as a result of optical excitation. We suggest that ININ derivatives could be used for such purposes, however, a conditions optimization would be required.

6 Solid state properties of indolo[3,2-*b*]indole

*In this chapter we present the solid state properties of indolo[3,2-*b*]indole derivatives, showing their solid state molecular arrangement and its influence on the photophysical and electronic properties. We find intermolecular interactions in these molecules result in excimer formation, which is the main radiative relaxation pathway in these molecules. We also demonstrate the state of art charge carrier mobility for one of the synthesised molecules, which is on the level of what has been reported for C8-BTBT.*

The single crystal and film X-Ray diffraction was performed and analysed by Dr. Craig Robertson. GIWAXS was performed and analysed by Dr. Daniel Toolan. Atomic force microscopy was performed and analysed by Guy E Mayneord at the University of Sheffield. Thin films field effect transistors were made and measured by Zahrah J Alqahtani at the University of Sheffield. OLEDs were prepared and measured in collaboration with Dr. Naoum Vaenas.

6.1 Introduction

The properties of a molecule in an active layer of a device depend both on intrinsic (effective conjugation, flexibility etc) and intermolecular (solid state molecular arrangements) properties. Understanding the design strategies to create necessary solid-state properties in organic thin films or crystals is one of the biggest challenges in material science.

Organic materials that possess both high charge carrier mobility and high PLQY are desirable for applications in organic light emitting diodes [171], organic light emitting transistors [172][173][174] and as a gain medium in organic lasers. [175][176] Combination of high charge carrier mobility and high PLQY is quite rare and hard to achieve. [23] This is due to contradicting requirements to the molecular structure, *i.e.* charge transport requires π - π overlap and ideally a face-to-face packing, whilst for optical properties such arrangement means H-aggregate formation with low PLQY. Nonetheless, molecules that possess both of the properties have been reported. [177] Generally, development of meaningful structure-property relationships requires careful investigation of intramolecular properties followed by the investigation of molecular packing and the desired intermolecular (opto)electronic properties. However, such studies are often limited by materials and techniques availability.

In this chapter, we present solid-state properties of ININ derivatives (structures in **Figure 5.1**). We previously mentioned that pyrrolo[3,2-*b*]pyrrole has a significantly lower ionization potential (7.27 eV) compared to other electron-rich heterocycles with similar structure, *e.g.* thieno[3,2-*b*]thiophene (8.1 eV), which suggests that this moiety could improve hole-transporting properties of aromatic heteroacenes. There are several reports on using pyrrolo[3,2-*b*]pyrrole and ININ derivatives in field effect transistors. [117][119] However, only low charge carrier mobilities were demonstrated (**Figure 6.1**). Interestingly, a report by Wang *et. al.* [117] suggests that N-substituted derivatives exhibit higher charge carrier mobility than unsubstituted ones. This is counter to the generally accepted knowledge that in N-heterocycles, N-H... π interactions could enhance bidirectional charge transport and improve the overall performance of an OFET device. [29] This effect of unsubstituted derivative compared to substituted ones was demonstrated for compounds 1 and 2 on **Figure 6.1**. [178]

Solid state optical properties of ININs in thin films were not previously reported. We synthesised N-substituted ININ derivatives with different substituents on the nitrogen atom, which allowed for different solid-state molecular packing. These molecules were then

investigated in thin film transistors, followed by investigation of optical properties of organic thin films.

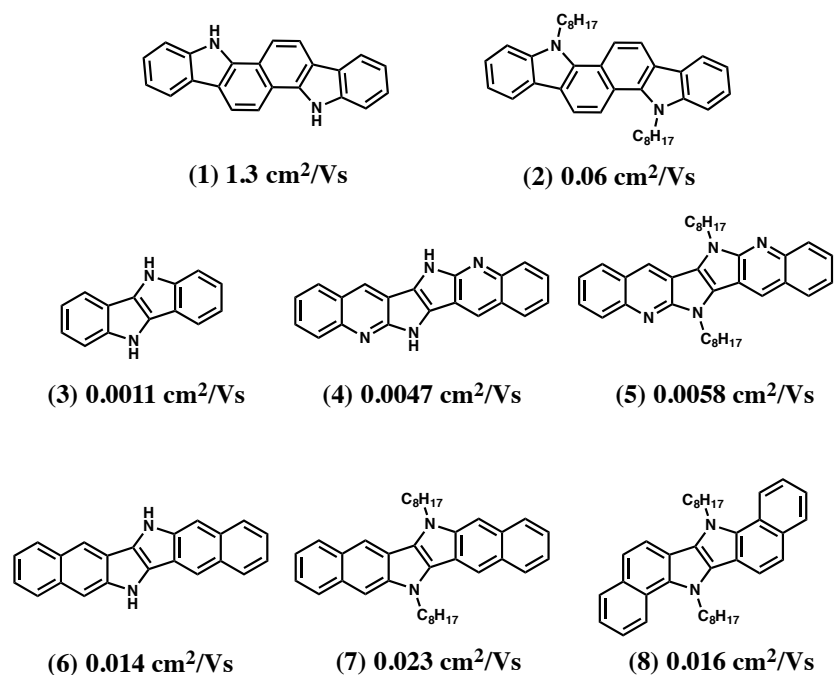


Figure 6.1. Structures of pyrrolo[3,2-*b*]pyrrole derivatives and corresponding hole mobility values found in literature. [117][178]

6.2 Results and Discussion

6.2.1 Thermal properties

We started characterization of ININ solid state properties with determination of their thermal stability (using thermal gravimetric analysis, TGA) and basic phase transition temperatures (using differential scanning calorimetry, DSC). The results of TGA are collected in **Table 6.1**. All of the molecules exhibit good thermal stability with 5% decomposition temperature above 200°C. In the case of C8-C-inin, the decomposition occurs in three stages. The first stage occurs between 301-385°C and results in more than 50 % decomposition of the molecule (**Figure 6.2**). The second stage occurs 400 and 500 °C and contributes to 10 % of weight loss. The final stage – third stage of the decomposition occurs between 500 and 750 °C, producing char yield of less than 3 %. The rest of the molecules exhibit a two-stage thermal degradation, which possibly follows a different mechanism. By the amount of the weight loss after first stage of degradation in C8-N-inin and Me-N-inin, we can make an assumption that the first stage weight loss is not only due to the cleavage of the alkyl chains but also due to some degradation

of aromatic ININ core. Me-N-inin is the least stable in the molecule series, which leads us to suggest that the presence of the longer alkyl chains somehow stabilizes the overall structure.

Table 6.1. Results of thermal analysis of ININ derivatives.

Sample	T _{5%} , °C	Melting point, °C
C8-C-inin	301.3	151.6
Me-N-inin	222.4	-
C8-N-inin	271.7	75
Ph-N-inin	304.4	-

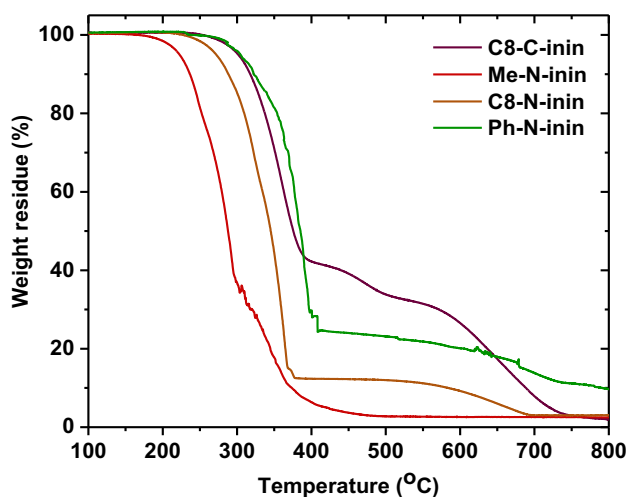


Figure 6.2. Thermogravimetric analysis results of ININ derivatives.

A calorimetric study was performed using differential scanning calorimetry (DSC). This method gives us information on phase transition of the substances. We performed DSC on all of the molecules; however Me-N-inin and Ph-N-inin did not show any phase transitions before decomposition temperature. This suggest strong intermolecular interaction in both of the molecules.

Calorimetric analysis of C8-C-inin (**Figure 6.3**) shows two endothermic transitions on first heating. We repeated this analysis on two different samples that were crystallized from different solvents and the phase transition phenomena are the same. Nonetheless, visual examination of obtained C8-C-inin suggests that there are two polymorphs (needle and rectangular-shaped). This was confirmed by XRD analysis (**Figure 6.7** and **Figure 6.8**).

Therefore, we assign both of the peaks in first DSC scan to melting. Only one melting transition (at 151.6 °C) is reversible, because we observe only one exothermic transition (crystallization) on cooling scan. This suggests preferential crystallization into more stable polymorph. The same phenomenon was reported by Yoon *et al.* for cyano distyrylbenzene derivatives that possess two-colour switchable emission. [179] Crystallization occurs at lower temperature compared to melting, which is a consequence of the supercooling effect.

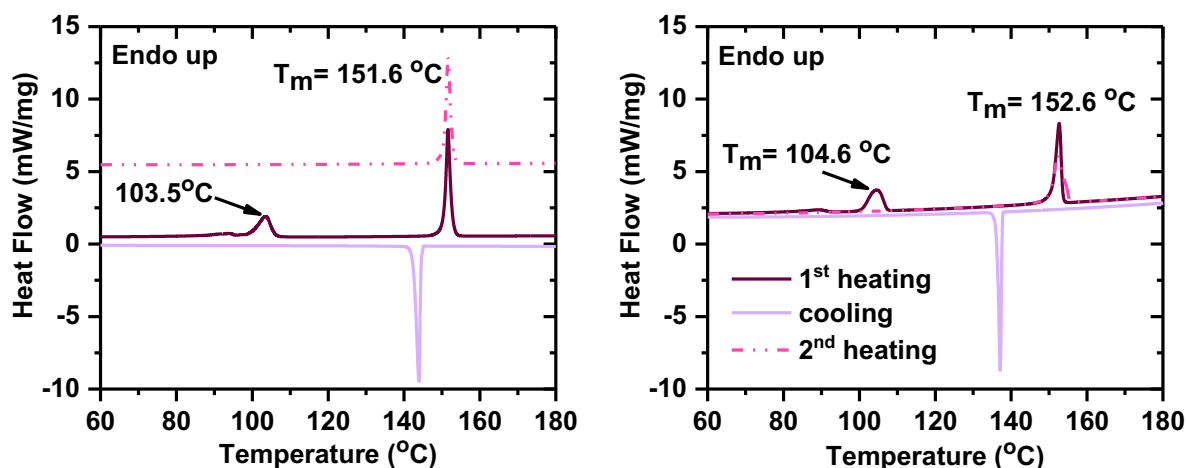


Figure 6.3. Calorimetric curves of the C8-C-inin (crystallized from toluene - left; crystallized from hexane - right) recorded at 10 °C/min.

C8-N-inin was also studied twice with two samples of different crystallinity. One of the samples (**Figure 6.4**) showed two melting transitions (67.6 °C and 75 °C) and two crystallization transitions (35 °C and 31 °C). The second peak of crystallization (31 °C) is significantly smaller than the first one which suggest preferential crystallization into one of the polymorphs. This suggestion is confirmed by the second heating scan where only one melting transition is observed (at 75 °C). Visual examination of crystals suggests two possible crystalline forms (needle and rectangular). However, XRD didn't confirm that there was a difference between these two types of crystals. The second sample of this material (**Figure 6.5**) showed only one melting transition at 75 °C. The full width of half maximum for all of the motioned transitions is less than 10 °C which confirms the high purity of materials.

One-degree difference in the temperatures of transitions between two different samples of C8-C-inin is because the measurements were performed on different devices with different working principle. The same explanation is applicable to a different degree of supercooling in C8-N-inin DSC results.

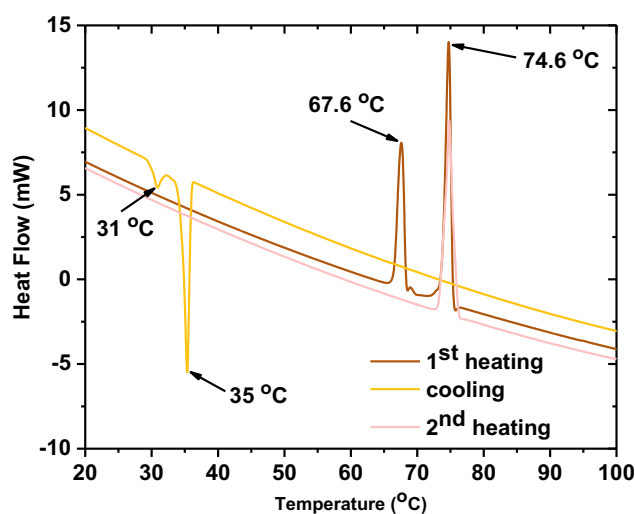


Figure 6.4. Calorimetric curves of the C8-N-inin (white needles) recorded at 10°C/min.

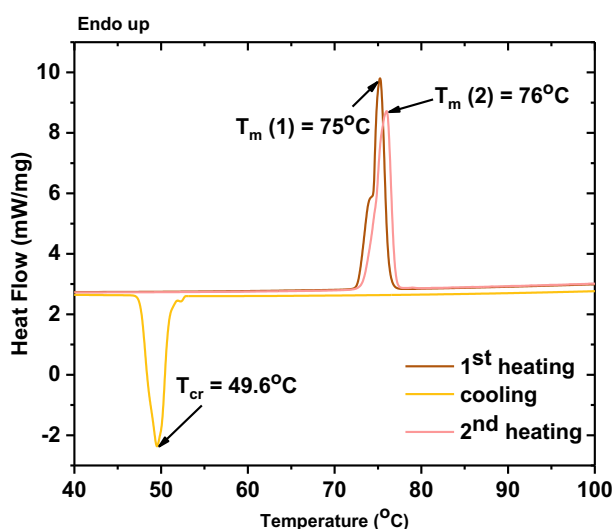


Figure 6.5. Calorimetric curves of C8-N-inin polycrystalline sample recorded at 10°C/min.

6.2.2 Single crystal X-ray diffraction (XRD) analysis

Morphology and molecular arrangement are very important for both field effect transistors and photophysical properties. We designed our molecules to pack differently in the solid state. For example, steric hinderance of aryl substituents on the short axis of the molecule is known to block herringbone packing and promote π - π overlap. [19] The long alkyl chains on the long axis is known to reduce dynamic disorder (thermal fluctuation in charge transfer integral) in the films [34], which could result in better charge carrier mobility. To evaluate molecular

arrangement of ININ derivatives we first studied it in single crystals. **Table 6.2** summaries properties of ININ crystals.

In C8-N-inin crystals, the ININ chromophores are essentially surrounded by alkyl chains which would only allow for very little interaction between the chromophores (**Figure 6.6**). The distance between nitrogen atoms is the largest among ININ derivatives (5.3-5.8 Å). The chromophores adopt face-to-edge orientation towards each other with the smallest distance between them being 4.01 Å. Due to edge-to-face orientation, the electronic interaction should not be efficient.

We discovered two polymorphs of C8-C-inin crystals, in which alkyl chains of the molecules are arranged slightly different in relation to ININ core (**Figure 6.8**), and the molecules adopt a different unit cell geometry. Polymorph 1 (needles) (**Figure 6.7**) represents a well-ordered system. On the b-axis of the crystal, the molecules are parallel to each other and displaced only along the short axis of the molecules (pair 1 on **Figure 6.7**). This allows for alignment of alkyl chains (with interchain distances of 2.89-3.67 Å) that results in a significant amount of weak interactions, which could add up to a significant force constant leading to reduced amplitude of vibrations. [34] The distance between nitrogen atoms is smallest on the b-axis (4.13 Å). On the a-axis, the molecules are also parallel to each other but significantly displaced both along short and long axis of the molecule (by approximately half of the molecule), this results in methyl groups being located near phenyl rings of the ININ core as indicated on the **Figure 6.7** (pair 2). The distance between nitrogen atoms is 5.49 Å.

Polymorph 2 (rectangle) (**Figure 6.8**) belongs to the orthorhombic crystal system, unlike polymorph 1 (monoclinic). In polymorph 2, the angle between one of the alkyl chains and the ININ core is different compared to that polymorph 1. The unit cell is composed of 4 molecules which can be grouped in two pairs with different arrangement. In pair 1 the distance between nitrogen atoms is 4.05 Å, whereas in pair 2 this distance is 4.77 Å. This indicates a larger displacement of molecules in pair 2. Unlike in polymorph 1, the molecules in the unit cell are not parallel to each other but slightly tilted towards each other in an angle of 36°. This could limit the orbital overlap between the molecules.

Molecules in Me-N-inin crystal, despite the planar structure and smaller size of Me-N-inin, do not exhibit face-to-face packing and π - π overlap (**Figure 6.9**). However, there are close-range interactions between carbon and hydrogen atoms (within 2.74 -2.84 Å). The distance between nitrogen atoms is 3.4 Å, which is slightly smaller than the distance between sulfur atoms

in n-BTBT (3.5 Å). Some of the methyl groups are located close to the aromatic core (3.2 Å). Interestingly, molecules are shifted relative to each other both on the long and short molecular axis. This results in the methyl group being close to the nitrogen atom (3.45 Å).

Ph-N-inin adopts co-facial one-dimensional slipped π - π stacking with significant molecular overlap (**Figure 6.10**). The torsional angle between the ININ core and the phenyl is 41°. Intermolecular distance between face-to-face oriented molecules is small (3.52 Å) and the distance between nitrogen atoms is 4.96 Å, which is larger than between sulfur atoms in BTBT derivatives. [53] There are also some close-range interactions, ranging from 2.74 Å to 2.89 Å, these distances represent interactions between phenyl substituents. The edge-to-edge distance between the two ININ cores is also quite small (3.89 Å). The face-to-face packing arrangement suggests possibility of high charge carrier mobility.

Table 6.2. XRD parameters of ININs single crystals.

	Me-N-inin	C8-C-inin (1)	C8-C-inin (2)	C8-N-inin	Ph-N-inin
Crystal system	<i>Monoclinic</i>	<i>Monoclinic</i>	<i>Orthorhombic</i>	<i>Monoclinic</i>	<i>Triclinic</i>
a, Å	17.044	8.162	8.3317	15.2252	9.7389
b, Å	5.5327	4.665	9.2951	9.0838	11.6666
c, Å	13.7413	35.98	35.265	18.8554	15.9535
α°	90	90	90	90	82.525
β°	113.761	96.292	90	101.361	81.155
γ°	90	90	90	90	77.940

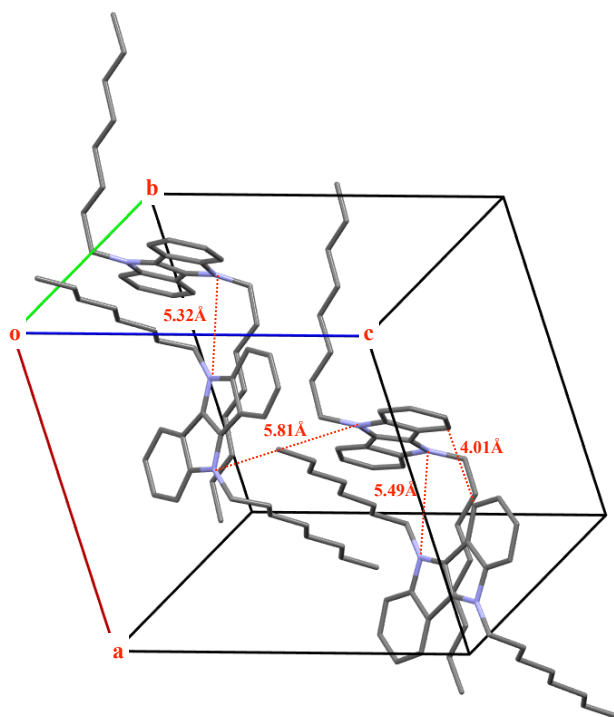


Figure 6.6. Unit cell structure of C8-N-inin single crystal.

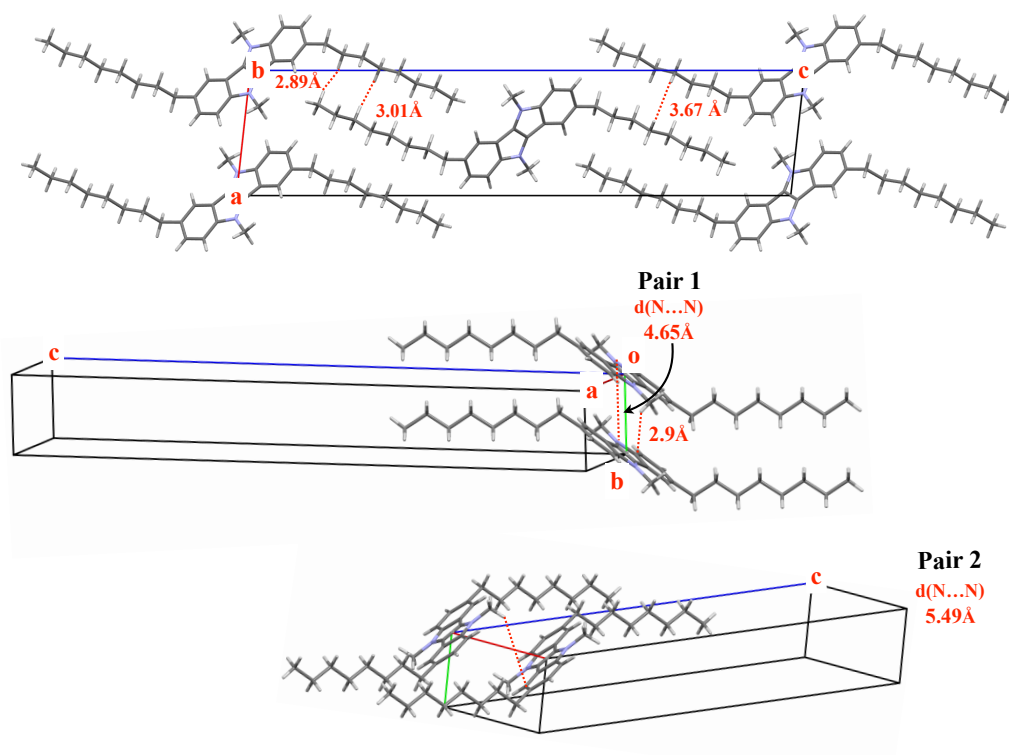


Figure 6.7. Unit cell structure of C8-C-inin single crystal polymorph (1).

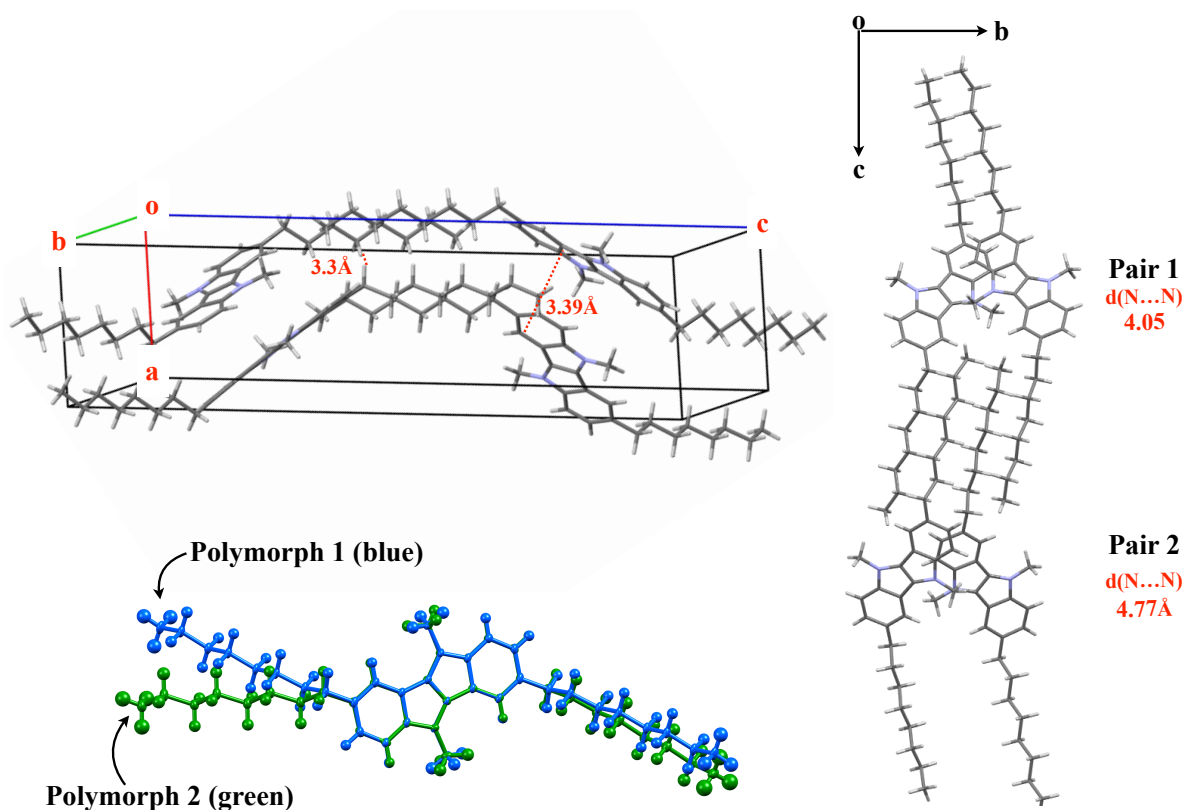


Figure 6.8. Unit cell of C8-C-inin single crystal polymorph (2).

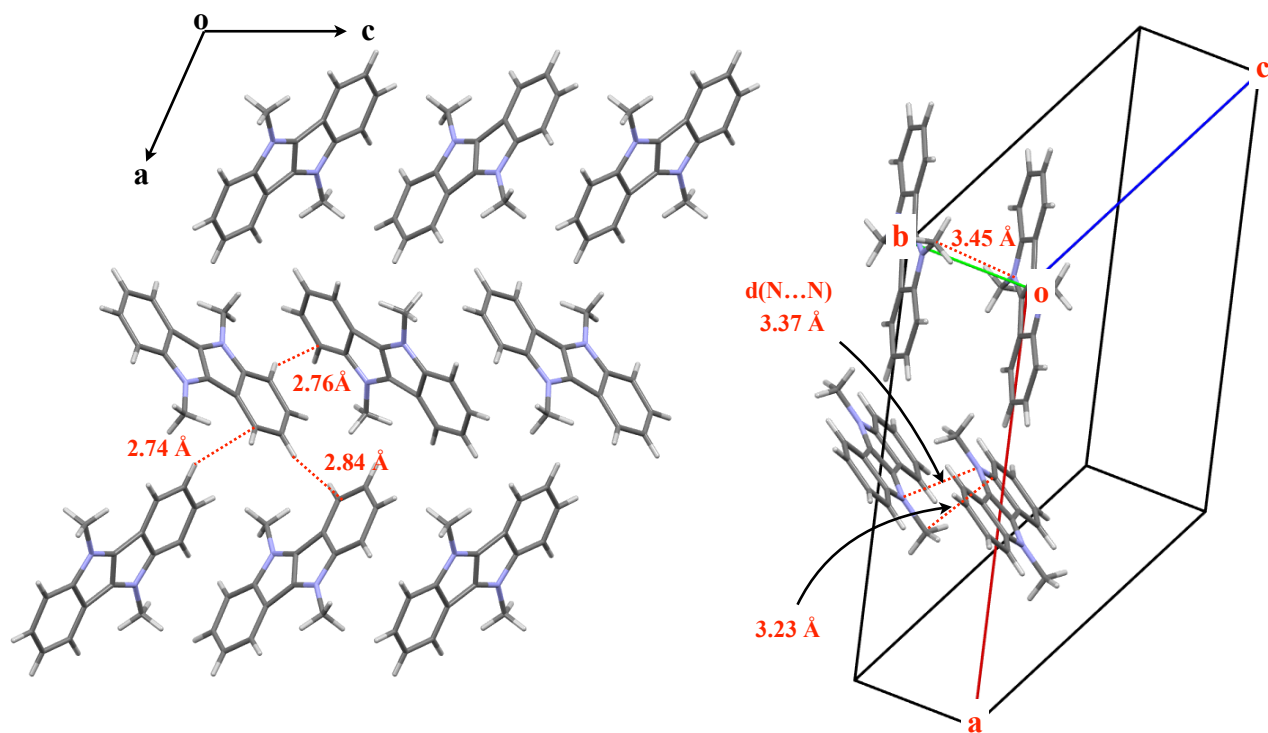


Figure 6.9. Unit cell structure of Me-N-inin single crystal.

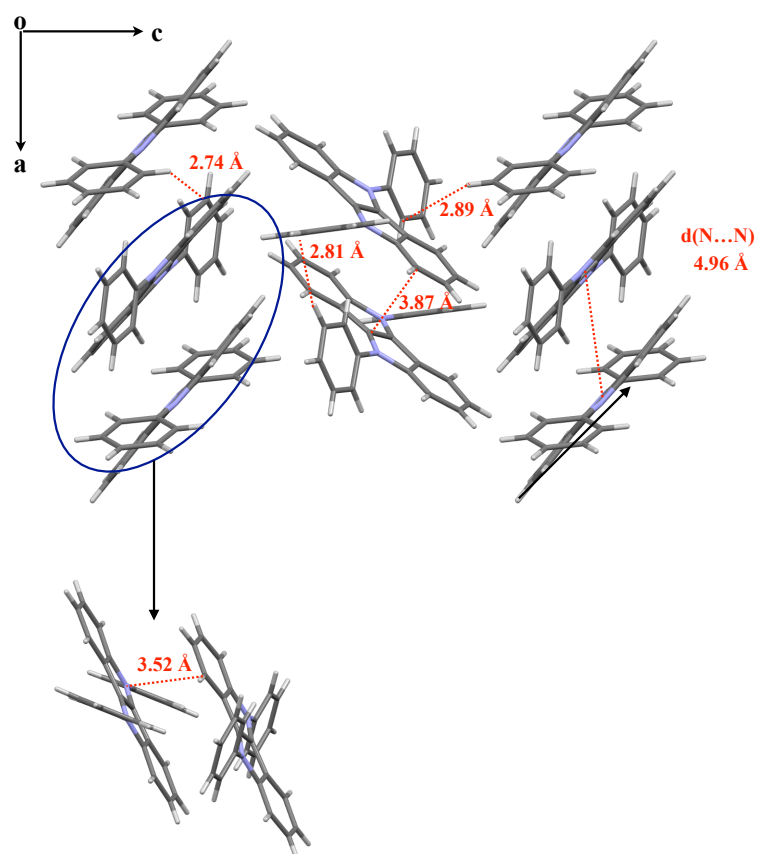


Figure 6.10. Unit cell structure of Ph-N-inin single crystal.

6.2.3 Crystallinity and morphology analysis of the films

We prepared thin films of ININ derivatives by vacuum deposition onto quartz glass and Si/SiO₂ substrates. The thickness of the films that we used for spectroscopy was 80 nm. We used AFM, XRD and GIWAXS to characterize molecular arrangement and physical properties of the films.

6.2.3.1 Atomic force microscopy (AFM) of ININ films

AFM images of the evaporated films show that C8-C-inin and C8-N-inin form crystalline arrays. In a C8-C-inin film, large molecular domains with terrace-like layers, and the minimum height of a terrace is ~ 2 nm are observed. (Figure 5.6.11, A). C8-N-inin film also exhibits large molecular domains but the height distribution of 1.5 – 5 nm (Figure 5.6.11, B). Me-N-inin film was extremely discontinuous (Figure 5.6.11, C) and exhibited large crystalline structures that were not connected to each other. Due to extreme roughness of the surface, AFM images of Ph-N-inin film could not be obtained.

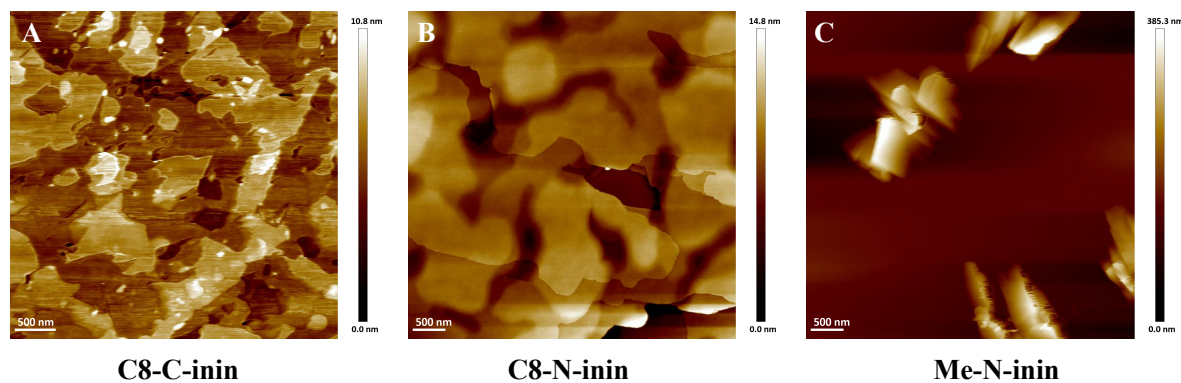


Figure 5.6.11. AFM of evaporated films: A - C8-C-inin (20 nm); B- C8-N-inin (80 nm); C- Me-N-inin (80 nm).

We monitored the morphology of films over a period of six months. AFM results suggest that films surfaces change with time for C8-C-inin and C8-N-inin. In C8-N-inin film the change is not very significant, we observed some sort of “aggregation” of smaller structures into bigger ones (**Figure 6.12, d, e, f**).

In contrast, C8-C-inin film morphology changes drastically: from terrace-like layers with the height of ~ 2 nm to a needle-like structures with a longer range molecular order, and a height distribution of the domains of 2 – 14 nm (**Figure 6.12 (a, b, c)**). The higher crystallinity of the film suggests that molecules move to maximize interactions between each other to form a more stable structure. We used AFM to monitor the freshly evaporated film over the period of 8 hours (**Figure 6.13**) and found that the film morphology changes significantly over this time, essentially, smaller molecular assemblies transform into larger aggregates. This change might be triggered by the heat generated during experiment, even though it was quite low ($\sim 25^\circ\text{C}$). Interestingly, the film morphology after this experiment does not correspond to what we have observed in the film that was stored in inert atmosphere of glovebox (**Figure 6.12, B**). We, therefore, conclude that ambient conditions have a strong influence on the film morphology and aggregation rate.

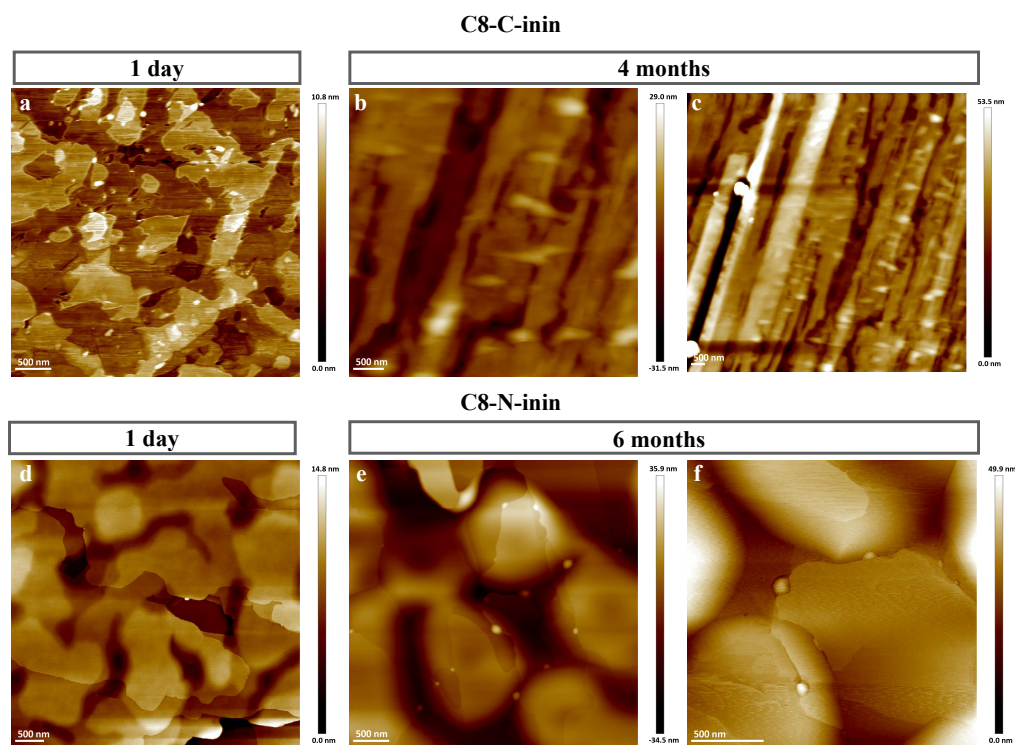


Figure 6.12. AFM of evaporated films: a - C8-C-inin (20 nm) 1 day after evaporation; b and c - C8-C-inin (80 nm) 4 months after evaporation; d - C8-N-inin (80 nm) 1 day after evaporation; e and f - C8-N-inin (80 nm) 6 months after evaporation.

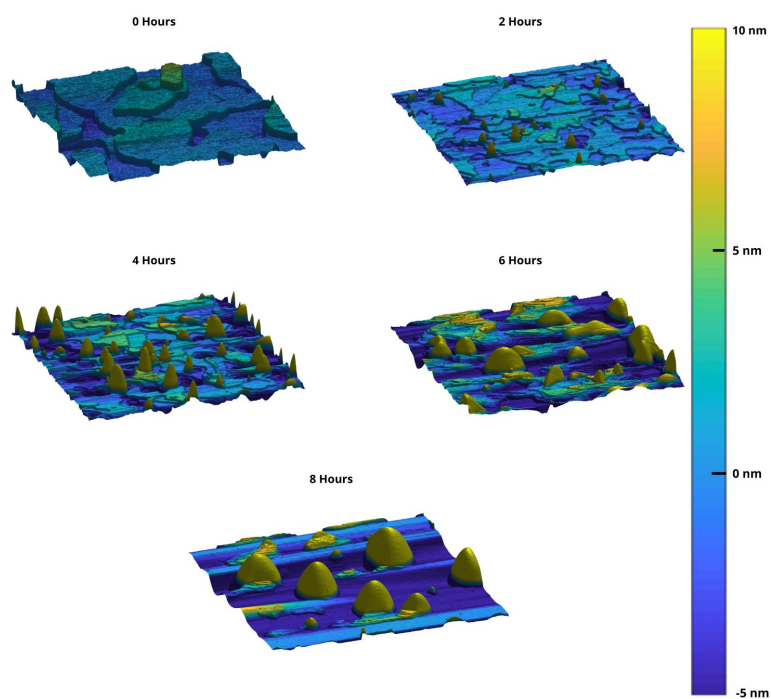


Figure 6.13. AFM images of C8-C-inin (20 nm) obtained by continuous measurement of the film over 8 hours. The size of the image is $2 \times 2 \mu\text{m}$.

6.2.3.2 Thin films XRD

C8-C-inin film exhibits three diffraction peaks, with primary peak at 2θ : 4.28° and $d(001)$ -spacing of 2.1 ± 0.1 nm. These 2θ and d -spacing correspond to a diffraction pattern calculated from single crystal XRD, but due to the lack of peaks in our film XRD data the type of the polymorph cannot be determined. The value of d -spacing roughly matches the height of the molecular terraces observed in AFM roughly (section 6.2.3.1). We found that the d -spacing is smaller than in C8-BTBT film evaporated in the same conditions, in which the d -spacing was found to be 2.7 ± 0.1 nm, and it corresponds to an on-edge molecular arrangement shown on **Figure 6.15** [53]. The size of the long axis of C8-C-inin and C8-BTBT is approximately the same. Smaller d -spacing in C8-C-inin film suggests that in C8-C-inin molecules are slightly tilted on the surface.

XRDs of C8-N-inin, Me-N-inin and Ph-N-inin films were obtained. However, the patterns (**Figure 6.16**) did not correspond to calculated patterns from single crystal data. This could be due to three reasons. First, the molecules do not adopt the same solid-state arrangement as in a single crystal. The evaporation conditions play an important role in the film structure. This was shown for pentacene, that was found to adopt amorphous molecular orientation in certain evaporation conditions even though normally pentacene can be easily crystallized. The temperature of a substrate during film deposition is crucial for molecular arrangement and, thus, heating the substrate during the vacuum deposition could yield a highly crystalline pentacene film in which molecular arrangement matches the crystal arrangement. [180] Therefore, the unfavourable evaporation conditions could be the reason why we do not observe diffraction peaks from Ph-N-inin and Me-N-inin films.

The second reason could be that the initial quality of film was poor and not suitable for XRD, according to AFM Me-N-inin didn't form a smooth film and Ph-N-inin film could not be recorded due to extreme roughness of the film.

The final reason, as we discussed in section 6.2.3.1, molecules in these films can change their arrangement over time. This means, that storage conditions of the films might have influenced their morphology and crystallinity, which could result in poor crystallinity of the films.

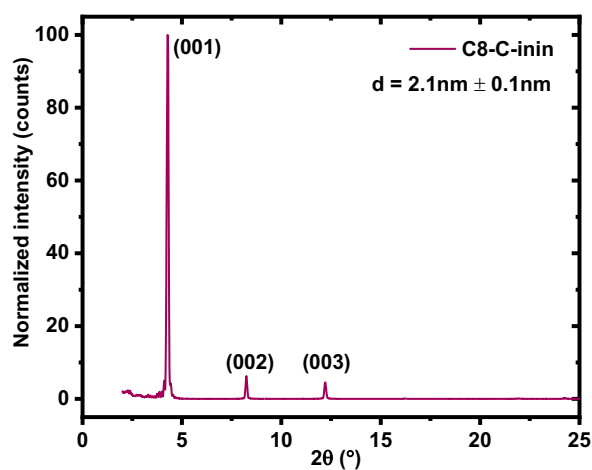


Figure 6.14. Out-of-plane XRD pattern of C8-C-inin 80 nm film on Si/SiO₂ substrate.

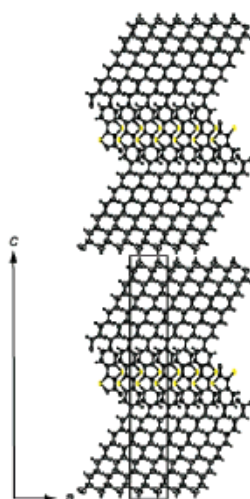


Figure 6.15. *b*-axis projection representing a lamella structure of C_n-BTBT derivatives, reported by Ebata *et al.* [53]

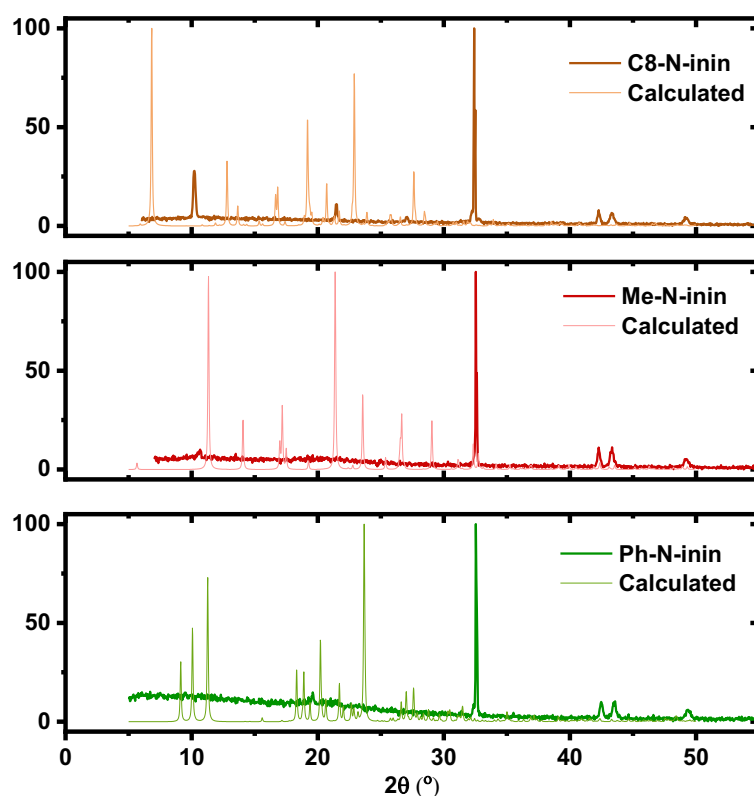


Figure 6.16. Out-of-plane XRD patterns of C8-N-inin, Me-N-inin and Ph-N-inin 80 nm film on Si/SiO₂ substrate.

6.2.4 Thin films characterization using grazing incidence x-ray scattering (GIWAXS)

Although we have not yet managed to fully analyse the GIWAXS data, which requires further careful experiments. Our preliminary data shows a clear transition in crystalline structure between fresh and aged sample (**Figure 6.17 left and right**, respectively). This is consistent with our AFM results. We tentatively assign the fresh sample to a more amorphous structure with some of the molecules in a perpendicular orientation to the surface (**Figure 6.17 left**, signal at high q). The aged sample show a significantly more ordered crystalline structure (**Figure 6.17 right**).

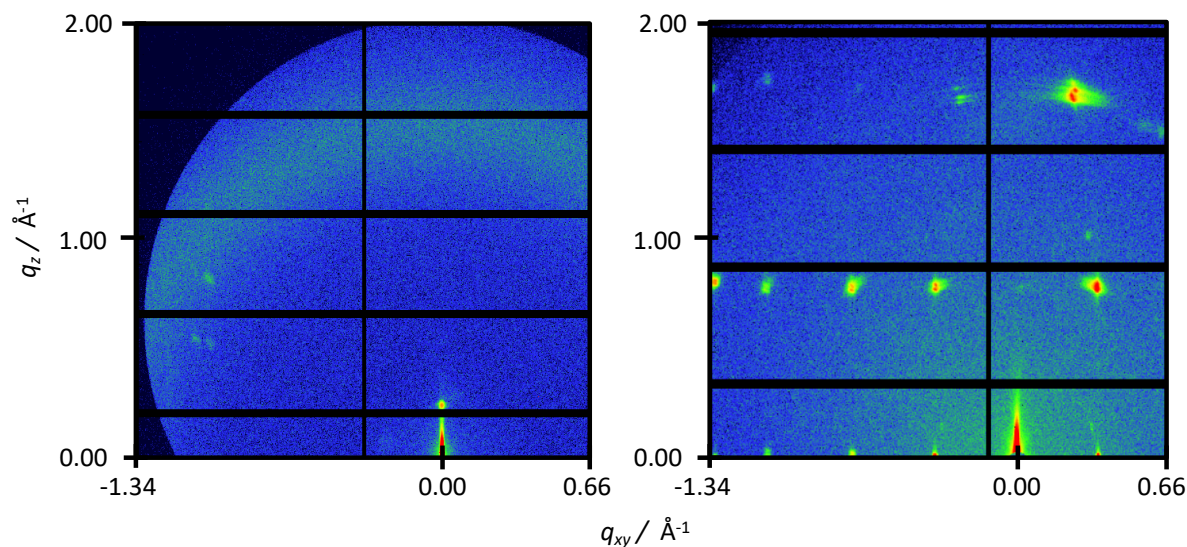


Figure 6.17. GIWAXS image of the evaporated films C8-C-inin on Si/SiO₂ substrate: left – one day old sample, right – one month old sample.

6.2.5 Thin film field effect transistors

The devices were prepared and measured within 3 days, unless otherwise is specified. We tested Me-N-inin, C8-N-inin and C8-C-inin as semiconductors in thin film field effect transistors. We used top contacts bottom gate transistor architecture for our measurements (**Figure 3.7**). We found that devices with C8-N-inin and Me-N-inin didn't act as transistors and showed no charge carrier mobility. In the case of C8-N-inin this is probably due to no π - π overlap. The absence of charge carrier mobility in Me-N-inin film we rationalize by poor film quality. The films obtained by evaporation were visibly crystalline and not smooth, which was clearly observed in AFM (**Figure 6.12c**). The morphology of the interface between insulator and semiconductor is known to have a significant impact on a transistor's performance. This is a very important factor because the charge carrier mobility itself occurs in a very narrow region (the accumulation layer), which has a thickness of only a few nanometres. [181] It is also possible that the interface influence is due to the localized nature of charges at the rough interface or poor arrangement of between hopping sites in a rough film. [4] Ph-N-inin also didn't form good films upon evaporation, this is why it has not been used it in transistors.

Table 6.3. FET characteristics of C8-BTBT and C8-C-inin devices fabricated on Si/SiO₂ substrates with different monolayers.

Transistor parameters	Molecules and corresponding monolayers			
	C8-BTBT	C8-C-inin	C8-C-inin	C8-C-inin
	HMDS	HMDS	CYTOP	-
V _{th, lin} (V)	-14.65	-6.2	-11.9	-26.7
V _{th, sat} (V)		-7.2	-19.5	-20.1
I _{ON} /I _{OFF}	8.27*10 ⁴	0.28*10 ⁴	3.6*10 ⁴	0.065*10 ⁴
Linear Mobility μ_{lin} (cm ² /V ⁻¹ s ⁻¹)	0.4186	0.0292	0.11	0.0062
Saturation Mobility μ_{lin} (cm ² /V ⁻¹ s ⁻¹)	0.4197	0.069	0.27	0.0125

C8-C-inin showed good p-channel FET responses with field-effect mobility of 0.01-0.27 cm²/Vs. To evaluate the efficiency and potential for improvement of devices based on C8-C-inin, we made a transistor with the well characterized semiconducting molecule C8-BTBT. [53] This molecule was reported to have a charge carrier mobility of 0.46-1.8 cm²/Vs in a polycrystalline film. [53][38] The mobility that we find (0.42 cm²/Vs) is similar to what has been previously reported. **Table 6.3** compares the charge carrier mobility of C8-BTBT and C8-C-inin, showing that in identical conditions (on HMDS monolayer) the charge mobility in C8-BTBT is 14 times higher than in C8-C-inin. To optimize the performance of C8-C-inin, we tested a different monolayer - CYTOP (**Figure 3.6**). Both of these monolayers (HMDS and CYTOP) have a nonpolar hydrophobic surface, which can improve surface morphology and mutual orientation of the charge transporting molecules. The surfaces treated with hydrophobic substances are also known to promote on-edge packing that is beneficial for charge injection. [182] We compared the performance of these devices with a device without a monolayer.

Our results show that for C8-C-inin on CYTOP charge carrier mobility is 3 times higher than on HMDS, whilst it is almost 5 times lower in a device without a monolayer. Comparing these results with devices based on C8-BTBT suggests that C8-C-inin could potentially have similarly high mobility in an optimized device structure.

Interestingly, the transistor performance improves slightly after a month of storage suggesting some degree of rearrangement of molecules on the surface. This is in an agreement with the higher crystalline order observed in AFM. The transistors characteristics after a month of storage (in air) are presented in **Table 6.4**.

Table 6.4. Aging of TFT devices based on C8-C-inin: transistor characteristics after one month of storage.

Monolayer	$V_{th, lin}$ (V)	$V_{th, sat}$ (V)	μ_{lin} (cm ² /V ⁻¹ s ⁻¹)	μ_{sat} (cm ² /V ⁻¹ s ⁻¹)
HMDS	-12.5	-11	0.063	0.122
CYTOP	-10.2	-14	0.12	0.25
Clean	-27.6	-27.6	0.023	0.052

6.2.6 Steady state spectroscopy of ININ derivatives in films

Figure 6.18 shows steady state absorption and emission in evaporated films of ININ derivatives. All of the films were prepared by vacuum deposition, however absorption spectra of Me-N-inin and Ph-N-inin could not be recorded from those films due to high scattering. Instead, we prepared different films by drop-casting of 30 mM solution onto the quartz glass. These films were used only for absorption measurements of Me-N-inin and Ph-N-inin and the resulted spectra might not be representative of absorption in vacuum deposited film. The non-zero background in absorption is due to scattering.

Figure 6.18 shows that films of ININ derivatives have a redshifted (~10 nm or 100 meV) film absorption spectra (panels A, B, C, D) compared to solutions. This is a very small solution-to-crystal shift compared to the similar C8-BTBT, in which this shift is almost 310 meV (**Figure 6.19**).

The steady state emission spectrum of C8-N-inin looks very similar to its emission in solution, whereas in C8-C-inin, Me-N-inin and Ph-N-inin spectra contributions from two emissive species are observed. A solution-like emission at 375-450nm is due to monomer emission. A redshifted broad emission (at 450-600 nm) is assigned to excimer emission, indicating strong intermolecular interactions in the films of these molecules.

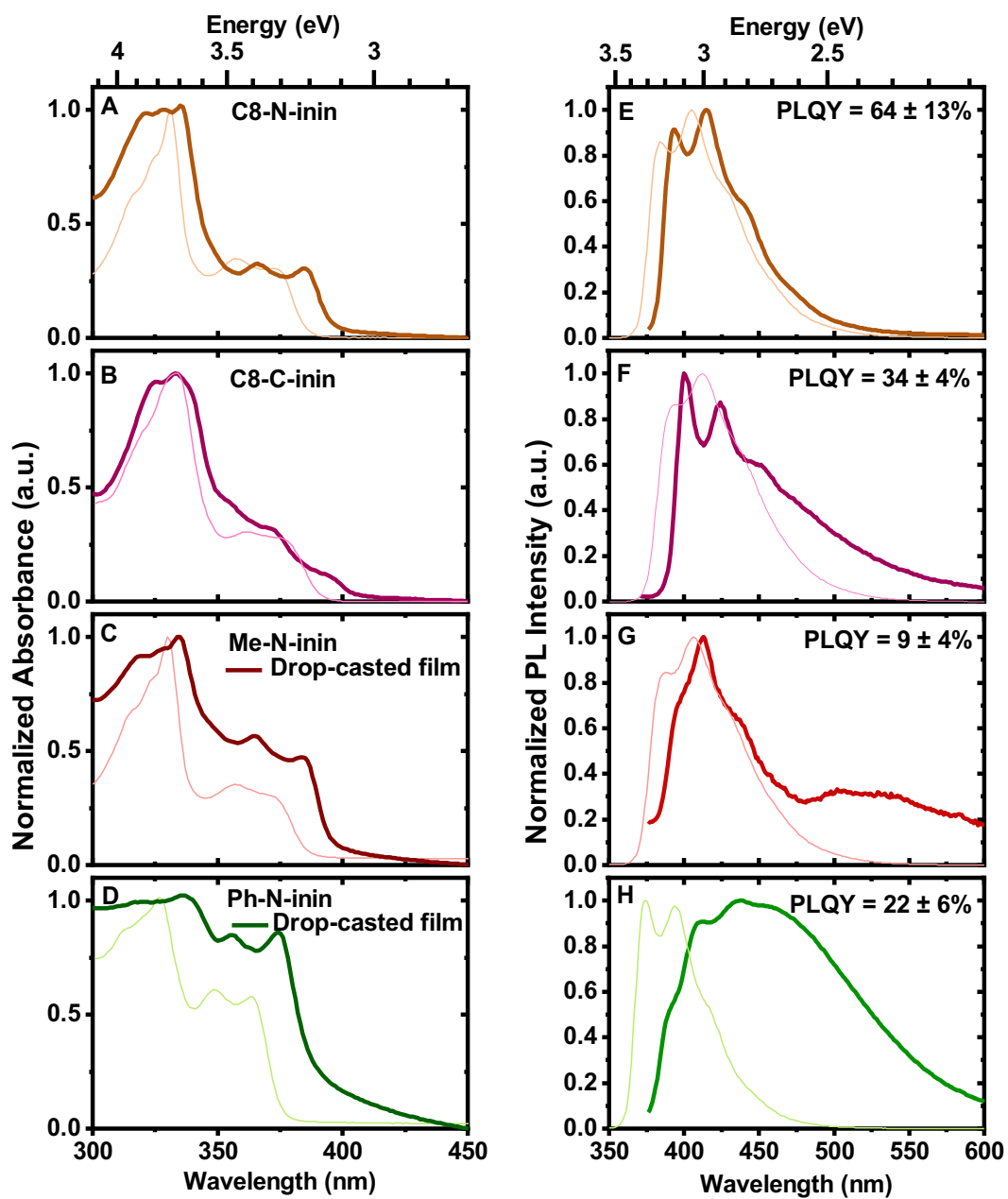


Figure 6.18. Steady state absorption, emission ($\lambda_{\text{ex}} = 355\text{nm}$) and PLQY of ININ evaporated (80nm) films (solid lines) compared to spectra in 10uM toluene solutions (thin solid lines).

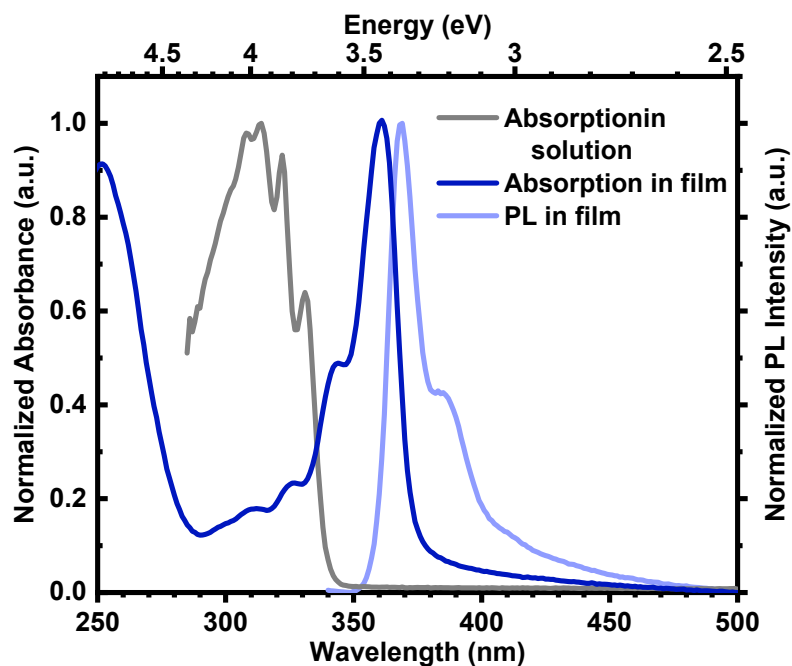


Figure 6.19. Steady state absorption and emission spectra of evaporated (60 nm) C8-BTBT film compared to 10 μM solution of C8-BTBT in toluene, ($\lambda_{\text{ex}} = 330 \text{ nm}$).

6.2.6.1 Film aging effects on absorption and emission

AFM results (section 6.2.3.1) suggest that films surfaces change with time for C8-C-inin and C8-N-inin. In C8-N-inin film the change is not very significant: we observed some sort of “aggregation” of smaller structures into bigger ones (Figure 6.12, d, e, f). Figure 6.20 shows that these changes in morphology have almost no influence on the optical properties.

C8-C-inin had a more significant changes in AFM (Figure 6.12, a, b, c) and these changes have a significant influence on the optical properties (Figure 6.21). There is an obvious redistribution of oscillator strength in absorption (Figure 6.21, left). The low energy absorption band (350-400 nm) gains intensity. Fluorescence spectra of C8-C-inin also reflects changes in the film structure (Figure 6.21, right): vibronic peaks maxima shift to higher energies and there is a redistribution of intensities compared to a freshly made film. The difference in intensities could be explained by stronger interaction and also stronger reabsorption of the molecules in the aged film.

Films of Me-N-inin and Ph-N-inin also undergo significant aging which translates onto their optical properties (Figure 6.22). Absorption of these films could not be recorded due to their high scattering. Fluorescence spectra of Me-N-inin aged film looks very similar to the fresh film, however, the intensity of the excimer emission is much higher in relation to high energy

monomer emission band (~ 400 nm). This change indicates that there are more molecules that can interact strongly or that energy transfer to these sites is more efficient, which is representative of smaller distances or different orientation between the chromophores. The change in Ph-N-inin emission spectra is more subtle, only the intensity of low energy part of the spectra is affected. Interestingly, it becomes less intense unlike in the case of Me-N-inin.

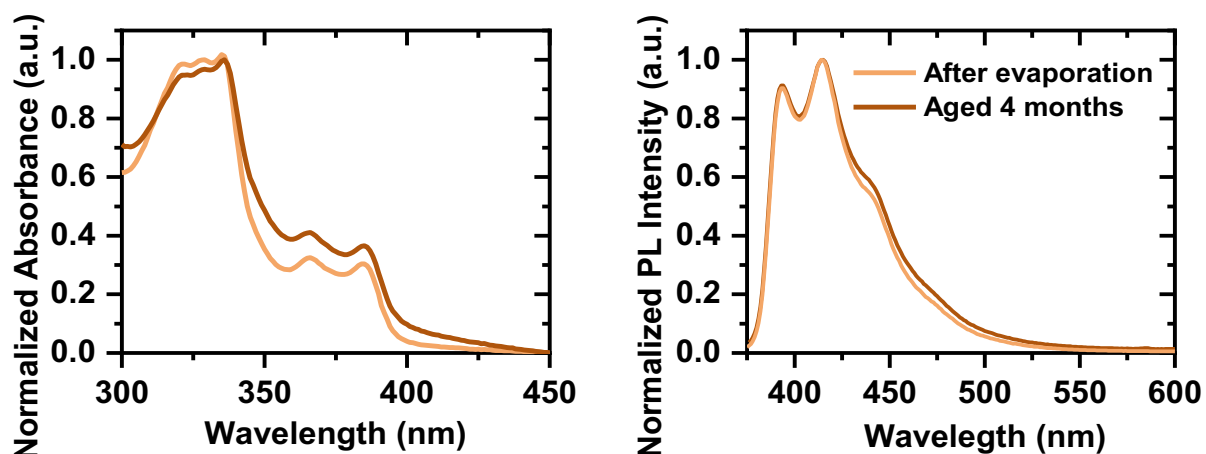


Figure 6.20. Aging of C8-N-inin vacuum deposited film (80nm), $\lambda_{\text{ex}} = 355$ nm.

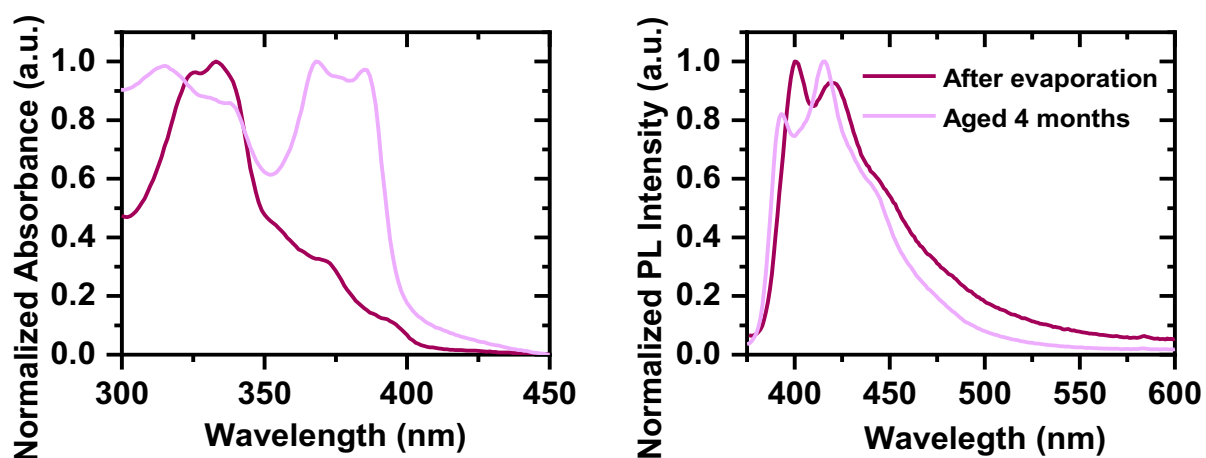


Figure 6.21. Aging of C8-C-inin films made by vacuum deposition, $\lambda_{\text{ex}} = 355$ nm.

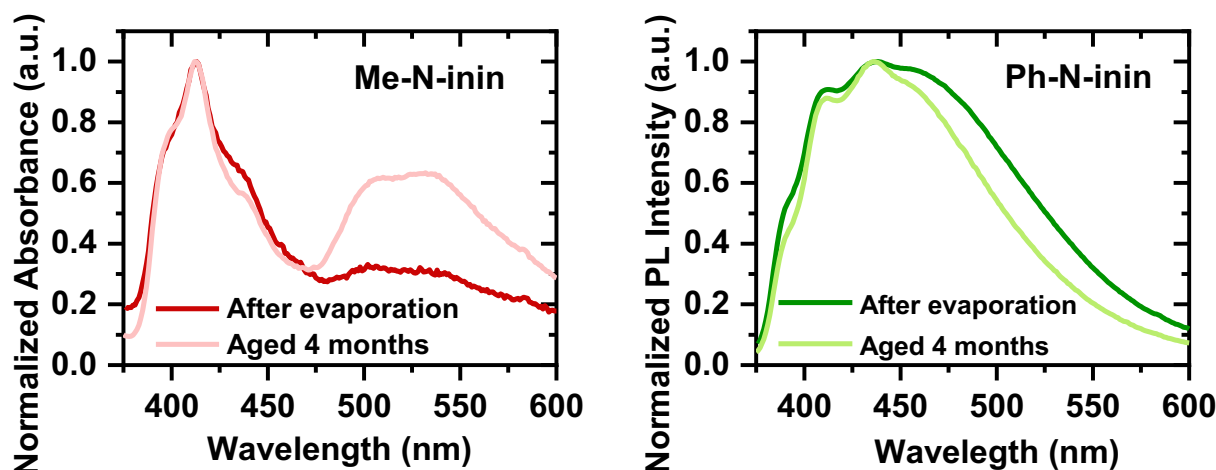


Figure 6.22. Aging of Me-N-inin and Ph-N-inin films made by vacuum deposition, $\lambda_{\text{ex}} = 355\text{nm}$.

6.2.7 Time-resolved temperature dependent photoluminescence

We will now discuss each molecule individually and try to understand how the intermolecular interactions influence photophysics of these derivatives. We used Nd:YAG laser to generate $\lambda_{\text{ex}} = 355\text{nm}$, the emission was recorded by a gated ICCD camera as described in section 3.4.8. All of the films were fresh and didn't exhibit any signs of aging. **Figure 6.23** shows kinetics and spectral evolution of the C8-N-inin film emission at different temperatures. The difference in shape of the spectra recorded by the ICCD compared and steady state spectra recorded by a fluorimeter is due to poor sensitivity of the ICCD in the region below 400nm which we were unable to correct for. All the data presented here were collected in vacuum; however, oxygen was found to have only minor effect on emission lifetime. In all the studied molecules the emission had linear dependence on laser power at 100 ns time-delay, which means no triplet-triplet annihilation was observed.

6.2.7.1 Photophysics of C8-N-inin

The single crystal X-Ray diffraction suggests that in C8-N-inin the ININ core is surrounded by alkyl chains (**Figure 6.6**). In thin films C8-N-inin most probably does not adopt exactly the same molecular arrangement as in the crystal, however, it is very likely that the chromophores will nonetheless be isolated by alkyl chains.

Absorption and emission of C8-N-inin film is redshifted by 10 nm compared to spectra in toluene solution (see comparison on **Figure 6.18 A and E**). This shift is due to stronger

polarization effect of the medium (D' in **Figure 2.8**) is ~ 100 meV, which allows for better singlet stabilization. The line shape of both absorption and emission in the film is very similar to the solution. The peak at 335 nm gained new vibronic structure, which is probably due to finite weak interaction between ININ chromophores. The PLQY remained the same as in solution (64%) and is the highest among the ININ derivatives measured in films. This allows us to conclude that only weak coupling between the chromophores is present and the resonance interaction energy (β) is, therefore, smaller than the reorganization energy.

Our time-resolved luminescence study in solution showed that the prompt emission decay was followed by the delayed luminescence with a non-exponential decay kinetics (**Figure 5.9**). Despite similar spectral characteristics of the film and solution, the emission decay dynamics in films shows only relatively short lived emission (**Figure 6.23**). The dynamics can be fitted with an exponential function with time constants of 12.5 ± 0.6 (this is higher than prompt singlet decay which we attribute to solid state effects, *e.g.* polarization etc). We observe that the integrated emission intensity decreases as the temperature increases (**Figure 6.24**), which is normally expected from organic molecules. This is due to decrease in non-radiative decay rate.

Therefore, we conclude that molecules are electronically separated from each other and, probably, form an amorphous film or adopt a similar arrangement to what we have observed in C8-N-inin single crystal. Thus, ININ the chromophore is essentially surrounded by alkyl chains, which would prevent it from π - π interactions, resulting in solution-like absorption and emission. This molecular arrangement could be of use for organic photonics where intermolecular interactions lead to unwanted quenching or degradation (*via* exciton migration to traps or exciton-exciton annihilation). These applications require high chromophore densities to maximize interaction with light. [183]

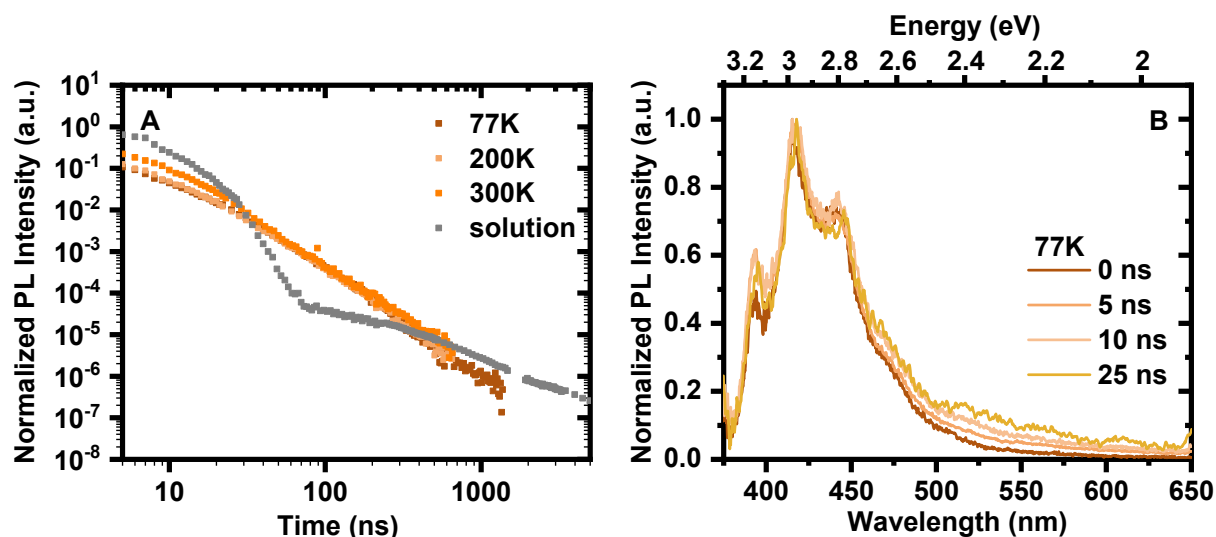


Figure 6.23. Kinetics (taken at 500-510 nm) of C8-N-inin evaporated (80nm) film excited state decay at different temperatures (A) and a spectral evolution at 77K (B), $\lambda_{\text{ex}} = 355\text{nm}$.

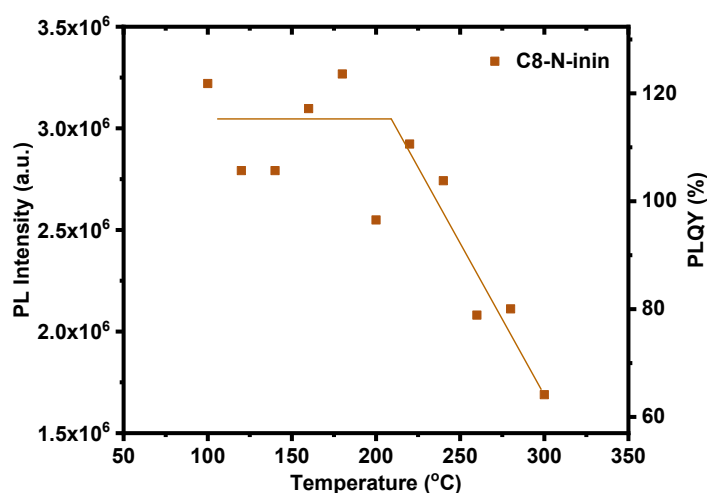


Figure 6.24. Dependence of C8-N-inin photoluminescence intensity on temperature. Left axis: steady state integrated PL intensity of C8-N-inin film (80nm) at different temperature; right axis: estimated PLQY based on the value taken at the room temperature (295K), the error of the measurement was $\pm 13\%$.

6.2.7.2 Photophysics of C8-C-inin

C8-C-inin film had a highly crystalline film structure (Figure 6.14) with d-spacing 2.1 nm. Despite structural similarities with C8-BTBT, C8-C-inin showed very different steady state spectroscopic characteristics. In C8-C-inin film both absorption and emission are redshifted (by

9 nm or 100 meV) compared to solution (**Figure 6.18 B and F**). This singlet energy stabilisation is much smaller than in C8-BTBT film (**Figure 6.19**, stabilization by 310 meV is observed).

In C8-C-inin film, the distribution of oscillator strength between vibronic peaks in absorption is slightly different compared to the spectra obtained in solution. In steady state emission spectrum of C8-C-inin film 0-0 vibronic peak is more intense than 0-1 peak, which is different to what we have observed in solutions. This could be due to smaller reorganization energy in the film. However, this could also be due to mild aggregation. In addition, the emission spectrum is broadened in the low energy region (around 500 nm), which is due to excimer emission.

The absence of large shifts, and presence of some oscillator strength changes in absorption and emission suggests an intermediate value of coupling between the molecules ($\beta \sim E_{\text{reorg}}$), therefore it is probably in the range between 180-220 meV (**Figure 5.6**). This should not significantly affect the emission characteristics such as radiative decay rate. Nonetheless, the PLQY is significantly lower than in solution (34% compared to $\sim 100\%$). The value of PLQY itself is quite large for a molecule with reasonably high mobility, for example the highest reported of a high mobility film is PLQY of $\sim 40\%$. [184]

To investigate this further, we performed a TRPL experiment. Based on time-resolved photoluminescence, we assign the broadening at 500 nm to an excimer emission (**Figure 6.25 B**). **Figure 6.25 (B)** shows excited states spectral evolution in C8-C-inin film, emission at first couple of nanoseconds is dominated by monomer-like singlet state (structured emission at ~ 400 - 450 nm), this is followed by rapid energy transfer to an excimer (broad structureless emission with maximum at 500 nm). Energy transfer from the monomer to the excimer is faster than the time-resolution of our instrument. Excimer emission decay (**Figure 6.25A**) has a complex kinetics that can be described by two time-constants of 5.4 ± 0.2 ns and 23 ± 2 ns (at 77K), however, it still does not describe the whole decay well. Nonetheless, this fitting gives us an idea of the processes that occur after excitation. We suggest that fast component is a monomer singlet decay and long-lived component is due to an excimer emission.

The emission does not exhibit strong temperature dependence (**Figure 6.25A**), the time constants change only slightly when comparing the data taken at different temperatures: 5.4 ± 0.2 ns and 23 ± 2 ns at 77K; 4.8 ± 0.2 ns and 19 ± 2 ns at 320K (collected at 500 nm). The overall integrated PL intensity slightly increases with temperature (**Figure 6.26**), which might be due to thermally activated exciton detrapping.

Therefore, the intramolecular interaction in C8-C-inin are stronger than in C8-N-inin, which leads to excimer formation. Monomer and excimer provide radiative deactivation paths in C8-C-inin film. The significant reduction in the PLQY suggests that non-radiative deactivation is a dominant process in the C8-C-inin film. The nonradiative deactivation can include triplet formation and their non-radiative decay or simple thermalization of excitation energy. The emission kinetics was found to be the same in vacuum and in air, thus triplet states are not the major nonradiative decay path in C8-C-inin film.

Another explanation of the low PLQY in the given circumstances is a presence of non-emissive trap-states that are isoenergetic (or close in energy) with excimer. Such a state could have high non-radiative rate and could be highly populated at low temperatures, but the exciton could detrap at higher temperatures (schematic illustration of the process is given in **Figure 6.27**). However, the decrease of PLQY with temperature is within 10% which is not enough to explain such a decrease in PLQY between the solution and the film. Therefore, we suggest that the low PLQY in films of C8-C-inin is due to a combination of factors: presence of the trap state and high non-radiative decay rate of the excimer.

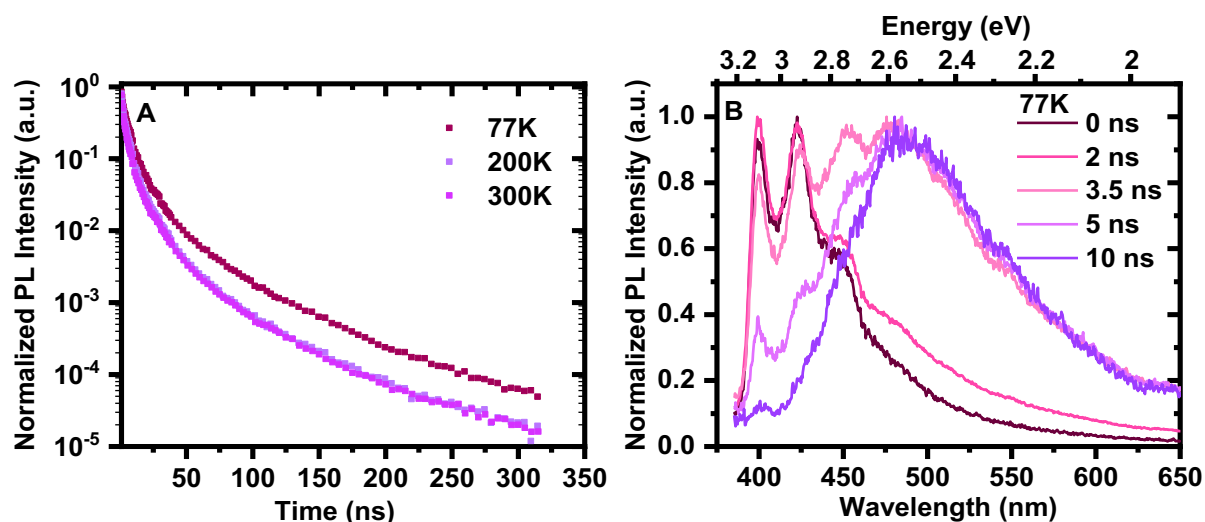


Figure 6.25. Kinetics (taken at 500-510 nm) of excited state decay of C8-C-inin evaporated (80nm) film at different temperatures (A) and spectral evolution at 77K (B), $\lambda_{\text{ex}} = 355\text{nm}$.

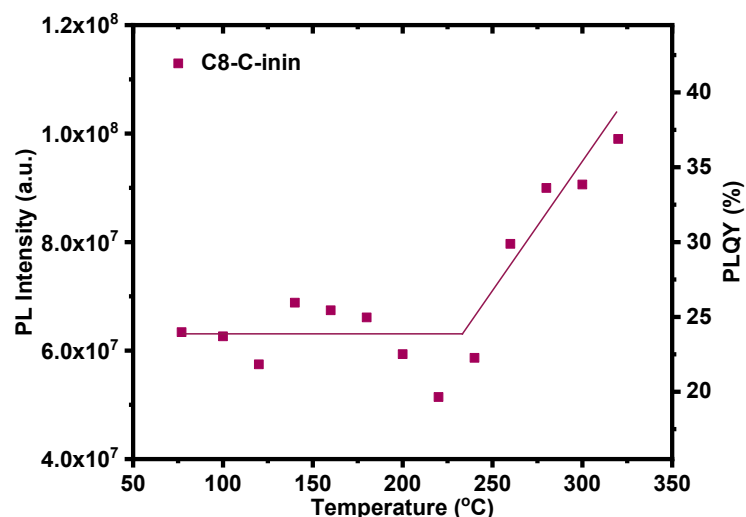


Figure 6.26. Dependence of C8-C-inin photoluminescence intensity on temperature. Left axis: steady state integrated PL intensity of C8-C-inin film (80nm) at different temperature; right axis: estimated PLQY based on the value taken at the room temperature (295K), the error of the measurement was $\pm 4\%$.

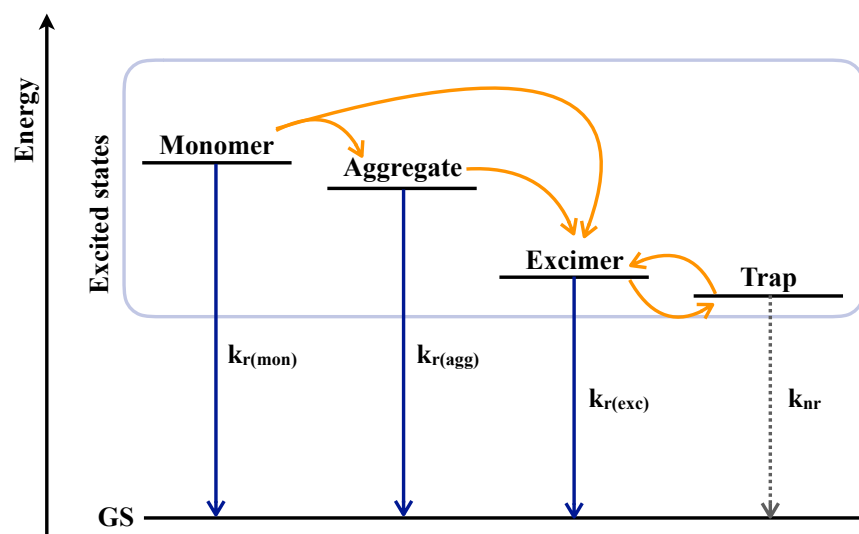


Figure 6.27. Schematic illustration of the photophysical process in C8-C-inin film.

6.2.7.3 Photophysics of Ph-N-inin films

XRD data suggests that Ph-N-inin can potentially have very strong interactions between the molecules in solid state due to π - π overlap. This is also supported by the absence of a melting transition before the decomposition temperature. However, the single crystal data did not

correspond to the film X-Ray diffraction pattern, hence these suggestions should be treated with caution.

Absorption of the drop-casted film exhibits just a 10 nm (~ 100 meV) redshift compared to absorption of the molecule in solution (**Figure 6.18 D**). The steady state emission of Ph-N-inin evaporated film is dominated by broad excimer emission with a peak at 450 nm, the efficiency of emission is lower than in the other derivatives ($22 \pm 6\%$). Evaluation of steady state emission at different temperatures (**Figure 6.28**) shows that the excimer emission peak shifts to lower energies at higher temperatures, with the overall shift of 150 meV from 77K to 320K. This blue shift can be due to hindered reorganization and, hence, stabilization opportunities at lower temperature due to reduction in molecular motion. Another explanation offered in literature suggests the blue shift due to reduced fluctuations at lower temperature. Thus, higher amplitude of fluctuation at high temperature can cause the excimer to emit at lower energy. [185]

The steady state emission intensity in Ph-N-inin film (**Figure 6.28**) shows $\sim 10\%$ increase in PLQY at room temperature compared to 77K. Therefore, the scheme suggested for C8-C-inin is valid for Ph-N-inin (**Figure 6.27**), the increase in emission intensity at higher temperature in Ph-N-inin film is due to thermally activated exciton detrapping.

Time-resolved spectroscopy confirms the existence of two emissive species: monomer and excimer (**Figure 6.30 A**). Excimer emission is temperature dependent and its decay rate increases at higher temperature. Comparison of spectral evolution at 77K and 320K (**Figure 6.30 B and C**) suggests that energy transfer is slower at 77K as the emission maximum is stabilized only at 30ns, whereas at 320K it stabilizes at 15 ns.

Therefore, the interactions between the chromophores in Ph-N-inin lead to formation of the excimers which suggest that resonance interaction energy is larger than the reorganization energy. Thus, we should have observed larger singlet energy stabilization in absorption. This could be explained by “null” aggregate formation, meaning that both H and J aggregates are present in the film. The stabilization energy cancelled as a result of interaction between these two sites.

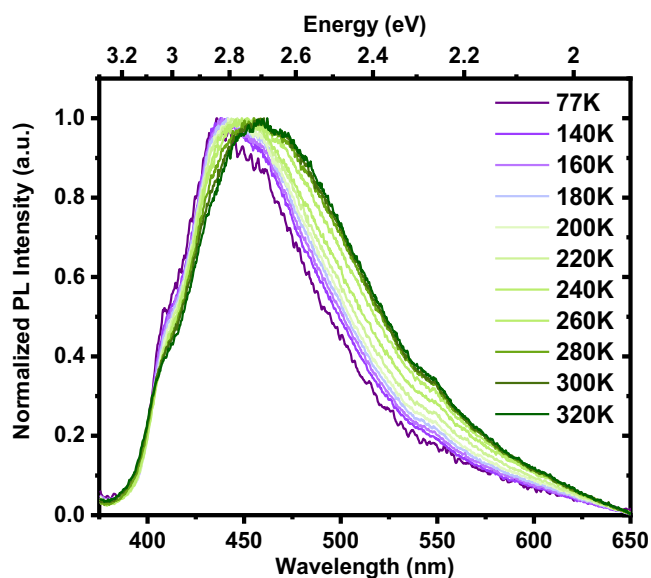


Figure 6.28. Steady state emission of Ph-N-inin evaporated (80nm) film at different temperatures, $\lambda_{ex} = 355\text{nm}$.

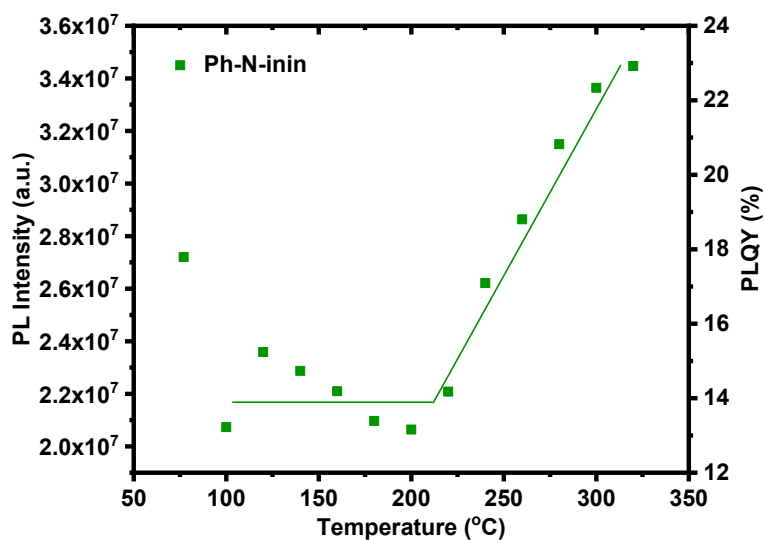


Figure 6.29. Dependence of Me-N-inin photoluminescence intensity on temperature. Left axis: steady state integrated PL intensity of Me-N-inin film (80nm) at different temperature; right axis: estimated PLQY based on the value taken at the room temperature (295K), the error of the measurement was $\pm 6\%$.

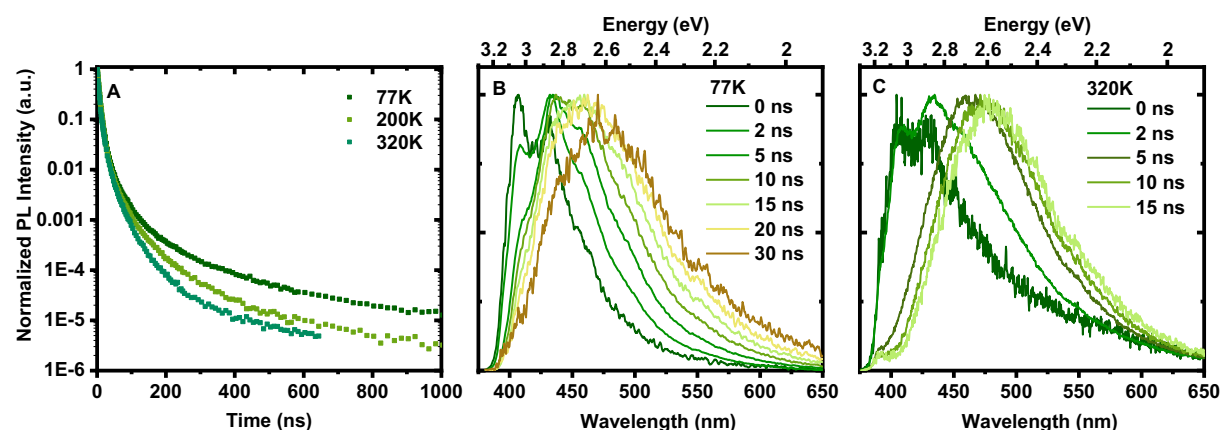


Figure 6.30. Kinetics (taken at 500-510 nm) of excited state decay of Ph-N-inin evaporated (80nm) film at different temperatures (A) and spectral evolution at 77K (B) and 320K (C), $\lambda_{\text{ex}} = 355\text{nm}$.

6.2.7.4 Photophysics of Me-N-inin

In single crystal XRD we observed no π - π overlap, however, the distances between the molecules were still very small (2.74 – 3.5 Å). Using single crystal XRD data we were unable to correctly predict the thin film X-Ray diffraction pattern. However, the absence of melting point before the decomposition temperature suggests that intermolecular interactions between the molecules could be strong.

Absorption of Me-N-inin film is redshifted by ~ 10 nm (100 meV) (**Figure 6.18C**). Relative vibronic peak intensity seems to remain the same as in solutions, suggesting no significant ground state interaction (*i.e.* aggregate formation). However, in the steady state emission spectrum (**Figure 6.18 G**), we clearly see two components: a high energy component with a maximum at 413 nm which corresponds to monomer emission, and a low energy component which corresponds to an excimer (532 nm). Due to presence of both of these components in the steady state spectra, we conclude that these originate from two competitive excitation deactivation paths in Me-N-inin films. This could be due simultaneous emission from two different molecular sites. The shape of the monomer emission is significantly different to what is observed in solutions, which could be explained by strong reabsorption. The PLQY of the Me-N-inin film is the lowest among the derivatives, which is partially due to reabsorption, but is likely to be due to nonradiative decay at non-emissive trap sites, as suggested for C8-C-inin. Therefore, the PLQY could be recovered in a single crystal.

We evaluate steady state emission of Me-N-inin films at different temperatures (**Figure 6.32**). We find that the maximum of excimer emission shifts to lower energies at lower

temperatures, the overall shift of the excimer peak between 320K and 77K is 350 meV. This is a very unusual phenomena, which only recently was explained in literature by Y. Shen *et al.* [186]. In their study, the redshift of emission at low temperatures is explained by the presence of π - π stacking. They studied an anthracene dimer and demonstrated by temperature dependent XRD that the π - π stacking distance decreases with temperature by up to 0.069 Å. As a result, there is a slight change in an alignment of the ground and excited state potential energy surfaces. It was suggested that for π - π stacking the vibrational mode at ~ 50 cm^{-1} is strongly coupled to the electronic transition and it is responsible for broadening in excimer emission. At 77K kT is 53.5 cm^{-1} , comparable to the vibrational energy. Therefore, at 77K only the 0th vibrational state is occupied, leading to emission only from the 0th vibrational level of the excited states. At room temperature, the molecules can be in a higher vibrational excited state and emit from there, resulting in a high energy emission. [186] This phenomenon is illustrated on **Figure 6.31**.

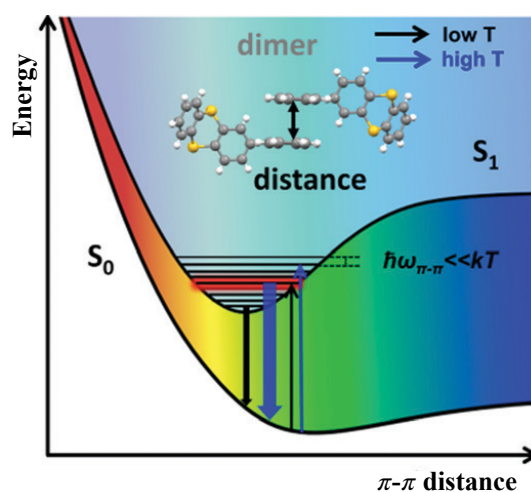


Figure 6.31. Schematic illustration of the mechanism of blueshift of excimer emission in a π - π stack given by Y. Shen *et al.* Republished with permission of Royal Society of Chemistry, from [186].

This study allows us to explain the emission temperature dependence in Me-N-inin film. Therefore, the shift in excimer emission energy shifts to higher energies at higher temperatures, can be associated with the suppression of the π - π stacking vibrational mode at ~ 50 cm^{-1} .

We observe that the overall emission intensity increases at higher temperatures, which might be due to thermally activated exciton detrapping. (**Figure 6.33**). This is similar to other molecules and the decay dynamics does not change significantly. In **Figure 6.34 (A)** emission kinetics of different spectral components at different temperatures are compared. Monomer decay kinetics is faster than temporal resolution of our spectrometer. Excimer emission is temperature

dependent with the rate of the emission slightly increasing at higher temperatures. **Figure 6.34 (B and C)** shows the spectral evolution of Me-N-inin emission at two temperatures: 77K and 320K. At both of the temperatures, similar dynamics is observed: monomer-like excited state with a peak at 400-450 nm decays within instrument response and the excimer with broad emission peak evolves and decays. Despite, the different energetic position of the excimer emission, its spectral evolution is the same at 77K and 320K.

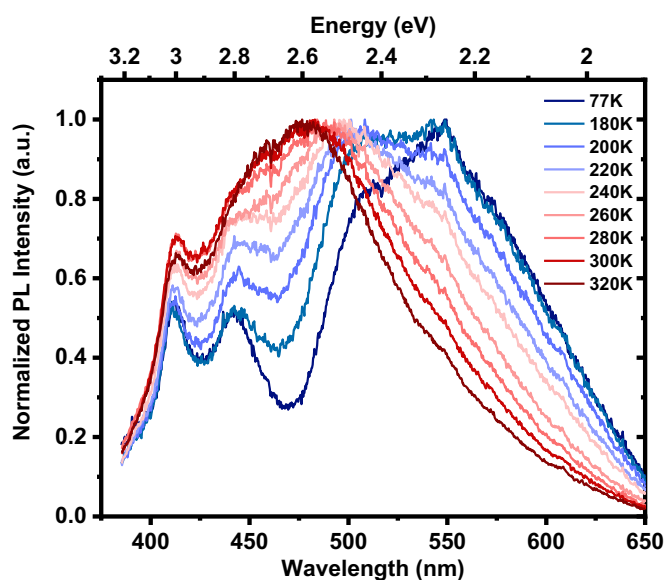


Figure 6.32. Steady state emission of Me-N-inin evaporated (80nm) film at different temperatures, $\lambda_{\text{ex}} = 355\text{nm}$.

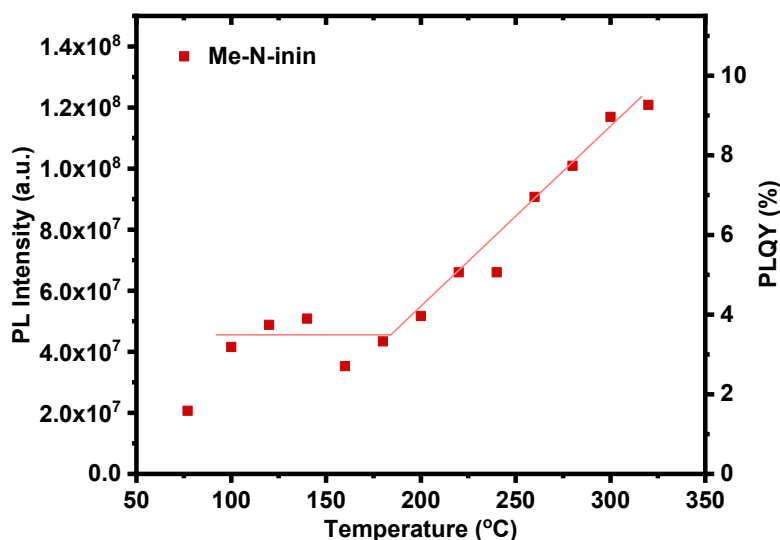


Figure 6.33. Dependence of Me-N-inin photoluminescence intensity on temperature. Left axis: steady state integrated PL intensity of Me-N-inin film (80nm) at different

temperature; right axis: estimated PLQY based on the value taken at the room temperature (295K), the error of the measurement was $\pm 4\%$.

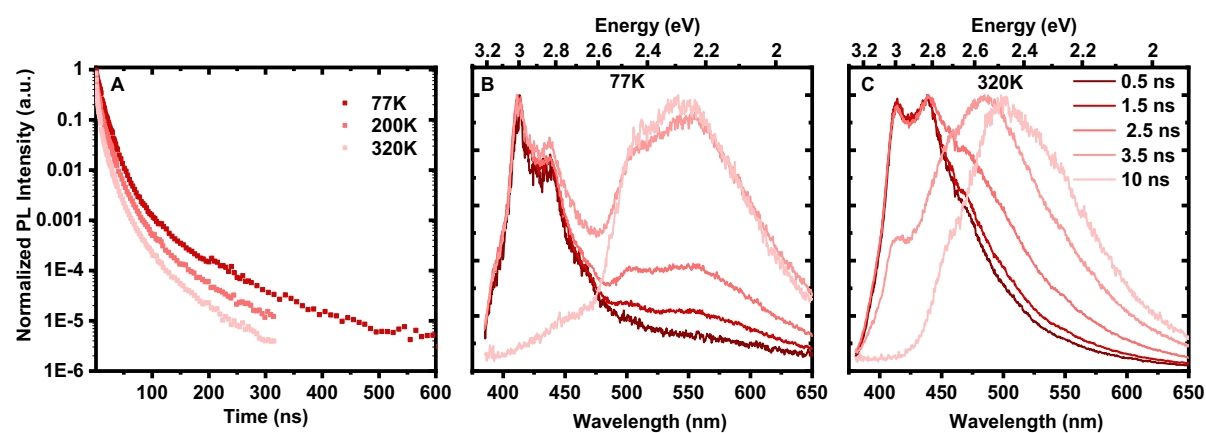


Figure 6.34. Kinetics (taken at 500-510 nm) of excited state decay of Me-N-inin evaporated (80nm) film at different temperatures (A) and spectral evolution at 77K (B) and 320K (C), $\lambda_{\text{ex}} = 355\text{nm}$.

6.2.8 OLEDs and electroluminescence

We prepared OLEDs using only C8-C-inin as an emissive layer. The OLED structure and preparation detail are described section 3.6.1. We chose this molecule simply because it forms good films and has the strong interactions between the molecules. The molecule was also the only derivative that performed well in field effect transistors giving the mobility of $0.27 \text{ cm}^2/\text{Vs}$.

Due to lack of the material, we could not prepare evaporated films. Hence, we decided to test if the spectral characteristics of the spin-coated films would be similar to what we observed in evaporated derivatives. **Figure 6.35** compares steady state absorption and emission of spin-coated (10mg/mL in toluene, 2000 rpm, 60 sec) and evaporated film of C8-C-inin. We conclude, that the films have very similar properties.

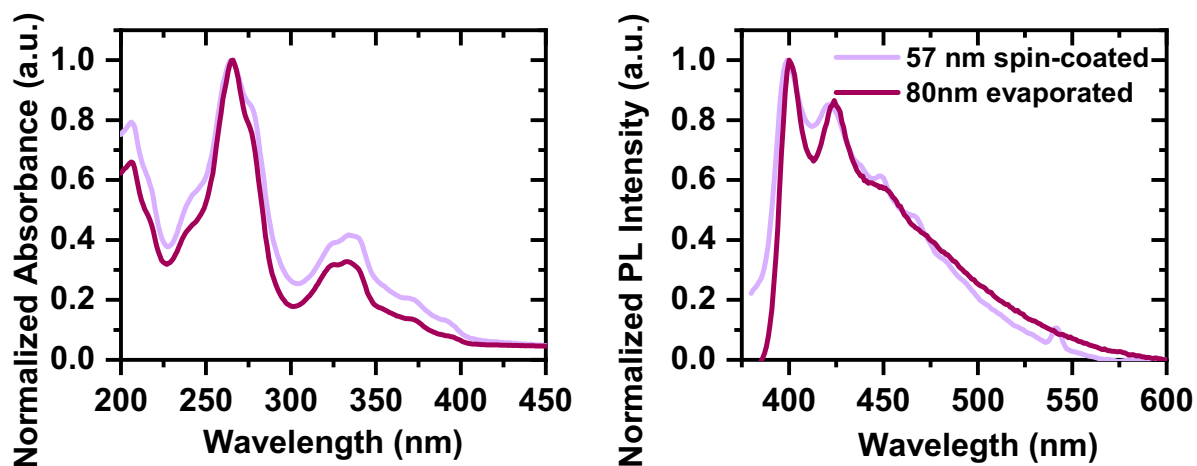


Figure 6.35. Steady state absorption and emission of C8-C-inin made by vacuum deposition (80nm) and spin-coating (57 nm), $\lambda_{\text{ex}} = 355\text{nm}$.

The electroluminescent spectra of the fabricated device is shown in **Figure 6.36**. The electroluminescence spectra exhibits both monomer and excimer emission components; the overall emission colour was blue.

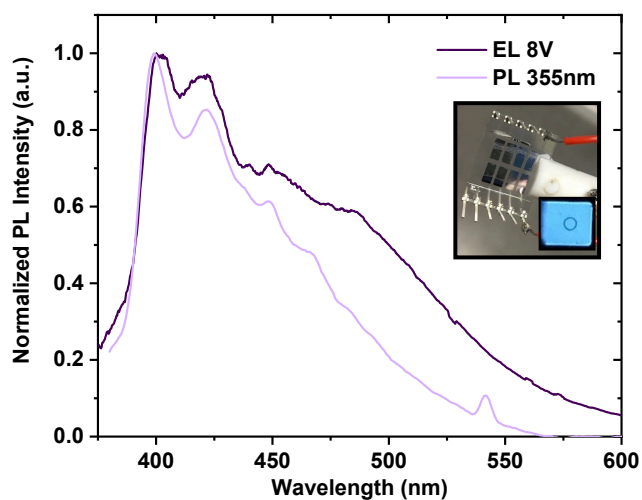


Figure 6.36. Comparison of electroluminescence and photoluminescence spectra of C8-C-inin.

6.3 Conclusions

We report electronic and photophysical properties of four ININ derivatives. We find that all of the ININ derivatives change molecular alignment over time, which results in increased intermolecular interactions.

In solutions all of the ININ derivatives show broadly identical behaviour. However, the different substitution leads to completely different behaviour in the solid state. For example, we find that long alkyl chains at nitrogen atom position in C8-N-inin completely isolate the chromophore from intermolecular interaction. This results in solution-like properties and high PLQY (64%), useful, for example, for polariton lasing. However, the effective isolation also results in an absence of carrier mobility.

On the contrary, C8-C-inin, despite having long alkyl chains, exhibits high charge carrier mobility ($0.27 \text{ cm}^2/\text{Vs}$), which is comparable to the mobility found for C8-BTBT (one of the best organic semiconductors) in similar conditions ($0.42 \text{ cm}^2/\text{Vs}$). Therefore, we suggest that in the case of C8-C-inin the long alkyl chains help packing and possibly reduce dynamic disorder in the film and stabilize the overall film structure. While the PLQY of C8-C-inin in film is significantly lower (34%) than in solution ($\sim 100\%$), it is nonetheless very high for a highly ordered molecule in the solid state. Thus, we show that C8-C-inin can be used as a blue emitter in OLEDs with potential for applications in emitting transistors.

Ph-N-inin and Me-N-inin both showed no charge carrier mobility due to poor film quality and relatively low PLQY. The low PLQY is likely due to trap states and excimer formation. It is, therefore, unlikely that Me-N-inin and Ph-N-inin could have high PLQY in films. Interestingly, Me-N-inin film shows a wavelength-dependence as a function of temperature, which could be used for temperature sensing.

This study sets up a good background for a more in-depth investigation of ININ derivatives solid state properties. The major factor that needs improvement is a better control over the film morphology which requires special facilities. Nonetheless, even these results allow us to conclude that even introducing only inert substituents in ININ core, we are able to significantly change the solid-state properties. Thus, showing solution-like emitter properties, temperature-dependent emission colour tuning and high charge carrier mobility combined with reasonably high PLQY in different derivatives of same chromophore.

7 Attempted synthesis of dicarbazolo[*a,c*]phenazines

In this chapter we explore the possibility of achieving thermally activated delayed fluorescence in thin films with high charge carrier mobilities ($>1\text{cm}^2/\text{Vs}$). This approach has the potential to drive new applications, such electrical-injection lasing in organic semiconductors. Aided by quantum chemical calculations, we have designed a series of planar, stiff molecules with singlet-triplet gaps on the order of 0.4eV . This value is expected to be significantly reduced in the solid-state due to stabilization of the singlet, leading to singlet-triplet gaps suitable for thermally activated delayed fluorescence. We will demonstrate work towards synthesis of these molecules.

All of the quantum calculations were performed by Dr. Anna Stradomska at the University of Glasgow.

7.1 Introduction

Spin statistics predicts that the ratio between singlet and triplet excitons formed during electrical excitation is 1:3 (section 2.1.2). Radiative decay of a triplet state in conventional hydrocarbons is spin-forbidden and, thus, photoluminescence quantum yields are low. Therefore, most of the energy stored in T_1 excited state is dissipated in the form of heat. This is one of the main problems for application of fluorescent materials in organic light emitting diodes (OLEDs).

One of the approaches to overcome this problem is to increase the fraction of the singlets formed upon electrical excitation by converting a triplet into a singlet state. This can be accomplished through thermally activated delayed fluorescence (TADF) mechanisms, which results in ~100% internal fluorescence efficiency. The TADF requires efficient reverse intersystem crossing between triplet (T) and singlet (S) states. This is usually achieved when the S-T energy splitting is less than 0.2 eV. [147] Such a low value of the energy gap could be obtained by spatially separating HOMO and LUMO of the molecule. Thus, molecules that display efficient TADF properties are usually composed of donor and acceptor moieties that are geometrically twisted through spiro connection, etc. Those molecules have non-flat geometries, that lead to poor crystal packing and low charge carrier mobilities. [145] In addition, in solid state the luminescence of TADF emitters is often quenched due to aggregation and exciton-exciton annihilation. Therefore, organic chromophores are usually used as a dopant (guest emitter) dispersed in a host matrix, whilst the application of non-doped materials is somewhat limited. [187][188]

However, materials that can be used without a host and retain high emission yields are extremely desirable. The benefits of such materials would be simplified device architecture and a more stable emissive layer morphology (no phase separation in host-guest system). Moreover, this approach could create materials that exhibit both high charge carrier mobility and high luminescence quantum yields which could be of use for applications in organic light emitting transistors and electrically pumped lasers. [172]

The aggregation induced TADF mechanism allows for efficient use of TADF molecules without a host. In this case, apart from internal (through bond) charge transfer, through space charge transfer is also observed. This phenomenon can improve the TADF efficiency when appropriate noncovalent interactions and aggregation architecture is employed. [189][190][191]

The aim of the project described in this chapter was to create a planar donor-acceptor molecule which could have high charge carrier mobility and exhibit TADF properties. We were especially interested in answering the question whether TADF is possible in planar molecules with singlet-triplet gap larger than 0.2 eV. It is expected that in a well-ordered solid, the singlet state will be stabilized due to intramolecular interactions (section 2.3.2), however, the triplet energy is expected to remain the same. [4] Therefore, it could result in singlet-triplet splitting being much smaller than in an isolated molecule, which could be suitable for TADF.

For this work, we designed a series of π -conjugated planar molecules (**Figure 7.1**) which are based on a phenazine core. The spectroscopy of many phenazine derivatives has been intensively studied and this moiety has been employed as an acceptor in TADF molecules. [192] [193] [194] Apart from phenazine these molecules contain carbazole moieties. Carbazole and its derivatives have been studied in depth for more than a hundred years, because carbazole is very important biologically active moiety. [195] In 1960s Hoegl established that poly-(N-vinylcarbazole) if sensitized with an electron acceptor enough exhibits reasonably high level of photoconductivity. [196] Since then it was discovered that carbazole has useful hole-transporting properties, strong absorption in the UV region and strong blue fluorescence. [197][198] All of that combined with high stability of the moiety and well-developed synthetic procedures made carbazole widely used as a building block of luminescent emitters (fluorescent[199][200], phosphorescent [201] and TADF[202][203]).

7.2 Theoretical calculations

Figure 7.1 shows the structures of the designed molecules. We used density functional theory to calculate vertical excitation energies of first singlet and triplet states, along with the oscillator strength of S_1 - S_0 transition. The results are summarised in Table 7.1. The singlet-triplet gaps are in the range from 0.4 to 0.8 eV. Designed molecules have S-T splitting energy in the range of 0.4 eV, which is higher than in already reported TADF materials. However, it is expected that singlet state will be stabilised due to intermolecular interactions in solid state.

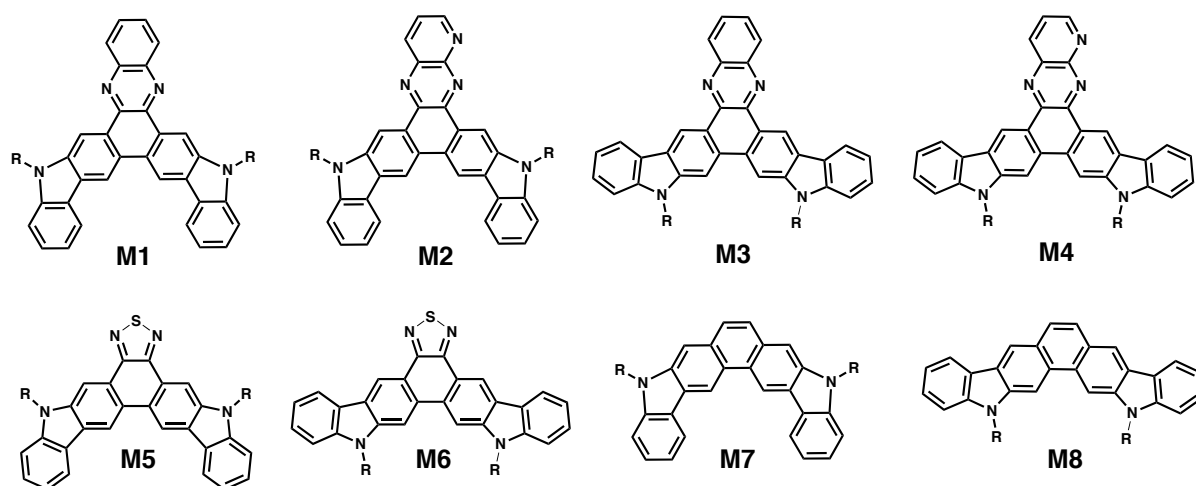


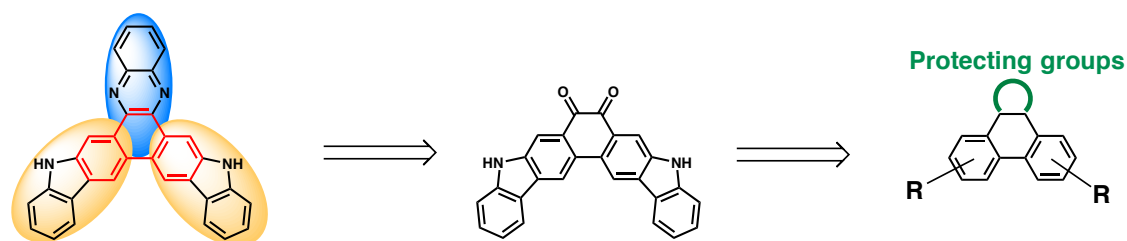
Figure 7.1. Structures of target compounds.

Table 7.1. Calculated vertical singlet and triplet excitation energies and oscillator strength.

Molecule	E_{S1} , eV	f	E_{T1} , eV	S-T, eV
M1	2.26	0.009	2.83	0.43
M2	3.14	0.012	2.74	0.40
M3	3.63	0.457	2.97	0.66
M4	3.42	0.0002	2.86	0.57
M5	3.6	0.0085	3.19	0.41
M6	3.86	0.079	3.05	0.81
M7	3.67	0.048	3.27	0.41
M8	3.57	0.031	3.15	0.42

E_{S1} – calculated energy of first singlet state,
 E_{T1} – calculated energy of first triplet state,
 f – calculated oscillator strength,
 $S-T$ – energy difference between first singlet and first triplet levels.

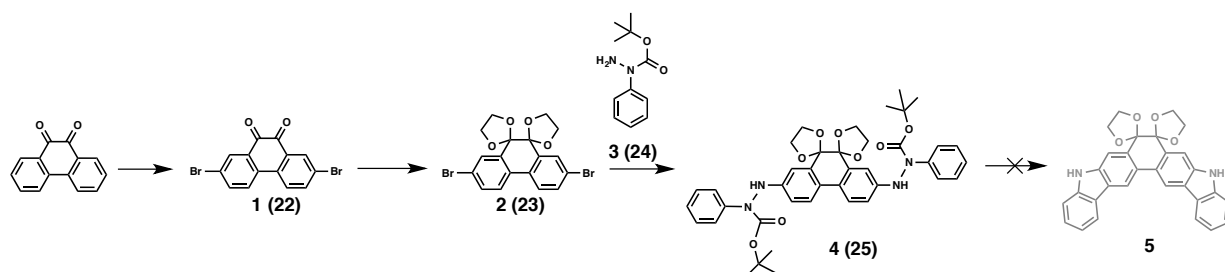
7.3 Synthesis of dicarbazo[a,c]phenazines



Scheme 7.1. General strategy for synthesis of dicarbazo[a,c]phenazines.

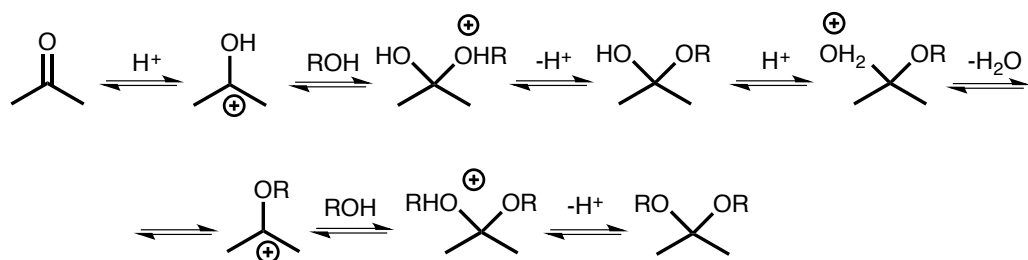
Synthesis of the target compounds was planned around the condensation reaction of phenanthren-9,10-dione derivative with either *o*-diaminobenzene or *o*-diaminopyridine (both are commercially available) (**Scheme 7.1**) Condensation reactions of di-ketones with diamines usually have quantitative yields. [64]

A number of synthetic strategies have been reported for the construction of the carbazole structure. There are two basic approaches to carbazole synthesis: formation of a benzene ring from substituted indole derivatives (*e.g.* using the Diels-Alder reaction) or formation of a pyrrole ring (*e.g.* using the Cadogan reaction). [204] We decided to obtain the carbazole structure through pyrrole ring formation. Thus, it was necessary to start from phenanthrene-9,10-dione and then form either a carbon-carbon bond or carbon-nitrogen bond *via* a palladium catalysed coupling reaction.



Scheme 7.2. 1st synthetic route for synthesis of dicarbazolo[a,c]phenazines (molecule M1). The numbers in brackets correspond to the numbers in Chapter 3.

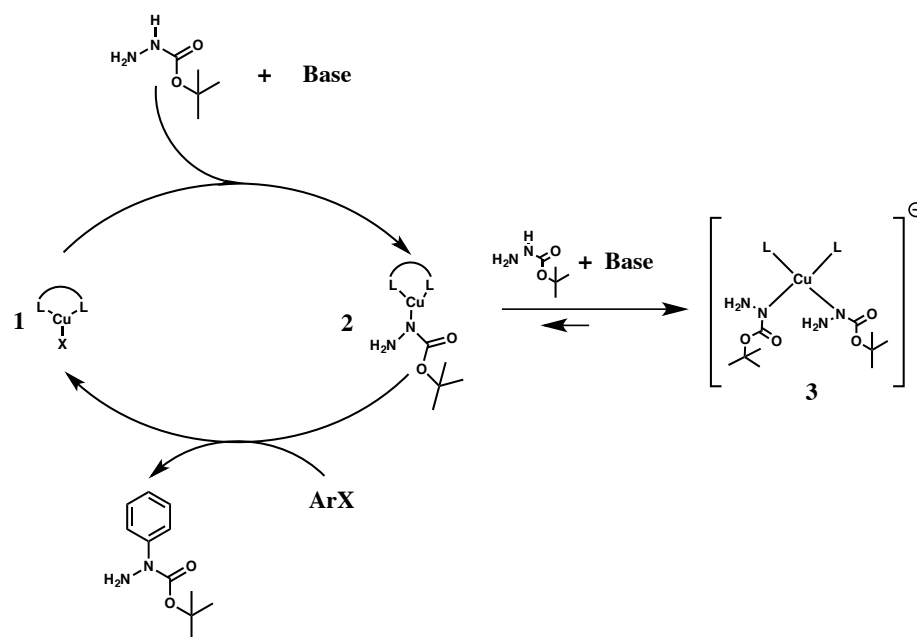
We started with synthesis of M1 molecule. **Scheme 7.2** represents our first synthetic strategy that allows to obtain the targeted molecules. Phenanthren-9,10-dione was brominated into the 2 and 7 positions. Due to poor solubility of phenanthren-9,10-dione derivatives, it was decided to protect carbonyl groups with ethylene glycol. The reaction between ketones and alcohols is reversible and ketals are easily hydrolysed back in acidic conditions. In order to shift equilibrium in favour of the ketal formation, water was removed by azeotropic distillation with toluene using the Dean-Stark apparatus. The reaction has the following mechanism (example for one carbonyl group of acetone was used for simplification): [205]



Scheme 7.3. Mechanism of acid catalysed reaction of carbonyl group with alcohols.

The type of structure formed in the case of phenanthren-9,10-dione was not investigated, however, it is either 1,3-dioxalane or 1,4-dioxane. In the NMR spectrum, these groups have two broad signals around 3.6 and 4.2 ppm. [206]

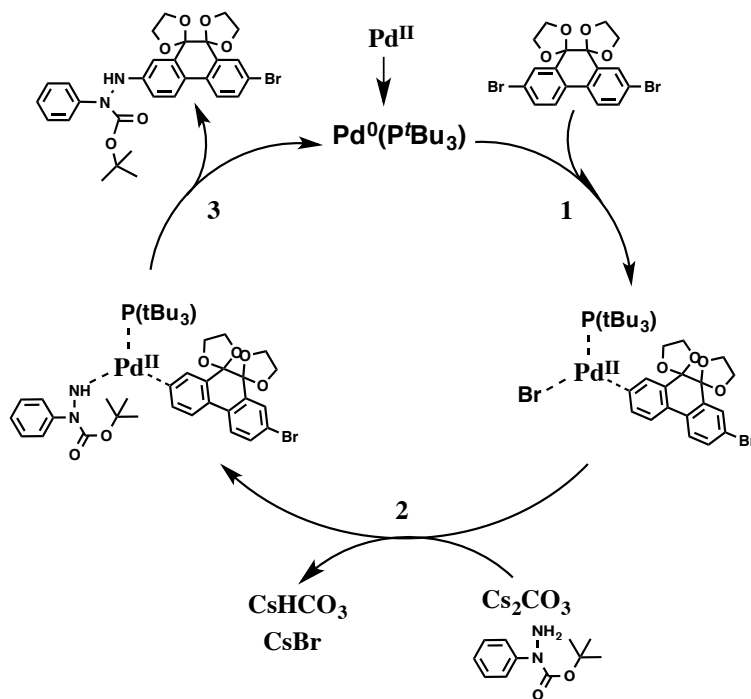
The carbazole moiety was supposed to be obtained through catalytic rearrangement of diaryl hydrazide (**4**, **Scheme 7.2**) with C-C bond formation at 3 and 6 positions in the phenanthrene core. One of the starting materials for hydrazide (**4**) synthesis is 1-tert-butoxycarbonyl-1-phenylhydrazine (**3**, **Scheme 7.2**). This molecule was synthesized by a copper-catalysed Goldberg type reaction. The traditional procedure for a Goldberg amidation reaction utilises simple copper salts or metal copper as a catalyst. However, in preparation of compound (**3**), the modified procedure using copper iodide along with a bidentate ligand was applied. [62] Usage of the chelating ligand allows the reaction to proceed at lower temperatures and with higher yields. [207][208][209] The catalytic cycle for this reaction is presented in the following scheme:



Scheme 7.4. Catalytic cycle of the modified Goldberg reaction.

The mechanistic studies reported in literature suggest that ratio between the catalyst and chelating ligand should be high, because at low concentration of ligand a non-reactive intermediate (**3** on **Scheme 7.3**) can be formed. [209]

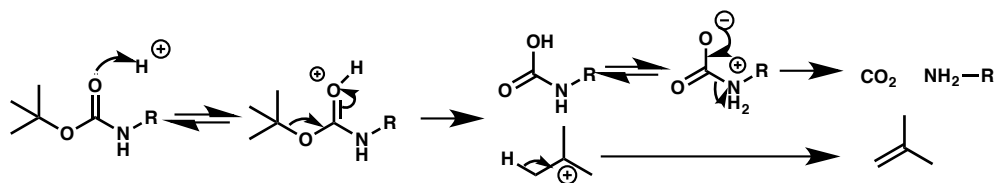
Diaryl hydrazide (**4**) was prepared by Pd-catalysed Buchwald-Hartwig coupling reaction. To understand the mechanism of this reaction, it is necessary to consider the palladium catalytic cycle:



Scheme 7.5. Proposed catalytic cycle of Buchwald-Hartwig coupling reaction.

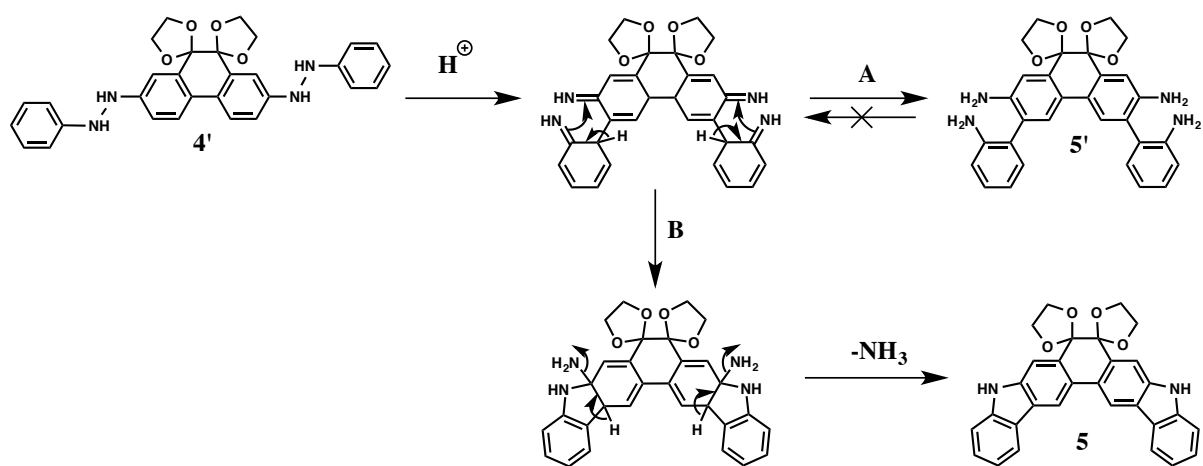
On **Scheme 7.5** the first step (**1**) of this reaction is oxidative addition of Pd (0) to an aromatic halide and the subsequent change of the oxidation state of palladium. The second step (**2**) is the formation of Pd(II) arylamine complex. This step involves the coordination of the amine to an existing organopalladium complex and subsequent elimination of the proton and halogen atom by the base. It was proved that this step does not occur in the absence of the base. [210] The final step (**3**) of the reaction is reductive elimination. It results in the formation of a new amine and recovery of the active Pd (0) complex with the ligand. [211][212]

The diaryl hydrazide (**4**) formed in this reaction, was used for the rearrangement which is suggested to allow a pyrrole ring formation. This reaction is acid catalysed; thus, the protecting Boc-group could be removed during the reaction. The process of hydrolysis of the Boc-group in presence of an acid is the following [93]:



Scheme 7.6. Mechanism of Boc-protecting group cleavage.

The mechanism for acid catalysed sigmatropic rearrangement of diaryl hydrazides was studied by Lim *et al.* [213][214] It has been proven that it is possible to obtain benzo[*c*]carbazoles with quite good yields. Therefore, it was decided to test this rearrangement for our system. The reaction would presumably have the following mechanism:



Scheme 7.7. Mechanism of formation of dicarbazo[a,c]phenazines as a result of acid catalysed sigmatropic rearrangement of corresponding hydrazide (4). Boc protective group is omitted for simplicity.

The rearrangement was first tested in ethanol with concentrated HCl at reflux. The mixture was kept at these conditions for 4 hours. The resulting solution was neutralized with NaHCO₃ and filtered off.

The precipitated solid could not be dissolved in any solvent except DMSO. NMR in DMSO-d₆ showed a lot of overlapping signals in the aromatic region between 7-8.5 ppm. Broad singlets from protecting groups were detected at 3.51 and 4.14 ppm. This means that protecting groups remain untouched in this reaction conditions despite the fact that glycol protection is sensitive to acidic treatment. Unfortunately, a better NMR spectrum could not be obtained. To investigate the nature of the precipitate further, the sample was analysed by mass spectrometry. Unfortunately, ions with suitable mass (**Figure 7.2**) were not detected, which could be because

the precipitate was simply a product of decomposition of the starting materials or due to product decomposition inside the mass spectrometer or poor ionization yields of the compounds of interest.

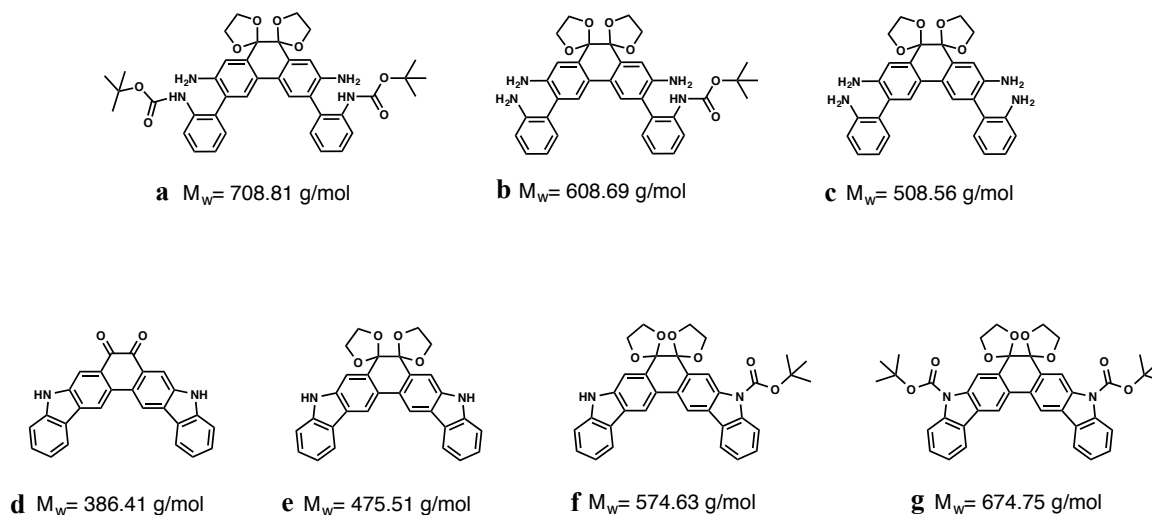


Figure 7.2. Structures and molecular weights of the possible products of the sigmatropic reorganization.

The filtrate from the reaction was purified by flash chromatography using petroleum ether and ethyl acetate mixture (2:1) as an eluent. The two main fractions were collected ($R_f = 0.28$ and $R_f = 0.75$ in petroleum ether : ethyl acetate, 2:1) and analysed by NMR spectroscopy and mass spectrometry (MALDI). We suggest that the fraction with $R_f = 0.28$ could be assigned to molecule **c** (Figure 7.2) by proton NMR (Figure 7.3). Despite the fact that silica gel column chromatography was used to purify this fraction, the proton NMR of the compound is not clean enough for clear peaks integration. Therefore, the integration on Figure 7.3 needs to be treated with caution. The high field region of NMR below 3.5 ppm contained a lot of solvent peaks, however, it was clear that Boc protecting group was eliminated (the peak at 1.43 ppm that was assigned to Boc group in the diaryl hydrazide (**4**) NMR spectra was absent). Peak at 3.74 ppm is significantly broadened compared to 4.06 ppm and a sharp small peak is observed at 3.76 ppm. We suggest that this peak might be a sign of tetraamine formation (Figure 7.2 structure **c**). The aromatic protons in the region between 6.5 and 8 ppm could be integrated to give 12 protons. Therefore, this might be our targeted product. However, this was not confirmed by mass spectrometry. We did not find any of the suggested masses from the Figure 7.2 including the structure **c**. This could be rationalized by decomposition of the product in mass spectrometer or by poor ionization of the molecule.

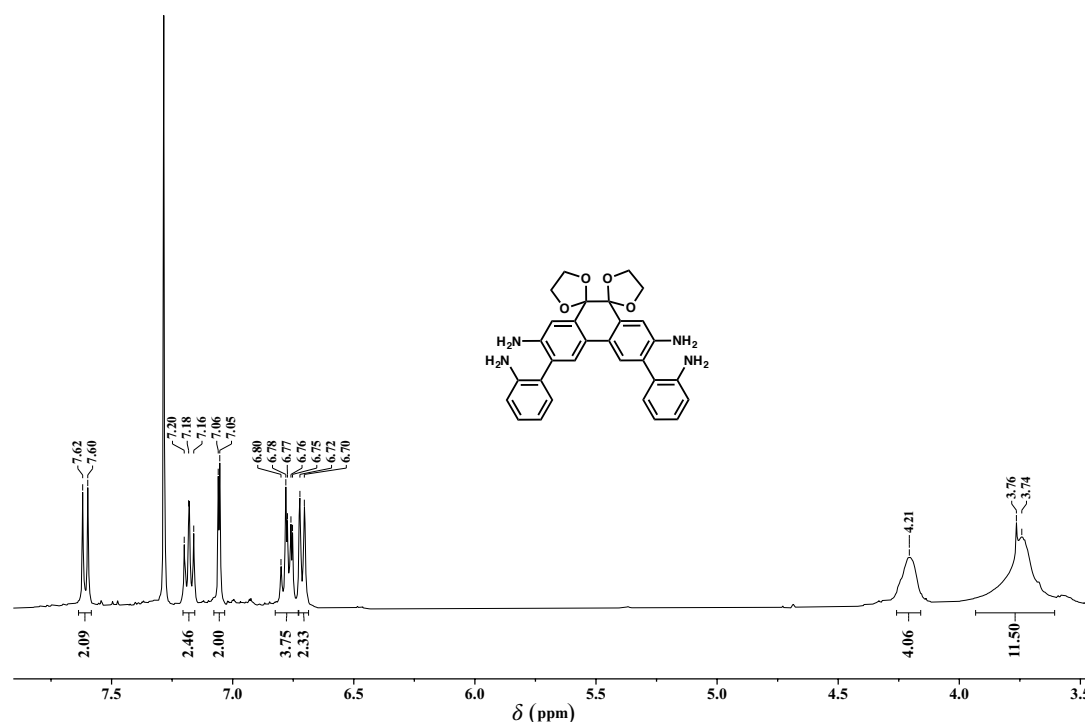


Figure 7.3. ¹H NMR in CDCl₃ of one of the fractions obtained from silicagel column chromatography.

Despite the promising NMR spectra, it was absolutely necessary to improve the reaction conditions, due to low yield and selectivity (5 side products could be clearly identified by TLC). High yield is very important for synthesis of functional materials as their analysis and testing for applications in the electronic devices would require large quantities. Thus, the reaction was repeated several times with different acid concentrations and times of reflux; however, the same results were observed. The reaction evidently had a lot of side products and their perfect separation was impossible. The difficulty of separation can be explained by presence of the amine groups that tend to strongly interact with silica gel resulting in long retention times and poor separation of the derivatives with likely decomposition of the molecules in process.

We also tested another solvent for the reaction: dioxane. As a result, even more side products were detected by TLC analysis. The reaction mixture was neutralised and extracted in dichloromethane and ethyl acetate (separately). The combined mixture was given for mass spectrometry analysis. The sample was run through the chromatography column prior to ionisation. 5 different fractions were separated, ionized (electron spray ionization) and analysed. One of the fractions contained molecule **d** from **Figure 7.2**. This reaction was also repeated with different acid concentration and reflux times; however, it was not possible to obtain better selectivity in this reaction.

Thus, we concluded that this approach to synthesis of dicarbazolo[*a,c*]phenazines is inefficient. We suggest that the main reason for inefficiency and poor reaction selectivity is the presence of multiple functional groups that can undergo various reactions in the given conditions (e.g. two amine groups, two Boc groups, two ethylene glycol protective groups). Therefore, it was decided to change the synthetic route to a more controllable one.

We considered several alternative strategies for obtaining carbazole structure:

- Formation of C-N bond which would be followed by direct arylation to form carbazole core;
- Formation of C-C bond which would be followed by cyclization reaction with nitro or amino-group.

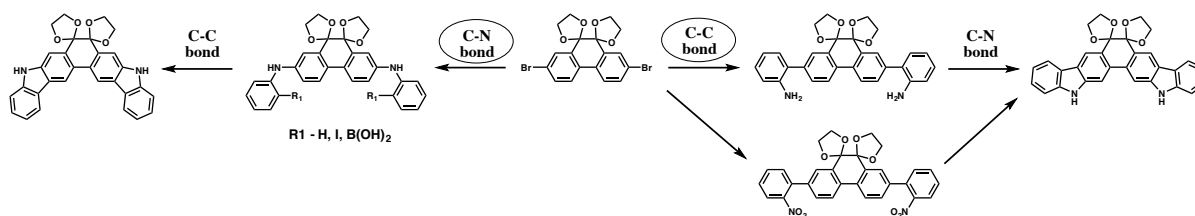
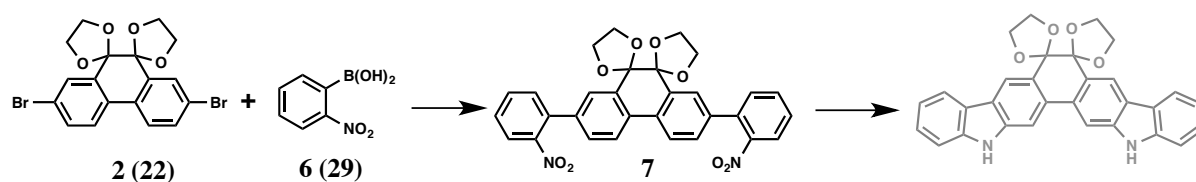


Figure 7.4. Using cross-coupling reactions for dicarbazolo[*a,c*]phenazines synthesis.

There are many reports of Pd-catalysed C-N bond formation followed by direct arylation [97][215][216], these procedures claim fairly high yields of carbazole formation, but the efficiency of the direct arylation reactions very much depends on substitution groups that are present in starting materials. [217][218][219]

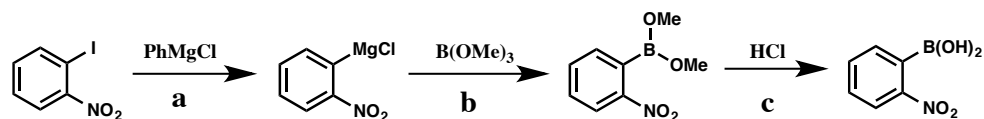
Thus, it was decided that it would be easier to form C-C bond followed by cyclization reaction. We chose Suzuki-Miyaura cross coupling reaction between 2,7-dibromophenanthren-9,10-(ethyleneglycol)ketal and orthonitroboronic acid (Scheme 7.8). This reaction route was reported to be successful for multiple similar systems, *i.e.* cross-coupling between orthonitroaromatic molecules and a brominated (or boronated) molecule. [220][221][222] Therefore, we switch to synthesis of the molecule M3, due to easiness of the starting material synthesis (compound 2 on **Scheme 7.8**).



Scheme 7.8. 2nd synthetic route to obtain dicarbazolo[*a,c*]phenazines (synthesis of the molecule M3).

The product of the Suzuki cross-coupling reaction - 2,7-bis(2-nitrophenyl)phenanthrene-9,10-di(ethyleneglycol)ketal (**7**) can be cyclized using Cadogan reaction. [223] Overall, this is a two-steps route to the fused heteroaromatic core should potentially give more control over side products.

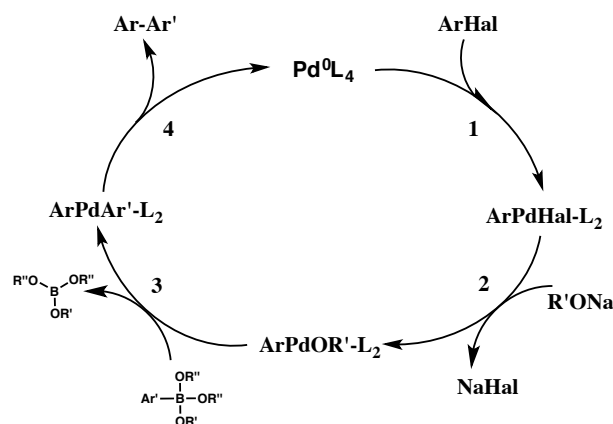
2-Nitrophenyl boronic (**6**) acid was prepared through a Grignard intermediate (**Scheme 7.9**). It is known that Grignard reagents can react with a nitro group by nucleophilic attack. [224] However, it is still possible to prepare 2-nitrophenyl magnesium compounds by I-Mg exchange at temperatures lower than -40°C . [65] The chelation of the nitro group to magnesium makes the 2-nitrophenyl magnesium compounds stable enough for usage in synthesis of 2-nitrophenyl substituted derivatives.



Scheme 7.9. Steps of synthesis of 2-nitrophenylboronic acid.

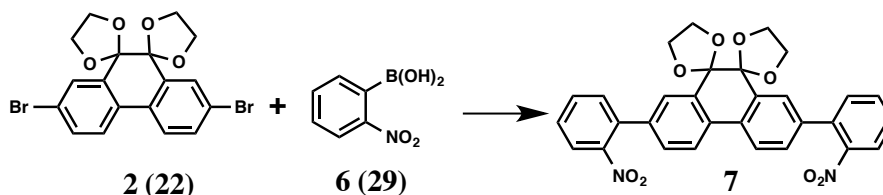
Therefore, 2-nitrophenyl boronic (**6**) was prepared through fast I-Mg exchange of 1-iodo-2-nitrobenzene with PhMgCl at -70°C . Afterwards, $\text{B}(\text{OMe})_3$ was added to the reaction mixture which resulted in boronic ester formation. The hydrolysis of this intermediate gave 2-nitrophenyl boronic (**6**).

The obtained 2-nitrophenyl boronic (**6**) and compound (**2**) were used in the Suzuki-Miyaura cross-coupling reaction. This is palladium catalysed reaction which proceeds *via* the following catalytic cycle:



Scheme 7.10. General catalytic cycle of Suzuki-Miyaura cross-coupling reaction.

The first stage of the cycle is oxidative addition (1) of the aryl halogenated compound to the palladium (0) complex. This step is followed by displacement of the halogen ion with anion of the base (step 2). The third step is the transmetalation between arylboranes and the palladium complex $\text{ArPdOR}'\text{L}_2$. The final step of this reaction is the reductive elimination of the coupled compound $\text{Ar-Ar}'$, and the subsequent regeneration of the catalyst. [225]



Scheme 7.11. 1st Suzuki coupling reaction method.

Suzuki-Miyaura coupling reaction was tested for preparation of dinitro compound (7) (**Scheme 7.11**). The reaction conditions are summarised in the **Table 7.2**, where column “Product” indicates only the products of interest, however, products of starting materials decomposition and starting materials were also detected. The full conversion of starting materials was never observed.

Reaction conditions 1 and 2 did not show any reaction products. We presumed that it is due to poor ability of the base to remove the halogen from the compound reactive Pd complex in the step 2 (**Scheme 7.10**). Therefore, it was decided to test a stronger base such as Na_2CO_3 or K_2CO_3 (conditions 3-6). In this reaction conditions only a small amount of mono-substituted derivative was obtained, the intensity of spots on TLC indicated that the major part of starting materials was not converted. **Figure 7.5** shows NMR of monosubstituted derivative obtained after purification of the reaction mixture by silica gel column. The NMR spectrum contains other

impurities that were hard to get rid of due to a very small amount of the obtained material. Nonetheless, it is possible to identify the compound. In the aromatic region (7.4-8.2 ppm), seven signals are present that give 10 protons when integrated. Broad singlets at 4.11 and 3.57 ppm correspond to glycol protective groups.

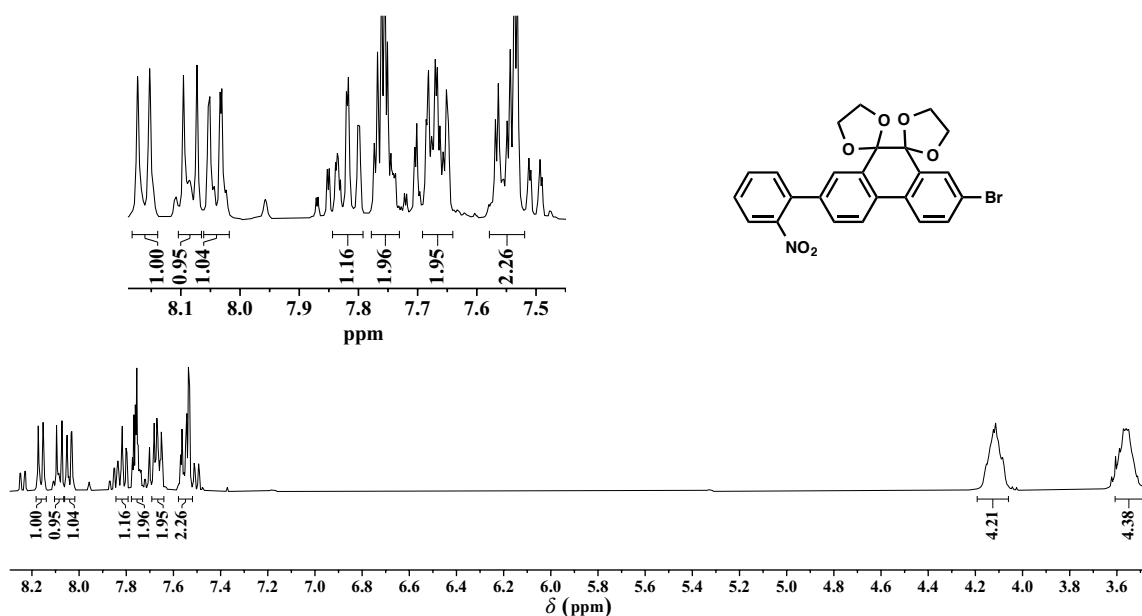


Figure 7.5. NMR in CDCl_3 of a monosubstituted product of the Suzuki cross-coupling reaction.

Poor reaction yields could be caused by steric hinderance of the reagents. Buchwald *et al.* [226][227] reported successful application of SPhos and DPEPhos (structures **Figure 7.6**) ligands for sterically hindered substrates. These ligands were also tested on halogen halides which possess an ortho electron withdrawing group (*e.g.* a nitro group). However, a significant amount of phenols could be formed in the process of the reaction due to hydrolysis of the halide. Therefore, anhydrous conditions along with a strong base, *e.g.* K_3PO_4 , are preferable.

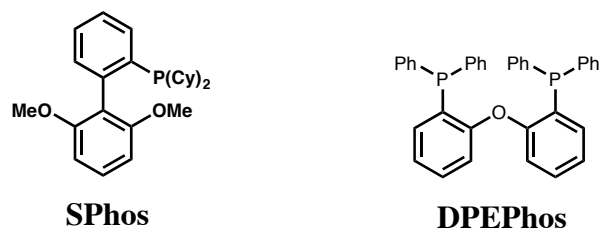


Figure 7.6. Structures of phosphine ligands.

We applied these catalysts in our reaction (conditions 7 and 8), but significant decomposition of the starting halide was observed. Nonetheless, the di-substituted product (**7**) was obtained with a very small yield. NMR of disubstituted product is shown on **Figure 7.7**. The number of peaks is reduced compared to monosubstituted derivative as it was expected. However, the impurities might result in misleading integration values. We also confirmed the structure of the product by mass spectroscopy, where the m/z of 538.1 (expected value 538.5) was found along with other peaks. Therefore, this result should be treated with caution.

Nonetheless, this was a promising result. To improve the yield, the base was changed for a weaker one (conditions 9, 10) with an aim to reduce starting materials degradation. Unfortunately, these attempts were not successful.

Table 7.2. Reaction conditions for Suzuki coupling reaction (Scheme 7.11).

Number	Base	Catalyst (2-10%)	Solvent	Product
1	NaHCO ₃	Pd(dba) ₂ <i>o</i> -tritolylphosphine	THF:H ₂ O	-
2	NaHCO ₃	Pd(PPh ₃) ₄	DMF:H ₂ O	-
3	Na ₂ CO ₃	Pd(OAc) ₂ <i>o</i> -tritolylphosphine	DMF:H ₂ O	Mono
4	Na ₂ CO ₃	Pd(PPh ₃) ₄	DMF:H ₂ O	Mono
5	K ₂ CO ₃	Pd(PPh ₃) ₄	DMF:H ₂ O	Mono
6	K ₂ CO ₃	Pd(PPh ₃) ₄	Toluene:H ₂ O	Mono
7	K ₃ PO ₄	Pd(OAc) ₂ <i>o</i> -tritolylphosphine	Toluene	Mono
8	K ₃ PO ₄	Pd(OAc) ₂ SPhos	Toluene	Mono + Di
9	Na ₂ CO ₃	Pd(OAc) ₂ SPhos	Toluene	-
10	Na ₂ CO ₃	Pd(OAc) ₂ DPEPhos	Toluene	Mono

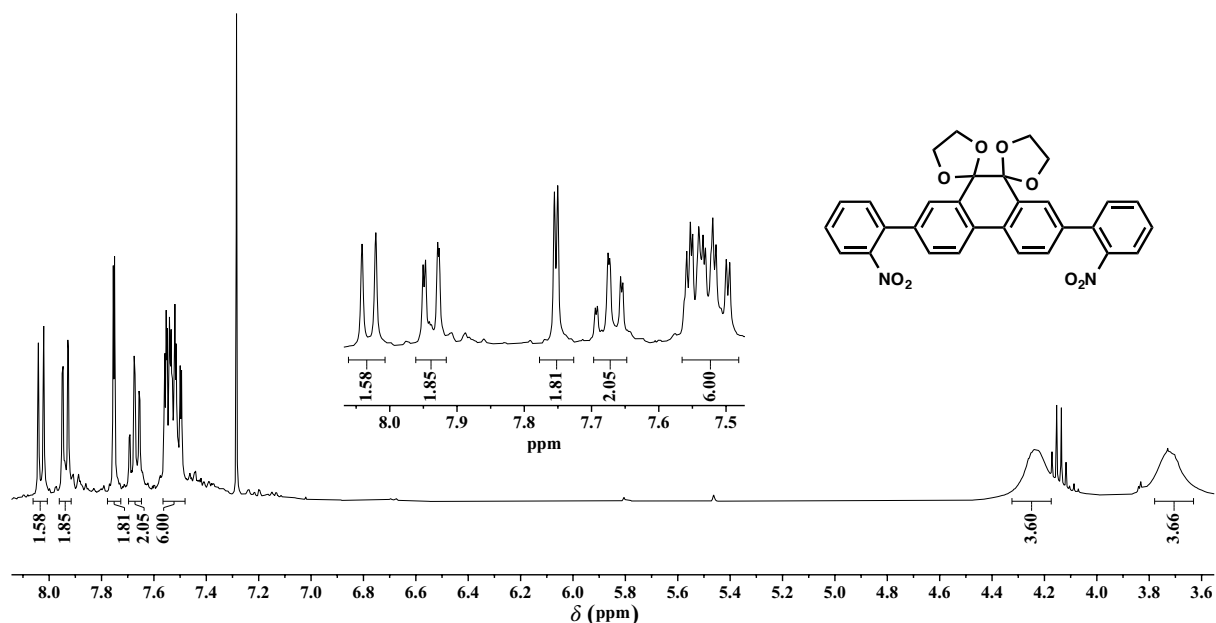
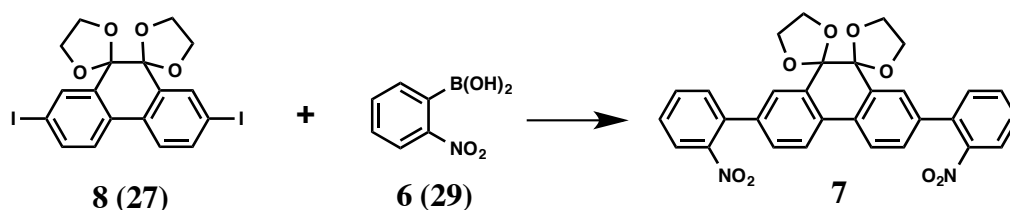


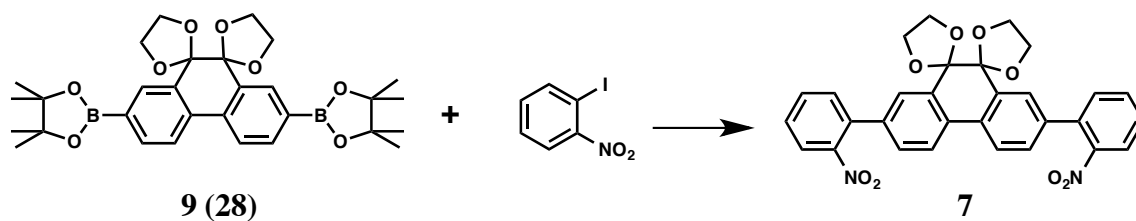
Figure 7.7. NMR in CDCl_3 of a disubstituted product of the Suzuki cross-coupling reaction.

Suzuki-Miyaura reaction yield could sometimes be improved by using iodinated compounds instead of brominated. Thus, 2,7-diiodophenanthren-9,10-di(ethyleneglycol)ketal was synthesised and tested in Suzuki reaction (**Scheme 7.12**). In this case oxidative addition could potentially go better because C-I bond is weaker than C-Br. This reaction was tested in several reaction conditions similar to those presented in the **Table 7.2**, but the yield was not improved.



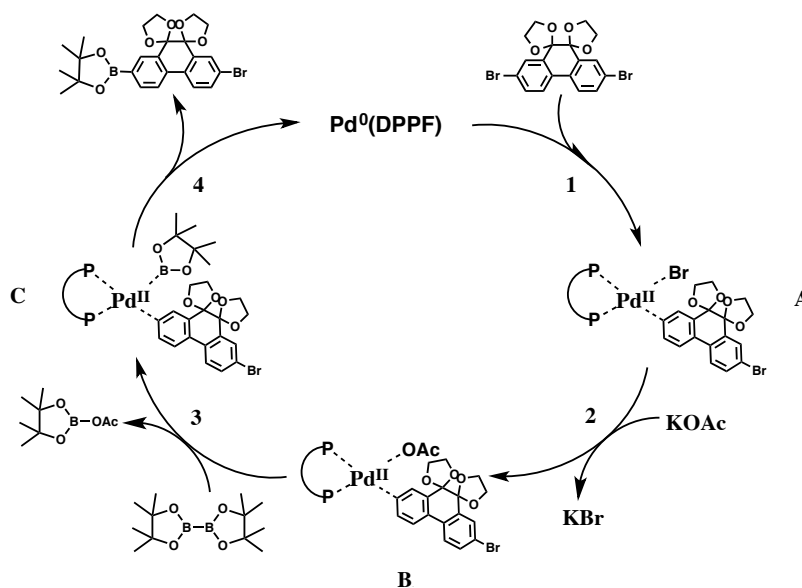
Scheme 7.12. 2nd Suzuki coupling reaction method.

Due to presence of a strong electron withdrawing group, such as the nitro group, boronic acid (**6**) could be quite unstable and, thus, might decompose before participation in the reaction. This is why our next step was to test if dioxaborolan phenanthrene (**9**) derivative and 2-iodonitrobenzene (commercially available chemical) would react better in Suzuki Miyaura reaction (**Scheme 7.13**). In this case, boron atoms would be attached to a molecule with electron donating groups (ethyleneglycol groups) and thus overall stability of compound will be higher.



Scheme 7.13. 3rd Suzuki coupling reaction method.

The dioxaborolan phenanthrene (**9**) was prepared *via* palladium catalysed Miyaura reaction, which follows the mechanism summarized in the scheme below:



Scheme 7.14. Catalytic cycle of the Miyaura coupling reaction.

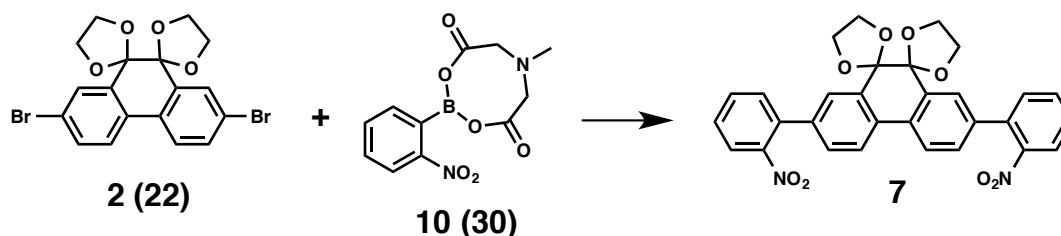
This reaction proceeds through similar steps as the Suzuki-Miyaura reaction. The first step is an oxidative addition of Pd (0) to an aryl halide (step 1). This step is followed by displacement of the halide ion from complex (A) to give complex (B). In the next step a transmetalation takes place between bis(pinacolato)diboron and Pd-complex (step 3). The final step of reaction is reductive elimination of the corresponding cross-coupling product. The catalyst is, therefore, regenerated. [228]

The reaction between dioxaborolan (**9**) and 2-iodonitrobenzene was tested in several conditions; however, it did not lead to an increased yield of the product (**7**).

Apart from testing dioxaborolan phenanthrene, there is a way to stabilize an electron deficient boronic acid itself by using a protective group on the boronic acid and forming a more stable derivative. The boronic acid was protected using methyliminodiacetic acid (MIDA). This compound can be easily hydrolysed back to the boronic acid in the Suzuki-Miyaura reaction

media. The advantage of this protection is that if used at low temperatures (60-70°C) hydrolysis occurs slowly and the probability of decomposition of boronic acid is lower. [229]

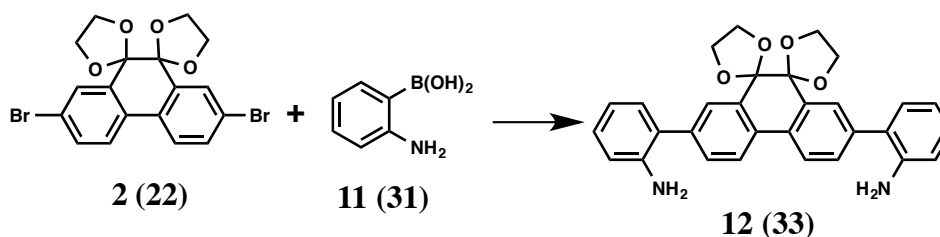
MIDA-boronic ester was prepared according to the procedure reported by Knapp *et al.* [229] and the reaction scheme of the corresponding Suzuki reaction is depicted in the Scheme 7.15 was tested. Unfortunately, this reaction did not give an improved yield of the product (**7**).



Scheme 7.15. Suzuki coupling reaction with MIDA-boronic ester.

Summarizing our experience in synthesis of dinitroderivative (**7**), it has to be noted that Suzuki-Miyaura coupling reaction between 2,7-bis(2-nitrophenyl)phenanthren-9,10-di(ethyleneglycol)ketal (**2**) and orthonitrophenyl boronic acid is proven to be challenging, since only very low yields of coupling products could be obtained. The reasons for this could be strong electron withdrawing nature of nitro group, steric hindrance created by the nitro group in orthoposition to the reactive centre or steric hindrance of ethyleneglycol protecting groups (or all of these factors). Figuring out the exact reason for the poor reaction performance is out of the scope of this thesis since we are only interested in the properties of the target materials. Thus, it was decided to move onto another synthetic strategy in order to obtain the molecules.

Considering that electron-withdrawing nature of the orthonitroboronic acid might have caused issues with our previous attempts using Suzuki-Miyaura reaction, we decided to synthesise an electron donating boronic acid (2-aminophenylboronic acid (**11**)). This boronic acid could be reacted with the phenanthrene derivative using Suzuki-Miyaura cross-coupling reaction Scheme 7.16. Due to the electron donating properties of amino group, this boronic acid could be more active and stable in Suzuki-Miyaura coupling.

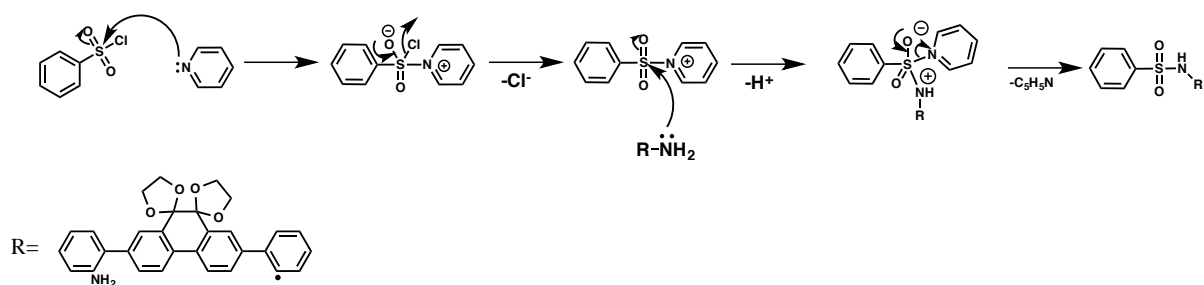


Scheme 7.16. 3rd synthetic route to obtain dicarbazolo[*a,c*]phenazines.

The reaction **Scheme 7.16** between 2,7-dibromophenanthren-9,10-(ethyleneglycol)ketal and 2-aminophenylboronic acid was successful and the compound (**12**) was obtained with a good yield (95%). Despite the presence of an amino group, which can participate in the Pd catalysed Buchwald-Hartwig amination reaction, this reaction proceeds through a Suzuki-Miyaura mechanism. The reaction conditions and catalysts were chosen in a way to facilitate the C-C bond formation rather than C-N. [230]

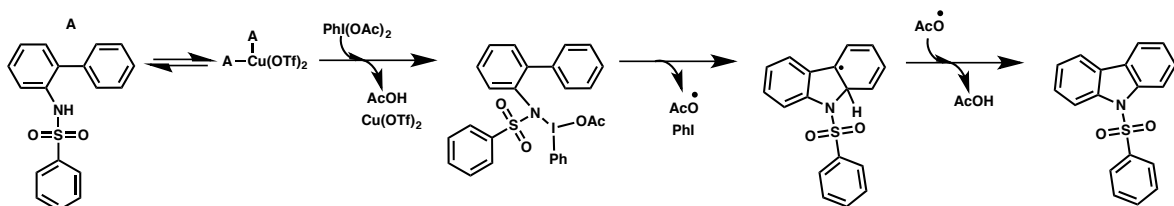
The obtained aromatic diamine (**12**) can be cyclized to form fused dicarbazole derivative. There are multiple ways to approach this problem. One of them is direct NH₂/C-H coupling, however, free amine group can have tight coordination to transition metals which could complicate the reaction mechanism. Nonetheless, there Ir-catalyzed dehydrogenative C-H/N-H coupling have been reported to give reasonably high yield of 74% for 2-amino-1,1'-biphenyl. [231] Ir-catalyst is used in combination with Cu(OAc)₂ and pyvalic acid. Pyvalic acid is frequently employed in direct arylation (C-C coupling) reaction as a co-catalyst for C-H bond activation. It has been reported that the acidity of C-H bond is an important parameter in direct arylation reactions. [232] Therefore, this reaction conditions do not give us certainty of obtaining the necessary products, due to the electron donating substituents on the 2,7-dibromophenanthren-9,10-(ethyleneglycol)ketal that might lower the acidity of C-H bond to the point where the reaction would be inefficient.

Next, we examined a method first reported by Buchwald *et al* [233], which involves usage of both Pd(0) and Cu(II) catalysts in air whilst amino group was activated by acetic protective group. The synthetic procedures advanced a lot since that report, and hence we used a modified version of this synthetic route. The procedure we followed offered utilization of only one catalyst – Cu(II) salt, oxidizing agent (PhI(OAc)₂) and activation of amino group by benzosulfonyl protection. [234] The procedure requires an electron withdrawing group on the amine, suggesting that sulfonyl group is the best option for the reaction. Thus, we used a simple pyridine catalysed reaction of the diamine precursor and phenylsulfonyl chloride to obtain the *N*-sulfonyl derivative (**Scheme 7.17**). The obtained derivative (**13**) was then used in the cyclization reaction.



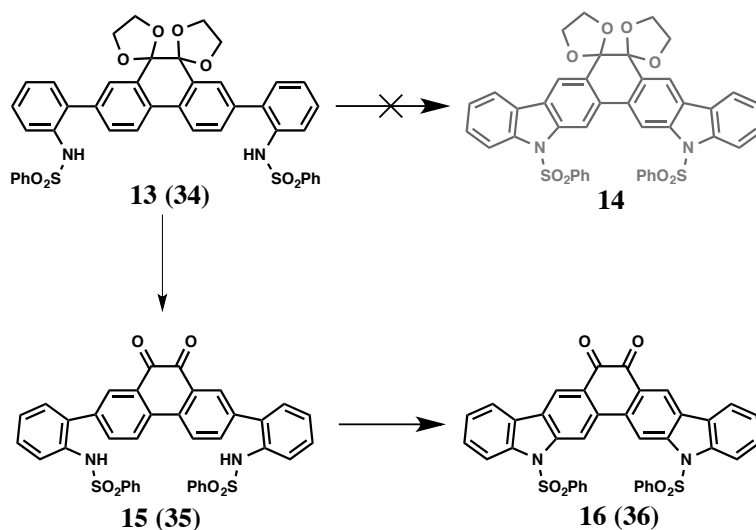
Scheme 7.17. Mechanism of benzosulfonyl protection of the aminogroup.

Scheme 7.18 shows the mechanism of the cyclization reaction according to the paper by Cho *et al.* [234] The first step of this reaction is reversible binding of two equivalents of amine to a copper catalyst. This step is followed by interaction with hypervalent iodine (III) reagent, forming an iodoamido intermediate and regenerating a catalyst. This complex allows electrophilic aromatic attack of orthophenyl fragment onto the amido fragment of the molecule through a radical mechanism. The reaction completes with a proton abstraction from acetoxy radical.

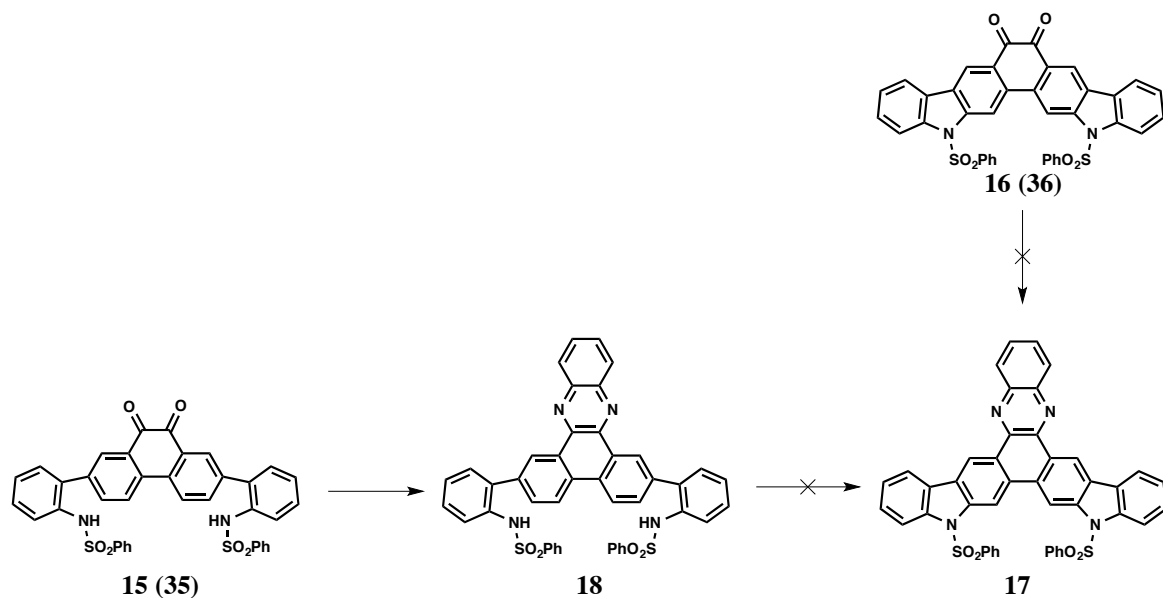


Scheme 7.18. Mechanism of copper-catalysed C-N bond formation. [234]

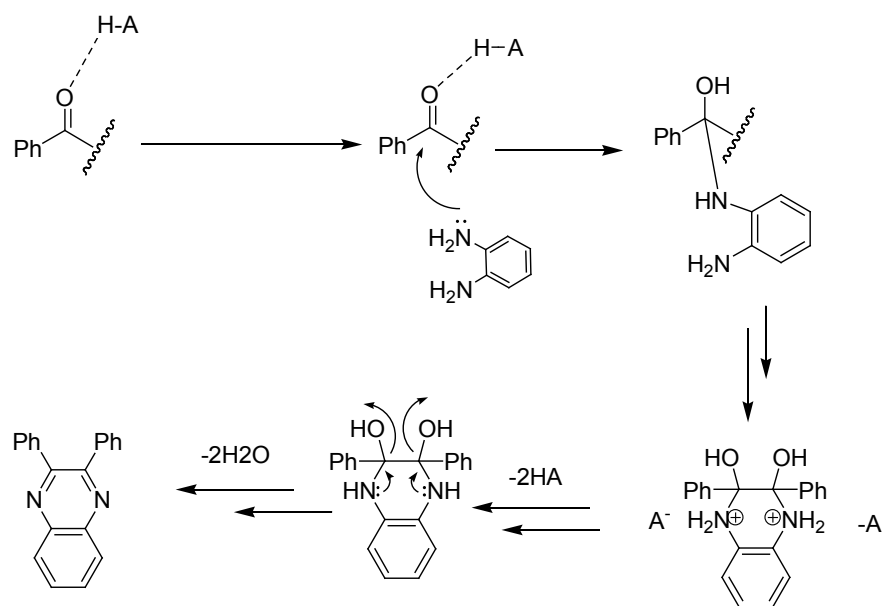
This paper also suggests that electron donating substituents can slow down reaction progress. We tested this coupling reaction on the derivative (**13**) and found that, indeed, the reaction is unsuccessful. Therefore, we had to deprotect the keto-groups to obtain the molecule (**16**) and use this derivative for the coupling reaction. The reaction was successful, giving 78% yield of the product (**Scheme 7.18**).

**Scheme 7.19. Cyclization substrates options.**

The next step in synthesis is condensation reaction of the product (16) with *o*-phenylenediamine as it is shown on the **Scheme 7.20**. We tested several reaction conditions for this process (the general procedure is given in section 3.7.3). This condensation reaction is usually performed in ethanol with addition of acid as a catalyst. [235] The mechanism of this reaction involves coordination of acid to a keto group. This is followed by a nucleophilic attack of the diamine to the activated carbonyl (**Scheme 7.21**). We tested acetic acid, hydrochloric acid and *p*-toluenesulfonic as catalysts for the condensation reaction. The necessary product was not obtained, we found that the major product of these reactions was the molecule on **Figure 7.8** (found both in NMR and in mass spectroscopy). Proton NMR of the obtained compound shows that the reaction did not go to completion, however, *o*-phenylenediamine did react with the diketone which can be deduced from presence of phenazine-like signals in NMR. The two singlets in the low field (9.85 and 9.55 ppm) can be assigned to NH and OH groups, respectively. The conversion of the starting material into this product was very poor. Further acid treatment of this molecule did not result in the conversion into dicarbazo[*a,c*]phenazine derivative.



Scheme 7.20. Condensation and alkylation synthetic options.



Scheme 7.21. Mechanism of acid catalysed condensation reaction with an aromatic diamine. [235]

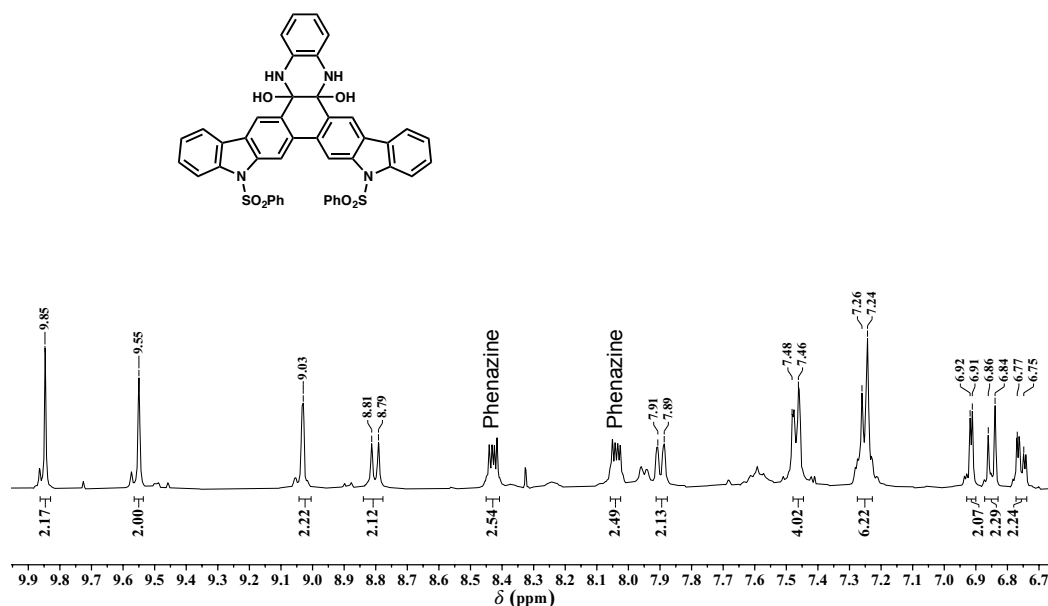
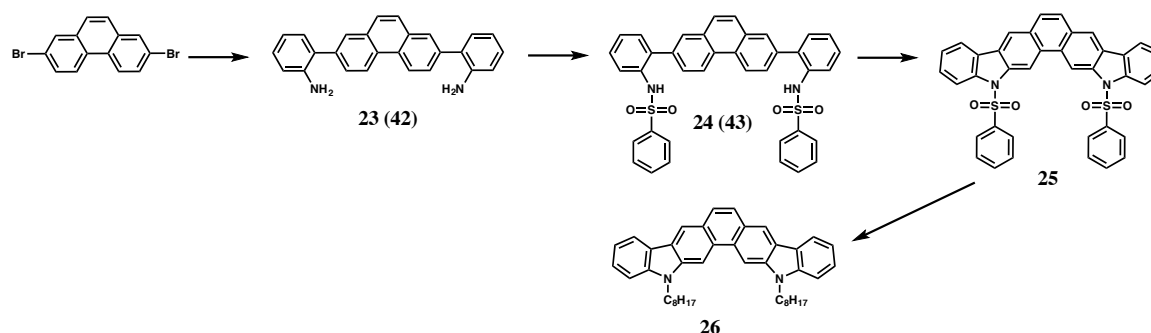


Figure 7.8. ^1H NMR of the condensation reaction (reflux in acetic acid : ethanol, 1:2) product in DMSO- d_6 .

We have also tested the condensation reaction of compound **(15)** and *o*-phenylenediamine. This reaction was successful; however, the yield was very low. The formation of the product was confirmed by mass spectroscopy and roughly by NMR. Due to poor solubility and, hence, limited options for purification, the material was not used in further synthesis.

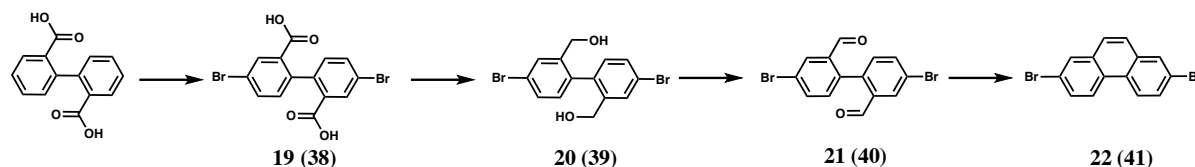
Therefore, the condensation reaction between the product **(16)** and *o*-phenylenediamine is challenging. This might be due to the poor reactivity of the carbonyl group in the product **(16)**. This is why we decided to stop pursuing the dicarbazolo[*a,c*]phenazines targets and focus on the aromatic core synthesis, thus, aiming to synthesise the benzo[*a,c*]dicarbazole (M8).

We chose to follow the route we already developed for dicarbazolo[*a,c*]phenazines, namely, Suzuki-Miyaura cross-coupling reaction to obtain the diamino compound followed by Cu-catalysed ring closure. When the core is obtained, the protective groups could be removed and N-alkyl derivatives can be synthesised (**Scheme 7.22**).



Scheme 7.22. Synthetic strategy to obtain benzo[*a,c*]dicarbazole.

Despite the seemingly simple structure, the starting material for this synthesis (2,7-dibromophenanthrene) is not commercially available. Hence, we synthesised it following previously reported procedure by Bösch *et al* [68] (**Scheme 7.23**). This procedure starts by bromination of a diphenic acid, followed by the reduction of the acid groups to primary alcohol. This reduction is very inefficient (37% yield), which limits the overall yield of the 2,7-dibromophenanthrene, even though the following two reactions can be accomplished with the yields over 70%.



Scheme 7.23. Synthetic route to preparation of 2,7-dibromophenanthrene. [68]

Products (**23**) and (**24**) on **Scheme 7.23** were obtained with good yields (80% and 75% respectively). The ring closure of the product (**25**) was performed in the same conditions as previously discussed for product (**15**). Proton NMR of the product is shown on **Figure 7.9**. Interestingly, there is only one singlet in this spectra which suggests that the ring closure does not result in formation of product (**25**) as shown on **Scheme 7.22**, unlike it is observed in the reaction of product (**15**). Further NMR study using correlation NMR spectroscopy technique (COSY) shows that indeed two protons (doublets at 8.81 and 8.79 ppm) have a close-range correlation with each other.

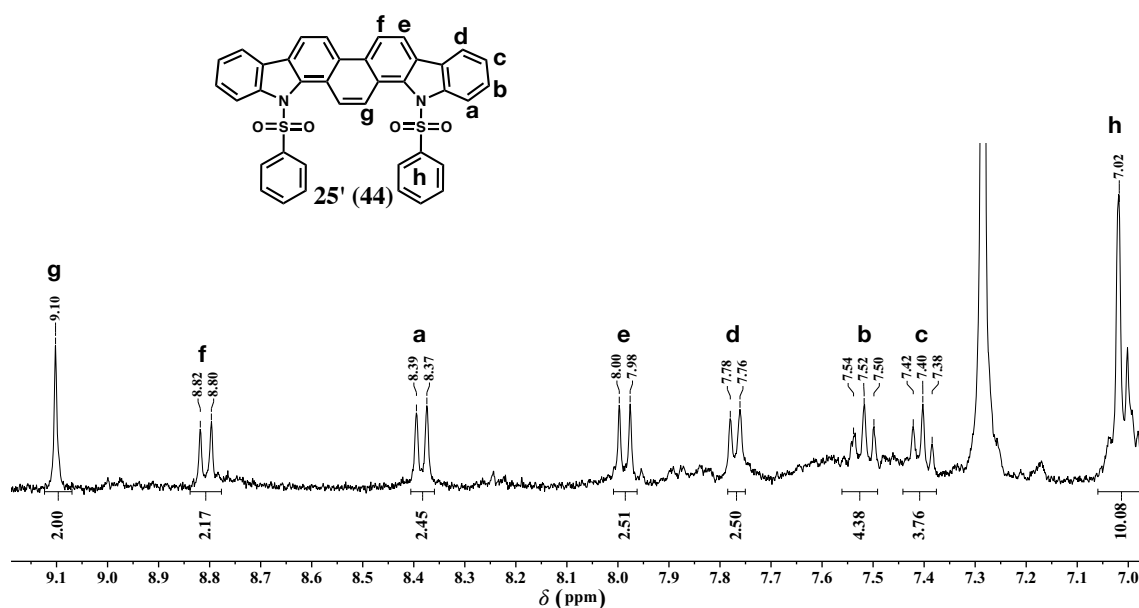


Figure 7.9. ^1H NMR spectrum of the compound (**25'**), peaks assigned using COSY NMR.

Therefore, we conclude that the ring closure reaction proceeds successfully with a yield of 80%. Despite this promising fact, at this point we had to terminate this synthesis due to the lack of the starting materials and time.

7.4 Conclusions

We designed a series of π -conjugated planar molecules - dicarbazolo[*a,c*]phenazines, as potential TADF materials. Singlet-triplet splitting for these molecules are in the range of 0.4 eV. These values are much higher than those found in previously reported TADF emitters. However, the calculation was performed for gas phase and the S-T gap is expected to be smaller in solid state due to singlet stabilization. Further, we showed our attempt to synthesise the designed molecules.

Several strategies for synthesis of dicarbazolo[*a,c*]phenazines were tested. All of the strategies utilized 2,7-dibromophenanthren-9,10-dione as a starting material. Ketal protective groups were used in order to increase solubility of this starting compound. The crucial step of all the strategies was the formation of pyrrole ring in order to obtain carbazole heterocyclic system. We tested several approaches to this ring-closure, namely, acid catalysed sigmatropic rearrangement of hydrazide derivative, Suzuki cross-coupling reaction between 2,7-dibromophenanthren-9,10-di(ethyleneglycol)ketal and 2-nitrophenylboronic acid, as well as, 2-aminophenylboronic acid. The use of electron rich 2-aminophenylboronic acid was found to be more efficient for the C-C coupling reaction with the given dibromo-compound. After this coupling reaction, we used a Cu-catalysed ring closure to successfully form the pyrrole ring. The next step towards synthesis of dicarbazolo[*a,c*]phenazines was a condensation reaction between the obtained aromatic core and *o*-phenylenediamine. This reaction failed which motivated us to move away from synthesis of dicarbazolo[*a,c*]phenazines derivatives to synthesis of a simpler benzo[*a,c*]dicarbazole.

For benzo[*a,c*]dicarbazole synthesis, we followed the route that we have developed for dicarbazolo[*a,c*]phenazines, namely, Suzuki-Miyaura cross-coupling reaction to obtain the diamino compound followed by Cu-catalysed ring closure. This synthesis was successful; however, the ring-closure yielded the unexpected isomer.

8 Summary and Outlook

In this thesis we considered photophysics of planar organic molecules in solution and in solid state. It is commonly expected that planar molecules should exhibit strong fluorescence due to the limited ISC pathways. In chapter 4 we showed that in sulfur-containing planar heterocycles (derivatives of benzo[*b*]thiophene) ISC occurs on sub-nanosecond time scale (~ 120 ps), which results in poor PLQY in solutions. To explain this unexpected result, we laid out the theory that allowed us to rationalize some of our experimental observables using *ensemble* geometries of singlet and triplet states involved in transition. We used Frank-Condon analysis to estimate the Frank-Condon density of states through Marcus-Levich-Jortner theory. This analysis showed that low energy vibrational mode (~ 110 meV) is crucial for ISC process in these planar derivatives. Nonetheless, some issues still remain unsolved, *e.g.* the classical reorganization energy that we find appropriate for prediction of the ratio between rate constants of different derivatives seems to be rather large (200 meV). Our theory also does not explain the experimentally observed temperature dependence. Therefore, a full time-dependent quantum approach might be needed to fully account for the photophysical processes in these molecules. At the same time, a more thorough time-resolved resonance Raman spectroscopy of both singlet and triplet states is necessary to experimentally confirm the change in vibrational modes as a result of ISC in all of the derivatives. This would also help to determine what structural components have the most prominent influence on the resonance Raman cross sections and might help to construct a clear set of the design rules.

The study of planar benzo[*b*]thiophene derivatives motivated us to look into structurally similar compounds – indolo[3,2-*b*]indoles. We synthesised the indolo[3,2-*b*]indoles derivatives that contain “neutral” substituents, namely alkyl and phenyl groups. In solutions of these

molecules (chapter 5) ISC is observed on nanosecond scale (~ 10 ns), even for brominated derivatives. The photophysical properties are similar for all of the derivatives. Interestingly, delayed luminescence is observed in the dilute solutions of these molecules, which could be explained by electron ejection from a molecule into a solvent, and further electron and radical-cation recombination which could result in an excited single state formation. This phenomenon is also observed in polymer films of indolo[3,2-*b*]indoles derivatives. Magnetic field dependent photoluminescence experiments could provide further details into the mechanism of this process. The effect should be taken into account when studying electron donating molecules, and it might be of use for applications that require a stable radical-cations. Further research needs to be done to figure out the ways to manipulate the yields of the radical-cation in order to be able to use this peculiar feature of the indolo[3,2-*b*] indoles derivatives in organic electronic devices.

The solid-state properties of indolo[3,2-*b*]indoles derivatives (chapter 6) were found to be more sensitive to different substituents. A significant difference in a solid-state molecular arrangement was observed between the derivatives, which resulted in a difference of photophysical properties. Long alkyl chains attached to a short axis (C8-N-inin) of the molecule gave rise to solution-like optical properties and no detectable carrier mobility. Whilst long alkyl chains attached to the long axis of the molecule (C8-C-inin) allowed for high hole mobility ($0.27 \text{ cm}^2/\text{Vs}$), while a reasonably good PLQY was also observed. This molecule was used to make OLEDs, showing blue emission; however, for a proper evaluation of its electroluminescent properties (i.e. the luminescence efficiency under electrical excitation) a more detailed study is required.

Me-N-inin in a thin film was found to have a blue shift of excimer emission with the increase of temperature. We explain this by suppression of the low energy vibrational modes of π - π stacking at low temperatures. The change in the emission energy is ~ 300 meV; this temperature-dependent colour change could be of interest for sensing applications. The evaporated thin films of Me-N-inin and Ph-N-inin did not exhibit charge carrier mobility and had a low PLQY. We explain this by a poor film morphology. The improved film morphology could result in higher PLQYs and charge carrier mobilities. A better evaporation technique, *i.e.* using variable substrate temperature, could help to improve the quality of the films and, hence, allow for a more accurate investigation of charge transporting properties in these molecules. Thermal or solvent annealing of the films might be another alternative to evaporation and could also have a strong influence on the electronic and photophysical properties of these films. We found that the molecular arrangement in films changes over time, and it is influenced by the ambient

Chapter 8: Summary and Outlook

conditions. A more thorough X-Ray study is required to understand the structure and rates of changes in the films of these materials in different conditions.

Finally, in chapter 7 we discussed our attempt to synthesise dicarbazolo[*a,c*]phenazines. Although these molecules could potentially exhibit interesting photophysical properties, their synthesis is unsustainable for practical applications due to poor yields and difficulties with purification.

Overall, we show that even small change in substituents can have a significant effect on photophysics of the molecules in solution and in solid state, this includes both radiative and non-radiative processes.

References

- [1] E. D. Williams, "Revisiting energy used to manufacture a desktop computer: Hybrid analysis combining process and economic input-output methods," *IEEE Int. Symp. Electron. Environ.*, pp. 80–85, 2004.
- [2] G. Fisher, M. R. Seacrist, and R. W. Standley, "Silicon crystal growth and wafer technologies," *Proc. IEEE*, vol. 100, pp. 1454–1474, 2012.
- [3] B. Valeur, *Molecular Fluorescence Principles and Applications*. Wiley-VCH Verlag GmbH, 2001.
- [4] A. Kohler and H. Bassler, *Electronic Processes in Organic Semiconductors: An Introduction*. Wiley-VCH Verlag GmbH & Co. KGaA, 2015.
- [5] N. J. Turro, V. Ramamurthy, and J. C. Scaiano, *Modern Molecular Photochemistry*. University Science Books, 2010.
- [6] A. Köhler and H. Bässler, "Triplet states in organic semiconductors," *Mater. Sci. Eng. R Reports*, vol. 66, pp. 71–109, 2009.
- [7] B. Milián-Medina and J. Gierschner, "Computational design of low singlet-triplet gap all-organic molecules for OLED application," *Org. Electron. physics, Mater. Appl.*, vol. 13, no. 6, pp. 985–991, 2012.
- [8] G. Davidson, *Group theory and vibrational spectroscopy*. Macmillan press ltd, 1993.
- [9] V. Balzani, P. Ceroni, and A. Juris, *Photochemistry and Photophysics. Concepts, Research, Applications*. Wiley-VCH Verlag GmbH & Co. KGaA, 2014.
- [10] A. B. Myers, "Relating absorption, emission, and resonance Raman spectra with electron transfer rates in photoinduced charge transfer systems: promises and pitfalls," *Chem. Phys.*, vol. 180, no. 2–3, pp. 215–230, Mar. 1994.
- [11] J.-L. Brédas, D. Beljonne, V. Coropceanu, and J. Cornil, "Charge-Transfer and Energy-Transfer Processes in π -Conjugated Oligomers and Polymers: A Molecular Picture," *Chem. Rev.* 2004, vol. 104, pp. 4971–5003, 2004.

References

- [12] K. Schmidt *et al.*, “Intersystem Crossing Processes in Nonplanar Aromatic Heterocyclic Molecules,” *J. Phys. Chem. A*, vol. 111, pp. 10490–10499, 2007.
- [13] R. Englman and J. Jortner, “The energy gap law for radiationless transitions in large molecules,” *Mol. Phys.*, vol. 18, no. 2, pp. 145–164, 1970.
- [14] T. J. Penfold, E. Gindensperger, C. Daniel, and C. M. Marian, “Spin-Vibronic Mechanism for Intersystem Crossing,” *Chem. Rev.*, p. acs.chemrev.7b00617, 2018.
- [15] S. P. McGlynn, T. Azumi, and M. Kinoshita, *Molecular Spectroscopy of the triplet state*. New Jersey: Prentice-Hall, Inc, 1969.
- [16] C. M. Marian, “Spin-orbit coupling and intersystem crossing in molecules,” *Wiley Interdiscip. Rev. Comput. Mol. Sci.*, vol. 2, pp. 187–203, Mar. 2012.
- [17] M. A. El-Sayed, “Spin-Orbit Coupling and the Radiationless Processes in Nitrogen Heterocyclics,” *Cit. J. Chem. Phys.*, vol. 38, no. 12, pp. 2834–2838, 1963.
- [18] G. Baryshnikov, B. Minaev, and H. Ågren, “Theory and Calculation of the Phosphorescence Phenomenon,” *Chem. Rev.*, vol. 117, pp. 6500–6537, 2017.
- [19] C. Wang, H. Dong, W. Hu, Y. Liu, and D. Zhu, “Semiconducting pi-conjugated systems in field-effect transistors: A material odyssey of organic electronics,” *Chem. Rev.*, vol. 112, no. 4, pp. 2208–2267, 2012.
- [20] V. C. Sundar, “Elastomeric Transistor Stamps: Reversible Probing of Charge Transport in Organic Crystals,” *Science (80-.)*, vol. 303, no. 5664, pp. 1644–1646, 2004.
- [21] S. Varghese and S. Das, “Role of Molecular Packing in Determining Solid-State Optical Properties of π -Conjugated Materials,” *J. Phys. Chem. Lett.*, vol. 2, pp. 863–873, 2011.
- [22] C. Wang, H. Dong, H. Li, H. Zhao, Q. Meng, and W. Hu, “Dibenzothiophene derivatives: From herringbone to lamellar packing motif,” *Cryst. Growth Des.*, vol. 10, no. 9, pp. 4155–4160, 2010.
- [23] J. Gierschner and S. Y. Park, “Materials for optical and electronic devices Luminescent distyrylbenzenes: tailoring molecular structure and crystalline morphology,” *J. Mater. Chem. C*, vol. 1, pp. 5818–5832, 2013.
- [24] N. J. Hestand and F. C. Spano, “Molecular Aggregate Photophysics beyond the Kasha Model: Novel Design Principles for Organic Materials,” *Acc. Chem. Res.*, vol. 50, pp. 341–350, 2017.

References

- [25] V. Coropceanu, J. Cornil, D. A. da Silva Filho, Y. Olivier, R. Silbey, and J.-L. Brédas, “Charge transport in organic semiconductors,” *Chem. Rev.*, vol. 107, no. 4, pp. 926–952, Apr. 2007.
- [26] Y. Shirota and H. Kageyama, “Charge carrier transporting molecular materials and their applications in devices,” *Chem. Rev.*, vol. 107, no. 4, pp. 953–1010, 2007.
- [27] J. L. Brédas, J. P. Calbert, D. a da Silva Filho, and J. Cornil, “Organic semiconductors: a theoretical characterization of the basic parameters governing charge transport,” *Proc. Natl. Acad. Sci. U. S. A.*, vol. 99, no. 9, pp. 5804–5809, 2002.
- [28] J. Zaumseil and H. Sirringhaus, “Electron and ambipolar transport in organic field-effect transistors,” *Chem. Rev.*, vol. 107, no. 4, pp. 1296–1323, Apr. 2007.
- [29] H. Dong, X. Fu, J. Liu, Z. Wang, and W. Hu, “25th Anniversary Article: Key Points for High-Mobility Organic Field-Effect Transistors,” *Adv. Mater.*, vol. 25, pp. 6158–6183, 2013.
- [30] S. T. Bromley, M. Mas-Torrent, P. Hadley, and C. Rovira, “Importance of intermolecular interactions in assessing hopping mobilities in organic field effect transistors: Pentacene versus dithiophene-tetrathiafulvalene,” *J. Am. Chem. Soc.*, vol. 126, no. 21, pp. 6544–6545, 2004.
- [31] S. F. Nelson, Y. Y. Lin, D. J. Gundlach, and T. N. Jackson, “Temperature-independent transport in high-mobility pentacene transistors,” *Appl. Phys. Lett.*, vol. 72, no. 15, pp. 1854–1856, 1998.
- [32] M. Mas-Torrent, M. Durkut, P. Hadley, X. Ribas, and C. Rovira, “High Mobility of Dithiophene-Tetrathiafulvalene Single-Crystal Organic Field Effect Transistors,” *J. Am. Chem. Soc.*, vol. 126, no. 4, pp. 984–985, 2004.
- [33] J. Yang, D. Yan, and T. S. Jones, “Molecular Template Growth and Its Applications in Organic Electronics and Optoelectronics,” *Chem. Rev.*, vol. 115, no. 11, pp. 5570–5603, 2015.
- [34] S. Illig *et al.*, “Reducing dynamic disorder in small-molecule organic semiconductors by suppressing large-amplitude thermal motions,” *Nat. Commun.*, vol. 7, p. 10736, 2016.
- [35] O. D. Jurchescu, M. Popinciuc, B. J. Van Wees, and T. T. M. Palstra, “Interface-controlled, high-mobility organic transistors,” *Adv. Mater.*, vol. 19, no. 5, pp. 688–692, 2007.

References

- [36] G. Giri *et al.*, “Tuning charge transport in solution-sheared organic semiconductors using lattice strain,” *Nature*, vol. 480, no. 7378, p. 504, 2011.
- [37] J. Mei, Y. Diao, A. L. Appleton, L. Fang, and Z. Bao, “Integrated materials design of organic semiconductors for field-effect transistors,” *J. Am. Chem. Soc.*, vol. 135, no. 18, pp. 6724–6746, 2013.
- [38] H. Minemawari *et al.*, “Inkjet printing of single-crystal films,” *Nature*, vol. 475, no. 7356, pp. 364–367, 2011.
- [39] N. Elgrishi, K. J. Rountree, B. D. McCarthy, E. S. Rountree, T. T. Eisenhart, and J. L. Dempsey, “A Practical Beginner’s Guide to Cyclic Voltammetry,” *J. Chem. Educ.*, vol. 95, pp. 197–206, 2018.
- [40] C. M. Cardona, W. Li, A. E. Kaifer, D. Stockdale, and G. C. Bazan, “Electrochemical considerations for determining absolute frontier orbital energy levels of conjugated polymers for solar cell applications,” *Adv. Mater.*, vol. 23, no. 20, pp. 2367–2371, 2011.
- [41] J. R. Lakowicz, *Principles of fluorescence Spectroscopy*, Third edit. Springer US, 1999.
- [42] A. M. Brouwer, “Standards for photoluminescence quantum yield measurements in solution (IUPAC Technical Report),” *Pure Appl. Chem.*, vol. 83, no. 12, pp. 2213–2228, 2011.
- [43] S. Leyre *et al.*, “Absolute determination of photoluminescence quantum efficiency using an integrated sphere setup,” *Rev. Sci. Instrum.*, vol. 85, p. 123115, 2014.
- [44] R. Schmidtat, C. Tanielian, R. Dunsbach, and C. Wolff, “Phenalenone, a universal reference compound for the determination of quantum yields of singlet oxygen sensitization,” 1994.
- [45] “High sensitivity cameras: Principle and Technology.” [Online]. Available: https://www.hamamatsu.com/resources/pdf/sys/e_dctn1.pdf. [Accessed: 14-Sep-2019].
- [46] “An Introduction to the ICCD Camera.” [Online]. Available: <https://www.oxinst.com/learning/view/article/intensified-ccd-cameras>. [Accessed: 14-Sep-2019].
- [47] C. Ruckebusch, M. Sliwa, P. Pernot, A. de Juan, and R. Tauler, “Comprehensive data analysis of femtosecond transient absorption spectra: A review,” *J. Photochem. Photobiol. C Photochem. Rev.*, vol. 13, no. 1, pp. 1–27, Mar. 2012.

References

- [48] E. Smith and G. Dent, *Modern Raman Spectroscopy - A Practical Approach*. 2005.
- [49] “Multimode Frank-Condon fitting.” [Online]. Available: <https://github.com/fast-spectroscopy-sheffield/franck-condon-fitting/tree/development>. [Accessed: 14-Sep-2019].
- [50] S. Mehta and R. C. Larock, “Iodine/Palladium approaches to the synthesis of polyheterocyclic compounds,” *J. Org. Chem.*, vol. 75, no. 5, pp. 1652–1658, 2010.
- [51] M. Iwasaki, T. Fujii, A. Yamamoto, K. Nakajima, and Y. Nishihara, “Palladium-catalyzed regio- and stereoselective chlorothiolation of terminal alkynes with sulfenyl chlorides,” *Chem. - An Asian J.*, vol. 9, no. 1, pp. 58–62, 2014.
- [52] T. Mori *et al.*, “Consecutive thiophene-annulation approach to pi-extended thienoacene-based organic semiconductors with [1]benzothieno[3,2-b][1]benzothiophene (BTBT) substructure,” *J Am Chem Soc*, vol. 135, pp. 13900–13913, 2013.
- [53] H. Ebata *et al.*, “Highly Soluble [1] Benzothieno [3 , 2-b] benzothiophene (BTBT) Derivatives for High-Performance, Solution-Processed Organic Field-Effect Transistors,” *J. Am. Chem. Soc.*, vol. 129, pp. 15732–15733, 2007.
- [54] C. M. S. Combe, L. Biniek, B. C. Schroeder, and I. McCulloch, “Synthesis of [1]benzothieno[3,2-b][1]benzothiophene pendant and norbornene random co-polymers via ring opening metathesis,” *J. Mater. Chem. C*, vol. 2, no. 3, pp. 538–541, 2014.
- [55] T. Qi *et al.*, “Synthesis and properties of the anti and syn isomers of dibenzothieno[b,d]pyrrole,” *Chem. Commun.*, pp. 6227–6229, Nov. 2008.
- [56] S. A. R. Mulla, S. S. Chavan, M. Y. Pathan, S. M. Inamdar, and T. M. Y. Shaikh, “Ligand-, base-, co-catalyst-free copper fluorapatite (CuFAP) as a versatile, ecofriendly, heterogeneous and reusable catalyst for an efficient homocoupling of arylboronic acid at ambient reaction conditions,” *RSC Adv.*, vol. 5, no. 31, pp. 24675–24680, Mar. 2015.
- [57] L. Qiu *et al.*, “Reductive ring closure methodology toward heteroacenes bearing a dihydropyrrolo[3,2- B]pyrrole core: Scope and limitation,” *J. Org. Chem.*, vol. 79, no. 23, pp. 11339–11348, 2014.
- [58] C. Coulson, “The preparation and photophysical investigations of indolo[3,2-b] indole derivatives with TADF properties for application in OLEDs,” University of Sheffield, 2018.

References

- [59] T. H. Vo *et al.*, “Bottom-up solution synthesis of narrow nitrogen-doped graphene nanoribbons,” *Chem. Commun.*, vol. 50, no. 32, pp. 4172–4174, 2014.
- [60] J. Zhao, X. Yang, M. Cheng, S. Li, and L. Sun, “New Organic Dyes with a Phenanthrenequinone Derivative as the π -Conjugated Bridge for Dye-Sensitized Solar Cells,” *J. Phys. Chem. C*, vol. 117, pp. 12936–12941, 2013.
- [61] Y. Zhang, L. Chen, K. Zhang, H. Wang, and Y. Xiao, “A Soluble Ladder-Conjugated Star-Shaped Oligomer Composed of Four Perylene Diimide Branches and a Fluorene Core: Synthesis and Properties,” *Chem. - A Eur. J.*, vol. 20, no. 32, pp. 10170–10178, Aug. 2014.
- [62] M. Wolter, A. Klapars, and S. L. Buchwald, “Synthesis of N -Aryl Hydrazides by Copper-Catalyzed Coupling of Hydrazides with Aryl Iodides Synthesis of N -Aryl Hydrazides by Copper-Catalyzed Coupling of Hydrazides with Aryl Iodides,” *Org. Lett.*, vol. 3, pp. 3803–3805, 2001.
- [63] D. S. Kopchuk *et al.*, “The extension of conjugated system in pyridyl-substituted monoazatriphenylenes for the tuning of photophysical properties,” *Chem. Heterocycl. Compd.*, vol. 50, no. 6, pp. 871–879, 2014.
- [64] L. A. Estrada and D. C. Neckers, “Synthesis and Photophysics of Dibenz- [a , c] phenazine Derivatives,” *Org. Lett.*, vol. 13, no. 7, p. 3304, 2011.
- [65] S. E. Collibee and J. Yu, “A facile and convenient synthesis of functionalized ortho-nitrophenylboronic acids,” *Tetrahedron Lett.*, vol. 46, no. 26, pp. 4453–4455, 2005.
- [66] D. Vonlanthen, J. Rotzler, M. Neuburger, and M. Mayor, “Synthesis of Rotationally Restricted and Modular Biphenyl Building Blocks,” *European J. Org. Chem.*, vol. 2010, no. 1, pp. 120–133, Jan. 2010.
- [67] M. Groziak, A. Ganguly, and P. Robinson, “Boron Heterocycles Bearing a Peripheral Resemblance to Naturally-Occurring Purines: Design, Syntheses, Structures, and Properties,” *J. Am. Chem. Soc.*, vol. 116, pp. 7597–7605, 1994.
- [68] C. D. Bösch, S. M. Langenegger, and R. Häner, “Light-Harvesting Nanotubes Formed by Supramolecular Assembly of Aromatic Oligophosphates,” *Angew. Chemie - Int. Ed.*, vol. 55, no. 34, pp. 9961–9964, 2016.
- [69] D. Vonlanthen, J. Rotzler, M. Neuburger, and M. Mayor, “Synthesis of rotationally restricted and modular biphenyl building blocks,” *European J. Org. Chem.*, vol. 2010, pp.

References

- 120–133, 2010.
- [70] A. B. Stephansen and T. I. Sølling, “Distortion dependent intersystem crossing: A femtosecond time-resolved photoelectron spectroscopy study of benzene, toluene, and p-xylene,” *Struct. Dyn.*, vol. 4, p. 044008, 2017.
- [71] W. Yang *et al.*, “Efficient Intersystem Crossing in Heavy-Atom-Free Perylenebisimide Derivatives,” *J. Phys. Chem. C* 2016, vol. 120, pp. 10162–101175, 2016.
- [72] A. B. Skov, M. A. B. Larsen, M. B. Liisberg, T. Hansen, and T. I. Sølling, “Conformationally controlled ultrafast intersystem crossing in bithiophene systems,” *Phys. Chem. Chem. Phys.*, vol. 20, pp. 13412–13418, 2018.
- [73] P. Kölle, T. Schnappinger, and R. De Vivie-Riedle, “Deactivation pathways of thiophene and oligothiophenes: Internal conversion versus intersystem crossing,” *Phys. Chem. Chem. Phys.*, vol. 18, no. 11, pp. 7903–7915, 2016.
- [74] G. Batignani, E. Pontecorvo, C. Ferrante, M. Aschi, C. G. Elles, and T. Scopigno, “Visualizing Excited-State Dynamics of a Diaryl Thiophene: Femtosecond Stimulated Raman Scattering as a Probe of Conjugated Molecules,” *J. Phys. Chem. Lett.*, vol. 7, no. 15, pp. 2981–2988, 2016.
- [75] N. I. Nijegorodov and W. S. Downey, “The Influence of Planarity and Rigidity on the Absorption and Fluorescence Parameters and Intersystem Crossing Rate Constant in Aromatic Molecules,” *J. Phys. Chem.*, vol. 98, pp. 5639–5643, 1994.
- [76] B. Kraabel, D. Moses, and A. J. Heeger, “Direct observation of the intersystem crossing in poly(3-octylthiophene),” *J. Chem. Phys.*, vol. 103, no. 12, pp. 5102–5108, 1995.
- [77] R. S. Becker, J. Seixas De Melo, A. L. Maçanita, and F. Elisei, “Comprehensive Evaluation of the Absorption, Photophysical, Energy Transfer, Structural, and Theoretical Properties of a-Oligothiophenes with One to Seven Rings,” *J. Phys. Chem.*, vol. 100, pp. 18683–18695, 1996.
- [78] J. Seixas de Melo, J. Pina, L. M. Rodrigues, and R. S. Becker, “A comprehensive study of the spectral and photophysical properties of arylthiophenes,” *J. Photochem. Photobiol. A Chem.*, vol. 194, no. 1, pp. 67–75, 2008.
- [79] B. Wex, B. R. Kaafarani, E. O. Danilov, and D. C. Neckers, “Altering the emission behavior with the turn of a thiophene ring: The photophysics of condensed ring systems

References

- of alternating benzenes and thiophenes,” *J. Phys. Chem. A*, vol. 110, no. 51, pp. 13754–13758, 2006.
- [80] S. A. Wolf *et al.*, “Spintronics: A Spin-Based Electronics Vision for the Future Downloaded from,” *Science (80-.)*, vol. 294, pp. 1488–1495, 1993.
- [81] S. Schott *et al.*, “Tuning the effective spin-orbit coupling in molecular semiconductors,” *Nat. Commun.*, pp. 1–10, 2017.
- [82] E. R. Mcnellis, S. Schott, H. Siringhaus, and J. Sinova, “Molecular tuning of the magnetic response in organic semiconductors,” *Phys. Rev. Mater.*, vol. 2, p. 74405, 2018.
- [83] R. Kumar Venkatraman, S. Kayal, A. Barak, A. J. Orr-Ewing, and S. Umopathy, “Intermolecular Hydrogen Bonding Controlled Intersystem Crossing Rates of Benzophenone,” *J. Phys. Chem. Lett. 2018*, vol. 9, pp. 1642–1648, 2018.
- [84] S. Aloise, C. Ruckebusch, L. Blanchet, J. Réhault, G. Buntinx, and J.-P. Huvenne, “The Benzophenone S 1 (n,π^*) f T 1 (n,π^*) States Intersystem Crossing Reinvestigated by Ultrafast Absorption Spectroscopy and Multivariate Curve Resolution,” *J. Phys. Chem. A*, vol. 112, pp. 224–231, 2008.
- [85] B. Soep, J.-M. Mestdagh, M. Briant, M.-A. Gaveau, and L. Poisson, “Direct observation of slow intersystem crossing in an aromatic ketone, fluorenone,” *Phys. Chem. Chem. Phys.*, vol. 18, p. 22914, 2016.
- [86] R. Mundt, T. Villnow, C. T. Ziegenbein, P. Gilch, C. Marian, and V. Rai-Constapel, “Thioxanthone in apolar solvents: ultrafast internal conversion precedes fast intersystem crossing,” *Phys. Chem. Chem. Phys.*, vol. 18, pp. 6637–6647, 2016.
- [87] A. M. Philip, M. Gudem, E. Sebastian, and M. Hariharan, “Decoding the Curious Tale of Atypical Intersystem Crossing Dynamics in Regioisomeric Acetylanthracenes,” *J. Phys. Chem. A, Just Accept. Manuscr. •*, 2019.
- [88] A. J. Tilley, R. D. Pensack, T. S. Lee, B. Djukic, G. D. Scholes, and D. S. Seferos, “Ultrafast triplet formation in thionated perylene diimides,” *J. Phys. Chem. C*, vol. 118, no. 19, pp. 9996–10004, 2014.
- [89] E. F. Plaza-Medina, W. Rodríguez-Córdoba, and J. Peon, “Role of Upper Triplet States on the Photophysics of Nitrated Polyaromatic Compounds: S 1 Lifetimes of Singly Nitrated Pyrenes,” *J. Phys. Chem. A*, vol. 115, pp. 9782–9789, Sep. 2011.

References

- [90] X. Hua, L. Hua, and X. Liu, "Ultrafast Excited-State Dynamics of 6-Azauracil Studied by Femtosecond Transient Absorption Spectroscopy," *J. Phys. Chem. A*, vol. 119, pp. 12985–12989, 2015.
- [91] S. Mai *et al.*, "The origin of efficient triplet state population in sulfur-substituted nucleobases," *Nat. Commun.*, vol. 7, pp. 1–8, 2016.
- [92] A. Wesley Horton, "The mechanism of the reactions of hydrocarbons with sulfur," *J. Org. Chem.*, vol. 14, no. 5, pp. 761–770, Sep. 1949.
- [93] J. Clayden, N. Greeves, S. Warren, and P. Wothers, *Organic Chemistry*. Oxford: Oxford University Press, 2000.
- [94] D. Yue and R. C. Larock, "Synthesis of 2,3-Disubstituted Benzo[b]thiophenes via Palladium-Catalyzed Coupling and Electrophilic Cyclization of Terminal Acetylenes," *J. Org. Chem.*, vol. 67, no. 6, pp. 1905–1909, 2002.
- [95] T. Kesharwani, S. A. Worlikar, and R. C. Larock, "Synthesis of 2, 3-Disubstituted Benzo [b] selenophenes via Electrophilic Cyclization," no. c, pp. 2307–2312, 2006.
- [96] D. Yue, T. Yao, and R. C. Larock, "Synthesis of 2, 3-Disubstituted Benzo [b] furans by the Palladium-Catalyzed Coupling of o- Iodoanisoles and Terminal Alkynes , Followed by Electrophilic Cyclization," *J. Org. Chem.*, vol. 70, no. 25, pp. 10292–10296, 2005.
- [97] D. Alberico, M. E. Scott, and M. Lautens, "Aryl-aryl bond formation by transition-metal-catalyzed direct arylation," *Chem. Rev.*, vol. 107, no. 1, pp. 174–238, Jan. 2007.
- [98] A. Rudnick *et al.*, "Spectroscopic Study of Thiophene–Pyrrole-Containing S,N-Heteroheptacenes Compared to Acenes and Phenacenes," *J. Phys. Chem. B*, vol. 121, no. 31, pp. 7492–7501, Aug. 2017.
- [99] N. M. Shavaleev, H. Adams, J. Best, R. Edge, S. Navaratnam, and J. A. Weinstein, "Deep-Red Luminescence and Efficient Singlet Oxygen Generation by Cyclometalated Platinum(II) Complexes with 8-Hydroxyquinolines and Quinoline-8-thiol," 2006.
- [100] J. G. Velasco, "PhD thesis," University of Sheffield, 2020.
- [101] H. Meng *et al.*, "Tetramethylpentacene: Remarkable Absence of Steric Effect on Field Effect Mobility," *Adv. Mater.*, vol. 15, no. 13, pp. 1090–1093, Jul. 2003.
- [102] A. Stanger, "Nucleus-Independent Chemical Shifts (NICS): Distance Dependence and Revised Criteria for Aromaticity and Antiaromaticity," *J. Org. Chem.*, vol. 71, no. 3, pp.

References

- 883–893, 2006.
- [103] J.-I. Aihara, H. Kanno, and T. Ishida, “Magnetic Resonance Energies of Heterocyclic Conjugated Molecules,” *J. Phys. Chem. A*, vol. 111, pp. 8873–8876, 2007.
- [104] B. L. Van Duuren, “Solvent Effects in the Fluorescence of Indole and Substituted Indoles,” *Arch. Biochem. Biophys.*, vol. 26, pp. 2954–2960, 1952.
- [105] M. S. Walker, T. W. Bednar, and R. Lumry, “Exciplex Formation in the Excited State of Indole,” *Intramol. Excimer Form. I. Diphenyl Triphenyl Alkanes J. Chem. Phys.*, vol. 45, p. 3163, 1966.
- [106] N. A. Shafakat Ali, B. Ahmad Dar, V. Pradhan, and M. Farooqui, “Chemistry and Biology of Indoles and Indazoles: A Mini-Review,” *Mini Rev. Med. Chem.*, vol. 13, no. 12, pp. 1792–1800(9), 2013.
- [107] D. Brisker-Klaiman and A. Dreuw, “Explaining Level Inversion of the L_a and L_b States of Indole and Indole Derivatives in Polar Solvents,” *ChemPhysChem*, vol. 16, no. 8, pp. 1695–1702, Jun. 2015.
- [108] M. Aubailly, M. Bazin, and R. Santus, “Trapped electrons produced by biphotonic photionisation and their relation with delayed emission of indole ring in ethanol glass,” *Chem. Phys. Lett.*, vol. 14, no. 4, pp. 422–424, Jun. 1972.
- [109] T. R. Hopkins and R. Lumry, “EXCIPLEX STUDIES–V. ELECTRON EJECTION FROM INDOLE AND METHYL-INDOLE DERIVATIVES,” *Photochem. Photobiol.*, vol. 15, no. 6, pp. 555–566, Jun. 1972.
- [110] M. Ewald, “Photo-injection of electrons in polyethylene film at 77 K via two-photon photoionization of guest aromatics, mechanism of electron detrapping and lowering of the guest ionization potential,” *Radiat. Phys. Chem.*, vol. 15, pp. 383–391, Jan. 1980.
- [111] R. F. Borkman, L. B. Hibbard, and J. Dillon, “THE PHOTOLYSIS OF TRYPTOPHAN WITH 337.1 nm LASER RADIATION,” *Photochem. Photobiol.*, vol. 43, no. 1, pp. 13–19, Jan. 1986.
- [112] M. Aubailly, M. Bazin, and R. Santus, “The role of photoejected electrons in the delayed fluorescence of indole derivatives in frozen aqueous solutions at 77°K,” *Chem. Phys. Lett.*, vol. 12, no. 1, pp. 70–74, Dec. 1971.
- [113] V. M. Mazhul’, D. G. Shcherbin, V. A. Shashilov, A. A. Sukhodola, E. M. Zaitseva, and

References

- G. B. Tolstorozhev, "RECOMBINATION PROLONGED LUMINESCENCE OF INDOLE AND TRYPTOPHAN IN A SOLUTION AT ROOM TEMPERATURE," *J. Appl. Spectrosc.*, vol. 70, no. 2, pp. 270–275, 2003.
- [114] S. Tanaka, T. Kumagai, T. Mukai, and T. Kobayashi, "1,4-Dihidropyrrolo[3,2-b]pyrrole: The Electronic Structure Elucidated by Photoelectron Spectroscopy," *Bull. Chem. Soc. Jpn.*, vol. 60, pp. 1981–1983, 1987.
- [115] A. Janiga and D. T. Gryko, "1,4-Dihidropyrrolo[3,2-b]pyrrole and Its π -Expanded Analogues," *Chem. - An Asian J.*, vol. 9, pp. 3036–3045, Nov. 2014.
- [116] O. Gidron and M. Bendikov, " α -oligofurans: An emerging class of conjugated oligomers for organic electronics," *Angew. Chemie, Int. Ed.*, vol. 53, no. 10, pp. 2546–2555, 2014.
- [117] X. Wang *et al.*, "The Influence of Structural Variations on the Heteroacenes Containing Dihidropyrrolo[3,2-b]pyrrole Core on Their OFET Performances," *ChemistrySelect*, vol. 4, pp. 5918–5924, May 2019.
- [118] I. Cho *et al.*, "Design, Synthesis, and Versatile Processing of Indolo[3,2-b]indole-Based π -Conjugated Molecules for High-Performance Organic Field-Effect Transistors," *Adv. Funct. Mater.*, vol. 26, pp. 2966–2973, 2016.
- [119] L. Qiu *et al.*, "An expedient synthesis of fused heteroacenes bearing a pyrrolo[3,2-b]pyrrole core," *Chem. Commun.*, vol. 48, no. 100, p. 12225, 2012.
- [120] C. H. Ryoo *et al.*, "Structure–Property Correlation in Luminescent Indolo[3,2-b]indole (IDID) Derivatives: Unraveling the Mechanism of High Efficiency Thermally Activated Delayed Fluorescence (TADF)," *ACS Appl. Mater. Interfaces*, vol. 9, pp. 41413–41420, Nov. 2017.
- [121] J. Sim *et al.*, "D-A-D-A-D push pull organic small molecules based on 5,10-dihydroindolo[3,2-b]indole (DINI) central core donor for solution processed bulk heterojunction solar cells," *Org. Electron.*, vol. 30, pp. 122–130, Mar. 2016.
- [122] Y.-Y. Lai, J.-M. Yeh, C.-E. Tsai, and Y.-J. Cheng, "Synthesis, Molecular and Photovoltaic Properties of an Indolo[3,2-b]indole-Based Acceptor-Donor-Acceptor Small Molecule," *European J. Org. Chem.*, pp. 5076–5084, Aug. 2013.
- [123] S. Hiinig and H. Steinmetzer, "Kondensierte Stickstoffheterocyclen," *Leibig. Ann. Chem.*, pp. 1090–1102, 1976.

References

- [124] M. M. Murray, P. Kaszynski, D. A. Kaisaki, W. Chang, D. A. Dougherty, and M. Beckman, "Prototypes for the Polaronic Ferromagnet. Synthesis and Characterization of High-Spin Organic Polymers," *J. Am. Chem. Soc.*, vol. 116, pp. 8152–8161, 1994.
- [125] C. He, Z. Li, Y. Lei, W. Zou, and B. Suo, "Unraveling the Emission Mechanism of Radical-Based Organic Light Emitting Diodes," *J. Phys. Chem. Lett.*, vol. 10, pp. 574–580, 2019.
- [126] X. Ai *et al.*, "Efficient radical-based light-emitting diodes with doublet emission," *Nature*, 2018.
- [127] M. López, D. Velasco, F. López-Calahorra, and L. Juliá, "Light-emitting persistent radicals for efficient sensor devices of solvent polarity," *Tetrahedron Lett.*, vol. 49, pp. 5196–5199, Aug. 2008.
- [128] S. Dobrin, P. Kaszynski, S. Ikeda, and J. Waluk, "Photophysics of trans-stilbene analogues: Indolo[3,2-b]indole and its heterosubstituted sulfur and selenium derivatives," *Chem. Phys.*, vol. 216, pp. 179–192, 1997.
- [129] S. Dobrin, P. Kaszynski, and J. Waluk, "Stilbene-like molecules: sulfur- and selenium-heterosubstituted indolo[3,2-b]indoles," *J. Photochem. Photobiol. A Chem.*, vol. 105, pp. 149–152, May 1997.
- [130] V. Sharma, P. Kumar, and D. Pathak, "Biological importance of the indole nucleus in recent years: A comprehensive review," *J. Heterocycl. Chem.*, vol. 47, no. 3, pp. 491–502, May 2010.
- [131] N. Kaushik *et al.*, "Biomedical Importance of Indoles," *Molecules*, vol. 18, no. 6, pp. 6620–6662, Jun. 2013.
- [132] A. V Karchava, F. S. Melkonyan, and M. A. Yurovskaya, "NEW STRATEGIES FOR THE SYNTHESIS OF N-ALKYLATED INDOLES (REVIEW)," *Chem. Heterocycl. Compd.*, vol. 48, no. 3, pp. 391–407, 2012.
- [133] T. V. Sravanthi and S. L. Manju, "Indoles — A promising scaffold for drug development," *Eur. J. Pharm. Sci.*, vol. 91, pp. 1–10, Aug. 2016.
- [134] P. Ruggli, "Über die Bildung eines zweifach kondensierten Indols," *Berichte der Dtsch. Chem. Gesellschaft*, vol. 50, no. 1, pp. 883–893, Jan. 1917.
- [135] S. A. Samsoniya and M. V Trapaidze, "The chemistry of indoloindoles," *Russ. Chem.*

References

- Rev.*, vol. 76, pp. 313–326, 2007.
- [136] P. V. Santhini *et al.*, “One-Pot MCR-Oxidation Approach toward Indole-Fused Heteroacenes.”
- [137] J. Yu, D. Zhang-negrerie, and Y. Du, “Cu(OAc)₂-Mediated Cascade Annulation of Diarylalkyne Sulfonamides through Dual C–N Bond Formation: Synthesis of 5,10-Dihydroindolo[3,2-b]indoles,” *Org. Lett.*, vol. 18, pp. 3322–3325, 2016.
- [138] F. C. Cooper and M. W. Partridge, “Cyclic Amidines. Part IV. 12-Tetrahydro-5 : 11-endo-methylenephnomazine and Troger’s Base,” *J. Chem. Soc.*, pp. 991–994, 1956.
- [139] W. Metlesics, R. Tavares, and L. H. Sternbach, “The reduction products of a Dibenzo[b,f][1,5]diazocine,” *J. Org. Chem.*, vol. 31, pp. 3356–3362, 1966.
- [140] K. Kunz, U. Scholz, and D. Ganzer, “Renaissance of Ullmann and Goldberg Reactions – Progress in Copper Catalyzed C – N-, C – O- and C – S-Coupling,” *Synlett*, no. 15, pp. 2428–2439, 2003.
- [141] Y. Kiso, K. Yamamoto, K. Tamao, and M. Kumada, “Selective Carbon-Carbon Bond Formation by Cross-Coupling of Grignard Reagents with Organic Halides. Catalysis by Nickel-Phosphine Complexes,” *J. Am. Chem. Soc.*, vol. 94, no. 12, pp. 4374–4376, 1972.
- [142] M. Kumada, K. Tamao, and K. Sumita, “Phosphine–Nickel complex catalysed cross-coupling of Grignard reagents with aryl and alkenyl halides: 1,2-dibutylbenzene,” *Org. Synth.*, vol. 58, p. 127, 1978.
- [143] M. Kumada, “NICKEL AND PALLADIUM COMPLEX CATALYZED CROSS-COUPPLING REACTIONS OF ORGANOMETALLIC REAGENTS WITH ORGANIC HALIDES,” *Pure Appl. Chem.*, vol. 52, pp. 669–679, 1980.
- [144] O. Vechorkin, V. Rie Proust, and X. Hu, “Functional Group Tolerant Kumada-Corriu-Tamao Coupling of Nonactivated Alkyl Halides with Aryl and Heteroaryl Nucleophiles: Catalysis by a Nickel Pincer Complex Permits the Coupling of Functionalized Grignard Reagents,” *J. Am. Chem. Soc.*, vol. 131, no. 28, pp. 9756–9766, 2009.
- [145] P. L. dos Santos *et al.*, “Engineering the singlet-triplet energy splitting in a TADF molecule,” *J. Mater. Chem. C*, vol. 4, pp. 3815–3824, 2016.
- [146] Y. Tao *et al.*, “Thermally Activated Delayed Fluorescence Materials Towards the Breakthrough of Organoelectronics,” *Adv. Mater.*, vol. 26, pp. 1–28, 2014.

References

- [147] T. J. Penfold, F. Dias, and A. P. Monkman, "The Theory of Thermally Activated Delayed Fluorescence for Organic Light Emitting Diodes.," *Chem. Commun.*, vol. 54, pp. 3926–3935, 2018.
- [148] M. K. Etherington, J. Gibson, H. F. Higginbotham, T. J. Penfold, and A. P. Monkman, "Revealing the spin–vibronic coupling mechanism of thermally activated delayed fluorescence," *Nat. Commun.*, vol. 7, p. 13680, Nov. 2016.
- [149] C. Torres Ziegenbein *et al.*, "Triplet Harvesting with a Simple Aromatic Carbonyl," *ChemPhysChem*, vol. 18, pp. 2314–2317, 2017.
- [150] P. Pander *et al.*, "Thermally Activated Delayed Fluorescence Mediated through the Upper Triplet State Manifold in Non-Charge-Transfer Star-Shaped Triphenylamine–Carbazole Molecules," *J. Phys. Chem. C*, vol. 122, pp. 23934–23942, 2018.
- [151] J. Liu *et al.*, "Experimental Evidence for 'Hot Exciton' Thermally Activated Delayed Fluorescence Emitters," *Adv. Opt. Mater.*, vol. 1801190, pp. 1–9, 2018.
- [152] H. Sternlicht, G. C. Nieman, and G. W. Robinson, "Triplet-Triplet Annihilation and Delayed Fluorescence in Molecular Aggregates," *J. Chem. Phys.*, vol. 38, pp. 1326–1335, 1963.
- [153] P.-Y. Chou *et al.*, "Efficient delayed fluorescence via triplet–triplet annihilation for deep-blue electroluminescence," *Chem. Commun.*, vol. 50, pp. 6869–6871, Jun. 2014.
- [154] H. Ohkita, W. Sakai, A. Tsuchida, and M. Yamamoto, "Charge Recombination Luminescence via the Photoionization of a Dopant Chromophore in Polymer Solids," *Macromolecules*, vol. 30, pp. 5376–5383, 1997.
- [155] R. Kabe and C. Adachi, "Organic long persistent luminescence," *Nat. Publ. Gr.*, vol. 550, pp. 384–387, 2017.
- [156] T. Northey, J. Eng, T. Keane, and T. J. Penfold, "Understanding the Potential for Efficient Triplet Harvesting with Hot Excitons," *Faraday Discuss.*, vol. 216, pp. 395–413, 2019.
- [157] L. J. Gijzeman, F. Kaufman, and G. Porter, "Oxygen Quenching of Aromatic Triplet States in Solution," *J. Chem. Soc., Faraday Trans. 2*, vol. 69, pp. 708–720, 1973.
- [158] P. L. Piciulo and J. K. Thomas, "Photoionization of pyrene in alkane liquids," *J. Chem. Phys.*, vol. 68, no. 7, pp. 3260–3264, 1978.
- [159] A. Kellmann and F. Tfibel, "Laser-induced two-photon ionization of acridine in aqueous

References

- solution,” *Chem. Phys. Lett.*, vol. 69, no. 1, pp. 61–65, Jan. 1980.
- [160] W. G. McGimpsey and H. Görner, “Photoionization of Indole, N-Methylindole and Tryptophan In Aqueous Solution upon Excitation at 193 nm,” *Photochem. Photobiol.*, vol. 64, no. 3, pp. 501–509, Sep. 1996.
- [161] M. Montalti, A. Credi, L. Prodi, and T. M. Gandolfi, *Handbook of Photochemistry*, 3rd ed. Taylor & Francis Group, 2006.
- [162] D. C. Walker, “The Hydrated Electron,” *Q. Rev.*, pp. 79–108, 1967.
- [163] L. . Lukin, A. . Tolmachev, and B. . Yakovlev, “The photoexcitation of trapped electrons produced in the photoionization of anthracene in liquid n-hexane,” *Chem. Phys. Lett.*, vol. 81, no. 3, pp. 595–598, Aug. 1981.
- [164] M. M. Fisher, B. Veyret, and K. Weiss, “Non-linear absorption and photoionization in the pulsed laser photolysis of anthracene,” *Chem. Phys. Lett.*, vol. 28, no. 1, pp. 60–65, Sep. 1974.
- [165] C. Pernot and L. Lindqvist, “Laser photolysis of indole in cyclohexane,” *J. Photochem.*, vol. 6, no. 3, pp. 215–220, Jan. 1976.
- [166] C. L. Ladner, K. Tran, M. Le, R. J. Turner, and R. A. Edwards, “Excited state photoreaction between the indole side chain of tryptophan and halocompounds generates new fluorophores and unique modifications,” *Photochem. Photobiol.*, vol. 90, no. 5, pp. 1027–1033, 2014.
- [167] R. A. Edwards, G. Jickling, and R. J. Turner, “The Light-induced Reactions of Tryptophan with Halocompounds,” *Photochem. Photobiol.*, vol. 75, no. 4, pp. 362–368, May 2007.
- [168] J. C. Scaiano, B. R. Arnold, and W. G. McGimpsey’, “Two-Laser, Two-Color Photochemistry from Upper Triplet States of 2-Bromonaphthalene and 9-Bromophenanthrene in Benzene,” *J. Phys. Chem*, vol. 98, pp. 5431–5434, 1994.
- [169] J. D. Satterlee, “Fundamental Concepts of NMR in Paramagnetic Systems,” *Concepts Magn. Reson.*, vol. 2, pp. 119–129, 1990.
- [170] P. S. Sherin, O. A. Snytnikova, and Y. P. Tsentalovich, “Tryptophan photoionization from prefluorescent and fluorescent states,” *Chem. Phys. Lett.*, vol. 391, pp. 44–49, Jun. 2004.
- [171] Z. Xie *et al.*, “Cross dipole stacking in the crystal of distyrylbenzene derivative: The approach toward high solid-state luminescence efficiency,” *J. Am. Chem. Soc.*, vol. 127,

References

- no. 41, pp. 14152–14153, 2005.
- [172] A. Dadvand *et al.*, “Maximizing Field-Effect Mobility and Solid-State Luminescence in Organic Semiconductors,” *Angew. Chemie Int. Ed.*, vol. 51, no. 16, pp. 3837–3841, Apr. 2012.
- [173] S. Z. Bisri *et al.*, “High mobility and luminescent efficiency in organic single-crystal light-emitting transistors,” *Adv. Funct. Mater.*, vol. 19, no. 11, pp. 1728–1735, 2009.
- [174] J. Zaumseil, C. L. Donley, J.-S. Kim, R. H. Friend, and H. Sirringhaus, “Efficient Top-Gate, Ambipolar, Light-Emitting Field-Effect Transistors Based on a Green-Light-Emitting Polyfluorene,” *Adv. Mater.*, vol. 18, no. 20, pp. 2708–2712, Oct. 2006.
- [175] I. D. W. Samuel and G. A. Turnbull, “Organic Semiconductor Lasers Organic Semiconductor Lasers,” *Chem. Rev.*, vol. 107, no. 4, pp. 1272–1295, 2007.
- [176] A. S. D. Sandanayaka *et al.*, “Indication of current-injection lasing from an organic semiconductor,” *Appl. Phys. Express*, vol. 12, no. 6, p. 061010, 2019.
- [177] J. Liu *et al.*, “High mobility emissive organic semiconductor,” *Nat. Commun.*, vol. 6, pp. 1–8, 2015.
- [178] M. Másmás-Montoya *et al.*, “Structure–Property Correlation behind the High Mobility of Carbazolocarbazole,” 2018.
- [179] S.-J. Yoon *et al.*, “Multistimuli Two-Color Luminescence Switching via Different Slip-Stacking of Highly Fluorescent Molecular Sheets,” *J. Am. Chem. Soc.*, vol. 132, pp. 13675–13683, 2010.
- [180] C. D. Dimitrakopoulos, A. R. Brown, and A. Pomp, “Molecular beam deposited thin films of pentacene for organic field effect transistor applications,” *J. Appl. Phys.*, vol. 80, p. 2501, 1996.
- [181] J. Veres, S. Ogier, G. Lloyd, and D. De Leeuw, “Gate insulators in organic field-effect transistors,” *Chem. Mater.*, vol. 16, no. 23, pp. 4543–4555, 2004.
- [182] C. D. Dimitrakopoulos and D. J. Mascaro, “Organic thin-film transistors: A review of recent advances,” *IBM J. Res. Dev.*, vol. 45, no. 1, pp. 11–27, 2001.
- [183] C. P. Dietrich, M. Siegert, S. Betzold, J. Ohmer, U. Fischer, and S. Höfling, “Exciton dynamics in solid-state green fluorescent protein,” *Appl. Phys. Lett.*, vol. 110, no. 4, p. 43703, 2017.

References

- [184] J. Liu *et al.*, “High mobility emissive organic semiconductor,” *Nat. Commun.*, vol. 6, no. May, p. 10032, 2015.
- [185] A. P. Arndt, M. Gerhard, A. Quintilla, I. A. Howard, M. Koch, and U. Lemmer, “Time-resolved charge-transfer state emission in organic solar cells: Temperature and blend composition dependences of interfacial traps,” *J. Phys. Chem. C*, vol. 119, no. 24, pp. 13516–13523, 2015.
- [186] Y. Shen, H. Liu, J. Cao, S. Zhang, W. Li, and B. Yang, “Unusual temperature-sensitive excimer fluorescence from discrete p-p dimer stacking of anthracene in a crystal,” *Phys. Chem. Chem. Phys.*, vol. 21, pp. 14511–14515, 2019.
- [187] G. Mehes, K. Goushi, W. J. Potscavage, and C. Adachi, “Influence of host matrix on thermally-activated delayed fluorescence: Effects on emission lifetime, photoluminescence quantum yield, and device performance,” *Org. Electron. physics, Mater. Appl.*, vol. 15, no. 9, pp. 2027–2037, 2014.
- [188] T. Chatterjee and K. T. Wong, “Perspective on Host Materials for Thermally Activated Delayed Fluorescence Organic Light Emitting Diodes,” *Adv. Opt. Mater.*, vol. 7, no. 1, pp. 1–34, 2019.
- [189] Y. Zhang *et al.*, “Supramolecular Structure-Dependent Thermally-Activated Delayed Fluorescence (TADF) Properties of Organic Polymorphs,” *J. Phys. Chem. C*, vol. 120, no. 35, pp. 19759–19767, 2016.
- [190] F. Ma, Y. Cheng, Y. Zheng, H. Ji, K. Hasrat, and Z. Qi, “Rational design of thermally activated delayed fluorescence emitters with aggregation-induced emission employing combined charge transfer pathways for fabricating efficient non-doped OLEDs †,” *J. Mater. Chem. C*, vol. 7, pp. 9413–9422, 2019.
- [191] Z. Yang *et al.*, “A sterically hindered asymmetric D–A–D’ thermally activated delayed fluorescence emitter for highly efficient non-doped organic light-emitting diodes,” *Chem. Sci.*, 2019.
- [192] Y. Hirata and I. Tanaka, “Intersystem crossing to the lowest triplet state of phenazine following singlet excitation with a picosecond pulse,” *Chem. Phys. Lett.*, vol. 43, no. 3, pp. 568–570, 1976.
- [193] D. Dey, A. Bose, D. Bhattacharyya, and S. Basu, “Dibenzo [a , c] phenazine : A Polarity-Insensitive Hydrogen-Bonding Probe,” *J. Phys. Chem. A*, vol. 111, pp. 10500–10506,

References

- 2007.
- [194] F.-M. Xie *et al.*, “Rational Molecular Design of Dibenzo[a , c]phenazine-Based Thermally Activated Delayed Fluorescence Emitters for Orange-Red OLEDs with EQE up to 22.0%,” *ACS Appl. Mater. Interfaces*, vol. 11, no. 29, pp. 26144–26151, 2019.
- [195] A. W. Schmidt, K. R. Reddy, and H.-J. Knölker, “Occurrence, Biogenesis, and Synthesis of Biologically Active Carbazole Alkaloids,” *Chem. Rev.*, vol. 112, no. 6, pp. 3193–3328, Jun. 2012.
- [196] H. Hoegl, “On Photoelectric Effects in Polymers and Their Sensitization by Dopants,” *J. Phys. Chem.*, vol. 69, no. 3, pp. 755–766, 1965.
- [197] J. V. Grazulevicius, P. Strohriegl, J. Pielichowski, and K. Pielichowski, “Carbazole-containing polymers: synthesis, properties and applications,” *Prog. Polym. Sci.*, vol. 28, no. 9, pp. 1297–1353, 2003.
- [198] B. Romero, M. Schaer, M. Leclerc, D. Ades, A. Siove, and L. Zuppiroli, “The role of carbazole in organic light-emitting devices,” *Synth. Met.*, vol. 80, no. 3, pp. 271–277, 1996.
- [199] G. E. Johnson, “Emission properties of vinylcarbazole polymers,” *J. Chem. Phys.*, vol. 62, no. 12, pp. 4697–4709, 1975.
- [200] S. Dong, Z. Li, and J. Qin, “New Carbazole-Based Fluorophores: Synthesis , Characterization , and Aggregation-Induced Emission Enhancement,” *J. Phys. Chem. B*, vol. 113, pp. 434–441, 2009.
- [201] Z. Liu *et al.*, “Red phosphorescent iridium complex containing carbazole-functionalized β -diketonate for highly efficient nondoped organic light-emitting diodes,” *Adv. Funct. Mater.*, vol. 16, no. 11, pp. 1441–1448, 2006.
- [202] A. Endo *et al.*, “Efficient up-conversion of triplet excitons into a singlet state and its application for organic light emitting diodes,” *Appl. Phys. Lett.*, vol. 98, no. 8, pp. 9–12, 2011.
- [203] T. Matulaitis *et al.*, “Impact of Donor Substitution Pattern on the TADF Properties in the Carbazolyl-Substituted Triazine Derivatives,” *J. Phys. Chem. C*, vol. 121, no. 42, pp. 23618–23625, 2017.
- [204] J. Roy, A. K. Jana, and D. Mal, “Recent trends in the synthesis of carbazoles : an update,”

References

- Tetrahedron*, vol. 68, no. 977, pp. 6099–6121, 2012.
- [205] M. B. Smith and J. March, *March's Advanced Organic Chemistry: Reactions, Mechanisms, and Structure: Sixth Edition*, 7th ed. Hoboken, New Jersey: John Wiley & Sons, Inc., 2013.
- [206] Y. Shirai *et al.*, “Surface-Rolling Molecules,” *JACS*, vol. 128, no. 4, pp. 4854–4864, 2006.
- [207] I. P. Beletskaya and A. V. Chepurkov, “Copper in cross-coupling reactions The post-Ullmann chemistry,” *Coord. Chem. Rev.*, vol. 248, pp. 2337–2364, 2004.
- [208] A. Klapars, X. Huang, and S. L. Buchwald, “A General and Efficient Copper Catalyst for the Amidation of Aryl Halides extensively utilized in the medicinal chemistry and process,” *J. Am. Chem. Soc.*, vol. 124, no. 8, pp. 7421–7428, 2002.
- [209] E. R. Strieter, D. G. Blackmond, and S. L. Buchwald, “The Role of Chelating Diamine Ligands in the Goldberg Reaction : A Kinetic Study on the Copper-Catalyzed Amidation of Aryl Iodides,” *J. Am. Chem. Soc.*, vol. 127, pp. 4120–4121, 2005.
- [210] J. P. Wolfe, S. Wagaw, and S. L. Buchwald, “An improved catalyst system for aromatic carbon-nitrogen bond formation: The possible involvement of bis(phosphine) palladium complexes as key intermediates,” *J. Am. Chem. Soc.*, vol. 118, no. 30, pp. 7215–7216, 1996.
- [211] M. W. Hooper, M. Utsunomiya, and J. F. Hartwig, “Scope and mechanism of palladium-catalyzed amination of five-membered heterocyclic halides,” *J. Org. Chem.*, vol. 68, no. 26, pp. 2861–2873, 2003.
- [212] L. Kürti and C. B., *Strategic application of Named Reactions in Organic Synthesis*. Elsevier, 2005.
- [213] B.-Y. Lim, M.-K. Choi, and C.-G. Cho, “Acid-catalyzed condensation of 2,2'-diamino-1,1'-biaryls for the synthesis of benzo[c]carbazoles,” *Tetrahedron Lett.*, vol. 52, no. 45, pp. 6015–6017, 2011.
- [214] Y. Lim, J. Jung, H. Lee, and C. Cho, “Acid-Catalyzed Rearrangement of Diaryl Hydrazides for the Efficient Synthesis of Functionalized 2,2'-Diamino-1,1'-biaryls,” *J. Org. Chem.*, vol. 69, no. 17, pp. 5778–5781, 2004.
- [215] D. Lee, M. P. Huestis, D. R. Stuart, K. Fagnou, and B. Liégault, “Intramolecular Pd (II)-Catalyzed Oxidative Biaryl Synthesis Under Air : Reaction Development and Scope

References

- Benoît Lie,” *J. Org. Chem.*, vol. 73, no. II, pp. 5022–5028, 2008.
- [216] H. R. Bjørsvik and V. Elumalai, “Synthesis of the Carbazole Scaffold Directly from 2-Aminobiphenyl by Means of Tandem C–H Activation and C–N Bond Formation,” *European J. Org. Chem.*, vol. 2016, no. 33, pp. 5474–5479, 2016.
- [217] M. Schmidt and H. J. Knölker, “Transition metals in organic synthesis, part 91:1 palladium-catalyzed approach to 2,6-dioxygenated carbazole alkaloids - First total synthesis of the phytoalexin carbalexin C,” *Synlett*, no. 15, pp. 2421–2424, 2009.
- [218] M. A. Martin and J. Carlos Menendez, “Synthesis of Oxygenated Carbazoles by Palladium-Mediated Oxidative Double C-H Activation of Diarylamines Assisted by Microwave Irradiation,” *Synlett*, vol. 15, pp. 2375–2378, 2006.
- [219] T. Watanabe, S. Oishi, N. Fujii, and H. Ohno, “Palladium-Catalyzed Direct Synthesis of Carbazoles via One-Pot *N*-Arylation and Oxidative Biaryl Coupling: Synthesis and Mechanistic Study,” *J. Org. Chem.*, vol. 74, no. 13, pp. 4720–4726, Jul. 2009.
- [220] H. Gao, Q.-L. Xu, M. Yousufuddin, D. H. Ess, and L. Kürti, “Rapid Synthesis of Fused N-Heterocycles by Transition-Metal-Free Electrophilic Amination of Arene C-H Bonds,” *Angew. Chemie Int. Ed.*, vol. 53, no. 10, pp. 2701–2705, Mar. 2014.
- [221] D. M. Chen, Q. Qin, Z. B. Sun, Q. Peng, and C. H. Zhao, “Synthesis and properties of B,N-bridged p-terphenyls,” *Chem. Commun.*, vol. 50, no. 7, pp. 782–784, 2014.
- [222] D. Curiel, M. Más-Montoya, A. Uruvakili, R. A. Orenes, H. Pallamreddy, and P. Molina, “Synthesis and characterization of new carbazolocarbazoles: Toward π -extended N-fused heteroacenes,” *Org. Lett.*, vol. 12, no. 14, pp. 3164–3167, 2010.
- [223] A. W. Freeman, M. Urvoy, and M. E. Criswell, “Triphenylphosphine-mediated reductive cyclization of 2-nitrobiphenyls: A practical and convenient synthesis of carbazoles,” *J. Org. Chem.*, vol. 70, no. 13, pp. 5014–5019, 2005.
- [224] F. Zhang, S. Zhang, and X. F. Duan, “Substitution of the nitro group with Grignard reagents: Facile arylation and alkenylation of pyridine N-oxides,” *Org. Lett.*, vol. 14, no. 21, pp. 5618–5620, 2012.
- [225] N. Miyaura, K. Yamada, H. Suginome, and A. Suzuki, “Novel and convenient method for the stereo- and regiospecific synthesis of conjugated alkadienes and alkenynes via the palladium-catalyzed cross-coupling reaction of 1-alkenylboranes with bromoalkenes and

References

- bromoalkynes,” *J. Am. Chem. Soc.*, vol. 107, no. 4, pp. 972–980, 1985.
- [226] T. E. Barder, S. D. Walker, J. R. Martinelli, and S. L. Buchwald, “Catalysts for Suzuki-Miyaura coupling processes: Scope and studies of the effect of ligand structure,” *J. Am. Chem. Soc.*, vol. 127, no. 13, pp. 4685–4696, 2005.
- [227] J. Yin, M. P. Rainka, X. Zhang, and S. L. Buchwald, “Communication A Highly Active Suzuki Catalyst for the Synthesis of Sterically Hindered Biaryls : Novel Ligand Coordination A Highly Active Suzuki Catalyst for the Synthesis of Sterically Hindered Biaryls : Novel Ligand Coordination,” *J. Am. Chem. Soc.*, vol. 124, pp. 1162–1163, 2002.
- [228] T. Ishiyama, M. Murata, and N. Miyaura, “Palladium(0)-Catalyzed Cross-Coupling Reaction of Alkoxydiboron with Haloarenes: A Direct Procedure for Arylboronic Esters,” *J. Org. Chem.*, vol. 60, no. 23, pp. 7508–7510, 1995.
- [229] D. M. Knapp, E. P. Gillis, and M. D. Burke, “A General Solution for Unstable Boronic Acids : Slow-Release Cross-Coupling from Air-Stable MIDA Boronates,” *J. Am. Chem. Soc.*, vol. 131, pp. 6961–6963, 2009.
- [230] B. S. Kim, S. Y. Lee, and S. W. Youn, “Pd-catalyzed sequential C-C and C-N bond formations for the synthesis of N-heterocycles: Exploiting protecting group-directed C-H activation under modified reaction conditions,” *Chem. - An Asian J.*, vol. 6, no. 8, pp. 1952–1957, 2011.
- [231] C. Suzuki, K. Hirano, T. Satoh, and M. Miura, “Direct Synthesis of N-H Carbazoles via Iridium(III)-Catalyzed Intramolecular C–H Amination,” *Org. Lett.*, vol. 17, no. 6, pp. 1597–1600, Mar. 2015.
- [232] M. Lafrance and K. Fagnou, “Palladium-Catalyzed Benzene Arylation: Incorporation of Catalytic Pivalic Acid as a Proton Shuttle and a Key Element in Catalyst Design,” 2006.
- [233] W. C. P. Tsang, N. Zheng, and S. L. Buchwald, “Combined C-H Functionalization/C-N Bond Formation Route to Carbazoles,” 2005.
- [234] S. H. Cho, J. Yoon, and S. Chang, “Intramolecular Oxidative C À N Bond Formation for the Synthesis of Carbazoles : Comparison of Reactivity between the Copper-Catalyzed and Metal-Free Conditions,” *J. Am. Chem. Soc.*, vol. 133, pp. 5996–6005, 2011.
- [235] S. Sajjadifar *et al.*, “Facile Method of Quinoxaline Synthesis Using Phenol as a New, Efficient and Cheap Catalyst at Room Temperature,” *Am. J. Org. Chem.*, vol. 2, no. 4, pp.

References

97–104, 2012.